Revealing the Webs

Insights from the Exploitation of Complementary Information from various Magnetic Resonance Imaging related Connectivity Methods

Dissertation
zur Erlangung des Grades eines
Doktors der Naturwissenschaften
(Dr. rer. nat.)
der Mathematisch-Naturwissenschaftlichen Fakultät
und
der Medizinischen Fakultät
der Eberhard Karls Universität Tübingen
vorgelegt von

Dipl.-Psych. Bálint Várkuti

aus Budapest, Ungarn

Tübingen
August, 2011

Tag der mündlichen Prüfung:	13.10.2011
Dekan der Math.-Nat. Fakulät:	Prof. Dr. Wolfgang Rosenstiel
Dekan der Medizinischen Fakulät:	Prof. Dr. I. B. Autenrieth
1. Berichterstatter:	Prof. Dr. Niels Birbaumer
2. Berichterstatter:	Prof. Dr. Martin Hautzinger
Prüfungskomission:	Prof. Dr. Kamil Uludag
	Prof. Dr. Christoph Braun

Declaration

I hereby declare that I have produced the work entitled: "Revealing the Webs", submitted for the award of a doctorate, on my own (without external help), have used only the sources and aids indicated and have marked passages included from other works, whether verbatim or in content, as such. I swear upon oath that these statements are true and that I have not concealed anything. I am aware that making a false declaration under oath is punishable by a term of imprisonment of up to three years or by a fine.

Tübingen, den 14.8.2011 .....

Acknowledgments

I would like to thank Professor Niels Birbaumer for giving me the opportunity to work in his lab, for his patience and for always bringing me back down to earth when it was necessary.

I would also like to thank the other members of my supervisory board for their support and advice during so many questions and lively debates.

I want to especially thank Ranganatha Sitaram for being my supervisor and close colleague over the years, for supporting me and for patiently reading through tons of my half-baked ideas.

I want to thank my colleagues and collaborators at the Institute of Medical Psychology and Behavioral Neurobiology for all their help and a great time.

Most of all I would like to thank my mother Iren and my father Geza for always supporting me no matter what I did, and for being there for me during this time. And I want to thank my friends who kept me sane throughout these years, and thank a certain foggy place in Freiburg where I had my best ideas.

And last but not least, I want to thank my wonderful wife Jessica who did not run away from the crazy brain scientist, but came with me and changed ours lives to the better.

We shall not cease from exploration. And the end of all our exploring will be to arrive where we started and know the place for the first time.

T.S. Eliot

Contents

1 Introduction

Information processing, memory storage or the adaptation of behavior do not occur solely within single specialized computational units of the human brain such as the single neuron, but require the ordered interplay of many such computational units. Although the physical manifestation of behavior can be caused by volitional control of a single neuron (Fetz, 2007), even in this case other neurons and entire neuronal ensembles play a central role in the conditioning processes involved with gaining volitional control over the spike trains of the target neuron. Consequentially, when we refer to any brain function we implicitly refer to phenomena generated by the ordered cooperation of neural computational units within neural networks.

When moving up the spatial scale, the first microscopic level of such interplay - if we ignore the role of astrocytes for now (Schummers et al., 2008) - is the ordered interaction of multiple neighboring neurons via synapses, followed by the interaction of larger neuronal ensembles in mesoscale structures such as cortical columns and finally the interaction of multiple neuronal ensembles across larger distances - and via white matter fibre bundles - in macroscale neuronal networks.

Beyond the spatial scale such interactions can be sorted along the temporal dimension as well, starting with the quasi-simultaneous firing of single neurons or neuron groups leading to strengthened associations between them based on Hebbian learning (Abbott and Nelson, 2000), followed by more sequential constellations of causally interdependent neuronal excitations - as in the case of neural avalanches (Beggs and Plenz, 2003) - or inhibitions and finally the more delayed forms of interactions, where the complex intra-modular interplay of a neural ensemble triggers the eventual intra-modular interplay of another distant neural ensemble, a constellation where distinct neural events can become distinguishable.

Clearly the healthy brain at large is practically never in a state of communicatory silence. The concept of such neural events does not refer to bursts of neural firing that break states of neural rest, but rather refers to temporally delimitable and spatially localized changes in the patterns of neurotransmission. Such changes can be causally linked in sequences, feedforward- or feedback loops, but might appear synchronous to an observer if for example the temporal resolution of the measurement method is too low.

Such distinctions strongly depend on the spatial and temporal scale of the measurement method and on how indirectly the measured metric is linked to the actual neuronal processing itself. In the case of Blood Oxygen Level-Dependent (BOLD) functional Magnetic Resonance Imaging (fMRI) the spatial scale is in the range of millimeters, the temporal scale is usually on the order of seconds

and the measured metric, namely the local ratio of oxygenated versus deoxygenated hemoglobin, represents a - not always unambiguous - delayed metabolic echo of macroscale neural processes (Logothetis, 2008). These limitations of our insight into in-vivo neural processes shape the appearance of neural networks to us (illustrated in Figure 1).

Neural networks on the macro- or mesoscale can appear to us in an fMRI analysis as one clump of synchronously activating points in the brain (e.g. the V1 area) which we then can associate with the assumed trigger event or the independent variable that we manipulated experimentally (e.g. the display of a checkerboard on the screen). But they can also appear as multi-site events, where synchronous neural activation or de-activation is detected at multiple distant sites but at the same time.

These formations of temporally coherent changes in activity are what we usually refer to as Functional Connectivity Network (FCN). Examples of such networks are the Default Brain Mode network (Raichle et al., 2001) which we associate with resting behavior, or the prefrontal executive control network which is associated with volitionally executed complex tasks (Seeley et al., 2007a). With other methods, such as electrophysiology, which measure neural activity more directly via the electromagnetic distortions that macroscale neural processes cause, FCNs appear mainly as statistical interactions between sensors (Micheloyannis et al., 2006). Although the temporal resolution of these methods is magnitudes higher than that of hemodynamics based methods such as fMRI, the spatial characterization, of where the functional interactions, that correspond to the changes in the electromagnetic field, occur exactly in the brain remains challenging (Wendel et al., 2009).

But irrespective of which method of study and which emphasis in analysis is chosen, it is clear that the underlying neural processes we try to gather when studying FCNs are not entirely understood with respect to how and why they form in their specific spatial and temporal configurations.

Beyond studying which stimuli, contexts or tasks elicit how much activity in which neural network, a second perspective on networks has co-evolved alongside classical experimentation (Van Dijk et al., 2010). This discipline is trying to answer such questions as how these networks are formed (Bullmore and Sporns, 2009), why we observe exactly this limited set of networks and not others or how the boundaries of the underlying static system these dynamic networks form within influence them (Honey et al., 2009), and vice versa. As such we have begun to study the complexity of the interaction of systems in the brain itself, rather than reducing our efforts to focusing merely on the complexity of single parts, scales or levels (Barabási, 2012). To deepen our

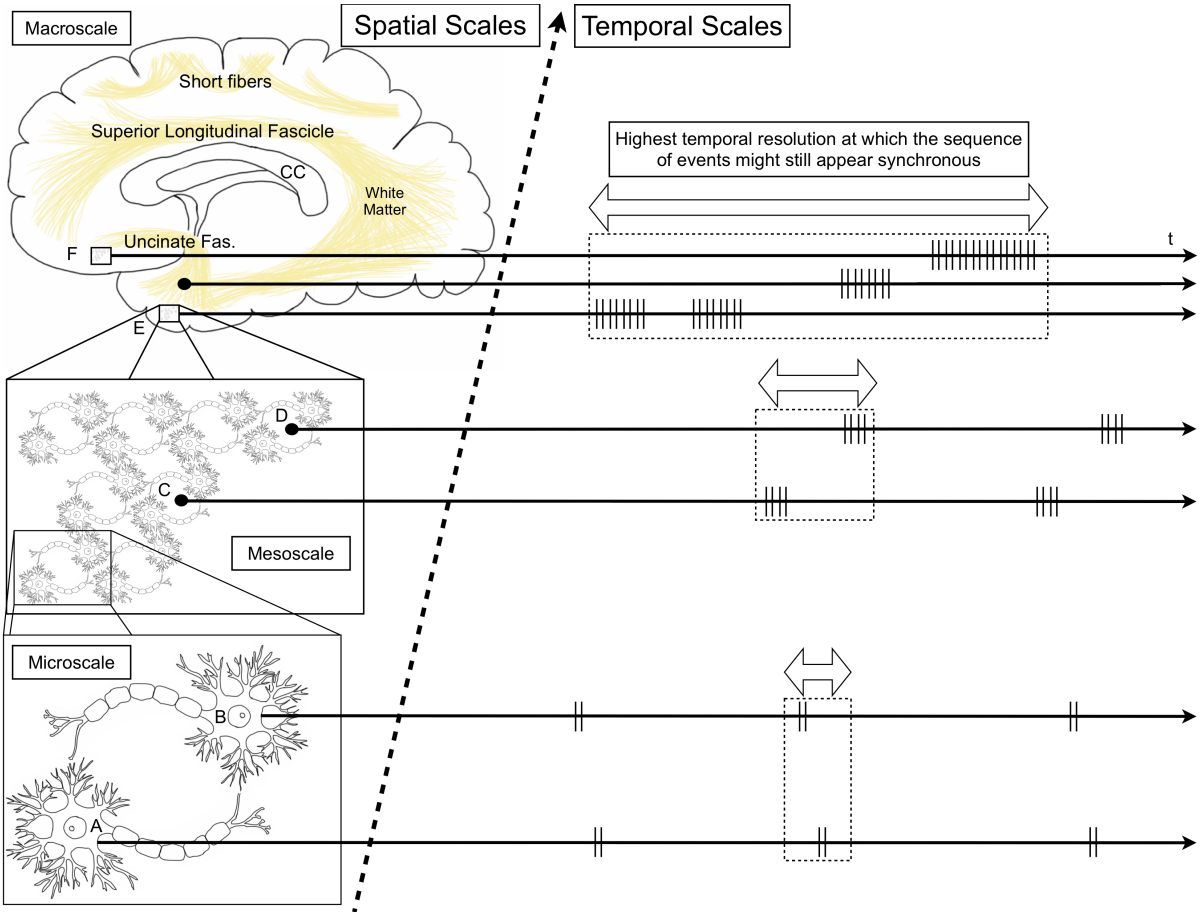

Figure 1 – Illustration of interactivity on various spatial and temporal scales. On the microscopic scale the quasi-simultaneous firing pattern of neuron A and B might appear synchronous is the temporal resolution of our recording method does not exceed the resolution indicated by the thick arrow (with higher temporal resolution the thick arrow becomes shorter), but if the temporal resolution is adequate the activity previously perceived as a singular event (indicated by the dotted line box) is resolved into two singular events (or even four single spikes if the resolution is increased further). The same principle applies to mesoscale interactivity where small groups or pairs of neurons might exchange spike trains within a cortical-column, if the resolution is poor the mesoscale structure might be perceived as being active as a whole, while actually subgroups C and D are communicating with temporal delay. When observing macroscale events, such as the illustration of activity in area E, the transmission of information through the Uncinate Fascicle (middle timeline) and the subsequent activity in area F, E and F might be perceived as being functionally connected at a poor temporal resolution but are actually active in a feedforward type of communication pattern. It is to be noted that E and F could not communicate in this example without the sketched white matter bundle connecting them. The figure illustrates, that with perfect spatial and temporal resolution single events and functional connectivity might be decomposed into a more complex interactivity pattern.

understanding of these links is relevant for basic research with healthy individuals, but even more so in the clinical context (Lawrie et al., 2008).

Neural networks in the brain change over time due to learning (Tamás Kincses et al., 2008), maturation (Dosenbach et al., 2010; Casey et al., 2005) or degradation (Greicius et al., 2004; Wu et al., 2011) but do this within the boundaries that are set by structure/function relationships. One region of the brain might for example not be able to provide all the neurocomputational processing or the right neuronal assemblies required for the successful execution of a certain behavior, so a second region is recruited that complements the processing of the first region. With more and more training, the interplay between these regions usually changes and becomes more fine-tuned and economical (Voss et al., 2011; Lee et al., 2011), but if the direct structural link between these regions is severed and no poly-synaptic neural detour is at disposal, the shape, capacity and behavioral significance of this neural network will be massively altered - one drastic example of how structure can restrict function.

But the brain can not simply add more and more neuronal ensembles to a neural process like a computer might activate more and more processors to solve a given problem quickly. Not all neuronal ensembles are capable of performing all neurocomputational processing tasks but quite the contrary. There are certain basic restrictions in the functional roles brain regions can assume, and because not each brain region can assume any functional role, the ensembles in which brain regions are associated in FCNs do not form arbitrarily but in a manner depending very specifically on the task at hand.

The restrictions that define the functional roles brain regions can assume are reflected in our dissociation of brain regions into primary sensory, primary motor, subcortical, secondary or association cortex regions. These regions differ with regard to multiple traits, such as their physical position in the brain, their anatomical connectivity via white matter fiber bundles, their local vasculature and relative perfusion, the range and type of neurons contained within such a region, the ordering of cortical layers, the integrity and Gray Matter Volume (GMV) in general, the intra-modular wiring pattern, neurotransmitter availability and many other factors. As such each region can be described as a point in a multi-dimensional feature space, where each feature in question is one of these multiple traits. This principle is illustrated for the properties perfusion, connectivity and GMV in Figure 2. Clearly all these factors have been shaped by both phylogenetic and ontogenetic development in the individual brain, resulting in relatively stable structural properties that restrict the formation of neural networks in specific ways.

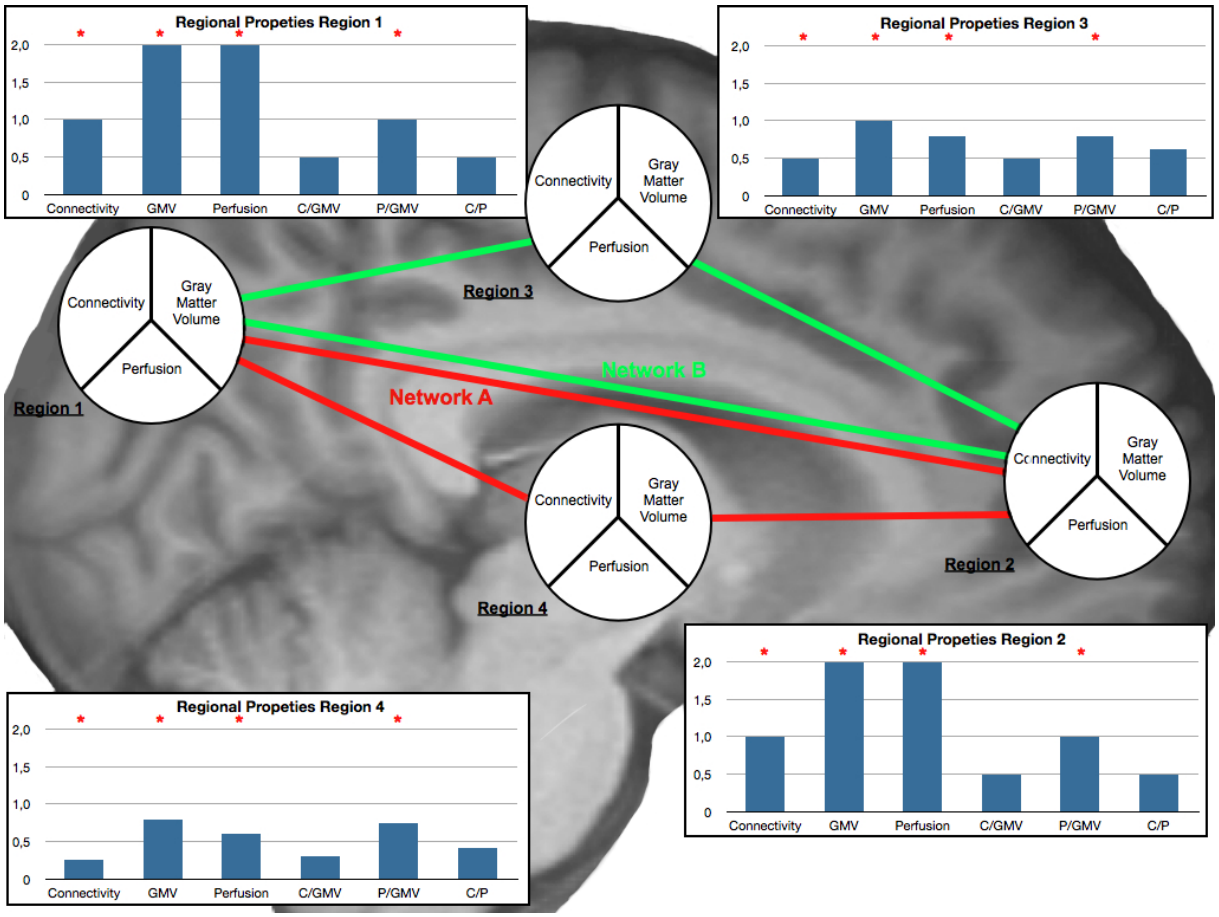

Figure 2 – Illustration of general principle, Regions 1 and 2 engage in both FCNs A (red) and B (green), but Regions 3 and 4 only engage in one network, either network A (Region 4) or B (Region 3) - a look at the regional properties shows that regions engaging in multiple networks differ from those that are only member of one network (marked by red asterisks), these regions have higher GMV, Perfusion and Connectivity than regions which are only members of one network and that these also have a more balanced perfusion and GMV ratio (Ratio P/GMV), the illustrated concept motivated one of our studies (Várkuti et al., 2011) which can be found in Chapter 1.

Multiple phenomena in neurological and psychiatric practice are related to restrictions or alterations of the brains' ability to form or maintain adaptive and economical neural networks (Lawrie et al., 2008; Whitfield-Gabrieli et al., 2009; Demirci et al., 2009; Rubinov et al., 2009; Jafri et al., 2008; Lynall et al., 2010; Whitford et al., 2010; Begré et al., 2003; Cammoun et al., 2009). This is reflected in findings on the biomarkers of disease, where structural differences in the brain can successfully be correlated with pathology.

Such biomarkers are being successively narrowed down for phenomena such as Amyotrophic Lateral Sclerosis (ALS) (Senda et al., 2011; Woolley et al., 2011; Filippini et al., 2010), autism spectrum disorders (Eigsti and Shapiro, 2003) or ageing and dementia (Head et al., 2004). Some of the structural changes that are identified as biomarkers might have co-evolved with the pathology,

some might have preceded or even caused the outbreak of a disease, while others might be the result of compensatory or other after-effects of certain functional abnormalities. Such changes can be rather sudden in terms of onset and effect, such as for example the paralysis due to disconnection of the motor system and the periphery after stroke, while others might emerge much slower such as for example cortical atrophy, disconnection and hypoperfusion in certain forms of neurodegenerative disease such as dementia (Grundman et al., 2002; Fellgiebel et al., 2004; Stam et al., 2007; Devanand et al., 2007; Stam et al., 2009; Chao et al., 2010; Seeley et al., 2009a; Bottino et al., 2002; Sugihara et al., 2004) or manifest in a contra-intuitive form (Madhavan et al., 2010).

Local structural traits are properties of a brain region that only change slowly, such as for example anatomical connectivity, tissue volume or vascularization. These traits either enable or restrict brain function in a specific way or can change themselves as a result of brain activity (e.g. the way extensive practice of a musical instrument can change the cortical representation of the hands). In the case of disease we often can identify biomarkers which are structural traits, because these have been either altered by the disease or played a role in the etiology, or both. From these cases we infer structure/function relationships that try to summarize our findings and allow for the deduction of new hypotheses.

In this sense, structure/function relationships are essentially formulated as rules, which are based on empirical evidence either from (quasi-)experimental (e.g. does structural similarity of monozygotic twins predict functional similarities?) or correlative studies (e.g. does anatomical connectivity predict the likelihood of functional connectivity between a pair of regions?).

Such rules can be very simple, such as that there can be no neural activity where metabolic prerequisites such as a supply of oxygen and glucose are not given. But these rules can as well be more complex, such as that functional connectivity on a specific timescale (e.g. milliseconds) between a group of regions is only possible if these regions are directly anatomically connected through white matter fibre bundles with intact myelinisation and hence good electrical conduction properties. Such rules can incorporate additional pathogenic factors, such as predictions where neural communication is expected to be macroscopically distorted for example as a function of amyloid plaque concentration in the brain (Ross and Poirier, 2004; Wu et al., 2011; Stam et al., 2009).

If we understand how the the entirety and interplay of local brain traits - further referred to

as the underlying system - generates neural networks in the absence of external stimuli (such as the Default Brain Mode network) or for example as a result of repeated activity patterns - which is the case in learning and training - we would be able to formulate rules by which structure restricts or enables function, or by which function alters structure over time. If we are able to broaden our understanding of these rules, our ability to predict and influence the progression of diseases would improve dramatically.

One example with which this can be illustrated are atlases and more generally brain parcellation schemes. The parcellation and functional description of brain regions did not evolve much further than uniting the early cytoarchitectonic distinction (Brodmann, 1909) of regions with long lists of functional observations detailing which experimental contexts led to localized activity in which brain region. Even when it became apparent that functional networks do span across cytoarchitectonic boundaries, only minimal changes to the standard parcellation schemes were made.

These parcellation schemes or atlases are closely based on neurological experience (lesion and stimulation studies) and experimental evidence (neuroimaging data) but primarily contain a list of cerebral landmark positions and the associated functions. As such, these descriptions have to remain on a qualitative level of distinction, as long as the rules that govern the emergence of functional from structural properties are not understood, and vice versa.

In essence, atlases contain information that is based on a simple rule - if the position A in the brain is defined by the following x,y and z coordinates, predictable alterations of activity in that spot A are expected in healthy/patient populations in a given context that we thus associate with that position. This context is defined by the presented stimuli, circumstantial factors and the task at hand. For example if we ask a participant to perform a fingertapping task with the right hand we expect directly an increase in activity in a landmark we termed the left primary motor cortex. By understanding the rules that govern the emergence of functional properties on a deeper level, the qualitative component of such a rule (the landmark part so to speak) can be replaced. Predictable alterations of activity are expected as a result of for example a fingertapping task in all areas of the brain that fulfill a set of criteria, such as direct connectivity to the motor pathways, the existence of pyramidal neurons in that region, no hypoperfusion, no cortical atrophy, the presence of the relevant motor assemblies on the mesoscale etc. Measures that describe these criteria can be acquired using measurement methods from multiple modalities whose combined data will thus allow us to predict where in the brain activity will be altered.

At first, such an approach might appear unnecessarily complex when compared with the classical

atlases, but it is the collection of such rules that delineate the transformation of atlases, away from being a combination of landmarks and function lists (or lists of lesions and their consequences), to becoming bottom-up generated models, where the emergence of certain brain states can be predicted from measuring a multitude of relevant local and global traits. Violations to the rule either call for an update or extension of the rule (a classical case where we mistook correlation for causality) or hint at pathological changes (e.g. no activity in the contralateral motor cortex after fingertapping in a fully connected and intact motor cortex is a sign that something is not right). Such rules are what transforms data into an interpretable form and allow us to understand why the lines we have been drawing for centuries to parcellate the human brain are exactly where they are.

Clearly this example is a crude simplification, but it is such rule sets and the predictions we generate based on them that are the implicit products of empirical neuroscience, even if we might seldom formulate them so naively.

In order to understand the rules that govern structure/function relationships with respect to the emergence of FCNs it is important to understand how the constituents of the underlying system are linked with one another, and how all the constituents act together in the formation or restoration of these neural networks.

In the present work we tried to understand how cerebral perfusion, macroscale anatomical connectivity through white matter fibre bundles and gray matter tissue volume are interrelated and how they influence certain local properties of the brain, which are essential for the formation of FCNs.

To do this, a comprehensive set of FCNs was characterized using fMRI in order to create a taxonomy of these networks and to study how network formation is related to properties of the underlying system. Following the main research focus of our institute, the results are finally applied to understand the effect of the underlying anatomy on particular electrophysiological features related to Brain-Computer Interface (BCI) aptitude, and the effects of training on pathologically altered FCNs after stroke.

1.1 Current Connectivity concepts and terminology

The three most relevant connectivity concepts in use in present days neuroimaging are anatomical connectivity, functional connectivity and effective connectivity (Sporns, 2007).

These concepts embody the notion that connectivity can either refer to a physical link between two areas, or to some kind of statistical association of their activity profile over time.

Although a multitude of physical links can exist between regions in the brain - they might share the same blood supply structure, be linked by the same ventricle, might by separated by the same type of cells - the term macroscopic anatomical connectivity is mostly understood as a measure reflecting the amount and quality of axonal connections (converging in fibre bundles) between two regions.

Notions of functional and effective connectivity on the other hand strongly rely on the temporal resolution with which brain activity is measured.

Functional connectivity - defined as temporally synchronous activity in at least two spatially remote regions - can dissolve into its underlying effective connectivity - defined as the directed influence that parts of a system exert onto one another - patterns when temporal resolution is increased (see Figure 1).

Unfortunately in the case of fMRI, increasing the temporal resolution of BOLD imaging is only of limited use, since we can not gain more direct information on neural activity by merely measuring a time delayed indirect indicator - the hemodynamic response - more precisely.

The three types of connectivity are systematically linked (van den Heuvel et al., 2009), since anatomical connectivity defines the temporal boundaries for communication between parts of the system - for example conduction delay times, path length in terms of direct vs. indirect connections - which in turn shapes global communicational hierarchies (e.g. association cortex vs. primary sensory cortex regions), the possibility of local feedback loops, information exchange rate and speed in the form of up- and downstream patterns and the extent of local information convergence and dispersion.

In effect, the hardwired and relatively (Lebel and Beaulieu, 2011) static system of white matter connections in the adult brain defines the boundaries within which patterns of neural interaction can emerge (Horwitz et al., 2005; Fonteijn et al., 2008). Effective connectivity patterns - essentially causally linked sequences of neural events - can only occur within these boundaries, and the coherent metabolic activity of entire networks, as observed with hemodynamics based functional connectivity methods, is often only the blurred reflection of many such fast neural event sequences.

In that context, neural events can occur on all scales (the micro-, meso- and macroscale), but it is mainly fast causal interactivity on smaller scales (the interaction of single neurons on the microscale e.g. within a neural column), that eventually produces patterns of activity on larger scales that have slower state transitions (such as the activity of cortical columns on the mesoscale or the activity of interregional networks on the macroscale, see Figure 1).

It is to be noted that univariate analysis methods that have dominated fMRI data analysis do not necessarily stand in opposition to connectivity analysis. A localized area of adjacent voxels that is more active in one condition than another is merely a FCN of adjacent voxels, whose common hemodynamic response reflects the metabolic demands originating from the sequence of neural events occurring within that brain region.

Neural functional connectivity though, in the true sense of the concept, can not directly be measured with hemodynamics based methods, as this type of connectivity is conceptually a measure of neural synchronization (Varela et al., 2001). Non-invasive electrophysiological methods such as the Electroencephalogram (EEG) or Magnetoencephalography (MEG) and invasive methods such as Electrocorticography (ECoG) are far better suited to resolve such relations due to their superior temporal resolution and the fact that neuroelectrical activity is a more direct measure of neuronal activation than the traces of indirectly related local metabolism, which we traditionally measure with methods like functional Near Infared Spectroscopy (fNIRS), Positron Emission Tomography (PET) or fMRI.

On this level, empirical studies and simulations have shown that neural synchronization is happening in predictable and ordered patterns in the human brain, pointing towards the existence of spatial and temporal restrictions for interactivity, imposed by a more static underlying system (Kitzbichler et al., 2009). It stands to reason, that this underlying system is defined by the anatomical traits of the brain, such as anatomical connectivity, type and conduction speed of fibers, relative spatial position and distance of brain regions to another, local and global metabolic supply characteristics, local neurocomputational capabilities of brain regions, local number and composition of certain neuron types, local neurotransmitter concentrations and availability and many more.

It is to be noted that although the spatial resolution of fMRI images is quite low, the small differences in spatial frequency in the underlying neural activity could have a summative effect on the macroscopic scale, especially when analyzed with sensitive techniques such as multivariate pattern analysis. Thus, in a surprising finding Kamitani and Tong (2005) have shown that minute

differences in neural activations pertaining to visual orientation gratings could be decoded from fMRI signals.

But if fMRI is mainly a macroscopic measure reflecting relatively slowly changing summation effects, then why study functional connectivity with hemodynamic methods at all?

Although fMRI FCNs are only an indirect and macroscopic measure of the underlying neural processes, these FCNs are of high diagnostic value. Every healthy human of a particular age group has a number of FCNs that can be termed the canonical FCNs (Beckmann et al., 2005; Dosenbach et al., 2007).

Some of these are related to normal motor function, execution and attention (Seeley et al., 2007b), others to consciousness, working memory or spatial orientation. If none of the measured FCNs correspond to the canonical FCNs or those observed are deformed, that is a clear indicator of severe brain dysfunction (Greicius et al., 2004) and probably underlying structural damage. Similarly FCNs that change over time have to correspond to effects of either structural plasticity, functional reorganization or both (see Chapter 3).

Among the entirety of fMRI observable FCNs the number of those which are actually observed represent only a minimal fraction of those networks that would theoretically be observable based on the number of parts in the system. If we assume 116 distinct brain regions - on the basis of the Automated Anatomical Labeling (AAL) atlas - we could theoretically observe any network with at minimum 2 and maximum 116 parts, leading to the astronomical number of $8.3077 * 10^{34}$ possible distinct networks. If we allow for a maximum of 8 network members (based on our findings in our taxonomy work in Chapter 2) this number is - with $6.8506 * 10^{11}$ - still much higher than any reported number of empirically observed distinct networks. Even if we do not follow the network stereotyping method proposed in our taxonomy paper (identifying 172 stereotypical networks), or assume that the initial value of 5812 networks represents the true value of plausible networks in the sample (please see Chapter 2 for details) in any way the identified (by us and others) variety of canonical networks represent only a minimal fraction, in any case less than 10^{-8} the number of the theoretically possible networks. This can be attributed to the fact that FCNs do neither form randomly nor form in just any theoretically possible configuration, but are an emergent property of the underlying system which sets the boundaries for FCN formation and maintenance (Honey et al., 2009).

Evidently the relationship of properties of the underlying system and FCNs needs to be studied

on a deeper level, to advance our understanding of to what extent FCN changes trigger plasticity processes and changes of the underlying structure or to which extent training and learning influence structure, and vice versa (Takeuchi et al., 2010). In that sense, the object of study are the rules with which we express observed structure/function relationships and that also define the possibility space for FCN formation in the human brain. But how did FCNs and structure/function relationships enter the focus of the neuroscientific community?

1.2 Localizationism, disconnection syndromes and systems neuroscience

Localizationism was a dominating paradigm in neuroscience in the 19th century, when experiments utilizing electrical stimulation of the animal cortex demonstrated that one organizational principle of the brain is anatomically segregated functional specialization.[1]

The excitation of specific areas of the cortex produces direct and clear behavioral responses, leading up to an idea essentially formulating the existence of distinct neural "organs"on the cortex, the concept for which Franz Joseph Gall coined the term cortical organs (Frackowiak, 2004).

Around the transition of the 19th and 20th century Theodore Meynerts work - the detailed neuroanatomical study of white matter bundles - influenced Karl Wernicke into formulating his doctrine of the associationist school and into interpreting observations of patients with specific - particularly white matter - brain lesions and specific symptomes (e.g. conduction aphasia) as disconnection syndromes (Catani and Ffytche, 2005).

This new school of thought envisioned that certain psychological phenomena can only emerge if the association pathways in the brain are uninterrupted and the brain can puzzle together perceptual inputs and motoric outputs with consciousness - much like a mosaic. The idea was born that multiple parts of the system needed to cooperate to provide certain functions.

Soon after that, the observation of dysfunction in brain areas distant but connected to a lesion site that could not be explained by the spread of structural damage delivered further evidence that opposed simple localizationism, leading to the term and concept of diaschisis in the early 20th century (coined by Constantin von Monakow in 1914).

The rise of refined anatomical methods - namely Alfred Walter Campbell's and Korbinian Brodman's cytoarchitectonic division of the cortex - and the culmination of observation data from brain lesion patients into cortical mappings of higher brain function (as by Karl Kleist in 1934) weak-

[1] Historical recapitulation closely based on the review work by Catani and Ffytche

ened the associacionist perspective and triggered at the same time a counter-movement opposed to localizationism or associationism, namely the holistic perspective that was present in neuroscience until Norman Geschwind.

Geschwind's work - particularly on callosal sections in animals and epilepsy patients - in the 70s on the concept of disconnection syndromes and the relevance of the association cortex revived the connectivity perspective. But it was his incorporation of Paul Flechsig's work on the association cortex as a relay station between lower order systems that marks an essential cesura in our perspective on brain parts (Catani and Ffytche, 2005).

In Wernicke's view, lesions of the connections - the edges in a network graph - produced syndromes such as conduction aphasia, but now the thought started to form that both - the damage to the edges in the graph and damage to important strongly interconnected nodes in the graph such as the association cortices - could produce complex syndromes.

The idea of relay stations in the brain itself entered a systems view into neuroscience that triggered the idea of novel functional roles of brain regions and changed the way we think about information flow in the brain. It was this shift in thinking that would later stimulate graph theoretical analyses of functional and anatomical brain connectivity and find a theoretical framework to relate their results to behavioral phenomena.

From here, further efforts were invested into understanding syndromes originating from lesions of the brain as syndromes originating from damaging parts of networks. The brain was not anymore regarded as one network - essentially the holistic view - but was constantly empirically and theoretically dis- and reassembled into one entity comprised of a multitude of interrelated subnetworks.

The rise of neuroimaging methods such as PET, Single Photon Emission Tomography (SPECT) and fMRI and of non-invasive in vivo connection tractography methods such as Diffusion Tensor Imaging (DTI) extended our perspective from mere disconnection syndromes (subcortical white matter lesions) to other alterations of connectivity such as hyperconnectivity in autism or state-dependent dynamic diaschisis. (Catani and Ffytche, 2005)

Today we know that while some basic processes - particularly those associated with basic afferent input into or efferent output from the brain - show a relatively invariant structure/function mapping and strengthen a localizationistic view, particularly in areas in which projection fibers originate or terminate such as the primary auditory cortex or the hand area in the motor cortex. But it is clear that many neural processes of higher order involve the association cortices and the interaction of multiple brain areas via short- and long-distance callosal and association fibers.

The dynamics - and complexity - of this perspective on functionally relevant networks was enriched after the 90s by neuroimaging methods with a temporal resolution of (or even below) a single second. Additionally to a spatial dimension - where spatially remote nodes of a network are the constituting parts - a temporal dimension was introduced. Context-dependent networks were observed to dynamically form and decompose as a reaction to stimuli and tasks and a limited number of canonical networks were beginning to be observed, such as the Default Brain Mode Network, (Raichle et al., 2001) that seemed to reflect traits of the underlying system (Achard et al., 2006).

In this form of network research, the notion that specialized cortical regions exist is neither discounted nor is it in any way functionally more or less relevant to the emergence of adaptive behavior. The proper functioning of each of these centers individually is as important as their ability to adaptively form functional networks to deal with the tasks presented to the brain. In that sense one can feel reminded of the idea of subagents coined by Marvin Minsky in the era of the Artificial Intelligence research boom in the 60s (Minsky, 1988), that hypothesized that one mechanism to reach effective processing is the distribution of one problem to a plurality of specialized subagents, which each complete a part of the task at hand and whose results are finally assembled into one output - which in the case of the brain is behavior. Extending that thought in the light of how anatomical and functional networks in the brain are structured on the macro-, meso- and micro-level (Bassett et al., 2006) it appears as if each task or function is again and again disassembled and distributed to ever smaller subagents, from the large-scale functional network to the mesoscale columns within the participating brain regions and all the way down to the single neuron, and that this is done in a similar fashion across all scales. Nevertheless the question remains open where and how the results are organized, since the functional network is certainly not the highest entity but a subagent itself. Interestingly in the human brain, subagents within functional networks are recruited from systems that have originated in different stages of human phylogenetic development, probably contributing to the uniqueness of human behavior.

When functional networks moved further into the focus of the neuroscience community, this happened mainly as a mere substitute for the earlier univariate voxel-by-voxel perspective that had dominated neuroimaging data analysis for decades. Now it is not anymore the association of voxel-by-voxel-activity with behavior, but the association of network activity with behavior. But in essence the bottom-up definition of multi-voxel entities (networks) does not serve us with funda-

mentally new information on brain function if we do not go further. Unfortunately until recently only little effort had been invested into understanding what the underlying rules are that govern the emergence of functional networks (Bullmore and Sporns, 2009).

Parallel to and potentially inspired by the rise of connectivity studies a trend towards multi-modal studies could be observed. Until recently multi-modal studies utilizing multiple methods - EEG, MEG, DTI, Arterial Spin Labeling (ASL), fMRI, MRI etc. - on the same subjects and at the sime time were rare and small sample size studies were very common, particularly in the field of fMRI.

It is this new exceeding flood of information within which we are now starting to look for systematic relations between systems in the brain (e.g. are anatomical connectivity hubs functional connectivity hubs?), rather than only for relations within systems (e.g. which is the largest and which is the smallest anatomical connectivity hub?) or only the association of system properties or functions with behavior (e.g. does white matter fibre bundle myelination predict certain aptitudes?).

The trend to layer information from multiple methods into qualitatively new models can as well be observed in general radiological practice. The combination of static Computer Tomography (CT) or Magnetic Resonance (MR) and PET images for the detection of tumor candidates (Antoch et al., 2003) and visualization of their tissue metabolism is only one example of how the combination of imaging methods is being leveraged in present day radiology.

It is now that, for example, the association cortices can be described at such a structural detail - regarding cell types, anatomical connections, metabolic supply and demand - that these models from multi-modal data might be used to explain why particularly this combination of features makes one particular area of tissue the area that is capable of serving that specific range of functions - functions such as functional integration. More precisely, we are beginning to understand which properties of the underlying system lay the trait-level framework for the emergence of state-dependent functional properties - such as integration, specialization or even dysfunction. It is certain, that in the coming years as the radiological state of the art progresses into integrating diagnostic information on properties of the anatomical system (e.g. DTI or anatomical MR images) with our understanding of how functional networks emerge, this will radically alter and individualize areas such as image guided patient-specific surgical path planning in neurosurgery or neurooncology and radiotherapy.

The present problem with this flood of data is that we can describe the brain of each subject with an exceedingly long vector of values describing a multitude of features, but it is not clear how to deal with that amount of information and how to identify which features are relevant. The multiple comparisons problem makes hypothesis-free mining for relevant features statistically highly complicated, which is as well the reason why many researchers (and clinicians) refrain from using all the information they can obtain from the measurements in a combined model. In a study with for example two groups of 20 subjects, a structural description of each individual brain on the levels of tissue volume anatomy and anatomical connectivity can result in up to many hundred values per person, already allowing the spurious statistical identification of group-differentiating features due to purely random variations. It is exactly this challenge to adapt our analysis paradigms to the sheer volume of data we can record that is currently marking the merge of data-mining methods and modern neuroimaging.

The rise of machine learning and data-mining methods in neuroimaging, and more generally in radiology and diagnostics, will enable the clinician to utilize information that could earlier only be obtained from these advanced scientific methods by analysis experts. These methods will improve clinical practice dramatically by offering analysis results and image-enrichment for better clinical decision making that result from harvesting information which can not be obtained by visual inspection (as it is common clinical practice amongst radiologists today with for example CT images) but only by a deeper computational analysis of imaging information (Whitfield-Gabrieli et al., 2009) using automated diagnostics. The key to the future application of scientific insights from this field of study is to find a way to communicate such results in an understandable and time-efficient manner to the practicing clinician.

1.3 Employed methodology

In 1736, Leonhard Euler published his paper on the "Seven Bridges of Königsberg", the first scientific proposition of a topological problem, namely how to cross each bridge over the river Pregel exactly once on a round trip over the islands, using graph theoretical methods (Euler, 1986).

For this he depicted the bridges and islands of Königsberg as a graph, consisting of edges for the bridges and nodes for the islands. On this simplified map he simulated the possible walks leading from one node to another and derived equations to describe them in terms of path length (How many bridges are there to cross?) and visitation frequency (How often can we visit a specific island

if we want to pass each bridge only once?).

Since that first prelude of graph theory, numerous researchers have advanced the field and its application (Sporns, 2010), so that today graph theory is applied in many areas (Barnes, 1969) such as the study of social graphs, financial systems (Boss et al., 2004) or complex biological phenomena like genetic expression (Xu et al., 2002), protein interactivity (Bolser et al., 2003), intracellular messaging cascades (Barabási and Oltvai, 2004) or predator-prey-networks and food-webs (Dunne et al., 2002).

The discipline is - amongst other topics - dedicated to the understanding of the emergence of certain global and local properties of a given system from the distribution of pairwise relations of parts of that system (e.g. if many parts have one connection to another single part, the sum of these connections make the latter the hub of the system).

In the present work, the graph theoretical perspective is one of the ways with which we seek to describe the brain in order to understand certain pathologies like stroke and more generally to understand the lines along which structure-function relationships form.

Towards this end DTI based probabilistic tractography is employed as a computational framework for graph theoretical analysis of structural brain connectivity (Gigandet et al., 2008). DTI based tractography can be used to characterize the quality and number of possible white matter tracks between two regions in the brain and allow for an estimation of connection probability (Kreher et al., 2008). For this purpose, probability density maps can be formed from the repeated propagation of curves (random walks) through the DTI based tensor field, which is representing local white matter orientation. From the resulting probability of inter-regional connectivity, network edges can be formed which are representing the direct macroscopic connectivity via white matter fiberbundles (Iturria-Medina et al., 2008). This map, is nothing less than a roadmap of the individual brain representing whole-brain anatomical connectivity.

The resulting brain connectivity graphs (also termed white matter network connectomes) can then be analyzed to identify the hubs of the system (e.g. the Posterior Cingulate or Precuneus) and to advance the understanding of the overall organization of connectivity (e.g. are parallel or strictly sequential pathways dominating?).

Continuing from this point, we try to understand the influence of anatomical connectivity on the emergence of functional traits (e.g. resting state FCNs) and states (the task dependent interactivity of regions).

Advanced MR methods are used such as Voxel-Based Morphometry (Mechelli et al., 2005) for

the quantification of volumetric differences of the brain based on anatomical MR images and this structural information of certain brain traits (e.g. local GMV) is combined (Várkuti et al., 2011) with functional information from methods like perfusion weighted imaging in order to deepen the understanding on the interplay of structural and functional local traits (e.g. larger GMV and high resting state perfusion) with connectivity (e.g. hub characteristics).

A simple analogy can be used to describe this approach more comprehensively. When trying to understand which regions of for example Europe are of central relevance, one can look at structure (Where are more buildings and which type of buildings?), local supply (Which regions receive more fuel, electricity etc.?), communication (Which regions communicate a lot with other regions?) and physical connectedness (How many streets link a city on short distance? ; How many roads and highways link cities on medium distance and how many long distance connections connect it to other airports?). It is clear that all of these measures are interrelated - in important cities (e.g. London) there is a dense, partially modern, functional architecture, a vast network of roads, streets and a big airport which is at a central position in the network of flight connections, with intense communication within and between the city over a plurality of channels and a strong supply of all kinds of material (e.g. fuel, gas, electricity).

While a city might look different to a rural area in all of these aspects, the basic relations or rules are always the same. Larger structures require more supplies, larger structures host more single entities and hence there is generally more communication within and between structures. Transportation hubs for example, are usually places with larger structures with more supplies coming in and a higher amount of communication.

In this analogy, each city has a number of within-connections (streets) and medium-distance connections (highways to other cities). The number and direction of the incoming and outgoing flights from its airport on the other hand represent the long-distance connections and constitute its position within the air-traffic network. A large city has a large international airport, but there are some airports - such as in London - that are different in terms of its network position to a less significant airport - such as Stuttgart.

The network position of an airport (its centrality in the network) shapes the amount and type of needed buildings (towers, terminals etc.), just as it shapes the infrastructure necessary to maintain normal function (personnel, fuel, electricity etc.) and the amount and type of communication to other airports (e.g. collaborative air traffic control). All these features are of relevance to describe the state and capability of that particular region (e.g. lack of supplies precedes overall deteriora-

tion).

If the balance of these features is violated (e.g. if no more supplies are reaching London) the effects are immediate. Functionality is interrupted, communication patterns are changed or lost, flight connections are decreased and if the problem is not solved on the long run structures will start to deteriorate.

The effects of changes in one property translate to changes in other properties over time following certain predictable patterns, which are the rules by which these properties are inherently linked. Eventually these changes on the ground will affect function (communication and traffic) in a specific way. While a power shortage will stop functioning of the airport immediately, cutting off both airport and city from fuel and electricity gradually will manifest in slower changes and reorganization.

In the very same manner, a brain region can be described by its network position in the white matter network (Gong et al., 2009), the local GMV (Chen et al., 2008), the regional Cerebral Blood Flow (rCBF) and the extent of functional connectivity with other brain regions in vivo using non-invasive imaging methods (Cohen et al., 2008). An extensive description each each region in terms of these structural and functional properties can help us understand how and why communication between brain regions and within FCNs changes or ceases as a result of structural changes in the underlying system. This data enables us to characterize individual brains and brain regions on a new level of information depth and to understand the connectivity rules by which communication networks (FCNs) in the brain emerge and collapse as a consequence of properties of the underlying system.

2 Motivation, hypotheses and approach

To understand the rules of influence of the underlying system onto FCN emergence is crucial for understanding the mechanisms of pathological processes that result in cognitive decline, as well as for optimizing interventions that target the maintenance of canonical FCNs to fight neurodegenerative disease (Seeley et al., 2009b) or even the creation of new adaptive networks within an altered set of system-boundaries as in post-stroke neurorehabilitation.

In the light of these concepts the following basic hypotheses and subgoals were defined:

Basic and application oriented hypotheses:

1. Regional system properties (GMV, anatomical connectivity and local perfusion) are systematically linked across the brain, naturally reflecting supply-demand relationships, so that highly anatomically connected regions of the brain (the hubs) show higher resting state perfusion. This demonstrates how structural properties of the underlying system are systematically linked.

2. fMRI measured FCNs of neural origin can be dissociated from false positive FCNs originating from non-neural sources (physiological noise, algorithm error) using Independent Component Analysis (ICA) for the detection of FCN candidates and Independent Component (IC) fingerprinting methods. With this method stereotypical neural communication patterns can be extracted from the data in a data-driven fashion.

3. A taxonomy of FCNs of neural origin can be derived, consequentially observed FCNs are not only similar across individuals or experimental contexts (canonical FCNs) but can be grouped under a subset of stereotypical networks which is significantly smaller than the entirety of all observed FCNs. As such each of the stereotypical networks represents a distinct area of increased occupation/population density both in the FCNs IC fingerprints feature space and the basic possibility space for FCN formation. These clusters in IC fingerprint feature space represent classes, into which the observed stereotypical neural communication patterns can be sorted.

4. The underlying system (with respect to the local properties of GMV, anatomical connectivity and local perfusion) allows systematic predictions on the observation of FCNs of neural origin. Larger and more connected brain regions with higher resting state perfusion should participate in more FCNs of neural origin. This hypothesis links observations of stereotypical communication patterns with the trait-level properties of the underlying system.

5. The results of the FCN taxonomy can be applied to data from patient populations to identify FCNs of interest.

6. Behavioral changes due to training in stroke patients can be related to changes within such identified FCNs over time. The extent of FCN reorganization (connectivity increase) reflects beneficial behavioral changes.

7. Properties of the underlying system such as anatomical connectivity influence electrophysiological phenomena as well, supposedly via alteration of inter-regional conduction properties, which affects phenomena which are relevant for example for BCI aptitude.

By empirically testing the first set of hypotheses (1 to 4) we were trying to answer some basic questions that can be counted into the domain of fundamental research and systems neuroscience. So in order to better understand rules which are substantiated in commonly observable structure/function relationships first a model was developed that unified information from multiple modalities into a comprehensive description of global and regional brain structure and perfusion dynamics to characterize the underlying system. Systematic relations of system properties were assessed (Hypothesis 1).

Secondly, a taxonomy of observable FCNs was created from a multitude of fMRI studies to build a bottom up catalogue of canonical FCNs. In order to obtain this goal, first a denoising system had to be created that dissociates FCNs of neural from FCNs of non-neural origin, to admit only the FCNs of interest into such a catalogue (relevant for Hypotheses 2 and 3).

The model of the underlying system (data from multiple subjects on brain perfusion, GMV and anatomical connectivity) was unified with the FCN taxonomy so that the hypotheses on systematic relations could be confirmed (Hypothesis 4).

In the second part of our work (Hypotheses 5 to 7) we focussed on the application of the gained models to more practical research questions of direct relevance to patient populations. The information from the taxonomy was applied to identify interesting FCNs in stroke survivors that had undergone an extensive rehabilitation training, and pre-post changes within these FCNs were quantified and related to behavioral changes (Hypotheses 5 and 6). Furthermore the white matter connectivity analysis methods were applied to study the link between anatomical connectivity and BCI control (Hypothesis 7).

3 Methodical developments and innovations

In order to test Hypotheses 1 and 4, we needed to derive individual macroscopic anatomical connectomes. For that purpose, a probabilistic tractography based pipeline for the automated analysis of DTI data had to be implemented (which did not exist in a publicly available format at the time), where the resulting white matter connectivity adjacency matrix was automatically analyzed with graph theoretical methods for each subject. For more details regarding the challenges and the

presently implemented system please see (Várkuti et al., 2011). Secondly, analysis methods had to be developed to process results from volumetric analysis - based on Voxel Based Morphometry (VBM) - and perfusion measurements (rCBF results from ASL) in one model and to control for critical factors.

The development of an IC fingerprinting based denoising system (relevant for Hypothesis 2) is illustrated in Chapter 2. The concept of data-driven clustering of high-dimensional IC fingerprinting feature data using Self-Organizing Feature Maps in combination with the Clusot toolbox, and the elimination of implausible IC clusters for the substantiation of denoising were implemented and tested in the course of this thesis. This system can theoretically be used outside the present context as a preprocessing tool to remove ICs not of interest from fMRI timeseries.
Furthermore a system for automated sorting and organization of FCN features had to be derived that allowed the bottom-up construction of useful taxonomy categories in order to test Hypothesis 3.

A paradigm for the unification of the taxonomy results with the multi-modal data from the first study had to be found, in order to test the influence of perfusion, GMV and anatomical connectivity on the features of FCNs (Hypothesis 4).

An analysis pipeline for the reliable identification of FCN changes over time had to be developed that took account of the structural differences in stroke subjects (Hypotheses 5 and 6) and that incorporated a cross-validation method to safeguard against false-positive results. The presently implemented multiple-regression with leave-one out cross-validation approach that was used to identify changes in FCNs that correspond to behavioral changes in stroke patients needed to be programmed as an extension of the standard Multiple Regression Implementation in the Statistical Parametric Mapping Software Package, Version 8 (SPM8).

To test Hypothesis 7, the DTI data from healthy EEG-BCI users were processed to derive Fractional Anisotropy (FA) images for each participant. FA is a measure of the microstructural integrity of white matter which is based on information from DTI data. In order to transfer the ICBM DTI atlas images into DTI native space to extract regionwise statistics on FA, a procedure of normalization and parameter inversion analogous to the method described in Gong et al. (2009)

needed to be adapted for the International Consortium for Brain Mapping (ICBM) atlas and the particularities of FA images.

4 Short summary of results

For a more detailed summary of the results please see Chapters 1 to 4 containing the original research work.

1. The structure of the macroscopic white matter anatomical connectivity network in the human brain and resting state perfusion show a significant degree of covariation. This could be shown for two independent samples of subjects and with different measurement schemes for a total of 23 healthy participants. As such the structural basis of neural cooperation and the resting state blood supply in healthy participants are linked systematically on a macroscopic level.

2. Based on a large body of data from 90 participants, FCNs of non-neural origin can be separated from FCNs of neural origin using a combination of IC fingerprinting features. More than 25 % of all identified ICs can be regarded as FCNs of non-neural origin and discarded.

3. The previously derived set of FCNs cleared from FCNs of non-neural origin can be organized into subgroups according to their spatial overlap, resulting in 172 stereotypical networks which represent the most frequently observable network types in the present sample (the sample-specific canonical brain networks).

4. By combining the FCN results and our results regarding Hypothesis 1 it can be shown that FCNs emerge preferably along direct anatomical connections. This finding is not restricted to resting state networks, nor is it solely based on experimental data from one single experimental paradigm, but proves this relationship for the first time for a high number of distinct FCNs from various contexts. Regions of the brain with high GMV, resting state perfusion and a high number of anatomical connections are more likely to participate in a high number of distinct functional connectivity networks and serving a number of distinct functions within these than brain regions with low GMV, perfusion and anatomical connectivity.

5. The distinction rules derived from IC fingerprinting and FCN clustering can be applied to other datasets (stroke dataset) to be used for denoising.

6. It could be shown in the analysis of a separate study, that if the correct canonical FCNs of neural origin are chosen, the extent of motor recovery in stroke survivors participating in an EEG-based motor rehabilitation program is positively correlated with the degree of resting state functional connectivity increase in certain (even extra-motorical) networks.

7. It could be shown in the analysis of a further study, that anatomical connectivity (operationalized as the FA of certain white matter systems) predicts EEG-BCI aptitude in healthy subjects.

5 Discussion

We successfully retrieved data from multiple-imaging modalities (MR, DTI, ASL) to construct a healthy-sample based model of system properties and analyzed their statistical interactions (covariation of connectivity and perfusion, Chapter 1). By subsequently extracting a range of basic neural communication patterns from a large sample of fMRI data (see Chapter 2), we were finally able to link local trait-level properties of the underlying system with the our observations on neural communication patterns of brain regions. High gray matter tissue volume, perfusion and a particular hub-like pattern of anatomical connectivity are those features that are statistically associated with participation in a higher number of distinguishable neural communication patterns. Our prediction model in Chapter 2 provides a quantifiable and testable manifestation of this structure/function relationship. For a more detailed discussion of the specific results please see Chapters 1 to 4 containing the original research work.

5.1 Implications of our findings

The presented results regarding Hypotheses 1, 3 and 4 allow us the formulation of new experimentally testable hypotheses, which to the best of our knowledge have not yet been systematically tested before. If the supply of metabolites is disturbed by diseases related to globally abnormal cerebral perfusion, the impact should be more dramatic at anatomical connectivity hubs and on FCNs that involve them. From this it follows that, if cerebrovascular fitness improves the ratio of perfusion and anatomical connectivity (or GMV) testable differences to subjects with low cerebrovascular fitness should be observable, specifically regarding functions that rely on the FCNs that involve anatomical connectivity hubs.

Regarding the observed interdependency of direct anatomical connectivity and FCN formation

we can assume, that the limited duration disruption of an anatomical connection should directly deform or disrupt the FCN which supposedly transmits information through it. If reversible functional disruption of specific fiber bundles (possibly by future developments in the field of optogenetics, Fenno et al. (2010)) should become a viable experimental tool, this would enable us to study the various functional roles anatomically segregated members of a FCN assume and potentially allow us to understand which information is transmitted via which fiber bundles.
Consequentially, some anatomical connections should be relevant for a higher total number of FCNs than others due to their physical position, conduction properties etc.. A comprehensive mapping of the roles of each white matter connection could lead to a ranked list of the most relevant connections. It is an interesting question, to which extent such experimentally proven relevancy of white matter bundles would be identical to our present notions of edge vulnerability (see Chapter 1) in white matter connectomes.

A deeper analysis of local properties (potentially including further methods such as Magnetic Resonance Spectroscopy) could reveal why the 172 stereotypical networks form in the observed ways and why a certain set of networks (e.g. FCNs that compromise more than 10 AAL regions) are never observed (Chapter 2). Why the observed FCNs are limited with respect to the maximum number of participating brain regions is a question of considerable interest, since the observed numbers might mark the natural coordination maximum of the brain. If this number is meaningful, we should be able to observe alterations of the maximum number of FCN members in certain forms of developmental disorders.
Another experimental tool to study FCN formation and a potential future intervention method might be the artificial induction of functional connectivity in identified target areas which should be beneficial for recovery for example in patients suffering from subcortical stroke (see Chapter 3). Such artificial induction of functional connectivity would require the precisely timed induction of activity in one region, as a reaction to activity in another region. One potential method to obtain this would be the triggering of neuronal activity in genetically manipulated neural tissue using fiberoptics (Fenno et al., 2010), by coupling the activity triggering to an implanted or surface electrode at the distant site of initial natural activity. The right timing of this artificially induced co-activation would be critical, in order to induce the right (Hebbian) processes. To which extent methods related to classical conditioning can be applied to such interventions, and what role augmentation methods based on brain stimulation transcranial Direct Current Stimulation

(tDCS) or medication (potentially targeting N-Methyl-D-aspartic acid receptors) might play, will be an interesting area of future research.

If our findings (Chapter 2) are correct and FCN formation is depending on direct anatomical connectivity, probably the inverse relation can be utilized for intervention purposes. If functional connectivity inducing trainings could target strengthening inter-hemispheric communication, this might increase white matter microstructural integrity in some target areas (e.g. Corpus Callosum). Based on our findings (Chapter 4) this could increase EEG-BCI aptitude and performance. Further implications are discussed extensively in the appended manuscripts, with a more comprehensive discussion of these issues in Chapter 2.

5.2 Supporting evidence from the field of developmental neurobiology

Considerable empirical evidence from neurobiological studies (Bocker-Meffert et al., 2002; Ruhrberg et al., 2008; Merrill and Oldfield, 2005; Jin et al., 2002; Sondell et al., 1999) strengthens the proposed link between neural connectivity and the vascular system (see Chapter 1).

For some central nervous projections the axon-growth cones migrate during development along the vascular structure and some factors that are distinctive for vascular growth - such as the Vascular Endothelial Growth Factor (VEGF) - are known to act as chemoattractants guiding that axonal growth.

Factors like VEGF have been shown to be neurotrophic in vitro and in vivo (Brockington et al., 2010) and lack of these factors is associated with developmental disorders affecting neuronal circuitry and more generally with neurodegeneration in the adult brain.

It is presently not possible to determine, whether areas of the brain have more axonal connections because they are stronger vascularised and that in turn attracts more axons - or whether the strong interconnectedness of certain areas lead to heightened neural activity and metabolic demand, which in turn activate vascular growth factors via hypoxia-inducible factors triggered by that heightened demand.

Another aspect to consider is the possibility that in areas containing a high number of axons, the supporting glial cells release signaling factors triggered by heightened metabolic demand. Furthermore not all types of tissue are equally permissive (for vascular structures or axons) so that highly permissive areas of the brain might simply allow for more vascularization and axonal connections.

In summary, it is likely that all of these links play some role in the crosstalk between the nervous

and the vascular system on a microscopic level.

Although such bidirectional interactions may play a role during the development of the nervous system, it is unclear whether these highly localized effects add up over time (the span of neural development and maturation) and space to influence brain structure and function on the macroscopically observable level of capillaries and fiber bundles.

Future experiments might resolve this question by manipulating genetic expression so that for example VEGF-production- or axon-growth cone VEGF-sensitivity-relevant genes are downregulated either early in ontogenetic neural development or in the adult animal and macroscopic neural connectivity and cerebral perfusion is assessed using DTI and ALS. It is to be expected that early disruption of such natural nervous- and vascular-system crosstalk might lead to severe impairments as the regulation of adequate metabolic supply is inhibited. It is to be expected that the natural resting state functional connectivity and common anatomical connectivity networks are deformed.

Present research into triggering localized vascular growth (Kusaka et al., 2005) in the adult brain might open a new possibility for intervention in cases where the local metabolic demand is not met anymore by adequate supply (hypoperfusion).

If the effects of neurobiological intervention methods can significantly overcome effects from either natural (such as e.g. atherosclerosis, hypoglycemia, hypotension) or aggravated causes (e.g. vascular dementia) for hypoperfusion in the adult brain our methods from the field of macroscopic neuroimaging could serve in future to guide such localized interventions to those spots in the adult brain where the connectivity/perfusion ratio is out of balance and where the cognitive deficits observed in neurodegenerative diseases arise.

5.3 Implications for stroke research

The impact of neurogenesis, synaptogenesis and axonal regrowth in post-stroke regeneration is subject to intense debate (Jin et al., 2006; Cramer, 2008), but the regeneration-hostile glial and extracellular environment in the adult brain and specifically the pathologically altered neurochemical environment after the stroke strongly limit the potential for regeneration in the sense of large-scale structural reconstruction/regrowth or adaptive macroscopic redesign of the system. Empirical evidence rather suggests degeneration of white matter connections and atrophy of tissue even beyond the perilesional regions of the brain in ischaemic stroke survivors and possibly

even months after the subacute phase of regeneration. As such, one proposed main mechanism of regeneration is functional adaptation substantiated by long-term potentiation (LTP) or long-term depression (LTD) within the limits of the underlying system that remained intact post-stroke (Albensi, 2001; Johansson, 2000). This functional adaptation does not occur under normal circumstances, as the neurochemical environment is altered specifically in the perilesional region immediately after the stroke and during the timewindow critical for rehabilitation. This is particularly apparent for alterations of the γ-aminobutyric acid (GABA) system that is known to be involved in motor-learning behavior (Stagg et al., 2011).

Only after the change of function are "the boundaries of the system pushed from within" (functional changes due to training do trigger structural changes) and the connections and tissue changed structurally on a macroscopic level as an effect of that. This is reflected in some limited evidence (Gauthier et al., 2008), suggesting that certain forms of therapy induce bilateral gray matter structural brain changes in motor and sensory regions, but only in specific training groups. Our results point towards an association of functional connectivity increase and motor rehabilitation outcome. Presently it can not be clearly answered, whether these results indicate that generally greater plasticity of a patient (in the sense of a resource, e.g. a more learning-friendly GABAergic system) lead to a stronger neural reorganization and to better motor outcome or whether these pre-post differences in resting state functional connectivity mirror variations in the effect size of the training intervention across patients.

It is noteworthy that increases in functional connectivity and not decreases were identified as being statistically associated with motor rehabilitation (Chapter 3). Increased functional connectivity indicates stronger neural cooperation within these networks, possibly reflecting an extension or change of the functional role of certain brain regions.

The outcome of optimal motor rehabilitation is mediated by pre-lesion brain connectivity, extent and impact of the lesion (particularly how much of the motor function relevant tissue is affected), effectivity of post-stroke training and general usage (or disuse) of the impaired limbs. As such the pre-lesion macroscopic anatomical connectome and the post-stroke vascular system might have a considerable influence on the effectivity of motor rehabilitation.

Stimulated by these results, we are currently gathering information on anatomy, perfusion and resting state functional connectivity from a number of stroke survivors to better understand whether a greater number of parallel anatomical connections post-stroke broaden the limits for and fascilitate functional reorganization (reflected in the global efficiency metric for the post-stroke white

matter connectome), whether post-stroke perfusion of regions that gained a higher relevancy in the network fits the new demands arising from changed function and whether this predicts recovery, as graph theoretical vulnerability values of a region as an indicator of connectivity/relevancy can increase after a lesion that shifts the usage of existing pathways (as for region X in Figure 3). It might be that perfusion does not fit the altered demands after a shift of functional roles and activity. Furthermore we wish to answer the question whether any of these features predict the extent of neural plasticity, operationalized as the extent of pre-post motor rehabilitation training functional connectivity increases.

It is of considerable interest whether white matter connections are as functionally specialized as certain regions of the cortex and whether such specialization is equivalent across all bundles in the brain, or whether there are some white matter bundles that have one primary role (e.g. the relaying of visual information in the optic radiation) and others that take on a multitude of roles, depending on whether they relay information only between their origin and terminus or as well as intermediate piece in long-distance communications along pathways that encompass white matter connections with a path length higher one (as edge number 4 in Figure 3, that has to relay information from A to B after the lesion). Certain implications of recent findings on the neural workspace theory might be taken as an indication, that the information transferred via certain white matter connections can be altered by the brain more dynamically, since if that was not the case, the neural workspace would be highly rigid (e.g. a pair of regions could always process only one specific type of information). This is highly relevant in understanding the limits to functional adaptation imposed by the properties of the white matter network.

5.4 Implications for BCI research

Recent findings (Halder et al. (2011) and Várkuti, Halder et al., 2011 in Chapter 4) point towards the relevancy of functional properties (SMA activation) and inter-hemispheric white matter quality in individual BCI aptitude. We found that the microstructural characteristics of cerebral white matter have a strong predictive power of Sensori-Motor-Rhythm (SMR) BCI performance, which has implications for the way the training is conducted. But as these implications are solely based on correlative research (structural brain traits correlating with BCI performance) the exact mechanism involved here is yet unclear. In the light of recent studies on the association of bundle specific white matter integrity and EEG features in healthy subjects (Valdés-Hernández

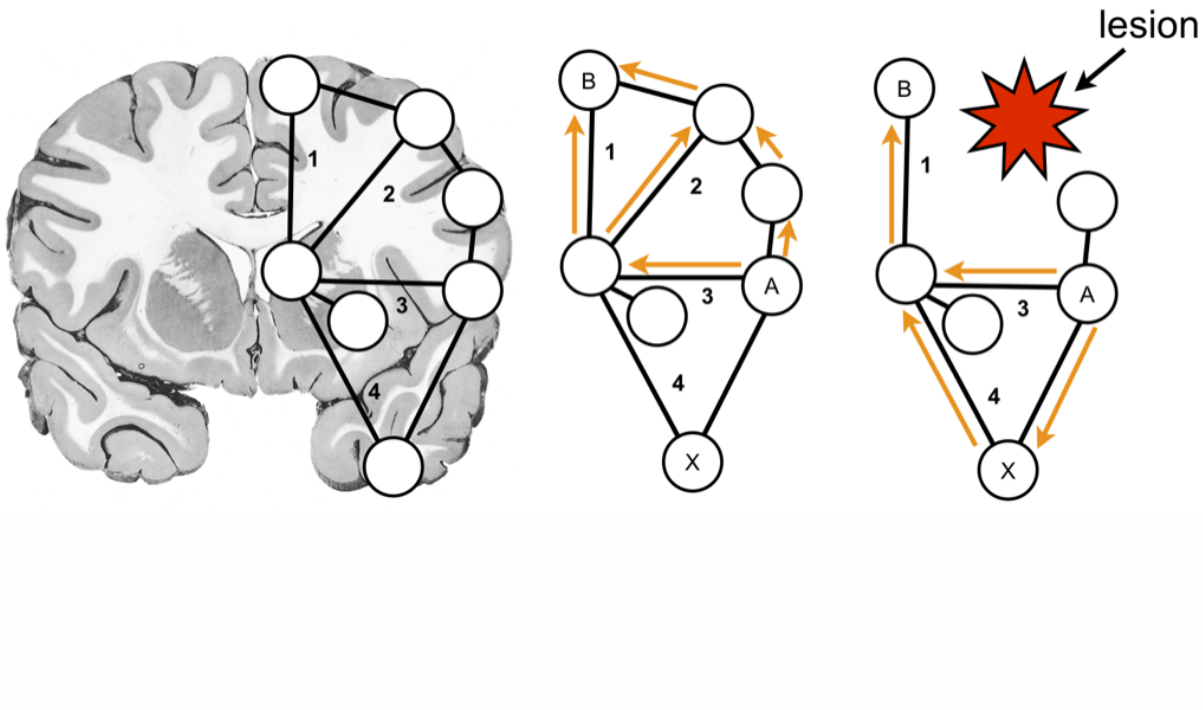

Figure 3 – Illustration of the alteration of functional roles through network lesions, coronal brain section from M Roberts and J Hanaway, Atlas of the human brain in section, 1971

et al., 2010), the link of interhemispheric white matter connectivity with EEG frontal coherence (Teipel et al., 2009) and the relation of interhemispheric transfer time to DTI derived measures of white matter integrity, it is apparent that the conduction properties (e.g. conduction velocity, myelination and local fiber density) of the brain are determined by the underlying white matter network and that these properties might in turn significantly influence EEG features on both the trait and state level. Specifically, the dynamics of the resting state alpha rhythm appear to be connected to white matter architecture (Valdés-Hernández et al., 2010).

One of the central purposes for BCIs is their potential to enable communication in patients suffering from progressive degeneration of the motor system in ALS. While ALS was long considered a disease with mainly motor system specific cerebral involvement, this notion is changing in the light of recent findings on the involvement of extra-motoric white matter structures such as the Corpus Callosum (Filippini et al., 2010), Cingulum (Woolley et al., 2011), Uncinate Fasciculus (Sato et al., 2010) or in regions such as the Insula, Hippocampal Formation, the ventrolateral Premotor Cortex, Parietal Cortex and bilateral Frontal Cortex (Senda et al., 2011). Based on these findings, it can be assumed that the pathology in ALS is spreading in later stages to multiple white matter regions, which can be considered critical for the control of those EEG features that are presently used in most BCI applications (e.g. P300, SMR), hence probably impairing the ability of the patients to utilize present BCIs.

We need to deepen our understanding of the impact of white matter myelination on the timing of macroscopic neural communication, as it is possible that learning is impaired in patients suffering from white matter degeneration due to the disturbed timing of classical or operant conditioning processes by the pathological alteration of white matter conduction delays. Unfortunately, the impact of white matter connectivity on conditioning processes in general, is a heavily understudied field in modern neuroscience.

Based on our findings on the relevancy of direct anatomical connections for the formation of FCNs, it can be assumed that patients suffering from degradation of white matter microstructure will show systematically altered canonical and task-induced FCNs. But currently we have no experimental means to reversibly manipulate the conduction properties of selected white matter connections in vivo, which would be necessary to quantify the strength of causal links between anatomical and functional connectivity.

However the results of this work lead to a set of hypotheses that can be tested in future experiments to understand this problem better. On the level of correlative research, patients with inadequate

perfusion of anatomical connectivity hubs should show impaired FCNs and in turn altered EEG features and potentially impaired BCI aptitude and healthy low- and high-aptitude BCI users should as well differ in the functional connectivity of their canonical brain networks. For the level of experimental research, we can assume that the identified white matter traits will not change due to a single session of BCI training. Our findings indicate that the best way of improving BCI performance of healthy low aptitude users is by conducting a long term BCI training program consisting of multiple sessions that do not only target to increase proficiency in BCI usage for communication and control but attempts to incorporate interventions that increase or stabilize the microstructural integrity of BCI-critical central white matter.

Fortunately, the notion that white matter microstructure and connectivity are unalterable in the adult brain had to be corrected in the light of present findings on the effectiveness of interventions such as meditation (Tang et al., 2010), training of working memory (Takeuchi et al., 2010) or juggling training (Scholz et al., 2009) in increasing local FA (a measure of white matter microstructure integrity) in certain motoric and extra-motoric structures. As such these findings suggest that the breakdown of white matter connections and the breakdown of functional networks could strongly contribute to the difficulties in BCI communication in later stages of neurodegenerative disease and should and can be the main focus of interventions targeting BCI aptitude. If training effects on microstructural cerebral white matter properties can be observed (e.g. by using an EEG connectivty BCI neurofeedback paradigm as described in Outlook) this method could be used as an intervention that optimizes or stabilizes the structural conditions in the brain for late-stage BCI communication.

If beneficial effects of such training on white matter structures relevant to the modulation of SMR BCI-EEG features are observed, these training methods possibly in combination with tDCS based augmentation could as well be promising for stroke survivors as it is known that this patient group benefits from SMR BCI training (Pichiorri et al., 2011).

6 Outlook

Currently we are developing two new neurofeedback BCI systems to offer new intervention options to patients suffering from localized hypoperfusion and functional disconnection syndromes. The first system is an ALS based real time BCI that allows the real time feedback of rCBF to the participant, enabling the person to learn upregulation techniques that target the reperfusion of

areas. Utilizing our knowledge on the macroscopic anatomical connectome, this intervention can be targeted precisely at those brain regions, which require perfusion the most and which are necessary to reinstate certain cognitive functions (e.g. the anatomical connectivity hubs).

The second system is an implementation for real time graph property feedback of functional networks measured with electrophysiological methods. Using fast algorithms for the calculation of real time EEG channel-to-channel coupling, the resulting adjacency matrices are analyzed using graph theoretical methods and real time feedback of graph features becomes possible. Utilizing these methods in combination with appropriate learning paradigms enables us to train a patient to not only learn to activate a single brain region or a network of brain regions anymore, but to learn how to shape the functional networks in his brain into a more efficient form and thus indirectly manipulate the underlying white matter structures.

It is an area of ongoing studies at our institute how FCNs can be formed, altered or modulated in their activity through the means of self-regulation (e.g. the role of the frontal cortex in patients suffering from Attention Deficit Disorder), and with real-time feedback of EEG-connectivity graph properties we hope to offer a new neurofeedback tool for this purpose.

To this day it remains to be proven, whether learning to directly manipulate such abstract graph features of brain networks in real-time is possible at all, but if it is, this method promises to become a highly relevant tool for neurofeedback based interventions for treatment and secondary prevention.

References

Abbott, L. F. and Nelson, S. B. (2000). Synaptic plasticity: taming the beast. *Nature neuroscience*, 3 Suppl(november):1178–83.

Achard, S., Salvador, R., Whitcher, B., Suckling, J., and Bullmore, E. (2006). A resilient, low-frequency, small-world human brain functional network with highly connected association cortical hubs. *The Journal of neuroscience : the official journal of the Society for Neuroscience*, 26(1):63–72.

Albensi, B. C. (2001). Models of brain injury and alterations in synaptic plasticity. *Journal of Neuroscience Research*, 65(4):279–283.

Antoch, G., Vogt, F. M., Freudenberg, L. S., Nazaradeh, F., Goehde, S. C., Barkhausen, J., Dahmen, G., Bockisch, A., Debatin, J. F., and Ruehm, S. G. (2003). Whole-body dual-modality

PET/CT and whole-body MRI for tumor staging in oncology. *JAMA : the journal of the American Medical Association*, 290(24):3199–206.

Barabási, A.-l. (2012). The network takeover. *Nature Physics*, 8(January):8–10.

Barabási, A.-L. and Oltvai, Z. N. (2004). Network biology: understanding the cell's functional organization. *Nature reviews. Genetics*, 5(2):101–13.

Barnes, J. A. (1969). Graph Theory and Social Networks: A Technical Comment on Connectedness and Connectivity. *Sociology*, 3(2):215–232.

Bassett, D. S., Meyer-Lindenberg, A., Achard, S., Duke, T., and Bullmore, E. (2006). Adaptive reconfiguration of fractal small-world human brain functional networks. *Proceedings of the National Academy of Sciences of the United States of America*, 103(51):19518–23.

Beckmann, C. F., DeLuca, M., Devlin, J. T., and Smith, S. M. (2005). Investigations into resting-state connectivity using independent component analysis. *Philosophical transactions of the Royal Society of London. Series B, Biological sciences*, 360(1457):1001–13.

Beggs, J. M. and Plenz, D. (2003). Neuronal Avalanches in Neocortical Circuits. *J. Neurosci.*, 23(35):11167–11177.

Begré, S., Federspiel, A., Kiefer, C., Schroth, G., Dierks, T., and Strik, W. K. (2003). Reduced hippocampal anisotropy related to anteriorization of alpha EEG in schizophrenia. *Neuroreport*, 14(5):739.

Bocker-Meffert, S., Rosenstiel, P., Rohl, C., Warneke, N., Held-Feindt, J., Sievers, J., and Lucius, R. (2002). Erythropoietin and VEGF Promote Neural Outgrowth from Retinal Explants in Postnatal Rats. *Invest. Ophthalmol. Vis. Sci.*, 43(6):2021–2026.

Bolser, D., Dafas, P., Harrington, R., Park, J., and Schroeder, M. (2003). Visualisation and graph-theoretic analysis of a large-scale protein structural interactome. *BMC bioinformatics*, 4(1):45.

Boss, M., Elsinger, H., Summer, M., and Thurner, S. (2004). Network topology of the interbank market. *Quantitative Finance*, 4(6):677–684.

Bottino, C. M. C., Castro, C. C., Gomes, R. L. E., Buchpiguel, C. A., Marchetti, R. L., and Neto, M. R. L. a. (2002). Volumetric MRI Measurements Can Differentiate Alzheimer's Disease, Mild Cognitive Impairment, and Normal Aging. *International Psychogeriatrics*, 14(01):59–72.

Brockington, A., Heath, P. R., Holden, H., Kasher, P., Bender, F. L. P., Claes, F., Lambrechts, D., Sendtner, M., Carmeliet, P., and Shaw, P. J. (2010). Downregulation of genes with a function in axon outgrowth and synapse formation in motor neurones of the VEGFdelta/delta mouse model of amyotrophic lateral sclerosis. *BMC genomics*, 11:203.

Brodmann, K. (1909). *Vergleichende Lokalisationslehre der Grosshirnrinde in ihren Prinzipien dargestellt auf Grund des Zellenbaues*, volume 13. Barth.

Bullmore, E. and Sporns, O. (2009). Complex brain networks: graph theoretical analysis of structural and functional systems. *Nature reviews. Neuroscience*, 10(3):186–98.

Cammoun, L., Gigandet, X., Sporns, O., Thiran, J. P., Maeder, P., Meuli, R., Hagmann, P., Bovet, P., and Do, K. Q. (2009). Connectome alterations in schizophrenia. *NeuroImage*, 47:S157.

Casey, B. J., Galvan, A., and Hare, T. a. (2005). Changes in cerebral functional organization during cognitive development. *Current opinion in neurobiology*, 15(2):239–44.

Catani, M. and Ffytche, D. H. (2005). The rises and falls of disconnection syndromes. *Brain : a journal of neurology*, 128(Pt 10):2224–39.

Chao, L. L., Buckley, S. T., Kornak, J., Schuff, N., Madison, C., Yaffe, K., Miller, B. L., Kramer, J. H., and Weiner, M. W. (2010). ASL Perfusion MRI Predicts Cognitive Decline and Conversion From MCI to Dementia. *Alzheimer Disease & Associated Disorders*, 24(1):19–27.

Chen, Z. J., He, Y., Rosa-Neto, P., Germann, J., and Evans, A. C. (2008). Revealing modular architecture of human brain structural networks by using cortical thickness from {MRI}. *Cerebral cortex*, 18(10):2374.

Cohen, A. L., Fair, D. a., Dosenbach, N. U. F., Miezin, F. M., Dierker, D., Van Essen, D. C., Schlaggar, B. L., and Petersen, S. E. (2008). Defining functional areas in individual human brains using resting functional connectivity MRI. *NeuroImage*, 41(1):45–57.

Cramer, S. C. (2008). Repairing the human brain after stroke: I. Mechanisms of spontaneous recovery. *Annals of neurology*, 63(3):272–87.

Demirci, O., Stevens, M. C., Andreasen, N. C., Michael, A., Liu, J., White, T., Pearlson, G. D., Clark, V. P., and Calhoun, V. D. (2009). Investigation of relationships between fMRI brain networks in the spectral domain using ICA and Granger causality reveals distinct differences between schizophrenia patients and healthy controls. *NeuroImage*, 46(2):419–31.

Devanand, D. P., Pradhaban, G., Liu, X., Khandji, A., De Santi, S., Segal, S., Rusinek, H., Pelton, G. H., Honig, L. S., Mayeux, R., Stern, Y., Tabert, M. H., and de Leon, M. J. (2007). Hippocampal and entorhinal atrophy in mild cognitive impairment: Prediction of Alzheimer disease. *Neurology*, 68(11):828–836.

Dosenbach, N., Nardos, B., and Cohen, A. (2010). Prediction of individual brain maturity using fMRI. *Science*.

Dosenbach, N. U. F., Fair, D. a., Miezin, F. M., Cohen, A. L., Wenger, K. K., Dosenbach, R. a. T., Fox, M. D., Snyder, A. Z., Vincent, J. L., Raichle, M. E., Schlaggar, B. L., and Petersen, S. E. (2007). Distinct brain networks for adaptive and stable task control in humans. *Proceedings of the National Academy of Sciences of the United States of America*, 104(26):11073–8.

Dunne, J. A., Williams, R. J., and Martinez, N. D. (2002). Food-web structure and network theory: The role of connectance and size. *Proceedings of the National Academy of Sciences of the United States of America*, 99(20):12917–22.

Eigsti, I.-M. and Shapiro, T. (2003). A systems neuroscience approach to autism: biological, cognitive, and clinical perspectives. *Mental retardation and developmental disabilities research reviews*, 9(3):205–15.

Euler, L. (1986). Das Königsberger Brückenproblem. *... Graphen. Mit einer Abhandlung von L. Euler. Teubner- ....*

Fellgiebel, A., Wille, P., Müller, M. J., Winterer, G., Scheurich, A., Vucurevic, G., Schmidt, L. G., and Stoeter, P. (2004). Ultrastructural Hippocampal and White Matter Alterations in Mild Cognitive Impairment: A Diffusion Tensor Imaging Study. *Dementia and Geriatric Cognitive Disorders*, 18(1):101–108.

Fenno, L., Yizhar, O., and Deisseroth, K. (2010). The Development and Application of Optogenetics. *Annual Review of Neuroscience*, 34(1):110301101035033.

Fetz, E. E. (2007). Volitional control of neural activity: implications for brain-computer interfaces. *The Journal of physiology*, 579(Pt 3):571–9.

Filippini, N., Douaud, G., Mackay, C. E., Knight, S., Talbot, K., and Turner, M. R. (2010). Corpus callosum involvement is a consistent feature of amyotrophic lateral sclerosis. *Neurology*, 75(18):1645–52.

Fonteijn, H. M. J., Norris, D. G., and Verstraten, F. a. J. (2008). Exploring the anatomical basis of effective connectivity models with DTI-based fiber tractography. *International journal of biomedical imaging*, 2008:423192.

Frackowiak, R. (2004). Human brain function.

Gauthier, L. V., Taub, E., Perkins, C., Ortmann, M., Mark, V. W., and Uswatte, G. (2008). Remodeling the brain: plastic structural brain changes produced by different motor therapies after stroke. *Stroke; a journal of cerebral circulation*, 39(5):1520–5.

Gigandet, X., Hagmann, P., Kurant, M., Cammoun, L., Meuli, R., and Thiran, J.-P. (2008). Estimating the confidence level of white matter connections obtained with MRI tractography. *PloS one*, 3(12):e4006.

Gong, G., He, Y., Concha, L., Lebel, C., Gross, D. W., Evans, A. C., and Beaulieu, C. (2009). Mapping anatomical connectivity patterns of human cerebral cortex using in vivo diffusion tensor imaging tractography. *Cerebral cortex (New York, N.Y. : 1991)*, 19(3):524–36.

Greicius, M. D., Srivastava, G., Reiss, A. L., and Menon, V. (2004). Default-mode network activity distinguishes Alzheimer's disease from healthy aging: evidence from functional MRI. *Proceedings of the National Academy of Sciences of the United States of America*, 101(13):4637–42.

Grundman, M., Sencakova, D., Jack, C. R., Petersen, R. C., Kim, H. T., Schultz, A., Weiner, M. F., DeCarli, C., DeKosky, S. T., Dyck, C., Thomas, R. G., Thal, L. J., and the Alzheimer's Disease Cooperative Study (2002). Brain MRI hippocampal volume and prediction of clinical status in a mild cognitive impairment trial. *Journal of Molecular Neuroscience*, 19(1-2):23–27.

Halder, S., Agorastos, D., Veit, R., Hammer, E. M., Lee, S., Varkuti, B., Bogdan, M., Rosenstiel, W., Birbaumer, N., and Kübler, a. (2011). Neural mechanisms of brain-computer interface control. *NeuroImage*.

Head, D., Buckner, R. L., Shimony, J. S., Williams, L. E., Akbudak, E., Conturo, T. E., McAvoy, M., Morris, J. C., and Snyder, A. Z. (2004). Differential Vulnerability of Anterior White Matter in Nondemented Aging with Minimal Acceleration in Dementia of the Alzheimer Type: Evidence from Diffusion Tensor Imaging. *Cereb. Cortex*, 14(4):410–423.

Honey, C. J., Sporns, O., Cammoun, L., Gigandet, X., Thiran, J. P., Meuli, R., and Hagmann, P. (2009). Predicting human resting-state functional connectivity from structural connectivity. *Proceedings of the National Academy of Sciences*, 106(6):2035.

Horwitz, B., Warner, B., Fitzer, J., Tagamets, M.-a., Husain, F. T., and Long, T. W. (2005). Investigating the neural basis for functional and effective connectivity. Application to fMRI. *Philosophical transactions of the Royal Society of London. Series B, Biological sciences*, 360(1457):1093–108.

Iturria-Medina, Y., Sotero, R. C., Canales-Rodríguez, E. J., Alemán-Gómez, Y., and Melie-García, L. (2008). Studying the human brain anatomical network via diffusion-weighted MRI and Graph Theory. *NeuroImage*, 40(3):1064–76.

Jafri, M. J., Pearlson, G. D., Stevens, M., and Calhoun, V. D. (2008). A method for functional network connectivity among spatially independent resting-state components in schizophrenia. *NeuroImage*, 39(4):1666–81.

Jin, K., Wang, X., Xie, L., Mao, X. O., Zhu, W., Wang, Y., Shen, J., Mao, Y., Banwait, S., and Greenberg, D. A. (2006). Evidence for stroke-induced neurogenesis in the human brain. *Proceedings of the National Academy of Sciences of the United States of America*, 103(35):13198–202.

Jin, K., Zhu, Y., Sun, Y., Mao, X. O., Xie, L., and Greenberg, D. A. (2002). Vascular endothelial growth factor (VEGF) stimulates neurogenesis in vitro and in vivo. *Proceedings of the National Academy of Sciences of the United States of America*, 99(18):11946–50.

Johansson, B. B. (2000). Brain Plasticity and Stroke Rehabilitation : The Willis Lecture. *Stroke*, 31(1):223–230.

Kamitani, Y. and Tong, F. (2005). Decoding the visual and subjective contents of the human brain. *Nature neuroscience*, 8(5):679–85.

Kitzbichler, M. G., Smith, M. L., Christensen, S. r. R., and Bullmore, E. (2009). Broadband criticality of human brain network synchronization. *PLoS computational biology*, 5(3):e1000314.

Kreher, B. W., Schnell, S., Mader, I., Il'yasov, K. A., Hennig, J., Kiselev, V. G., and Saur, D. (2008). Connecting and merging fibres: Pathway extraction by combining probability maps. *NeuroImage*, 43(1):81–89.

Kusaka, N., Sugiu, K., Tokunaga, K., Katsumata, A., Nishida, A., Namba, K., Hamada, H., Nakashima, H., and Date, I. (2005). Enhanced brain angiogenesis in chronic cerebral hypoperfusion after administration of plasmid human vascular endothelial growth factor in combination with indirect vasoreconstructive surgery. *Journal of neurosurgery*, 103(5):882–90.

Lawrie, S. M., McIntosh, A. M., Hall, J., Owens, D. G. C., and Johnstone, E. C. (2008). Brain structure and function changes during the development of schizophrenia: the evidence from studies of subjects at increased genetic risk. *Schizophrenia bulletin*, 34(2):330–40.

Lebel, C. and Beaulieu, C. (2011). Longitudinal Development of Human Brain Wiring Continues from Childhood into Adulthood. *Journal of Neuroscience*, 31(30):10937–10947.

Lee, S., Ruiz, S., Caria, A., Veit, R., Birbaumer, N., and Sitaram, R. (2011). Detection of cerebral reorganization induced by real-time fMRI feedback training of insula activation: a multivariate investigation. *Neurorehabilitation and neural repair*, 25(3):259–67.

Logothetis, N. K. (2008). What we can do and what we cannot do with fMRI. *Nature*, 453(7197):869–78.

Lynall, M.-E., Bassett, D. S., Kerwin, R., McKenna, P. J., Kitzbichler, M., Muller, U., and Bullmore, E. (2010). Functional Connectivity and Brain Networks in Schizophrenia. *The Journal of neuroscience : the official journal of the Society for Neuroscience*, 30(28):9477–9487.

Madhavan, S., Rogers, L. M., and Stinear, J. W. (2010). A paradox: after stroke, the non-lesioned lower limb motor cortex may be maladaptive. *The European journal of neuroscience*, 32(6):1032–9.

Mechelli, A., Price, C. J., Friston, K. J., and Ashburner, J. (2005). Voxel-based morphometry of the human brain: methods and applications. *Current Medical Imaging Reviews*, 1(2):105–113.

Merrill, M. J. and Oldfield, E. H. (2005). A reassessment of vascular endothelial growth factor in central nervous system pathology. *Journal of neurosurgery*, 103(5):853–68.

Micheloyannis, S., Pachou, E., Stam, C. J., Vourkas, M., Erimaki, S., and Tsirka, V. (2006). Using graph theoretical analysis of multi channel EEG to evaluate the neural efficiency hypothesis. *Neuroscience letters*, 402(3):273–7.

Minsky, M. (1988). The society of mind.

Pichiorri, F., De Vico Fallani, F., Cincotti, F., Babiloni, F., Molinari, M., Kleih, S. C., Neuper, C., Kübler, A., and Mattia, D. (2011). Sensorimotor rhythm-based brain-computer interface training: the impact on motor cortical responsiveness. *Journal of neural engineering*, 8(2):025020.

Raichle, M. E., MacLeod, A. M., Snyder, A. Z., Powers, W. J., Gusnard, D. A., and Shulman, G. L. (2001). A default mode of brain function. *Proceedings of the National Academy of Sciences of the United States of America*, 98(2):676.

Ross, C. A. and Poirier, M. A. (2004). Protein aggregation and neurodegenerative disease. *Neurodegeneration*, (July).

Rubinov, M., Knock, S. a., Stam, C. J., Micheloyannis, S., Harris, A. W. F., Williams, L. M., and Breakspear, M. (2009). Small-world properties of nonlinear brain activity in schizophrenia. *Human brain mapping*, 30(2):403–16.

Ruhrberg, C., Rosenstein, J. M., and Krum, J. M. (2008). *VEGF in Development*. Springer New York, New York, NY.

Sato, K., Aoki, S., Iwata, N. K., Masutani, Y., Watadani, T., Nakata, Y., Yoshida, M., Terao, Y., Abe, O., Ohtomo, K., and Tsuji, S. (2010). Diffusion tensor tract-specific analysis of the uncinate fasciculus in patients with amyotrophic lateral sclerosis. *Neuroradiology*, 52(8):729–33.

Scholz, J., Klein, M. C., Behrens, T. E. J., and Johansen-Berg, H. (2009). Training induces changes in white-matter architecture. *Nature neuroscience*, 12(11):1370–1.

Schummers, J., Yu, H., and Sur, M. (2008). Tuned responses of astrocytes and their influence on hemodynamic signals in the visual cortex. *Science (New York, N.Y.)*, 320(5883):1638–43.

Seeley, W. W., Crawford, R. K., Zhou, J., Miller, B. L., and Greicius, M. D. (2009a). Neurodegenerative diseases target large-scale human brain networks. *Neuron*, 62(1):42–52.

Seeley, W. W., Crawford, R. K., Zhou, J., Miller, B. L., and Greicius, M. D. (2009b). Neurodegenerative diseases target large-scale human brain networks. *Neuron*, 62(1):42–52.

Seeley, W. W., Menon, V., Schatzberg, A. F., Keller, J., Glover, G. H., Kenna, H., Reiss, A. L., and Greicius, M. D. (2007a). Dissociable intrinsic connectivity networks for salience processing and executive control. *The Journal of neuroscience : the official journal of the Society for Neuroscience*, 27(9):2349–56.

Seeley, W. W., Menon, V., Schatzberg, A. F., Keller, J., Glover, G. H., Kenna, H., Reiss, A. L., and Greicius, M. D. (2007b). Dissociable intrinsic connectivity networks for salience processing and executive control. *The Journal of neuroscience : the official journal of the Society for Neuroscience*, 27(9):2349–56.

Senda, J., Kato, S., Kaga, T., Ito, M., Atsuta, N., Nakamura, T., Watanabe, H., Tanaka, F., Naganawa, S., and Sobue, G. (2011). Progressive and widespread brain damage in ALS: MRI voxel-based morphometry and diffusion tensor imaging study. *Amyotrophic lateral sclerosis : official publication of the World Federation of Neurology Research Group on Motor Neuron Diseases*, 12(1):59–69.

Sondell, M., Lundborg, G., and Kanje, M. (1999). Vascular endothelial growth factor has neurotrophic activity and stimulates axonal outgrowth, enhancing cell survival and Schwann cell proliferation in the peripheral nervous system. *The Journal of neuroscience : the official journal of the Society for Neuroscience*, 19(14):5731–40.

Sporns, O. (2007). Brain connectivity. *Scholarpedia*, 2(10):4695.

Sporns, O. (2010). *Networks of the Brain*. The MIT Press.

Stagg, C. J., Bachtiar, V., and Johansen-Berg, H. (2011). The role of GABA in human motor learning. *Current biology : CB*, 21(6):480–4.

Stam, C. J., de Haan, W., Daffertshofer, a., Jones, B. F., Manshanden, I., van Cappellen van Walsum, a. M., Montez, T., Verbunt, J. P. a., de Munck, J. C., van Dijk, B. W., Berendse, H. W., and Scheltens, P. (2009). Graph theoretical analysis of magnetoencephalographic functional connectivity in Alzheimer's disease. *Brain : a journal of neurology*, 132(Pt 1):213–24.

Stam, C. J., Jones, B. F., Nolte, G., Breakspear, M., and Scheltens, P. (2007). Small-world networks and functional connectivity in Alzheimer's disease. *Cerebral cortex (New York, N.Y. : 1991)*, 17(1):92–9.

Sugihara, S., Kinoshita, T., Matsusue, E., Fujii, S., and Ogawa, T. (2004). Usefulness of Diffusion Tensor Imaging of White Matter in Alzheimer Disease and Vascular Dementia. *Acta Radiologica*, 45(6):658–663.

Takeuchi, H., Sekiguchi, A., Taki, Y., Yokoyama, S., Yomogida, Y., Komuro, N., Yamanouchi, T., Suzuki, S., and Kawashima, R. (2010). Training of working memory impacts structural connectivity. *The Journal of neuroscience : the official journal of the Society for Neuroscience*, 30(9):3297–3303.

Tamás Kincses, Z., Johansen-Berg, H., Tomassini, V., Bosnell, R., Matthews, P. M., and Beckmann, C. F. (2008). Model-free characterization of brain functional networks for motor sequence learning using fMRI. *NeuroImage*, 39(4):1950–8.

Tang, Y.-Y., Lu, Q., Geng, X., Stein, E. A., Yang, Y., and Posner, M. I. (2010). Short-term meditation induces white matter changes in the anterior cingulate. *Proceedings of the National Academy of Sciences of the United States of America*, 107(35):15649–15652.

Teipel, S. J., Pogarell, O., Meindl, T., Dietrich, O., Sydykova, D., Hunklinger, U., Georgii, B., Mulert, C., Reiser, M. F., Möller, H.-J., and Hampel, H. (2009). Regional networks underlying interhemispheric connectivity: an EEG and DTI study in healthy ageing and amnestic mild cognitive impairment. *Hum Brain Mapp*, 30(7):2098–2119.

Valdés-Hernández, P. a., Ojeda-González, A., Martínez-Montes, E., Lage-Castellanos, A., Virués-Alba, T., Valdés-Urrutia, L., and Valdes-Sosa, P. a. (2010). White matter architecture rather than cortical surface area correlates with the EEG alpha rhythm. *NeuroImage*, 49(3):2328–39.

van den Heuvel, M. P., Mandl, R. C. W., Kahn, R. S., and Hulshoff Pol, H. E. (2009). Functionally linked resting-state networks reflect the underlying structural connectivity architecture of the human brain. *Human brain mapping*, 30(10):3127–41.

Van Dijk, K. R. a., Hedden, T., Venkataraman, A., Evans, K. C., Lazar, S. W., and Buckner, R. L. (2010). Intrinsic functional connectivity as a tool for human connectomics: theory, properties, and optimization. *Journal of neurophysiology*, 103(1):297–321.

Varela, F., Lachaux, J. P., Rodriguez, E., and Martinerie, J. (2001). The brainweb: phase synchronization and large-scale integration. *Nature reviews. Neuroscience*, 2(4):229–39.

Várkuti, B., Cavusoglu, M., Kullik, A., Schiffler, B., Veit, R., Yilmaz, O., Rosenstiel, W., Braun, C., Uludag, K., Birbaumer, N., and Sitaram, R. (2011). Quantifying the link between anatomical connectivity, gray matter volume and regional cerebral blood flow: an integrative MRI study. *PloS one*, 6(4):e14801.

Voss, M. W., Prakash, R. S., Erickson, K. I., Boot, W. R., Basak, C., Neider, M. B., Simons, D. J., Fabiani, M., Gratton, G., and Kramer, A. F. (2011). Effects of training strategies implemented in a complex videogame on functional connectivity of attentional networks. *NeuroImage*.

Wendel, K., Väisänen, O., Malmivuo, J., Gencer, N. G., Vanrumste, B., Durka, P., Magjarević, R., Supek, S., Pascu, M. L., Fontenelle, H., and Grave de Peralta Menendez, R. (2009). EEG/MEG source imaging: methods, challenges, and open issues. *Computational intelligence and neuroscience*, 2009:656092.

Whitfield-Gabrieli, S., Thermenos, H. W., Milanovic, S., Tsuang, M. T., Faraone, S. V., McCarley, R. W., Shenton, M. E., Green, A. I., Nieto-Castanon, A., LaViolette, P., Wojcik, J., Gabrieli, J. D. E., and Seidman, L. J. (2009). Hyperactivity and hyperconnectivity of the default network in schizophrenia and in first-degree relatives of persons with schizophrenia. *Proceedings of the National Academy of Sciences of the United States of America*, 106(4):1279–84.

Whitford, T. J., Kubicki, M., Ghorashi, S., Schneiderman, J. S., Hawley, K. J., McCarley, R. W., Shenton, M. E., and Spencer, K. M. (2010). Predicting inter-hemispheric transfer time from the diffusion properties of the corpus callosum in healthy individuals and schizophrenia patients: A combined ERP and DTI study. *NeuroImage*, 54(3):2318–2329.

Woolley, S. C., Zhang, Y., Schuff, N., Weiner, M. W., and Katz, J. S. (2011). Neuroanatomical correlates of apathy in ALS using 4 Tesla diffusion tensor MRI. *Amyotrophic lateral sclerosis : official publication of the World Federation of Neurology Research Group on Motor Neuron Diseases*, 12(1):52–8.

Wu, X., Li, R., Fleisher, A. S., Reiman, E. M., Guan, X., Zhang, Y., Chen, K., and Yao, L. (2011). Altered default mode network connectivity in alzheimer's disease-A resting functional MRI and bayesian network study. *Human brain mapping*, 00(November 2009).

Xu, Y., Olman, V., and Xu, D. (2002). Clustering gene expression data using a graph-theoretic approach: an application of minimum spanning trees. *Bioinformatics*, 18(4):536–545.

7 Publications, manuscripts and contributions

Publications, manuscripts and contributions				
Title	Authors	Reception	Chapter Number	Own contribution
Quantifying the Link between Anatomical Connectivity, Gray Matter Volume and Regional Cerebral Blood Flow: An Integrative MRI Study	Bálint Várkuti Mustafa Cavusoglu Alexander Kullik Björn Schiffler Ralf Veit Özge Yilmaz Wolfgang Rosenstiel Christoph Braun Kamil Uludag Niels Birbaumer Ranganatha Sitaram	Published	1	BV designed and conducted the experiments, analyzed the data and wrote the paper.
Towards a taxonomy of functional connectivity networks	Bálint Várkuti Sebastian Halder Colleen Dockery Markus Schneider Philipp Keune Eric Fimbel Kamil Uludag Wolfgang Rosenstiel Niels Birbaumer Ranganatha Sitaram	Ready for Submission	2	BV designed and conducted 5/8 of the experiments, analyzed the data and wrote the paper.
Resting state functional connectivity changes predict movement recovery due to robot assisted BCI training in stroke patients	Bálint Várkuti Cuntai Guan Yaozhang Pan Kok Soon Phua Kai Keng Ang Christoph W.K. Kuah Karen Chua Beng Ti Ang Niels Birbaumer Ranganatha Sitaram	Under Revision	3	BV analyzed the data and wrote the paper.
SMR EEG-BCI aptitude in healthy subjects varies with the integrity of Corpus Callosum white matter in stroke patients	Bálint Várkuti Sebastian Halder Martin Bogdan Andrea Kübler Wolfgang Rosenstiel Ranganatha Sitaram Niels Birbaumer	Accepted	4	BV analyzed the data and wrote the paper.

7.1 Chapter 1 - The link between Anatomical Connectivity, Perfusion and regional Cerebral Blood Flow

Quantifying the link between Anatomical Connectivity, Gray Matter Volume and regional Cerebral Blood Flow – an integrative MRI study

Author list and affiliation:

Bálint Várkuti[1,2]

Mustafa Cavusoglu[3]

Alexander Kullik[4]

Björn Schiffler[7]

Ralf Veit[1]

Özge Yilmaz[1]

Wolfgang Rosenstiel[4]

Christoph Braun[1,5]

Kamil Uludag[3]

Niels Birbaumer[1,6]

Ranganatha Sitaram[1]

1 Institute of Medical Psychology and Behavioral Neurobiology, University of Tübingen, Tübingen, Baden-Württemberg, Germany

2 Graduate Training Centre of Neuroscience, International Max Planck Research School, Tübingen, Baden-Württemberg, Germany

3 Max Planck Institute for Biological Cybernetics, Tübingen, Baden-Württemberg, Germany

4 Wilhelm-Schickard Institute for Computer Engineering, University of Tübingen, Tübingen, Baden-Württemberg, Germany

5 CIMeC - Centro interdipartimentale Mente/Cervello, Rovereto, Trento, Italy

6 Ospedale San Camillo, Istituto di Ricovero e Cura a Carattere Scientifico, Venezia, Veneto, Italy

7 Institute of Psychology, Albert-Ludwigs-University, Freiburg im Breisgau, Baden-Württemberg, Germany

Abstract

Background:

In the graph theoretical analysis of anatomical brain connectivity, the white matter connections between regions of the brain are identified and serve as basis for the assessment of regional connectivity profiles, to e.g. locate the hubs of the brain. But regions of the brain can be characterised further with respect to their gray matter volume or resting state perfusion. Local anatomical connectivity, gray matter volume and perfusion are traits of each brain region that are likely to be interdependent, however particular patterns of systematic covariation have not yet been identified.

Methodology/Principal Findings:

We quantified the covariation of these traits by conducting an integrative MRI study on 23 subjects, utilising a combination of Diffusion Tensor Imaging, Arterial Spin Labeling and anatomical imaging. Based on our hypothesis that local connectivity, gray matter volume and perfusion are linked, we correlated these measures and particularly isolated the covariation of connectivity and perfusion by statistically controlling for gray matter volume. We found significant levels of covariation on the group- and regionwise level, particularly in regions of the Default Brain Mode Network.

Conclusions/Significance:

Connectivity and perfusion are systematically linked throughout a number of brain regions, thus we discuss these results as a starting point for further research on the role of homology in the formation of functional connectivity networks and on how structure/function relationships can manifest in the form of such trait interdependency.

Introduction

Recent findings are beginning to shed light on the organisational principles behind the structure of the brain [1]. Instead of studying the brain merely as an agglomeration of individual regions with their very specific functions and structural idiosyncrasies, this research, with its new and more systemic perspective, is trying to understand the fundamental lines along which structure/function relationships form [2-5].

Such principles are identified by studying the parts (e.g. brain regions) and analysing the global properties of the entire system that emerge from links between the parts (e.g. white matter connections). The network of white matter connections in the brain seems to adhere to a small-world organisation principle, defined by short path lengths for reaching any part from any other part, while providing high clustering and highly efficient wiring.

Once such a property is established, relations to properties of other systems can be analysed.

The shared small-world properties of interregional gray matter structural similarity [6-7] and white matter connectivity, and the small-world properties of functional brain networks as assessed with

electroencephalography [8], are recent examples that certain common principles of organisation can be found in a multitude of brain systems and on a number of scales [9].

As some of these traits, such as number of synapses, cell body population, perfusion and type and quantity of neural fiber bundles have proven to be examinable using advanced imaging methods of spectroscopy, perfusion, structural or diffusion MRI, brain regions can now be characterised regarding multiple traits at once. In certain cases the relationship between different structural properties is formed in a systematic way, e.g. larger brain regions tend to have more connections than smaller brain regions. In other cases, structural and functional traits are also systematically coupled, e.g. the neural computations that take place in a particular brain region are partially shaped by the quantity, quality and usage of the in- and outgoing connections of that region. In turn the principle of functional (computational) segregation - as reflected in the typology of unimodal motor and sensory or heteromodal association areas of the cortex - is known to be mirrored both in the macroscopic white matter network topology [10] and in functional connectivity networks [11]. The afferent and efferent white matter connections of the motor system, the ascending pathways of the primary sensory cortices and the rich interconnectivity of the association areas are not uncoupled from the function of these areas, but rather allow us to formulate hypotheses on their functional roles.

Mounting evidence suggests [12-15] that certain functional traits - such as the activity profile of a brain region arising from its function and its metabolic demand as reflected e.g. by local capillary density - are closely coupled [16, 17]. Local metabolic demand and perfusion are directly linked in the healthy brain, thus allowing the indirect assessment of metabolism through means of perfusion weighted imaging.

If local white matter connectivity shapes neurocomputational processes, and these processes influence local function and therefore metabolic demand, one could hypothesise that local white matter connectivity and local perfusion might be coupled throughout the brain as well. If this were the case, such coupling would constitute the manifestation of a supply-and-demand-principle - the metabolic demand being shaped by connectivity - in the formation of a previously undocumented structure/function relationship.

In order to quantify the outlined traits of perfusion and white matter connectivity we conducted an integrative MRI study on 23 healthy subjects (divided into two groups of 11 and 12 participants), utilising a combination of Diffusion Tensor Imaging (DTI), Arterial Spin Labeling (ASL) and anatomical imaging. DTI and ASL are methods to non-invasively characterise white matter structure and gray matter function of the brain, respectively [18-19]. While DTI allows for the estimation of anatomical connectivity between regions of the brain, ASL represents a MRI method for the quantification of global and regional Cerebral Blood Flow (rCBF).

DTI based tractography can be used to characterise the amount and integrity of white matter tracks between two regions and allows for an estimation of connection probability. For this purpose, probability density maps can be formed from the repeated propagation of curves through the DTI-based tensor field, which is representing local white matter orientation. Currently, DTI data are integrated into graph

representations [20, 21] of the white matter network in order to analyse the relation of network topology to function [22] and its impairment [23]. This type of network modelling has originated from the broader discipline of graph theory [24], which is dedicated to the understanding of the emergence of certain global and local properties of a given system from the distribution of pairwise relations of parts of that system (e.g. if many nodes have one connection to another single node, the sum of these connections or edges make that node the hub of the system).

This approach allows for the quantification of node specific traits (e.g. the number of edges connecting one node to others nodes, termed degree), edge specific traits (e.g. how severely a network is affected by the removal of an edge) and general graph properties (e.g. how efficient is the information transfer from any point A to any point B in general).

ASL [25, 26] on the other hand has proven to be a sensitive and reliable method for the quantification of gray matter perfusion, defined as the volume of arterial blood delivered to the capillary bed per unit volume of brain tissue per unit time. It has been utilised to study brain function following neuronal activation, as well as for the detection of changes of perfusion occurring during brain pathology, maturation and aging [27, 28]. This is done by assessing the inflow of magnetically labelled arterial water spins into an imaging slice. For quantitative measurement of rCBF, ASL constructs images following a tagging of inflowing arterial blood by a 180° radiofrequency inversion pulse and, in an interleaved fashion, acquiring control images without prior tagging, so that the subtraction of these two images (control-tag) only leaves magnetisation proportional to the blood flow.

So far, only limited attention has been paid to possible synergies from the combined use of these two imaging modalities. As a result, the link between white matter network connectivity and rCBF has not yet been systematically addressed. Currently, there are a few studies focusing on rCBF alterations and changes in white matter integrity (e.g. level of myelinisation, orientation of fibers) as markers of Alzheimer´s disease (AD) and mild cognitive impairment [29], but the number of systematic studies using state of the art imaging of both modalities in the same sample is low. White matter lesions in the frontal lobe were found [30] to be correlated with a lower CBF in the elderly. [31] reported that rCBF reductions in the parietal cortex are correlated with white matter integrity reductions in the Posterior Cingulum in a healthy sample. However, evidence for a systematic relationship between white matter network topology and rCBF has yet to be established.

Following our hypothesis that local metabolic demands are largely determined by the connectivity profile of a brain region, we assumed that local perfusion and local connectivity measures of gray matter regions are to be correlated. In order to take into account the properties of the gray matter regions themselves (e.g. a region with larger volume might show higher perfusion and higher degree), we integrated a Voxel-based Morphometry (VBM) analysis into our design. VBM is an established method [32, 33] for the quantification of volumetric differences for the entire brain and its subparts based on anatomical MRI images.

Our approach allows for the analysis of the entire trait triplet of gray matter volume (GMV), white matter connectivity and perfusion at once.

Using this multi-facetted data we analysed the connectivity/perfusion-covariation profiles for regions of the Automated Anatomical Labeling (AAL) atlas, while controlling for GMV (see Figure 1).

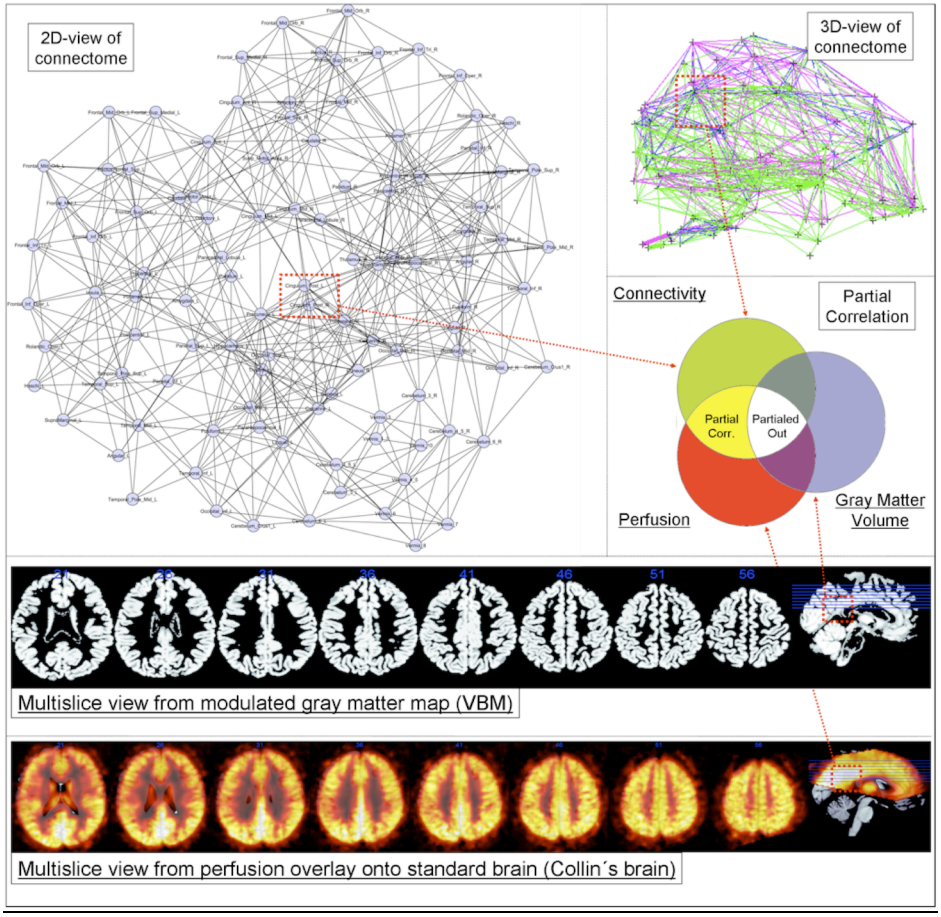

Figure 1, General principle - Graph theoretical properties of the nodes (in this example Posterior Cingulate) are correlated with their relative perfusion (multi-slice example in low row) while controlling for GMV (multi-slice example in upper row) - left-upper 2D graph in background formed by using the Spring Embedder Algorithm on a group averaged connectome for cortico-cortical sparsity 11%. In our PC approach we partial out the statistical influence of GMV in order to assess the covariation of perfusion and connectivity directly.

For the further analysis we divided the regions into the region classes cortical, subcortical and regions of the Default Brain Mode Network (DMN). The rationale for this division are manifold, on the one hand the graph theoretical and perfusion specific characterisation of subcortical regions is a novelty of this study, on the other hand it stands to reason that vasculature and connectivity systematically differ between cortical and subcortical regions and thus should be considered separately. Because we were particularly interested in the covariation profiles of regions with documented high resting state activity, we subdivided the class of cortical regions further into a DMN regions class. These region classes were comprehensively analysed on the individual-, group- and regionwise levels while controlling for local GMV. Furthermore we report on the

correlation between perfusion with GMV, as well as GMV and perfusion with graph theoretical properties of white matter connectivity, respectively.

We employed a probabilistic tractography approach for the estimation of our white matter connectivity graphs and provide results from not one, but many plausible white matter networks (connectomes). Whereas the state of the art does currently not serve with unambiguous properties of a commonly accepted connectome standard, we provide results from a sweep over plausible edge probability thresholds and resulting cortico-cortical sparsity values.

Results

2.1 White matter network topology

Adjacency graphs such as connectomes can be described regarding their small-world properties using path length, clustering and the ratio of both. Relative path length is calculated as the current path length in a given adjacency graph relative to the path length in an equal random graph and expressed in the coefficient Lambda. The coefficient Gamma is calculated analogously for clustering and the coefficient Sigma is defined as Gamma/Lambda ratio, respectively.

The estimated connectomes of all subjects showed small-world characteristics (Group 1, Lambda M=1.3413 SD=0.0121; Gamma M=5.1155 SD=0.5179; Sigma M=3.6525 SD=0.3181; Group 2, Lambda M=1.3283 SD=0.0218; Gamma M=4.6459 SD=0.54341; Sigma M=4.2216 SD=0.3260) as described by [10] for the plausible cortico-cortical sparsity sweep range of 11-17 %.

The different DTI scanning parameters (higher number of diffusion directions and better spatial resolution for Group 2) for both groups resulted in Group 2 showing higher Sigma values for the sweep range than Group 1 for comparable sparsity values. Further it is to note that thresholding with equal edge probability values in both groups consistently lead to a higher number of accepted edges for the connectomes of Group 2.

Small-world property analyses for interregional GMV and perfusion correlations are provided in the supporting information files.

2.2 General sample characteristics

To address relation between the total rCBF in non-cerebellar regions of the brain and whole-brain graph theoretical metrics, we tested for such correlations in each group. For this analysis, whole-brain connection density, Lambda, Gamma, average degree, clustering coefficient and global efficiency values for the brain of each subject were paired with the same individual´s average rCBF values (ASL measured in resting state), derived from of all non-cerebellar brain regions. These variables were tested for potential correlations (Spearman´s rho) with graph metrics resulting from each step of the sweep over plausible edge probability thresholds. For each group p-values for all thresholding steps were False Discovery Rate (FDR, $p<0.05$) corrected. No significant results were obtained.

With respect to regional properties, as expected relative perfusion (after within-subject normalisation) was found to be higher in DMN regions than in other regions of the cortex (two-sample t-test, p=0.0019), in accordance with our hypothesis. The difference between total perfusion (unnormalised rCBF) in regions of the DMN and the rest of the cortex showed a tendency towards significance (two-sample t-test, p=0.0723). Regions of the DMN had significantly higher relative GMV than other regions of the cortex (two-sample t-test, $p=7.6283*10^{-8}$).

2.3 Correlation between perfusion, connectivity and GMV

The correlation between perfusion and graph metrics for cortical, subcortical and DMN regions for connectomes from the plausible cortico-cortical sparsity range of 11-17 % [20] with their respective minima and maxima magnitudes (Spearman´s rho correlation, all FDR, p<0.05 corrected) are reported for both groups in Figures 3-5 and Table 1.

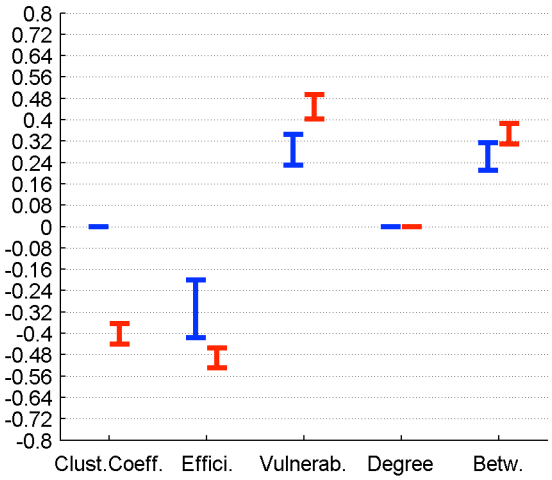

Figure 3, Correlation between graph theoretical metrics and perfusion for Group 1 (in blue) and Group 2 (in red), for the subcortical region class; the minima and maxima of correlation magnitudes are provided for FDR (p<0.05) corrected significant correlations (Spearman´s rho), calculated with graph metrics from connectomes resulting from the sweep over plausible cortico-cortical sparsity levels (11-17 % range)

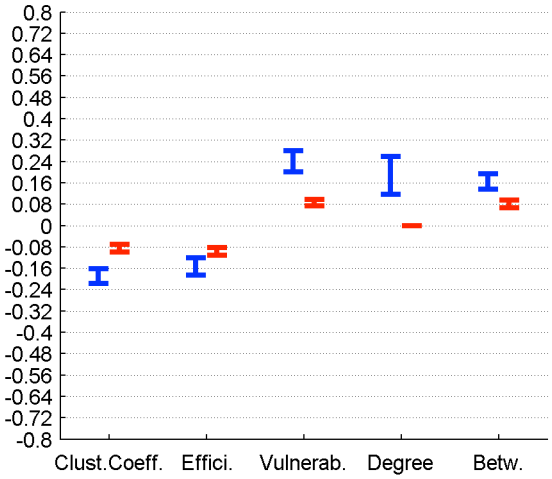

Figure 4, Correlation between graph theoretical metrics and perfusion for Group 1 (in blue) and Group 2 (in red), for the cortical region class; the minima and maxima of correlation magnitudes are provided for FDR ($p<0.05$) corrected significant correlations (Spearman´s rho), calculated with graph metrics from connectomes resulting from the sweep over plausible cortico-cortical sparsity levels (11-17 % range)

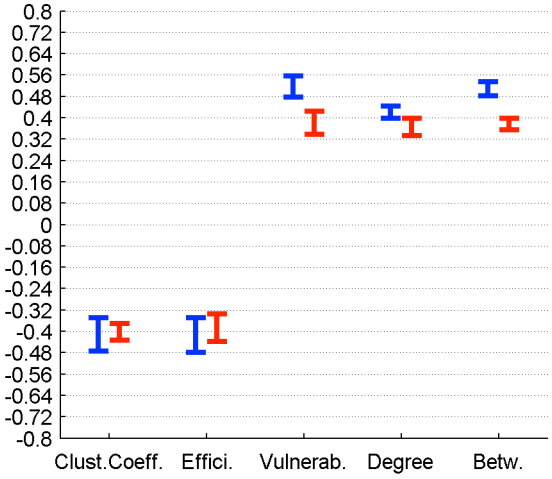

Figure 5, Correlation between graph theoretical metrics and perfusion for Group 1 (in blue) and Group 2 (in red), for the DMN region class; the minima and maxima of correlation magnitudes are provided for FDR ($p<0.05$) corrected significant correlations (Spearman´s rho), calculated with graph metrics from connectomes resulting from the sweep over plausible cortico-cortical sparsity levels (11-17 % range)

The correlation between GMV and graph metrics for cortical, subcortical and DMN regions for connectomes from the plausible cortico-cortical sparsity range of 11-17 % [20] with their respective minima and maxima magnitudes (Spearman´s rho correlation, all FDR, $p<0.05$ corrected) are reported for both groups in Figures 6-8 and Table 2.

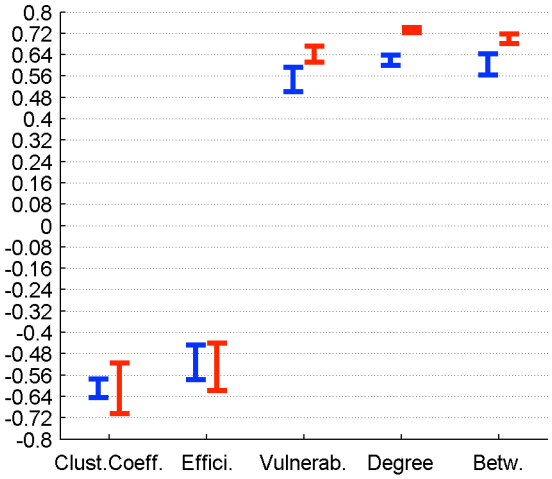

Figure 6, Correlation between graph theoretical metrics and GMV for Group 1 (in blue) and Group 2 (in red), for the subcortical region class; the minima and maxima of correlation magnitudes are provided for FDR ($p<0.05$) corrected significant correlations (Spearman´s rho), calculated with graph metrics from connectomes resulting from the sweep over plausible cortico-cortical sparsity levels (11-17 % range)

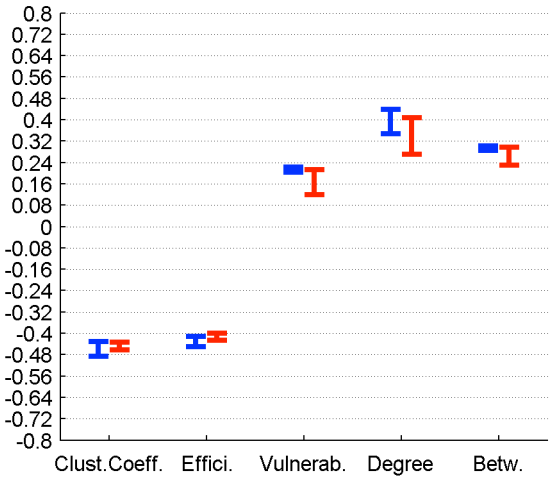

Figure 7, Correlation between graph theoretical metrics and GMV for Group 1 (in blue) and Group 2 (in red), for the cortical region class; the minima and maxima of correlation magnitudes are provided for FDR ($p<0.05$) corrected significant correlations (Spearman´s rho), calculated with graph metrics from connectomes resulting from the sweep over plausible cortico-cortical sparsity levels (11-17 % range)

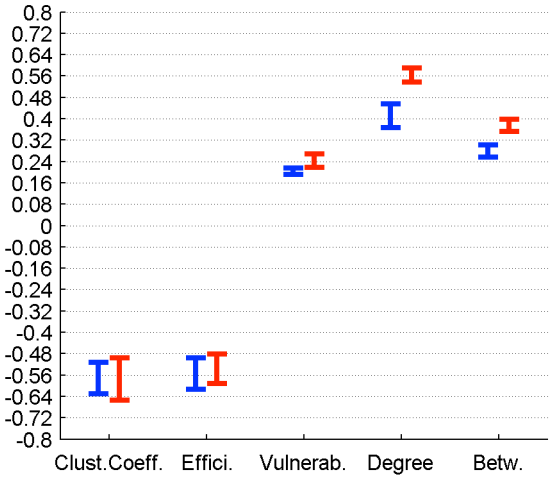

Figure 8, Correlation between graph theoretical metrics and GMV for Group 1 (in blue) and Group 2 (in red), for the DMN region class; the minima and maxima of correlation magnitudes are provided for FDR ($p<0.05$) corrected significant correlations (Spearman´s rho), calculated with graph metrics from connectomes resulting from the sweep over plausible cortico-cortical sparsity levels (11-17 % range)

The correlation between GMV and perfusion for cortical, subcortical, all non-cerebellar and DMN regions (Pearson´s correlation, all FDR, $p<0.05$ corrected) are reported for a whole-sample analysis (perfusion and anatomical image acquisition were similar in both groups, therefore a whole-sample analysis can be conducted exclusively for this trait pair) in Figure 9 and Table 3.

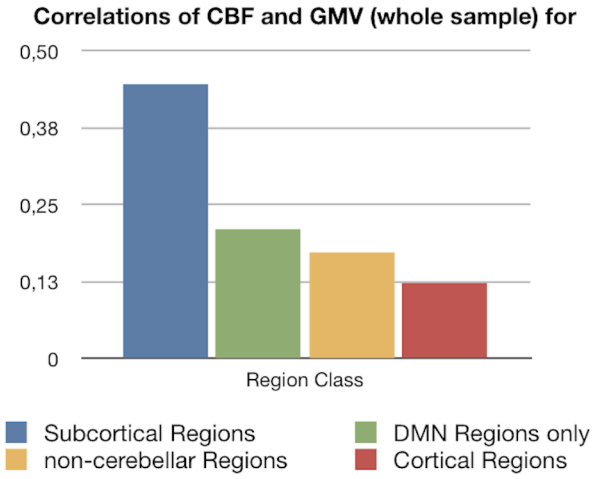

Figure 9, Correlation between GMV and perfusion for the whole-sample level are provided for the region classes cortical, subcortical, all non-cerebellar and DMN, all results FDR ($p<0.05$) corrected

Both GMV and perfusion are systematically correlated with graph metrics, hence we repeated our analysis using GMV as a control variable.

2.4 Partial correlation between perfusion and connectivity controlling for GMV

2.4.1 Group Level

2.4.1.1 Cortical Nodes

For the 78 cortical nodes the partial correlations (PCs) of perfusion and the graph theoretical metrics local clustering coefficient, local efficiency, local vulnerability, degree and betweenness (control variable: local GMV) fail to reach significance (FDR correction applied for each metric and group separately, $p<0.05$) in both groups for all connectome estimations from the cortico-cortical sparsity range 11 - 17 %. Significant PCs are found for Group 1 in the form of a negative covariation of the clustering coefficient (in range 13-16 %, rho between -0.095 and -0.077) and a positive covariation of vulnerability (in range 10-16 %, rho between 0.144 and 0.23), degree (in range 13.5-16 %, rho between 0.093 and 0.148) and betweenness (in range 11.5 - 16 %, rho between 0.074 and 0.11) with perfusion, but are minor in magnitude. Group 2 only shows a minor covariation of perfusion and degree (in range 11.5-13.5 %, rho between -0.129 and -0.09).

2.4.1.2 Subcortical Nodes

For the 10 subcortical nodes the PCs of perfusion and the graph theoretical metrics namely local clustering coefficient and betweenness (control variable: local GMV) fail to reach significance (FDR correction applied for each metric and group separately, $p<0.05$) in both groups for all connectome estimations from the cortico-cortical sparsity range 11 - 17 %.

Significant PCs are found for both groups in the sparsity range of 13-16 % in the form of a negative covariation of local efficiency with perfusion (Group 1, rho between -0.351 and -0.249, Group 2 rho between -0.3940 and -0.2979), and a positive covariation of vulnerability and perfusion (in range 12-13 %, Group 1 rho between 0.2276 and 0.257, Group 2 rho between 0.1858 and 0.3012).

When groups are analysed separately, significant PCs are found for Group 2 in the form of a negative covariation of degree (in range 11.8 - 17 %, rho between -0.2523 and -0.1932) with perfusion, but are not supported by results from Group 1.

2.4.1.3 DMN Nodes

In order to specifically characterise regions (such as Medial Prefrontal Gyrus, Medial Temporal Lobe and Pole, Posterior Cingulate Cortex, Precuneus, Inferior Parietal Lobe) which are associated with the Default Brain Mode [34] we singled these cortical nodes out and repeated the groupwise analysis.

For these 12 cortical nodes the PCs of perfusion and the graph theoretical metrics local clustering coefficient, local efficiency, vulnerability, degree and betweenness (control variable: local GMV) reached significance (FDR correction applied for each metric and group separately, $p<0.05$) in both groups for all connectome estimations from the cortico-cortical sparsity range 11 - 17 %. The results are summarised in Figure 10 and Table 4.

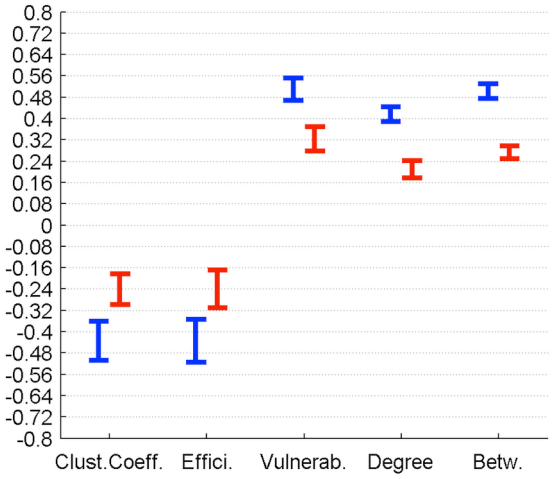

Figure 10, PC of graph theoretical metrics and perfusion for Group 1 (in blue) and Group 2 (in red) for the region class DMN are provided with the minima and maxima of correlation magnitudes for FDR ($p<0.05$) corrected significant correlations (Spearman´s rho), calculated with graph metrics from connectomes resulting from the sweep over plausible cortico-cortical sparsity levels (11-17 % range)

2.4.2. Individual Level

For each group, double FDR correction ($p<0.05$) was applied separately for the PC analyses carried out for each single subject and each single edge threshold (for the plausible sparsity range). On the individual level only five subjects showed any significant covariation (four from Group 1).

The significant correlations on the individual level were all positive and minor to medium in magnitude, found only for the graph metrics degree, betweenness and vulnerability and only for nodes from the DMN and cortical regions.

2.3.3. Regionwise Level

The perfusion, GMV and five graph theoretical metric trait measures of each non-cerebellar brain region of the AAL atlas were collected from each subject into two groupwise tables, one seven-value vector per person for each edge probability threshold. As a result each region can be characterised with respect to the covariation profile of perfusion and graph theoretical anatomical connectivity metrics while controlling for local GMV. For each group, double FDR correction ($p<0.05$) was applied separately for the PC analyses carried out for each single region and each single edge threshold. Only covariation profiles of regions are reported that passed the double FDR correction in both groups for more than half of the edge thresholds in the plausible cortico-cortical sparsity range. The statistically significant regional covariation profiles of the five graph theoretical metrics with local perfusion are provided in the supporting information files with a visualisation in Figure 11.

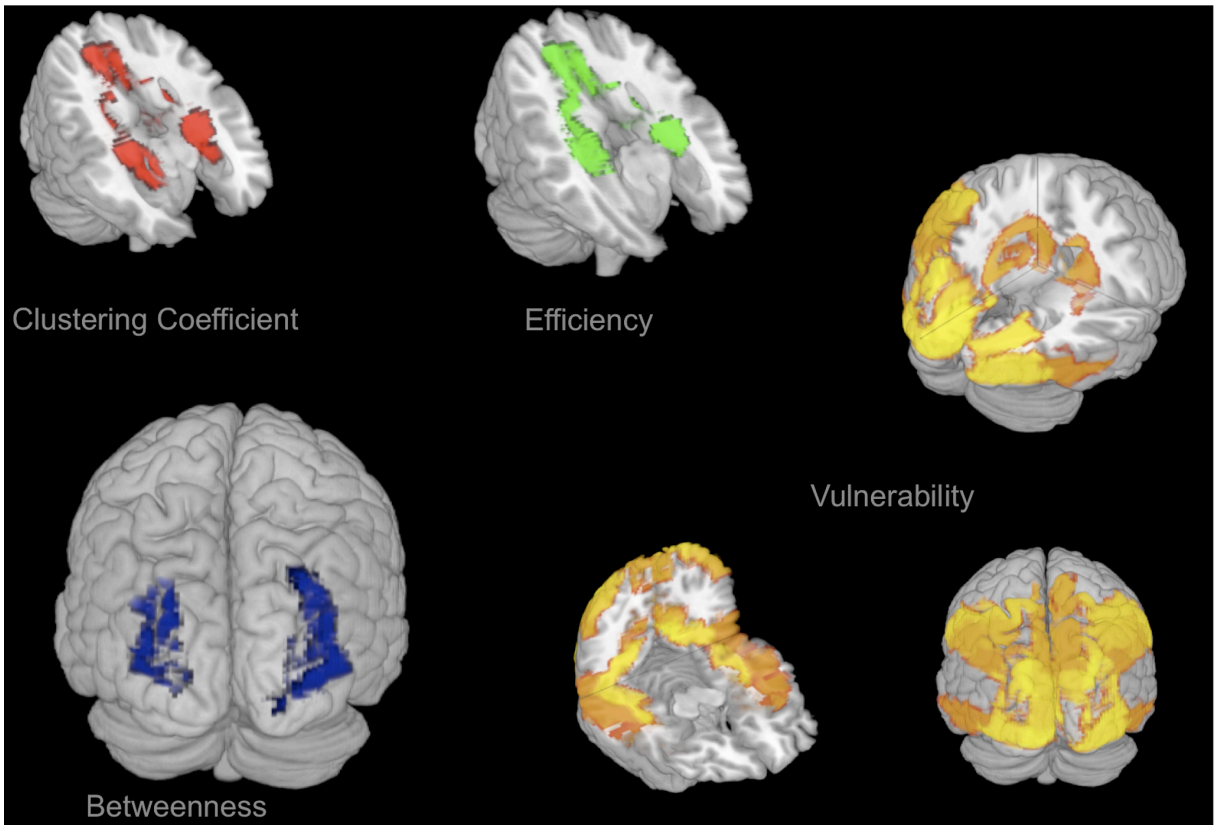

Figure 11, PC of graph theoretical metrics and perfusion for Group 1 and Group 2 for regionwise FDR ($p<0.05$) corrected significant non-contradictory correlations (Spearman´s rho) are visualised with colour intensity based on the absolute maxima of correlation magnitudes, PCs calculated with graph metrics from connectomes resulting from the sweep over plausible cortico-cortical sparsity levels (11-17 % range) - PC of local clustering coefficient and perfusion is negative (red, upper left), PC of local efficiency and perfusion is negative (green, upper middle), PC of local betweenness and perfusion is positive (blue, lower left), PC of local vulnerability and perfusion is positive (yellow, lower right)

Discussion

To the best of our knowledge, this study represents the first attempt to quantify the relation of local perfusion and local anatomical connectivity, using the described MR sequences in combination with a probabilistic estimation of the connectivity graph. Our results on the robust small-world properties of the white matter connectomes are in accordance with previous findings.

3.1. Connectome topology

When conducting a sweep over the range of plausible edge probability thresholds, the properties of the white matter networks from both groups of participants show marked differences. For identical edge probability thresholds the sparsity of the resulting connectomes from Group 2 (DTI measured with a higher

number of diffusion directions and a higher spatial resolution) is higher than the sparsity of connectomes in Group 1. On the other hand small-world property (Sigma) values are numerically higher for the same sparsity levels in Group 2.

It can be assumed that more edges of the white matter network are reliably identified with the superior DTI measurement parameters used in Group 2, and that the entirety of these reliably identifiable edges tend to display small-world properties. The numerically higher path length ratio values (Lambda) in Group 1 might indicate that long-distance white matter connections are measured more reliably with the superior DTI measurement parameters, thus facilitating their probabilistic tracking and acceptance as edge in the subsequent edge probability thresholding process. The acceptance of only a few more long-distance edges can decrease path length drastically, while influencing the sparsity value only minimally.

The deviating Sigma values for equal cortico-cortical sparsity in the two groups might indicate that two qualitatively different white matter networks are compared with one another. But as we presently provide whole-connectome Sigma over cortico-cortical sparsity the deviation in small-world properties may as well be attributable to superior reliability in measuring non-cortico-cortical edges for the DTI sequences applied to Group 2.

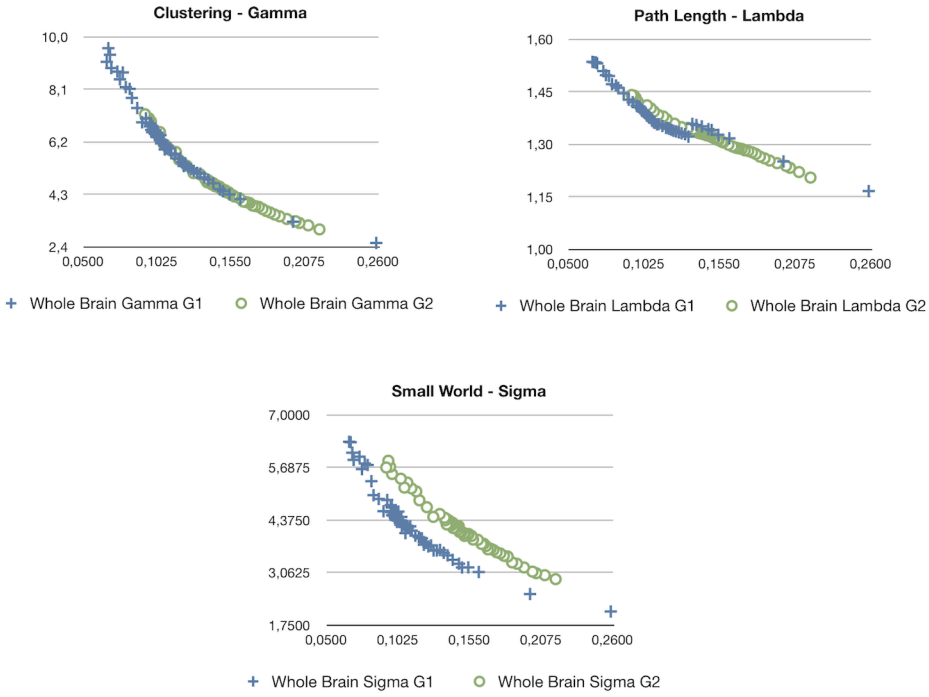

Figure 2, Changes in white matter topology for the whole-connectome values of Gamma, Lambda and Sigma (y-axis) and cortico-cortical sparsity (x-axis, 1 = 100 %) for Group 1 and Group 2

As can be seen in Figure 2 a sudden rise in path length Lambda can be observed in Group 1 between 13.3 and 13.6 % cortico-cortical sparsity. A rise in path length occurring when more edges are added is unusual and indicates that a new cluster of nodes was connected to the rest of the connectome with the additional edges passing a decreasing threshold (leading to higher sparsity level). As clusters unconnected to the rest of

the connectome are unlikely, this might be an indication that the true level of cortico-cortical sparsity might be in a range above 13.6 %.

3.2. General sample characteristics

The lack of any significant relation of whole-brain graph metrics and average perfusion values indicates that there is no relation of overall absolute perfusion and overall connectivity in our healthy sample.

3.3. Correlation between perfusion, connectivity and GMV

Both local GMV and local perfusion show a pattern of significant covariation with local graph theoretical metrics in both groups and for all three described region classes. This pattern of covariation indicates that higher perfusion and higher GMV are more likely to be found in hub-like regions of the brain, with high degree, betweenness and vulnerability, thus with low clustering coefficient and local efficiency.
GMV and perfusion show a marked covariation profile on the whole-sample level, with the strongest correlation for subcortical regions, followed by regions of the DMN and finally non-cerebellar regions in general and cortical regions. The marked correlations of perfusion and GMV could theoretically be a confound due the fact that relatively larger regions contain more large vessels and have a superior ASL Signal-to-Noise ratio (SNR) when compared with smaller regions. Alternatively the correlations could indicate a genuine association of average perfusion and relative GMV.

3.4 Covariation of perfusion and connectivity

Cortical and subcortical nodes were characterised with respect to their graph theoretical properties, which were further correlated with measures of perfusion, while controlling for local GMV.

3.4.1 Group Level

The covariations found on a group level, analysing the trait correlations of all cortical nodes, were only minor (<0.25) in magnitude and inconclusive in terms of cross-group stability. The covariation profile of traits from subcortical nodes on the other hand shows a negative covariation of local efficiency and a positive covariation of vulnerability with perfusion in a minor to medium (<0.6) range of magnitude.
For regions associated with the DMN we observe similar patterns of covariation, but complemented by a positive covariation of degree and betweenness and a negative covariation of the clustering coefficient with perfusion, in a range of minor to medium magnitude.
For all three classes of nodes, the magnitude of covariation observed in Group 1 exceeds the magnitude of covariations in Group 2.

3.4.2. Individual Level

On the individual level correlations for all cortical, subcortical and DMN regions largely fail to reach significance in a stable pattern.

3.4.3. Regionwise Level

On a regionwise level, frontal, cingular and hippocampal regions show a negative covariation of perfusion with the clustering coefficient and local efficiency, while mainly posterior portions of the brain show a positive covariation particularly with vulnerability. All covariations remain minor to medium in magnitude and have the same sign in both groups, except for the Frontal Inferior Cortex (pars triangularis and orbitalis), the Frontal Superior Medial Gyrus, the Supplementary Motor Area, the Olfactory Cortex and the Rolandic Operculum, where the signs of covariation are contradictory.

3.5. General covariation pattern

The present results do not allow for a clear and global falsification of a perfusion/connectivity-covariation in the brain. Rather the results on group- and regionwise levels point towards a positive covariation of rCBF with degree, betweenness and vulnerability and a negative covariation of rCBF with the clustering coefficient and efficiency for some particular regions of the brain.

The correlation results for the covariation of GMV, perfusion and connectivity (no statistical control of GMV) point into the same direction, thus could be influenced by the issues indicated in the methods section.

This might indicate that for some areas of the brain an increased rCBF is more likely to be found in regions, which have a central position in the white matter network and possess hub-like properties, but have poor local clustering and number of parallel pathways to any other node (local efficiency). This might be the manifestation of a structural organisation principle, which strives to minimise the potential of metabolic deficiencies in central nodes, which are part of a rather sequential connection architecture.

The failure of the correlations to reach significance on the individual level could be attributed to the low statistical power, since for the DMN twelve and for the subcortical regions merely ten pairs of values are correlated for each participant, further decreasing the degrees of freedom by using PC and using conservative multiple comparison correction. The same holds for results on the regionwise level (the number of value pairs correlated for each region is equal to the number of subjects in that group, which are eleven and twelve, respectively), which might offer one explanation for the contradictory findings in some regions.

The most stable results are obtained for regions of the DMN on a group- and regionwise level. Regions of the DMN are known to possess hub-like properties in terms of both anatomical and functional connectivity [4]. Possibly the present results point towards an exclusive realisation of an observable linear supply-and-demand-principle of perfusion and connectivity in these regions, although it can not be excluded that regions show possibly non-linear relations, which we did not test for in this present study.

3.6. Implications

These results might have implications on our understanding of resting state networks in general, not only those exclusively involving nodes of the DMN network [34-39].

The finding that DMN regions (e.g. Posterior Cingulate) might play a role as bottlenecks in a potentially task-negative default mode of macroscopic neural traffic might be underlined by past [34] [40] and present results on the coincidence of heightened resting state perfusion and hub characteristics (marked by high degree and vulnerability) in DMN regions. Just like the hubs of any traffic network can form bottlenecks where traffic might dam up, some nodes with a central position within the white matter network might show heightened activity during distinct global states, such as rest. But whether the apparent functional connectivity of these hubs can be attributed to genuine joint information processing in a functionally relevant network or merely to similar activity arising from e.g. coincidentally relaying traversing neural signals, or parts of both, can currently not be conclusively answered.

It is possible that the common traits (high perfusion, hub-like connectivity, large relative GMV) and the strong covariation of these traits contribute either causally to the formation, or confoundingly to our awareness of resting state networks. Similar Blood Oxygen Level Dependent (BOLD) activity profiles might in principle be caused by node interactivity in a functionally relevant information processing network or alternatively by mere similarity of isolated neural processes in individual nodes [3]. It is unclear, to what extent the coincidence of high resting state perfusion and hub-like connectivity can distort estimations of functional connectivity between such nodes, by influencing the BOLD signal from these nodes generally with their mutually high perfusion and the underlying activity in these nodes with their common hub-like connectivity.

Understanding the link between local function and local connectivity better, might help understand the apparent link between functional and anatomical connectivity networks [4] [5] and resolve the role of mere homology in our perception of resting state networks.

It is a further open question of interest, whether there is any causal neurobiological link between a regional perfusion profile and the emergence of hub characteristics or vice versa.

3.7. Conclusion

The method described might hold potential for the diagnosis of various diseases, as the identified dependency of perfusion and connectivity might reflect the balance resulting from organisational principles inherent to the structural architecture of the healthy brain. Although the identified coefficients from the present healthy sample are only minor to medium in magnitude, it is to note that two traits might be only rudimentarily related in the healthy brain, but might show stronger links in the pathologically altered brain (e.g. hypoperfusion preceding gray matter atrophy).

However, to better understand the relevance of the identified relationships and to explore changes of the derived coefficients due to ageing or disease future studies have to be performed on the respective populations.

3.8. Potential confounds

It can be assumed that during our resting state ASL measurement, the regions of the DMN showed their - by definition - heightened resting state activity and metabolic demand and it is possible that our measurements were therefore systematically biased. If the metabolic profile of a region is best assessed when this region shows a stable amount of activity over time, the metabolic demand of the resting state active brain regions (the DMN) was eventually captured more clearly by our resting state experiment, than the metabolic demand profile of a less resting state involved region such as e.g. the Fusiform Gyrus. This issue touches on the general question whether stimulus-free measurements constitute a reliable baseline measurement for the whole brain, or only for regions active under stimulus-free conditions.

Thus it can not be excluded that covariations of the present form could be identified more conclusively for others regions of the brain as well. For such experiments, these regions would need to be consistently activated for a prolonged amount of time (e.g. by presentation of a series of faces for characterisation of the Fusiform Gyrus), what might allow us to assess their metabolic demand during activity better.

It might be argued that the prospect of such studies might be limited, as brain regions do not merely show a straightforward type of homogeneous functional specialisation, but are rather able to perform heterogenous functions that depend on the task-specific network(s) they are integrated in at a point of time. Nevertheless it should be possible to capture the range of metabolic demand spanned by the conditions of activity and rest for each region of the brain, as any computational process is likely to influence metabolic demand in a specific way.

Studies on the relation of functional and anatomical connectivity networks in general might be influenced by a similar aspect. The definition of functional connectivity is always limited to the state of the brain the connectivity is observed in, therefore the definition of network nodes is not state-independent (the stable association of the nodes with a network is one but not the only defining trait of the nodes) and thus probably not one-by-one mappable onto other data, e.g. to adequately assess the underlying anatomical connectivity network.

It stands to reason that both the range of metabolic demand states, local connectivity and GMV, and the probability ranking of affiliations to functional connectivity networks of a brain region might be related in some manner to the shape of the Hemodynamic Response Function in that region.

Alternatively to a direct causal interpretation, the co-variation of perfusion and connectivity could as well be caused by a confounding third, presently unregarded variable other than GMV. Our initial hypothesis on the link between local connectivity and local neural computations, neural computations and neural activity,

and neural activity and metabolic demand involves a series of dependencies, making the influence of intermediary variables highly likely.

A more comprehensive model, including more potentially intermediate variables beyond merely GMV, could be used in future studies to investigate the relations of local computational processes (e.g. using electroencephalographic methods), neural circuitry (e.g. by utilising information on local cell body types), neurotransmitter concentrations (e.g. by using Magnetic Resonance Spectroscopy), metabolism and connectivity at once. With such a larger and more comprehensive dataset it is likely that the particular perfusion/connectivity balance profile of each region could be resolved further.

3.9. Methodological issues

Several methodological issues need to be addressed. Although we employed a probabilistic tracking approach with a high number of random walks and conservative thresholding, presently it is not possible to ensure the validity of one singular estimated connectome with complete certainty due to the methodological difficulty of proper edge falsification and the strong dependency of the results upon the chosen brain parcellation scheme (the AAL atlas in this case). For a more precise estimation, the methodology has to be refined by extending it to more sophisticated graph estimation methods e.g. based on Q-ball imaging data [41] or diffusion tensor studies utilising multi b-value imaging - and by combining these advanced measurements with advanced brain function atlases, derived from large databases of functional connectivity data, since the optimal anatomical connectivity network nodes stem from the parcellation of the brain into those regions, which eventually form a multitude of functional cooperations with others but always do this as a whole [4].

The combination of multiple methods (DTI based connectivity estimation, VBM, ASL) allows for quantifying and describing brain regions with a high number of measures, both on a global as well as on a regional scale. The proper interpretation of this multifaceted data, with respect to the multiple comparisons problem and open questions on the combination of non-gaussian measures with classical statistical approaches, needs to be advanced in an integrative manner.

Further as the present findings are based on cross-sectional data from small samples, the results could be influenced by potential cohort or small sample size effects. A longitudinal study design with a higher number of subjects is necessary to broaden our understanding of the link of these structural and functional brain properties.

It is to note that many different methods with their individual assumptions and errors are combined in an integrative study, and that any of the modules (probabilistic tractography, graph theoretical analysis, anatomical image segmentation, perfusion measurement, artefact control, normalisation etc.) could clearly be improved on their own. Our approach is merely intended as a starting point for the combination of the provided measures.

Therefore the present findings are of a preliminary nature, as for the integration of information about local perfusion, connectivity and gray matter properties, the issues of natural variability versus the distribution of measurement error have to be further resolved. Other quantification approaches for measuring integrity or impairment of gray matter such as spectroscopy of synaptic density or recently introduced Positron Emission Tomography methods [42] focussing on the quantification of plaques and tangles in AD might complement the present approach in the future [4].

Methods

4.1. Subjects and data acquisition

Eleven participants (5 females) were recruited for Group 1 from a student sample (average age=25.4 years, SD=3.4 years, Range: 21-32). After an update of scanner software twelve further participants (7 females) were recruited, referred to as Group 2 (average age=36.7 years, SD=10.7 years, Range: 23-57). Participants of both groups gave written informed consent. All participants were right handed (as confirmed by the Edinburgh Handedness Questionnaire) and both physically (confirmed by extensive health questionnaire) and mentally healthy (confirmed by the german ICD-10-Symptomrating questionnaire). The experiments were approved by the local ethics committee. All MR data were acquired on a 3T Siemens MAGNETOM Trio TIM (Erlangen, Germany) scanner using a 12-channel head coil. The head of each subject was bedded in a deflatable pillow so as to minimise head motion artefacts.

4.2. Anatomical data acquisition and processing

Anatomical images were acquired using a T1 weighted sequence using a 3D MP-RAGE (magnetisation prepared - rapid acquisition gradient echo) sequence (1x1x1 mm voxels, TR=7.92, TE=2.48, Flip Angle=16°, FoV=256*256, 192 transversal slices, Group 1 - 1x1x1.1 mm voxels, TR=2.3, TE=2.98, Flip Angle=9°, FoV=230*256, 160 sagittal slices, Group 2). The brain was extracted from the raw image using the robust iterative estimation function (Fractional intensity threshold=0.5) of the Brain Extraction Tool and subsequently segmented into gray and white matter ([43], distributed within the FMRIB's Software Toolbox - FSL 4.0; http://www.fmrib.ox.ac.uk/fsl).

4.3. DTI data acquisition

Each subject in Group 1 participated in a DTI measurement (1.3x2.4x2.4 mm voxels, no gap, TR=8.83 sec, TE=98 ms, FoV=1360*1360, Flip Angle=90°, 50 transversal slices, 12 diffusion directions, two averages, b-value=1000 s/mm^2) with the field of view (FoV) comprising the full cerebrum and parts of the rostral cerebellum like the Uvula and Tuber of Vermis, Flocculus and Crus Cerebelli (dependent on individual overall brain size).

Each subject in Group 2 participated in a DTI measurement (1.8x1.8x2.2 mm voxels, no gap, TR=6.8 sec, TE=93 ms, FoV=1782*1840, Flip Angle=90°, 50 transversal slices, 64 diffusion directions, two averages, b-

value=1000 s/mm^2) with the FoV comprising the full cerebrum and parts of the rostral cerebellum. The DTI data were processed using the DTI and Fibertools Software Package [44] as described in the section Network Edge Definition.

4.4. Connectome construction and edge calculation

For an overview on data flow for each participant and employed analysis schemes please see Figure S1 and Figure S2.

4.4.1. Network node definition

In order to define the network nodes, gray matter areas were labelled for each subject individually based on the AAL atlas [45], resulting in 116 nodes (80 cortical, 10 subcortical, 26 cerebellar) by using the procedure of normalisation and parameter inversion analogous to the method described in [20].

In order to transfer the images into DTI native space, T1 weighted structural images were coregistered with the B0 (non-diffusion) image and then normalised to the Montreal Neurological Institute (MNI) space. The resulting transformation was inverted to warp the AAL template from MNI space to the DTI space. The discrete labeling values were preserved by using a nearest neighbour interpolation method. Normalisation and inverse transformation were implemented using the SPM8 package.

All available subcortical (Caudate, Putamen, Pallidum, Hippocampus and Thalamus) and cerebellar areas, which were within the individual DTI FoV were included as nodes in order to round out the validity of the individual connectivity graph estimation.

4.4.2 Network edge tracking

Using in-house code, the white matter voxels, which were neighbouring the gray matter of each network node, were defined as seed voxels of that area.

Only voxels with a Fractional Anisotropy (FA) value above 0.3 (gray matter FA can reach values up to ~0.2, [46]) were admitted to this procedure. In addition, these voxels also had to be labelled as white matter by the segmentation step and reside within the brain outline mask resulting from the iterative Brain Extraction Step.

Probabilistic tracking from the seed points was realised by using the PiCo [47] approach. The number of random walks was adjusted to the number of voxels within the white matter tracking area for each single seed point.

The algorithms implemented in the DTI and Fibertools Software Package [44] allow for creating extended visitation maps for the tracking from each seed set (all seed voxels of an AAL area) separately, based on the curves originating from the seed points and being propagated through the tensor field (number of curves equalling the number of random walks) and combine this information with statistical estimates on the plausibility of confluence of two white matter tracts anywhere in the brain. Please see [44] for more precise

information, as our definition of edge probability is based on the Probability Index of forming a part of the Bundle of Interest (PIBI) value concept developed by [44].

Although theoretically one single edge probability value can be chosen for edge-thresholding based on estimates of the cortico-cortical white matter network sparsity (the percentage of accepted edges, relative to the amount of possible edges) derived from the literature, we provide our results in the form of a sweep over a range of plausible thresholds - in order to avoid false conclusions originating in the limitations of only one threshold-specific white matter network (see [48]).

In order to substantiate this sweep, to ensure the validity of the present findings and to avoid false conclusions due to erroneous selection of the edge probability threshold, we performed a number of connectome estimations based on a large range of thresholds (step width $2.5*10^{-9}$). The applied thresholds ranged from implausibly low thresholds (average edge probability in non-zero voxels min. 10^{-10}) allowing for a very high number of accepted edges to overly conservative high thresholds (average non-zero edge probability min. $8*10^{-7}$) making the adjacency matrix very sparse respectively. The selection of the threshold for calculation of the graph metrics employed in the present work was based on both empirical and theoretical considerations and reproduces values for cortico-cortical sparsity, clustering, average path length and resulting small-world coefficients, which are comparable with the results described by [20]. For better comparison the figures are provided with our measure of sparsity of cortico-cortical edges only, resulting from the applied thresholds. Changes of overall graph metrics over various thresholds (decreasing small-world coefficient Sigma with decreasing threshold, resulting from higher Gamma values and constant Lambda) are as well in concordance with the literature.

It is to be noted that a less conservative threshold, allowing for a higher number of edges within each individuals' connectome seems to result in increasing PCs of vulnerability (and other metrics) with perfusion for both cortical and subcortical network nodes. This might indicate that the real relation is even stronger than depicted in this context, since there is no other overt reason why the consideration of implausible edges with lower connection probability (which appear only when the threshold is decreased) should systematically increase the PCs. Instead the presented results of our sweep over possible thresholds show that reforming the white matter network topology by adding more edges systematically strengthens statistical relations of perfusion and connectivity.

Further, as for the same threshold more edges are identified for the superior DTI measurement scheme (please see Figure S3), this could mean that equal sparsity for both groups can only be attained by using a more conservative threshold for Group 2. The deviating Sigma for identical cortico-cortical sparsity in Group 2 indicates that either other cortico-cortical or additional non-cortico-cortical edges can be found with higher statistical plausibility, when data from advanced DTI measurements is utilised. The fact that with a higher statistical plausibility higher Sigma can be observed for identical sparsity further validates the small-world property as an inherently stable feature of the white matter connectome.

Particularly interesting is the fact that edge probability shows a power-law style distribution (as well for far lower thresholds, data not shown), indicating that for a low number of edges probability values are very high, while for a very large number of possible edges probability values are very low. How this is related to the observed power-law distribution of hubs for certain edge probability thresholds could be subject of further numerical simulations.

4.4.3. Definition of Graph metrics

For each node, edge and resulting overall graph the available metrics were calculated using the scripts provided within the Brain Connectivity Toolbox [49]. The vulnerability metric was calculated as described by [20]. Please see Figure 12 for illustration of the different graph metrics.

It is to be noted, that graph analysis of white matter connectivity has the advantage that connectivity is not restricted to concepts of direct links only, which is often the case in classical Region-of-Interest to Region-of-Interest deterministic tractography, but incorporates notions of indirect (path length > 1) connectivity in all utilised graph metrics but degree.

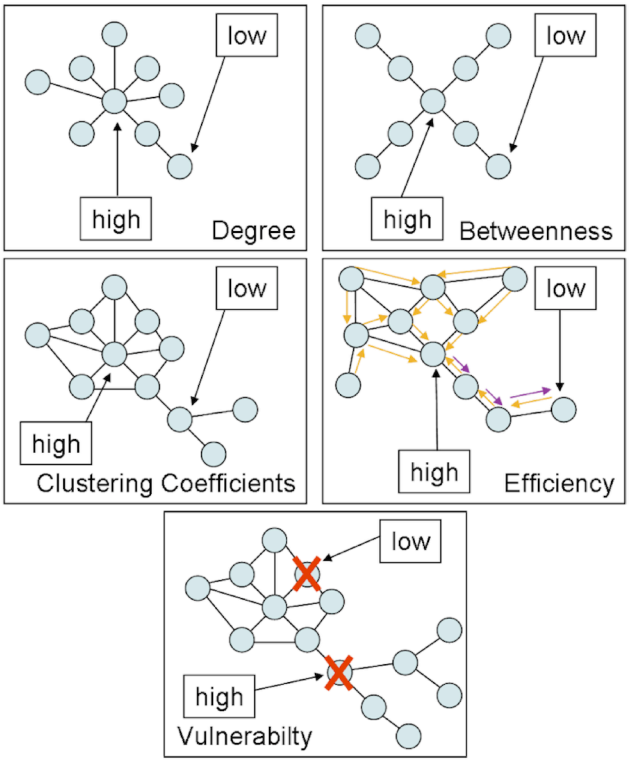

Figure 12, Illustration of utilised node-level graph metrics

4.4.3.1.Degree

The number of edges connecting one node by a path length of one with other nodes (e.g. a hub has a high degree vs. an isolated node with only one connection to the rest of the network has a low degree). In order

to normalise local degree values to make them comparable across graphs, the values are divided by the sum of all node degree values.

4.4.3.2. Betweenness

A node with high betweenness is at a central position of the network, meaning that many of the paths connecting any node A and any node B traverse that node (e.g. while a central hub has high betweenness, a node forming a cul-de-sac has the lowest betweenness). Betweenness is calculated as the fraction of all shortest paths in the network, which traverse a given edge/node. In order to normalise local betweenness values to make them comparable across graphs, the values are divided by the sum of all node betweenness values within the graph.

4.4.3.3. Clustering coefficient

If the nearest neighbours (path length = 1) of a node are also directly connected to each other they form a cluster (e.g. when an individual´s friends are also friends with one another). The clustering coefficient quantifies the number of connections that exist between the nearest neighbours of a node as a proportion of the maximum number of possible connections amongst them. This normalisation allows comparing the clustering coefficient of two nodes directly, irrespective of their individual degree.

4.4.3.4. Efficiency

Efficiency is inversely related to minimum path length (shortest) and quantifies how easily one node can be reached from any other node. Nodes with a high efficiency have many interconnected neighbours and are thus more easily reachable via a number of (parallel) direct paths from any other node. Local efficiency of a node is therefore calculated as the harmonic mean for neighbour-neighbour distances.

4.4.3.5. Vulnerability

This metric describes how strongly the average shortest path lengths (the mean distance to get from any node A to any node B) in a network grow if a node is removed. If a node with high betweenness, high degree, low efficiency and low clustering coefficient is removed, a central hub is eliminated leading to insufficient cost-effective (short) detours for reconnecting severed nodes and high node vulnerability. If a network is fully connected (all nodes are connected to all other nodes) degree, efficiency and clustering coefficient might be high for all nodes, but vulnerability might be low, as the removal of one node would not affect the average distance of any pair of nodes significantly, due to the high number of parallel connecting paths / cost-effective detours.

4.5. ASL data acquisition

ASL data were acquired with a FAIR-QUIPSSII PASL encoding scheme with echo-planar imaging (EPI) readout. A total of 201 alternating tag and control images were obtained in each run (total scan time 10 min, TI1=700 ms, TI2=1100 ms, TE=20ms, TR=3000 ms, voxel size=3.5x3.5x10mm). For ASL measurements of Group 2 the number of slices was increased from ten to eleven (TI2 was changed to 1400 respectively). In order to determine the equilibrium magnetisation for absolute CBF quantification, the same parameters as above were used except that the TR and TI2 were 10000ms and 4000ms, respectively [50]. For analysing the ASL data, FSL software (http://www.fmrib.ox.ac.uk/fsl), self-written MATLAB (The Mathworks, Natick, MA, USA) and Linux shell script routines were used. Time courses of all voxels were motion-corrected utilising the MCFLIRT module of FSL using the mean volume of the corresponding run as reference. CBF time series were created by calculating control-tag difference images using surround subtraction (i.e., computing the difference between each image and the average of its two nearest neighbors), thereby reducing BOLD signal contamination of the CBF time course [50].

For the ASL resting state data acquisition subjects were instructed to relax with closed eyes while staying awake. The ASL values for the nodes were extracted by averaging the absolute CBF (in ml/100g-min) from the voxels within each network node Volume of interest (VOI) for each subject.

Regional absolute and within-subject normalised rCBF values are provided for all non-cerebellar regions of the AAL atlas in the Figure S4.

4.6. Gray matter characterisation through Voxel-Based Morphometry

In order to address the relation between gray matter characteristics, graph theoretical measures and resting state perfusion, we performed a VBM Analysis of the T1 weighted anatomical scans so as to derive descriptives regarding the relative volume of each AAL region. As described in the section Network Node Definition, each anatomical image was skull stripped and the Voxel-based Morphometry Toolbox (VBM5.1, v.1.15, by Christian Gaser) was used subsequently for estimation of the individual modulated and unmodulated segmentation outputs. As the modulated outputs can be corrected for non-linear warping only and therefore make any further correction for different brain size redundant, these images can be used directly for volume estimations.

For the unified segmentation approach (repeated segmentation, bias correction and warping iterations as described in [51]) used in this study the tissue probability maps provided within the SPM5 template set were used since the subjects were drawn from the appropriate population. We applied the thorough clean-up option of the VBM toolbox and made use of a medium Hidden Markov Random Field model for an optimal denoising of the T1 image.

A check of sample homogeneity of the modulated images (using the standard deviation approach within VBM5.1) revealed that the VBM results of the images were all within a tolerable range.

So as to optimise the validity of our GMV estimation, we performed a voxel-wise multiplication of each modulated gray matter image with the coregistered corresponding perfusion image (containing absolute

CBF information). Although perfusion imaging of white matter regions of the brain is possible in principle [52], with many sequences estimation accuracy is limited due to the longer transit delay time (the travelling time of blood from labelling region to reach the tissue) of white matter. As perfusion in gray matter is higher, such a multiplication significantly sharpens the gray matter image histogram, thus facilitating the valid estimation of GMV. In order to smooth the image histogram we applied a three dimensional Gaussian smoothing kernel (FWHM=3 mm, being significantly below the rounded down cubic root of the volume of the smallest AAL-region in equal voxel-space). For each AAL region (network node) the number of gray matter voxels within the atlas derived volumes of interest was counted - equalling the regional volume as relative to the entire individual brain. Naturally these volume values are strongly correlated across our healthy sample as they all measure brain part volumes for identical regions.
Regional GMV values are provided for all non-cerebellar regions of the AAL atlas in Figure S5.

4.7. Employed data level and artefact control

As a univariate factor analysis revealed significant interindividual variability of rCBF values and an effect of gender, the analysis was performed using within-subject z-scored rCBF values. Following this approach, graph metrics and the GMV of nodes were all normalised (z-scored) on a within-subject level. The normalisation was performed separately for cortical and subcortical nodes.
Cortical or subcortical regions for which no connections could be found (due to a tracking failure) or for which no perfusion data could be obtained (due to localisation outside of the ASL imaging FoV) were excluded pairwise from the analysis (in Group 1 seven missing values in different regions, in Group 2 four missing values in two different regions). Cerebellar regions were not considered for correlation analysis, as for 30.94 % of cerebellar regions rCBF could not be measured.
VOI specific artefacts in the estimation of rCBF can not be fully eliminated, due to the generally increased SNR ratio of the ASL signal and the higher chance of intravascular artefacts in larger VOIs, which naturally contain more large arteries and veins that distort rCBF estimations. Also imperfect slice profiles, remaining magnetisation transfer effects and blood tissue water exchange time are factors, which cause artefacts on rCBF estimation. In order to decrease the impact of VOI size on the estimation of relations, we included GMV estimations from VBM as a control variable into our analysis and restricted the presented results to the significant PCs calculated with Spearman's rho.
The data derived from the entirety of these measures constitute for each member of the sample a subjectwise region-by-trait table, with the columns representing local perfusion, local GMV and five graph theoretical metrics of local white matter connectivity, and with 116 rows - one for each region of the AAL atlas.
In order to interpret such multifaceted data one can take various perspectives. The data can be sorted and the trait measurements can be correlated on an individual subjectwise level, to answer the question, whether there is a significant PC - controlling for local GMV - between local perfusion and local connectivity for all

the 116 regions of the AAL atlas in the brain of a given subject. Alternatively the data can be normalised on a within-subject level and integrated with data from all other subjects into a group table, to answer the question whether the previously outlined PC is significant in an analysis of pooled data as well. As a second alternative approach, the data can be sorted by region, so as to answer the question whether in pooled group data local perfusion and local connectivity of some regions shows stronger correlation than others (e.g. the left Precentral Gyrus displays a stronger PC, than the same two traits of the right Precentral Gyrus). Figures of dataflow and analaysis schemes are depicted in Figure S1 and Figure S2.
Results are presented for white matter connectomes that show plausible cortico-cortical sparsity (between 11 and 17 %).

Acknowledgements

The authors would like to thank Dr. Andrea Caria, Dr. Karsten Rauss, Linda van der Heiden and Sarah Wyckoff for their constant help and support. We would also especially like to thank the developers of the DTI and Fibertools Software Package from the Department of Radiology, Medical Physics, University Hospital Freiburg Dr. Björn Kreher, Dr. Marco Reisert, Susanne Schnell and Dr. Kamil Il'yasov for allowing us to use their software package.

References:

1. Bassett DS, Bullmore E (2006) Small-world brain networks. The neuroscientist 12: 512.

2. Greicius MD, Supekar K, Menon V, Dougherty RF (2008) Resting-state functional connectivity reflects structural connectivity in the default mode network. Cerebral Cortex.

3. van den Heuvel M, Mandl R, Luigjes J, Hulshoff Pol H (2008) Microstructural organization of the cingulum tract and the level of default mode functional connectivity. Journal of Neuroscience 28: 10844.

4. Buckner RL, Sepulcre J, Talukdar T, Krienen FM, Liu H, et al. (2009) Cortical hubs revealed by intrinsic functional connectivity: mapping, assessment of stability, and relation to Alzheimer's disease. Journal of Neuroscience 29: 1860.

5. Honey CJ, Sporns O, Cammoun L, Gigandet X, Thiran JP, et al. (2009) Predicting human resting-state functional connectivity from structural connectivity. Proceedings of the National Academy of Sciences 106: 2035.

6. He Y, Chen ZJ, Evans AC (2007) Small-world anatomical networks in the human brain revealed by cortical thickness from MRI. Cerebral Cortex 17: 2407.

7. Chen ZJ, He Y, Rosa-Neto P, Germann J, Evans AC (2008) Revealing modular architecture of human brain structural networks by using cortical thickness from MRI. Cerebral cortex 18: 2374.

8. Stam C, Jones B, Nolte G, Breakspear M, Scheltens P (2007) Small-World Networks and Functional Connectivity in Alzheimer's Disease. Cerebral Cortex, 17(1), 92 -99.

9. Sporns O (2006) Small-world connectivity, motif composition, and complexity of fractal neuronal connections. Biosystems 85: 55–64.

10. Sporns O, Zwi JD (2004) The small world of the cerebral cortex. Neuroinformatics 2: 145–162.

11. Achard S, Salvador R, Whitcher B, Suckling J, Bullmore E (2006) A resilient, low-frequency, small-world human brain functional network with highly connected association cortical hubs. Journal of Neuroscience 26: 63.

12. Kuschinsky W (1991) Coupling of function, metabolism, and blood flow in the brain. Neurosurgical review 14: 163–168.

13. Farkas E, Luiten PG (2001) Cerebral microvascular pathology in aging and Alzheimer's disease. Progress in Neurobiology 64: 575–611.

14. Arthurs OJ, Boniface S (2002) How well do we understand the neural origins of the fMRI BOLD signal? TRENDS in Neurosciences 25: 27–31.

15. Magistretti PJ (2006) Neuron-glia metabolic coupling and plasticity. Journal of Experimental Biology 209: 2304.

16. Gjedde A, Diemer NH (1985) Double-tracer study of the fine regional blood-brain glucose transfer in the rat by computer-assisted autoradiography. Journal of cerebral blood flow and metabolism: official journal of the International Society of Cerebral Blood Flow and Metabolism 5: 282.

17. Klein B, Kuschinsky W, Schrock H, Vetterlein F (1986) Interdependency of local capillary density, blood flow, and metabolism in rat brains. American Journal of Physiology- Heart and Circulatory Physiology 251: H1333.

18. Detre JA, Wang J, Wang Z, Rao H (2009) Arterial spin-labeled perfusion MRI in basic and clinical neuroscience. Current opinion in neurology 22: 348.

19. Jellison BJ, Field AS, Medow J, Lazar M, Salamat MS, et al. (2004) Diffusion tensor imaging of cerebral white matter: a pictorial review of physics, fiber tract anatomy, and tumor imaging patterns. American Journal of Neuroradiology 25: 356.

20. Gong G, He Y, Concha L, Lebel C, Gross DW, et al. (2009) Mapping anatomical connectivity patterns of human cerebral cortex using in vivo diffusion tensor imaging tractography. Cerebral Cortex 19: 524.

21. Bullmore E, Sporns O (2009) Complex brain networks: graph theoretical analysis of structural and functional systems. Nature Reviews Neuroscience 10: 186–198.

22. Li Y, Liu Y, Li J, Qin W, Li K, et al. (2009) Brain anatomical network and intelligence. PLoS Comput Biol 5: e1000395.

23. Cammoun L, Gigandet X, Sporns O, Thiran JP, Maeder P, et al. (2009) Connectome alterations in schizophrenia. NeuroImage 47: S157.

24. Barabási AL, Crandall RE (2003) Linked: The new science of networks. American journal of Physics 71: 409.

25. Williams DS, Detre JA, Leigh JS, Koretsky AP (1992) Magnetic resonance imaging of perfusion using spin inversion of arterial water. Proceedings of the National Academy of Sciences of the United States

of America 89: 212.

26. Wong EC, Buxton RB, Frank LR (1997) Implementation of quantitative perfusion imaging techniques for functional brain mapping using pulsed arterial spin labeling. NMR in Biomedicine 10: 237–249.

27. Parkes LM, Rashid W, Chard DT, Tofts PS (2004) Normal cerebral perfusion measurements using arterial spin labeling: reproducibility, stability, and age and gender effects. Magnetic Resonance in Medicine 51: 736–743.

28. Biagi L, Abbruzzese A, Bianchi MC, Alsop DC, Del Guerra A, et al. (2007) Age dependence of cerebral perfusion assessed by magnetic resonance continuous arterial spin labeling. Journal of Magnetic Resonance Imaging 25: 696–702.

29. Schuff N, Zhu XP (2007) Imaging of mild cognitive impairment and early dementia. British Journal of Radiology 80: S109.

30. Kawamura J, Meyer JS, Ichijo M, Kobari M, Terayama Y, et al. (1993) Correlations of leuko-araiosis with cerebral atrophy and perfusion in elderly normal subjects and demented patients. British Medical Journal 56: 182.

31. Jahng G, Schuff N, Du A, Zhang Y, Mueller S, et al. (2007) Age-related Reductions of Cerebral Blood Flow and White Matter Integrity by High-Field Perfusion and Diffusion MRI. World Congress on Medical Physics and Biomedical Engineering 2006. S. 1380–1383.

32. Ashburner J, Friston KJ (2001) Why voxel-based morphometry should be used. Neuroimage 14: 1238–1243.

33. Mechelli A, Price CJ, Friston KJ, Ashburner J (2005) Voxel-based morphometry of the human brain: methods and applications. Current Medical Imaging Reviews 1: 105–113.

34. Raichle ME, MacLeod AM, Snyder AZ, Powers WJ, Gusnard DA, et al. (2001) A default mode of brain function. Proceedings of the National Academy of Sciences of the United States of America 98: 676.

35. Gusnard DA, Raichle ME (2001) Searching for a baseline: functional imaging and the resting human brain. Nature Reviews Neuroscience 2: 685–694.

36. Calhoun VD, Adali T, Hansen LK, Larsen J, Pekar JJ (2003) ICA of functional MRI data: an overview. in Proceedings of the International Workshop on Independent Component Analysis and Blind Signal Separation.

37. Jafri MJ, Pearlson GD, Stevens M, Calhoun VD (2008) A method for functional network connectivity among spatially independent resting-state components in schizophrenia. Neuroimage 39: 1666–1681.

38. Fair DA, Cohen AL, Dosenbach NU, Church JA, Miezin FM, et al. (2008) The maturing architecture of the brain's default network. Proceedings of the National Academy of Sciences 105: 4028.

39. Buckner RL, Vincent JL (2007) Unrest at rest: default activity and spontaneous network correlations. Neuroimage 37: 1091–1096.

40. van den Heuvel MP, Mandl RC, Kahn RS, Hulshoff Pol HE (2009) Functionally linked resting-state networks reflect the underlying structural connectivity architecture of the human brain. Human brain mapping 30: 3127–3141.

41. Sotiropoulos SN, Bai L, Morgan PS, Constantinescu CS, Tench CR (2010) Brain tractography using Q-

ball imaging and graph theory: Improved connectivities through fibre crossings via a model-based approach. NeuroImage 49: 2444–2456.

42. Nordberg A (2010) Amyloid Imaging in Early Detection of Alzheimer's Disease. Neurodegenerative Diseases 7: 136–138.

43. Smith SM (2002) Fast robust automated brain extraction. Human Brain Mapping 17: 143–155.

44. Kreher BW, Schnell S, Mader I, Il'yasov KA, Hennig J, et al. (2008) Connecting and merging fibres: Pathway extraction by combining probability maps. NeuroImage 43: 81–89.

45. Tzourio-Mazoyer N, Landeau B, Papathanassiou D, Crivello F, Etard O, et al. (2002) Automated anatomical labeling of activations in SPM using a macroscopic anatomical parcellation of the MNI MRI single-subject brain. Neuroimage 15: 273–289.

46. Le Bihan D, Mangin JF, Poupon C, Clark CA, Pappata S, et al. (2001) Diffusion tensor imaging: concepts and applications. Journal of magnetic resonance imaging 13: 534–546.

47. Parker GJ, Haroon HA, Wheeler-Kingshott CA (2003) A framework for a streamline-based probabilistic index of connectivity (PICo) using a structural interpretation of MRI diffusion measurements. Journal of Magnetic Resonance Imaging 18: 242–254.

48. Sporns O, Tononi G, Kotter R (2005) The human connectome: a structural description of the human brain. PLoS Comput Biol 1: e42.

49. Rubinov M, Sporns O (2009) Complex network measures of brain connectivity: uses and interpretations. Neuroimage.

50. Cavusoglu M, Pfeuffer J, Ugurbil K, Uludag K (2009) Comparison of pulsed arterial spin labeling encoding schemes and absolute perfusion quantification. Magnetic resonance imaging 27: 1039–1045.

51. Ashburner J, Friston KJ (2005) Unified segmentation. Neuroimage 26: 839–851.

52. van Osch MJ, Teeuwisse WM, van Walderveen MA, Hendrikse J, Kies DA, et al. (2009) Can arterial spin labeling detect white matter perfusion signal? Magnetic Resonance in Medicine 62: 165–173.

Tables:

Correlation of graph theoretical metrics and perfusion	Group		Clustering Coefficient	Efficiency	Vulnerability	Degree	Betweenness
Subcortical Regions	**1**	**min Value**	n.s.	-0,42	0,23	n.s.	0,21
Subcortical Regions	**1**	**max Value**	n.s.	-0,20	0,34	n.s.	0,31
Subcortical Regions	**2**	**min Value**	-0,44	-0,53	0,40	n.s.	0,31
Subcortical Regions	**2**	**max Value**	-0,36	-0,46	0,49	n.s.	0,39
Cortical Regions	**1**	**min Value**	-0,22	-0,19	0,20	0,12	0,14
Cortical Regions	**1**	**max Value**	-0,16	-0,12	0,28	0,26	0,19
Cortical Regions	**2**	**min Value**	-0,10	-0,11	0,07	n.s.	0,07
Cortical Regions	**2**	**max Value**	-0,07	-0,08	0,10	n.s.	0,09
DMN Regions	**1**	**min Value**	-0,48	-0,48	0,48	0,40	0,48
DMN Regions	**1**	**max Value**	-0,35	-0,35	0,56	0,44	0,53
DMN Regions	**2**	**min Value**	-0,43	-0,44	0,34	0,33	0,35
DMN Regions	**2**	**max Value**	-0,37	-0,33	0,42	0,40	0,40

Table 1, Correlation between graph theoretical metrics and perfusion for Group 1 and Group 2, for the region classes subcortical, cortical and DMN; the minima and maxima of correlation magnitudes are provided for FDR ($p<0.05$) corrected significant correlations (Spearman´s rho), calculated with graph metrics from connectomes resulting from the sweep over plausible cortico-cortical sparsity levels (11-17 % range)

Correlation of graph theoretical metrics and GMV	Group		Clustering Coefficient	Efficiency	Vulnerability	Degree	Betweenness
Subcortical Regions	**1**	**min Value**	-0,64	-0,58	0,50	0,60	0,56
Subcortical Regions	**1**	**max Value**	-0,57	-0,45	0,59	0,64	0,64
Subcortical Regions	**2**	**min Value**	-0,70	-0,62	0,61	0,72	0,68
Subcortical Regions	**2**	**max Value**	-0,52	-0,44	0,67	0,74	0,72
Cortical Regions	**1**	**min Value**	-0,49	-0,45	0,20	0,35	0,29
Cortical Regions	**1**	**max Value**	-0,43	-0,41	0,22	0,44	0,30
Cortical Regions	**2**	**min Value**	-0,46	-0,43	0,12	0,27	0,23
Cortical Regions	**2**	**max Value**	-0,43	-0,40	0,21	0,41	0,30
DMN Regions	**1**	**min Value**	-0,63	-0,61	0,19	0,37	0,26
DMN Regions	**1**	**max Value**	-0,51	-0,50	0,22	0,46	0,30
DMN Regions	**2**	**min Value**	-0,65	-0,59	0,22	0,54	0,35
DMN Regions	**2**	**max Value**	-0,50	-0,48	0,27	0,59	0,40

Table 2, Correlation between graph theoretical metrics and GMV for Group 1 and Group 2, for the region classes subcortical, cortical and DMN; the minima and maxima of correlation magnitudes are provided for FDR ($p<0.05$) corrected significant correlations (Spearman´s rho), calculated with graph metrics from connectomes resulting from the sweep over plausible cortico-cortical sparsity levels (11-17 % range)

Correlations of CBF and Gray Matter Volume (whole sample) for	p-value	r
Subcortical	1E-12	0,45
DBM	0,00042	0,21
non-cerebellar	5E-15	0,17
Cortical	2E-07	0,12

Table 3, Correlation between GMV and perfusion for the whole-sample level are provided for the region classes cortical, subcortical, all non-cerebellar and DMN, all results FDR ($p<0.05$) corrected

Partial Correlation (Spearman´s Rho) with Perfusion in		Clustering Coefficient	Efficiency	Vulnerability	Degree	Betweenness
Group 1	**min Value**	-0,51	-0,52	0,47	0,39	0,47
Group 1	**max Value**	-0,36	-0,35	0,55	0,44	0,53
Group 2	**min Value**	-0,30	-0,31	0,28	0,18	0,25
Group 2	**max Value**	-0,18	-0,17	0,37	0,24	0,30

Table 4, PC of graph theoretical metrics and perfusion for Group 1 and Group 2 for the region class DMN are provided with the minima and maxima of correlation magnitudes for FDR ($p<0.05$) corrected significant correlations (Spearman´s rho), calculated with graph metrics from connectomes resulting from the sweep over plausible cortico-cortical sparsity levels (11-17 % range)

Supplementary Text S1

Small-World characteristics and gray matter

Following earlier findings on the organisation of cortical thickness [6,7] we analysed the small- world properties of binary adjacency graphs defined by the significant correlations (Pearson´s) of the GMVs of cortical AAL regions (n=78) for the entire sample. As recommended by He, Chen and Evans [6] we used a False Discovery Rate (FDR) procedure for the definition of an appropriate threshold ($p<0.01$). Our results for the small-world properties (Gamma=1.1423, Lambda=1.0219, Sigma=1.3925) of regional GMVs show weaker small-world properties for regional GMV correlations than published literature findings on the correlations of regional cortical thickness.

Small-World characteristics and perfusion

By applying the same method, previously used for the gray matter analysis, but now for cortical rCBF values the binary adjacency graphs obtained by the significant interregional correlations ($p<0.01$, FDR) do show the small-world properties Gamma=1.3582, Lambda=1.0624, Sigma=1.2784 for non-normalised rCBF values and Gamma=1.0161, Lambda=1.0743, Sigma=0.9458 for within subject normalised perfusion values (relative perfusion). The fact that interregional correlations of perfusion did not show strong small-world properties in our study, indicates that whereas small-world properties are a rather robust feature of related networks the small-world principle might not necessarily be omnipresent in every feature of the brain.

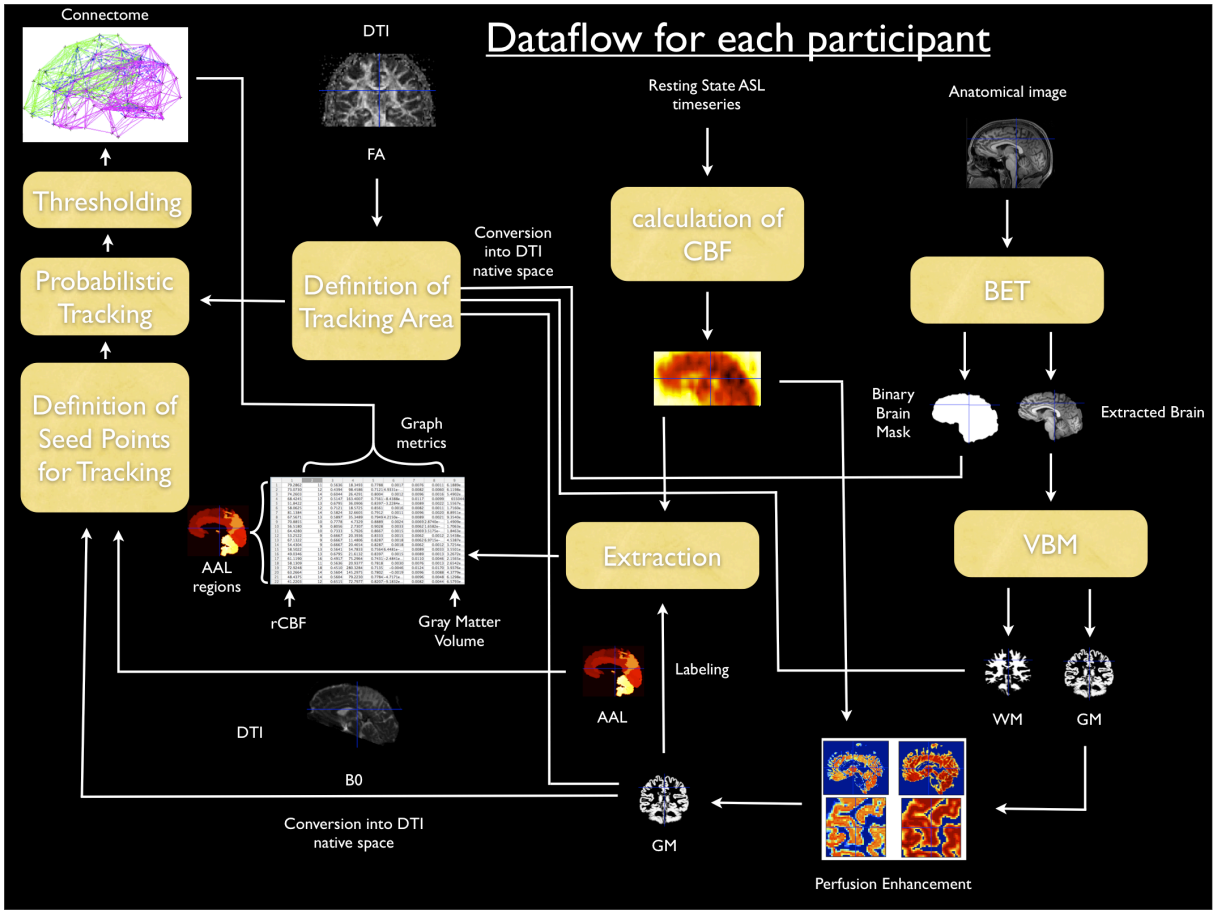

Figure S1.

Dataflow of each participant is illustrated; please see Methods section for details. For each participant one table like in the lower left corner of the image results from the combination of all the measures, the node-specific graph metrics part of that table changes for each edge probability thresholding step while the rCBF and GMV parts stay constant.

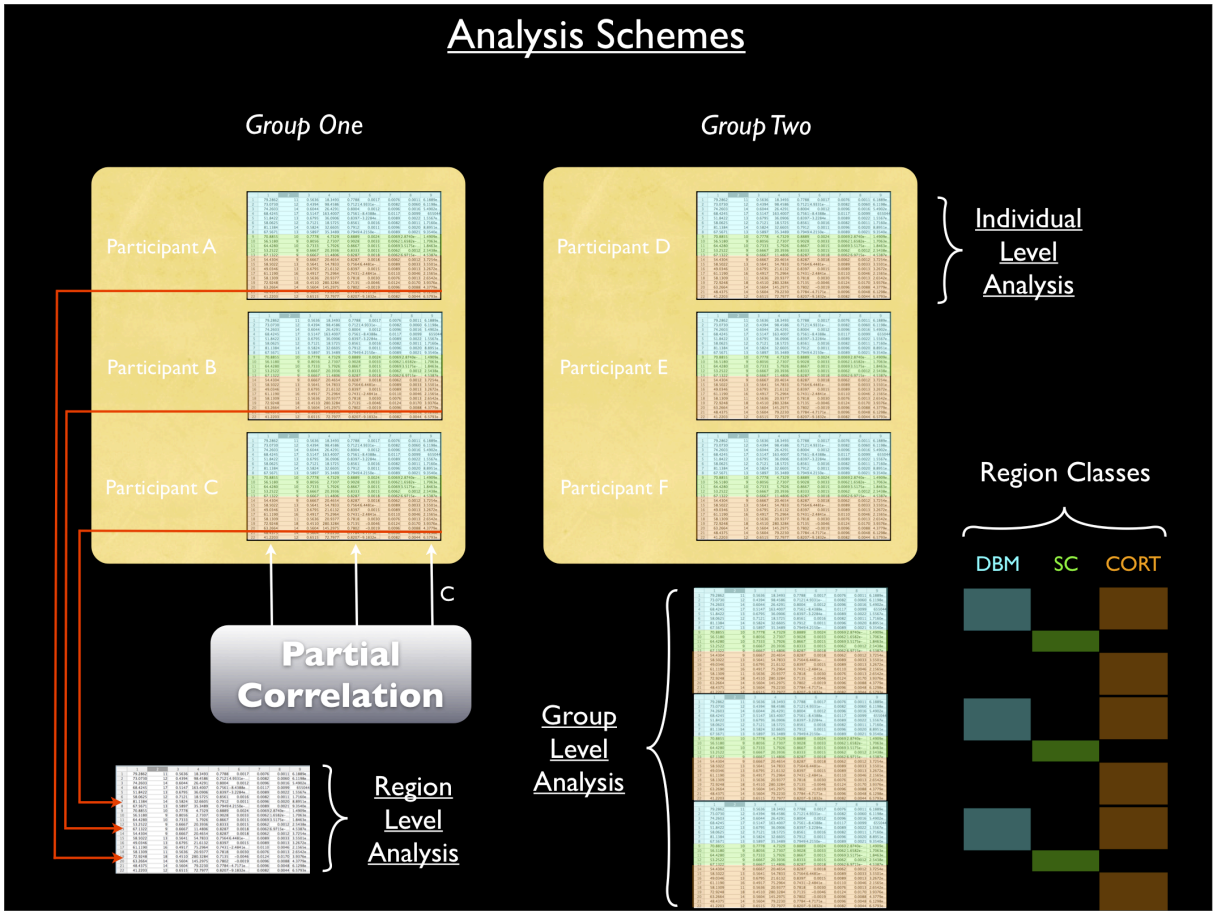

Figure S2.

Illustration for the group, individual and regionwise analysis schemes. C indicates the control variable GMV in the PC approach.

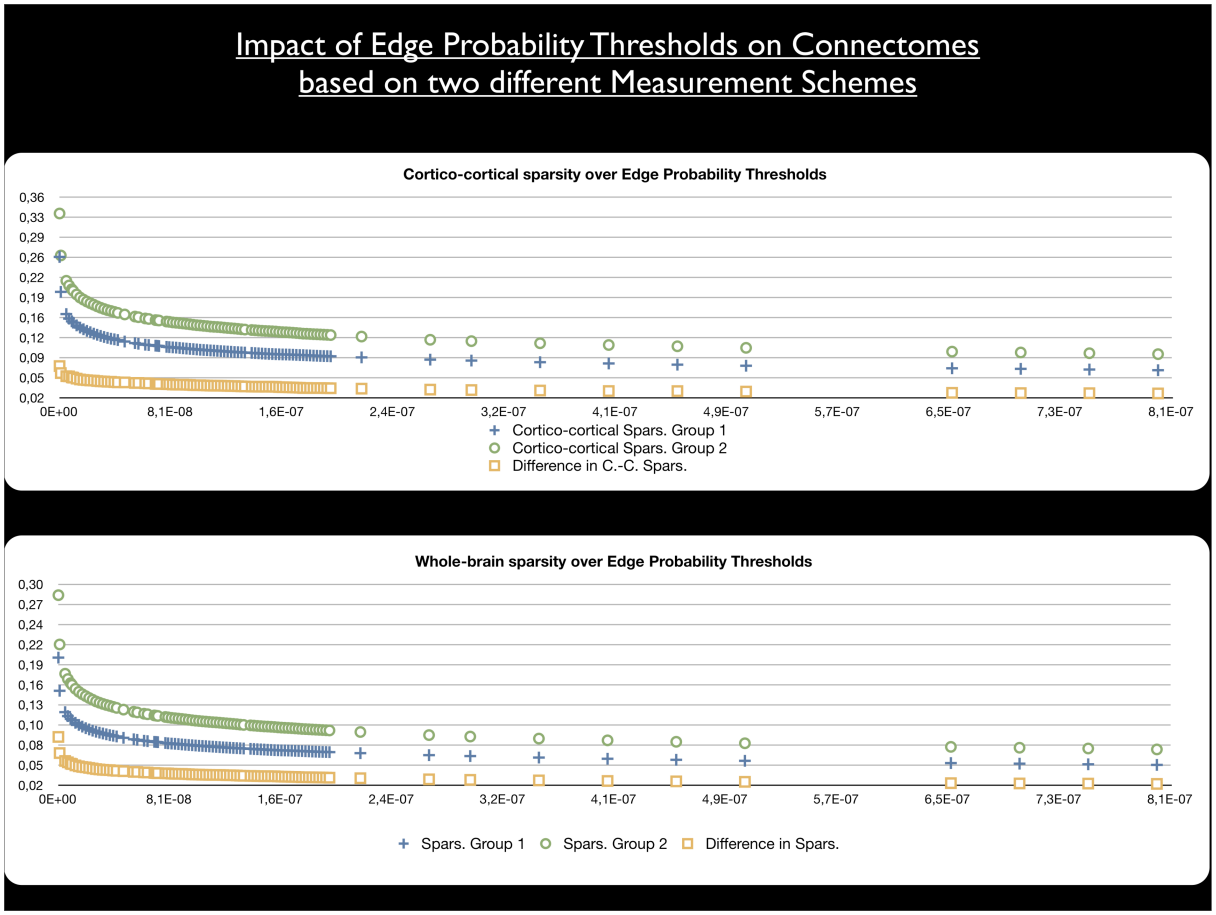

Figure S3.

Upper: Distribution of cortico-cortical sparsity over identical edge probability thresholds for both groups. Lower: Distribution of whole-brain sparsity over identical edge probability thresholds for both groups; edge probability thresholds (x-axis) become more conservative towards the right end of the x-axis (higher threshold) leading to lower resulting sparsity due to less accepted edges.

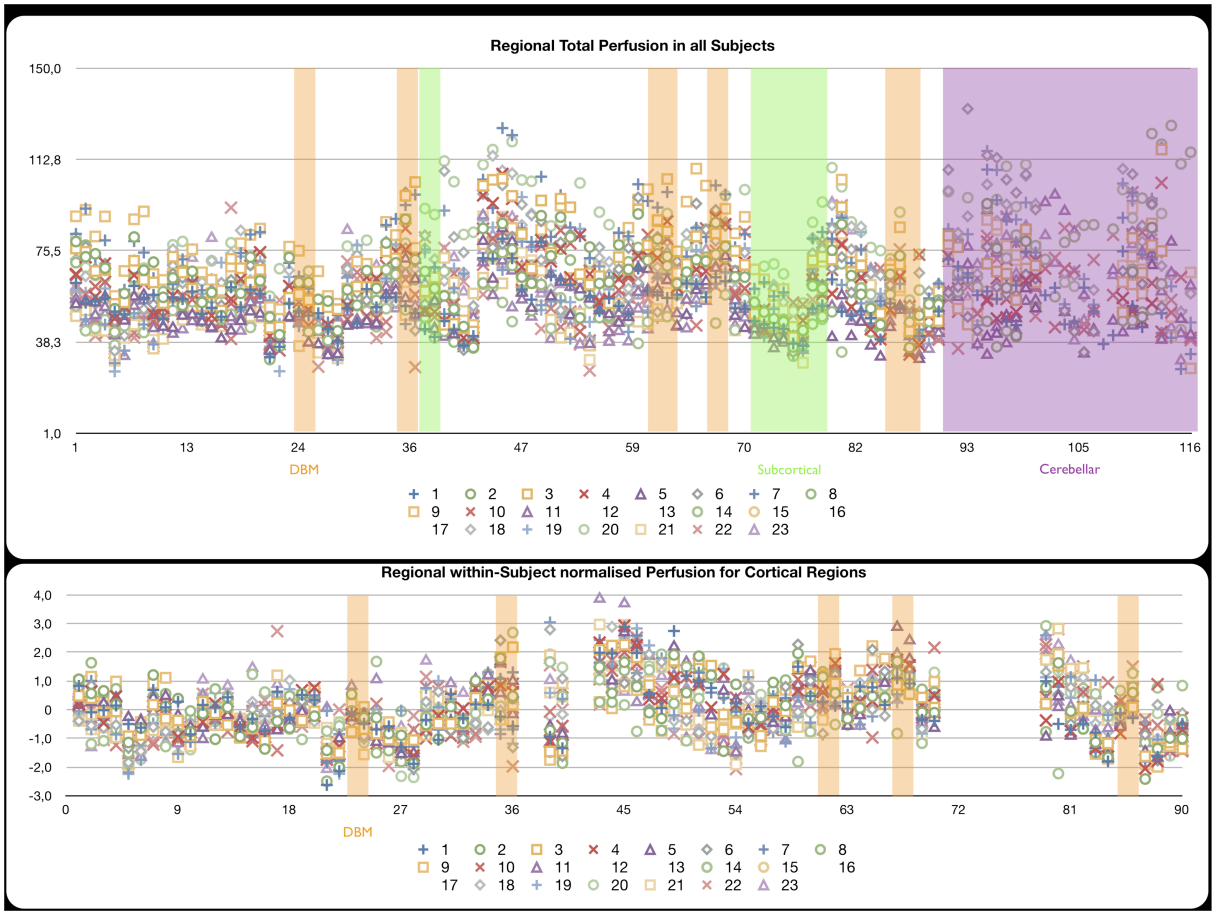

Figure S4.

Upper: Regional total perfusion in all 23 subjects (y-axis in ml/100g-min, x-axis AAL region code). Lower: Regional within-subject normalised perfusion in all 23 subjects for cortical regions (y-axis z-score, x-axis AAL region code).

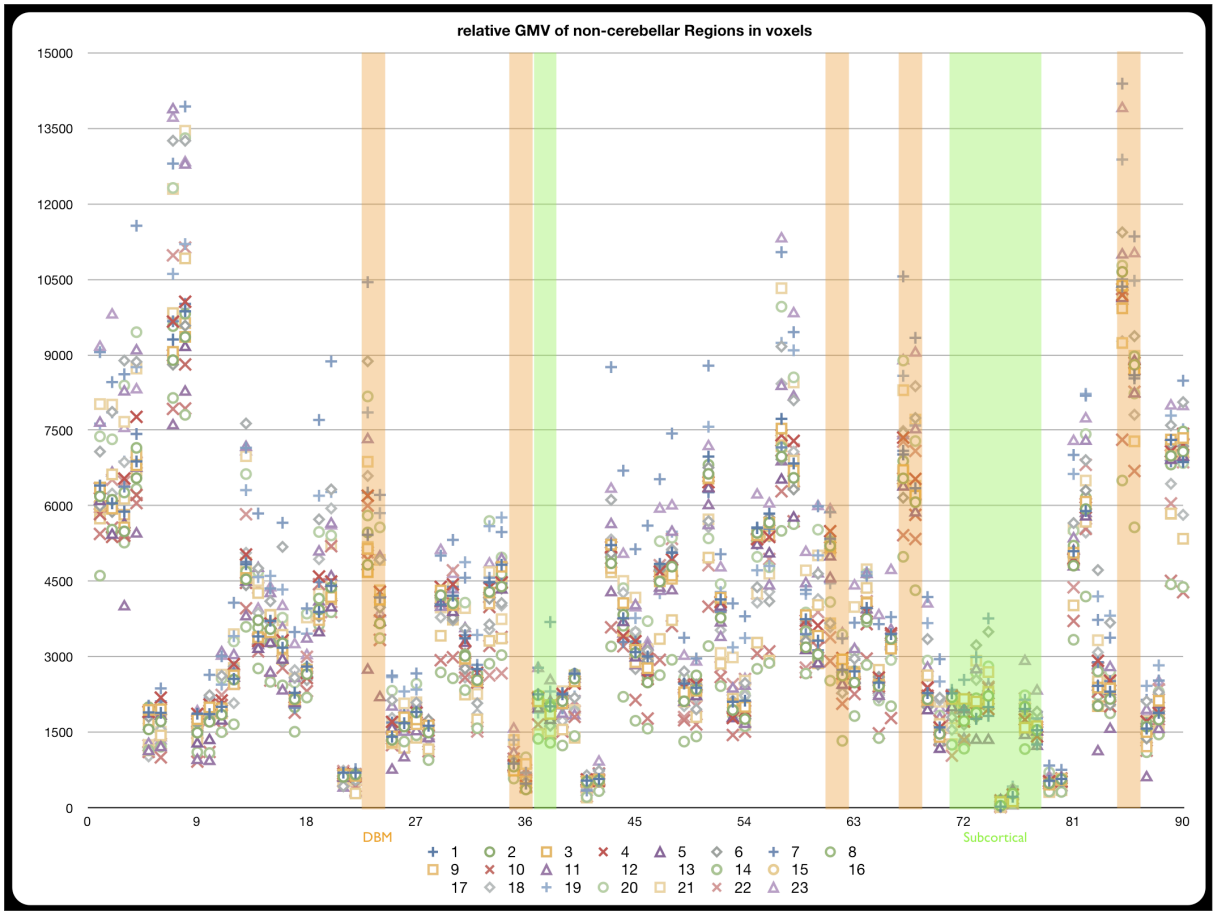

Figure S5.

Relative GMV of non-cerebellar Regions for all 23 subjects (y-axis number of voxels from non-linear warping only corrected modulated output image-space, x-axis AAL region code).

Partial Correlation (Spearman´s Rho) with perfusion in		**Clustering Coefficient**	**Efficiency**	**Vulnerability**	**Degree**	**Betweenness**
Frontal_Mid_L						
	Min. Group 1		-0,52			
	Max. Group 1		-0,38			
	Min. Group 2		-0,31			
	Max. Group 2		-0,22			
Frontal_Mid_R						
	Min. Group 1	-0,51	-0,47			
	Max. Group 1	-0,36	-0,32			
	Min. Group 2	-0,30	-0,30			
	Max. Group	-0,22	-0,22			

	2					
Frontal_Inf_Tri_L						
	Min. Group 1	-0,24				
	Max. Group 1	-0,16				
	Min. Group 2	0,14				
	Max. Group 2	0,23				
Frontal_Inf_Tri_R						
	Min. Group 1	-0,26	-0,24			
	Max. Group 1	-0,17	-0,15			
	Min. Group 2	0,15	0,15			
	Max. Group 2	0,25	0,25			
Frontal_Inf_Orb_L						
	Min. Group 1	-0,23				
	Max. Group 1	-0,14				
	Min. Group 2	0,20				
	Max. Group 2	0,29				
Frontal_Inf_Orb_R						
	Min. Group 1	-0,27	-0,21			
	Max. Group 1	-0,18	-0,13			
	Min. Group 2	0,21	0,19			
	Max. Group 2	0,31	0,31			
Rolandic_Oper_L						
	Min. Group 1	-0,27	-0,22			
	Max. Group 1	-0,18	-0,13			
	Min. Group 2	0,16	0,14			
	Max. Group 2	0,27	0,27			
Rolandic_Oper_R						
	Min. Group 1	-0,27	-0,22			
	Max. Group 1	-0,20	-0,16			
	Min. Group 2	0,14	0,13			
	Max. Group 2	0,26	0,24			
Supp_Motor_Area_L						
	Min. Group	-0,29	-0,23			

	1					
	Max. Group 1	-0,22	-0,17			
	Min. Group 2	0,13	0,12			
	Max. Group 2	0,23	0,21			
Supp_Motor_Area_R						
	Min. Group 1	-0,30	-0,25			
	Max. Group 1	-0,23	-0,18			
	Min. Group 2	0,10	0,09			
	Max. Group 2	0,19	0,18			
Olfactory_L						
	Min. Group 1	-0,21				
	Max. Group 1	-0,14				
	Min. Group 2	0,12				
	Max. Group 2	0,21				
Frontal_Sup_Medial_L						
	Min. Group 1	-0,17				
	Max. Group 1	-0,09				
	Min. Group 2	0,10				
	Max. Group 2	0,18				
Frontal_Sup_Medial_R						
	Min. Group 1	-0,17				
	Max. Group 1	-0,08				
	Min. Group 2	0,09				
	Max. Group 2	0,19				
Frontal_Mid_Orb_R						
	Min. Group 1	-0,17				
	Max. Group 1	-0,08				
	Min. Group 2	0,10				
	Max. Group 2	0,19				
Rectus_L						
	Min. Group 1	-0,18				

	Max. Group 1	-0,10				
	Min. Group 2	0,07				
	Max. Group 2	0,16				
Insula_R						
	Min. Group 1			-0,23		
	Max. Group 1			-0,10		
	Min. Group 2			-0,14		
	Max. Group 2			-0,04		
Cingulum_Post_L						
	Min. Group 1	-0,19	-0,15			
	Max. Group 1	-0,13	-0,11			
	Min. Group 2	-0,14	-0,14			
	Max. Group 2	-0,10	-0,10			
Cingulum_Post_R						
	Min. Group 1	-0,20	-0,16			
	Max. Group 1	-0,13	-0,10			
	Min. Group 2	-0,15	-0,14			
	Max. Group 2	-0,09	-0,10			
Hippocampus_L						
	Min. Group 1	-0,18	-0,14			
	Max. Group 1	-0,11	-0,09			
	Min. Group 2	-0,19	-0,18			
	Max. Group 2	-0,12	-0,14			
Hippocampus_R						
	Min. Group 1	-0,17	-0,13			
	Max. Group 1	-0,11	-0,08			
	Min. Group 2	-0,21	-0,20			
	Max. Group 2	-0,14	-0,15			
ParaHippocampal_L						
	Min. Group 1	-0,14				
	Max. Group 1	-0,09				
	Min. Group 2	-0,19				
	Max. Group	-0,10				

	2					
ParaHippocampal_R						
	Min. Group 1	-0,14				
	Max. Group 1	-0,10				
	Min. Group 2	-0,18				
	Max. Group 2	-0,09				
Calcarine_R						
	Min. Group 1			0,07		
	Max. Group 1			0,14		
	Min. Group 2			0,15		
	Max. Group 2			0,20		
Cuneus_L						
	Min. Group 1			0,09		
	Max. Group 1			0,15		
	Min. Group 2			0,17		
	Max. Group 2			0,21		
Cuneus_R						
	Min. Group 1			0,10		
	Max. Group 1			0,16		
	Min. Group 2			0,18		
	Max. Group 2			0,21		
Lingual_L						
	Min. Group 1			0,11		
	Max. Group 1			0,17		
	Min. Group 2			0,20		
	Max. Group 2			0,23		
Lingual_R						
	Min. Group 1			0,11		
	Max. Group 1			0,17		
	Min. Group 2			0,21		
	Max. Group 2			0,25		
Occipital_Sup_L						
	Min. Group 1			0,13		

	Max. Group 1			0,18		
	Min. Group 2			0,22		
	Max. Group 2			0,25		
Occipital_Sup_R						
	Min. Group 1			0,14		
	Max. Group 1			0,20		
	Min. Group 2			0,21		
	Max. Group 2			0,25		
Occipital_Mid_L						
	Min. Group 1			0,16		0,10
	Max. Group 1			0,21		0,18
	Min. Group 2			0,20		0,13
	Max. Group 2			0,23		0,16
Occipital_Mid_R						
	Min. Group 1			0,16		0,09
	Max. Group 1			0,21		0,18
	Min. Group 2			0,18		0,12
	Max. Group 2			0,22		0,16
Occipital_Inf_L						
	Min. Group 1			0,15		
	Max. Group 1			0,20		
	Min. Group 2			0,18		
	Max. Group 2			0,22		
Occipital_Inf_R						
	Min. Group 1			0,15		
	Max. Group 1			0,20		
	Min. Group 2			0,18		
	Max. Group 2			0,22		
Fusiform_L						
	Min. Group 1			0,14		
	Max. Group 1			0,19		
	Min. Group 2			0,18		
	Max. Group			0,22		

	2					
Fusiform_R						
	Min. Group 1			0,13		
	Max. Group 1			0,18		
	Min. Group 2			0,18		
	Max. Group 2			0,21		
Postcentral_L						
	Min. Group 1			0,14		
	Max. Group 1			0,19		
	Min. Group 2			0,18		
	Max. Group 2			0,21		
Postcentral_R						
	Min. Group 1			0,14		
	Max. Group 1			0,19		
	Min. Group 2			0,18		
	Max. Group 2			0,21		
Parietal_Sup_L						
	Min. Group 1			0,14		
	Max. Group 1			0,19		
	Min. Group 2			0,17		
	Max. Group 2			0,20		
Parietal_Sup_R						
	Min. Group 1			0,14		
	Max. Group 1			0,19		
	Min. Group 2			0,17		
	Max. Group 2			0,20		
Parietal_Inf_L						
	Min. Group 1			0,14		
	Max. Group 1			0,19		
	Min. Group 2			0,16		
	Max. Group 2			0,19		
Parietal_Inf_R						
	Min. Group 1			0,11		
	Max. Group			0,16		

	1					
	Min. Group 2			0,14		
	Max. Group 2			0,17		
SupraMarginal_L						
	Min. Group 1			0,10		
	Max. Group 1			0,16		
	Min. Group 2			0,13		
	Max. Group 2			0,15		
SupraMarginal_R						
	Min. Group 1			0,10		
	Max. Group 1			0,15		
	Min. Group 2			0,11		
	Max. Group 2			0,14		
Angular_L						
	Min. Group 1			0,08		
	Max. Group 1			0,13		
	Min. Group 2			0,09		
	Max. Group 2			0,12		
Angular_R						
	Min. Group 1			0,08		
	Max. Group 1			0,13		
	Min. Group 2			0,09		
	Max. Group 2			0,11		
Precuneus_L						
	Min. Group 1			0,09		
	Max. Group 1			0,14		
	Min. Group 2			0,10		
	Max. Group 2			0,13		
Precuneus_R						
	Min. Group 1			0,10		
	Max. Group 1			0,15		
	Min. Group 2			0,11		
	Max. Group 2			0,14		

Paracentral_Lobule_L						
	Min. Group 1			0,10		
	Max. Group 1			0,15		
	Min. Group 2			0,11		
	Max. Group 2			0,14		
Paracentral_Lobule_R						
	Min. Group 1			0,10		
	Max. Group 1			0,15		
	Min. Group 2			0,10		
	Max. Group 2			0,14		
Caudate_L						
	Min. Group 1			0,08		
	Max. Group 1			0,14		
	Min. Group 2			0,09		
	Max. Group 2			0,13		
Caudate_R						
	Min. Group 1			0,07		
	Max. Group 1			0,12		
	Min. Group 2			0,08		
	Max. Group 2			0,13		
Putamen_L						
	Min. Group 1			0,06		
	Max. Group 1			0,11		
	Min. Group 2			0,08		
	Max. Group 2			0,12		
Pallidum_L						
	Min. Group 1			0,05		
	Max. Group 1			0,11		
	Min. Group 2			0,08		
	Max. Group 2			0,12		
Pallidum_R						
	Min. Group 1			0,06		

	Max. Group 1			0,11		
	Min. Group 2			0,08		
	Max. Group 2			0,13		
Thalamus_L						
	Min. Group 1			0,05		
	Max. Group 1			0,11		
	Min. Group 2			0,09		
	Max. Group 2			0,14		
Thalamus_R						
	Min. Group 1			0,06		
	Max. Group 1			0,11		
	Min. Group 2			0,11		
	Max. Group 2			0,15		
Heschl_L						
	Min. Group 1			0,05		
	Max. Group 1			0,10		
	Min. Group 2			0,09		
	Max. Group 2			0,12		
Temporal_Pole_Mid_R						
	Min. Group 1			0,06		
	Max. Group 1			0,11		
	Min. Group 2			0,06		
	Max. Group 2			0,08		
Temporal_Inf_L						
	Min. Group 1			0,06		
	Max. Group 1			0,11		
	Min. Group 2			0,06		
	Max. Group 2			0,08		
Temporal_Inf_R						
	Min. Group 1			0,06		
	Max. Group 1			0,11		
	Min. Group 2			0,06		

	Max. Group 2			0,08		

Table S1.

Results of the regionwise PC analysis (graph theoretical metrics with perfusion, controlling for local GMV), presented for statistically significant (FDR corrected, $p<0.05$) regions only provided with minima and maxima of correlation magnitudes for Group 1 and Group 2.

7.2 Chapter 2 - A taxonomy of Functional Connectivity Networks and the influence of regional brain properties on network formation

Towards a taxonomy of Functional Connectivity Networks

Author list and affiliation:

Bálint Várkuti[1]

Sebastian Halder[1,2]

Colleen A. Dockery[1]

Markus Schneider[1]

Philipp M. Keune[3]

Eric Fimbel[4]

Kamil Uludag[5]

Wolfgang Rosenstiel[2]

Niels Birbaumer[1,6]

Ranganatha Sitaram[1]

1 Institute of Medical Psychology and Behavioral Neurobiology, University of Tübingen, Tübingen, Baden-Württemberg, Germany

2 Wilhelm-Schickard Institute for Computer Science, University of Tübingen, Tübingen, Baden-Württemberg, Germany

3 Institute of Psychology, Department of Clinical and Developmental Psychology, University of Tübingen, Tübingen, Baden-Württemberg, Germany

4 Fatronik Tecnalia, Donostia - San Sebastian, Gipuzkoa, Spain

5 Department of Cognitive Neuroscience, Maastricht University, Maastricht, Limburg, Netherlands

6 Ospedale San Camillo, Istituto di Ricovero e Cura a Carattere Scientifico, Laboratorio di Neuroscience comportamentale, Venezia, Italy

Abstract

Macroscopic Functional Connectivity Networks have received growing attention in recent years, as these manifestations of distributed neural processing are successively associated with tasks - e.g. executive control networks in the Tower-of-London task - and traits like altered Default Brain Network connectivity in Alzheimers disease. Many such networks are identified in fMRI studies employing resting state or single-task designs and are described only in that context. Until now larger pools of data have not yet been processed with one single tool in order to create a comprehensive typology of such networks. In the present work we assessed and sorted a multitude of networks using data from 90 participants performing 8 different experiments to identify the most stereotypical Functional Connectivity Networks. Furthermore we combined this data with data on region specific structure/function relationships in order to understand their influence on the formation of networks in the healthy brain. We demonstrate that brain regions with larger gray matter mass and higher relative perfusion are members of more distinct networks and that all observed Functional Connectivity Networks tend to form along direct anatomical connections. The number of stereotypical networks a region participates in can be predicted from such local properties.

Introduction

A Functional Connectivity Network (FCN) - when measured with functional Magnetic Resonance Imaging (fMRI) - is the temporally coherent hemodynamic echo of a macroscopic communication mode that the brain enters during relatively long (mostly supra-second) durations (Beckmann et al., 2005; Dodel et al., 2005). Brain regions which are members of such networks commonly consume energy by utilizing metabolites in a fashion that allows their detection as one synchronously activating or deactivating entity (Horwitz, 2003).

The appropriate and timely formation of such a communication mode (e.g. the neural communication between the parts of the motor system) is essential for adaptive behavior (Dosenbach et al., 2007; Seeley et al., 2007; Sridharan et al., 2008). The brain combines multiple of these communication modes to form the complex interactivity patterns that we can observe when a person is confronted with complex tasks (e.g. visuo-motor integration, motor execution, conscious thought). fMRI is - due to its dependency on the Blood Oxygen Level-Dependent (BOLD) effect - mainly capable of registering elevated levels of (inter-)activity. Such signals represent activity from which

the information that is exchanged within a network can not be directly extracted (Logothetis, 2008). Therefore using fMRI alone, neural communication can not be comprehensively tapped.

Despite these strong limitations of fMRI, large-scale events like the coherent activation of an entire neural mass or even the synchronous co-activation of two activation centers in a network can be detected (e.g. bilateral activations of V1 and V2 as a reaction to visual stimuli). Although we are presently only able to indirectly infer what information is communicated within such an activation network, such activations and co-activation patterns are of a high diagnostic value, as they may allow the experimenter to investigate the responsiveness and overall integrity of the communication modes the brain is capable of establishing.

Not all of these communication modes are task-dependent (Beckmann et al., 2005) and many can be observed in a task-free resting state. Some of these networks have been noted to undergo change over the course of maturation (Fair et al., 2008), and to vanish or be disrupted in certain disorders. One example for the latter is the association of loss of consciousness with impaired Default Brain Mode (DBM) activity (Raichle et al., 2001; Greicius et al., 2004).

Furthermore, not all detected FCNs necessarily represent patterns of macroscopic neural cooperation and communication, but are in some cases confounds which are observed due to vasomotor oscillations, temporally coherent pollution of the BOLD signal with physiological noise or other reasons (McKeown et al., 1998; McKeown, 2003; Perlbarg et al., 2007). Other FCNs extracted from activation data might be false-positives originating in a similar appearance of local activation patterns over time in parts of the brain (homology), but without any information exchange within these false-positive FCNs.

The creation of an extensive taxonomy of FCNs would serve us with a reference system that allows us to classify newly observed networks into distinct classes, facilitate the interpretation of network phenomena and aid the detection of network abnormalities in patient data. This approach is already beginning to spread into clinical practice (Dosenbach et al., 2010).

Furthermore, such data could be mined with a multitude of methods to answer presently unresolved questions on network formation and network properties. Functional hubs which belong to many networks have mostly been characterized using data from single sites and single experiments (Achard et al., 2006; Bassett et al., 2006; Cohen et al., 2008; Bullmore and Sporns, 2009a; Demirci et al., 2009; van den Heuvel et al., 2009; Van Dijk et al., 2010) but only seldom by unifying larger amounts of data to identify global relationships between regional properties and local functional network connectivity (Honey et al., 2009). Presently there are no comprehensive lists yet, which

would list all networks observed with fMRI, and allow us to answer the question, of how networks in the human brain are generally constituted. Such a list of observed networks could be used to identify families of spatially and functionally similar networks, and not only answer which are the canonical brain networks that each healthy brain should be capable of establishing, but as well answer how many families of similar networks there are in the healthy human brain.

To assure that only FCNs of neural origin are used for the formation of such a taxonomy, FCNs as observed using fMRI have to be dissociated into networks of interest (networks representing neural communication patterns) and networks not of interest (noise based confounds, phenomena occurring due to homology and so on).

In order to dissociate the observed FCNs into these three basic types, the networks can be extensively fingerprinted (Sporns et al., 2004; Smolders et al., 2007; Sui et al., 2009) by recording their features (spatial extent, fractionality, spectral properties, interactivity patterns and correlations with noise) and by clustering the FCNs based on their individual profile in such a multi-dimensional feature space. We hypothesized that certain types of networks should form interpretable types of clusters and allow us to label these clusters as network classes that contain FCNs of neural-origin or otherwise. For example, physiological noise in the form of ventricular pulsations does occur more in Cerebro-spinal fluid (CSF) than in gray matter (GM) and this ratio can be quantified for each single FCN candidate and used for sorting.

Finally, the remaining networks of presumably neural origin can be clustered again based on their spatial profile (regions of the brain involved) and characterized using their feature fingerprint (e.g. networks containing the left and right temporal lobe always have low correlations of their activity with ventricular pulsations). The technical problem at hand - with such a comprehensive list of component features - is the appropriate clustering of this high-dimensional data into meaningful classes and the proper interpretation of subspace clusters.

We decided to use Independent Component Analysis (ICA) to organize and extract the functional connectivity data of 90 participants performing 8 different experiments over a total of 175 sessions in a data-driven way, and to characterize each Independent Component (IC) with respect to its IC fingerprint features. The data was organized using Self-Organizing Feature Maps (SOFM) (Kohonen, 1990) and this bottom-up organized feature space was further organized with the Clusot (Bogdan and Rosenstiel, 1999; Bogdan et al., 1999) software package by clustering the FCN fingerprint feature maps. This latter cycle of SOFM organization and Clusot sorting is repeated step by step first for spatial and subsequently for noise features in order to dissociate noise compo-

nents (confounds) from components representing networks of neural origin. These latter networks were further organized with respect to their spatial extent in order to derive the most prominent stereotypes of FCNs, equalling the taxonomy class centroids. This set of resulting - presumably canonical - networks and the regions which were members of each respective network were further characterized in terms of their anatomical connectivity, perfusion and regional tissue volume using data from an earlier study (Várkuti et al., 2011). By combining these datasets, we were able to study the most common properties of observed networks and aid our understanding of why the observed networks form in the manner they were observed.

Such a dataset could be organized, clustered and mined with other methods, which is why we supply the entire FCN x feature data in the online Supplementary Material and invite the reader to conduct his own preferred type of analysis.

Materials and Methods

Experiments

All experiments were approved by the Internal Review Board of the Medical Faculty, University of Tübingen. All participants provided written informed consent and all investigation was conducted according to the principles expressed in the Declaration of Helsinki. Participants had no history of neurological diseases, were mostly right handed and German native speakers. All MRI measurements were performed in one Siemens Magneton Trio Tim 3T whole body scanner using a standard 12 channel head coil.

Experiment 1 - Tower of London

Sixteen healthy subjects (7 male, average age 24.9 SD 3.9) participated in a training session prior to the experiment where they were presented with 30 Tower of London (ToL) (Baker et al., 1996) problems with different difficulty levels (number of necessary moves ranging from 1 to 5). For each problem, two possible solutions were presented and subjects had to select the correct solution by button press. Subjects were admitted to the fMRI experiment (EPI TR=1.3 sec, 3x3x3.2 mm voxels, gap=1 mm, 21 transversal slices, TE 30ms, descending acquisition, 90 ° flip angle) as soon as they were able to complete all training problems correctly. Once placed in the scanner, subjects completed a pseudo-randomized sequence of 50 new ToL problems (within the allowed time of 20 seconds), with 10 problems per difficulty level.

Experiment 2 - Tracking task with a joystick

Eight healthy participants (3 male, average age 25 SD 3.1) were trained inside the scanner (EPI TR=1.84 sec, 3x3x4 mm voxels, gap=1 mm, 30 transversal slices, TE 30ms, descending acquisition, 74 ° flip angle) to steer a dot through an animated landscape that consisted of two sine waves, one placed above the other. The participant had to steer the dot through the cave of the sine waves using a MR-safe joystick without touching the boundaries or leaving the cave. If the participant crossed the boundaries, the dot turned red. The dot could only be moved along the vertical axis. In the subsequent actual task, the participant had to master the task with changing precision demands (distance of the boundaries was closer or further apart), disturbances (random wind) and switches of the joystick direction polarity.

Experiment 3 - Tapping task with a button box

Nine healthy participants (6 male, average age 24.1 SD 1.6) were trained inside the scanner (EPI TR=1.84 sec, 3x3x4 mm voxels, gap=1 mm, 30 transversal slices, TE 30ms, descending acquisition, 74 ° flip angle) to respond to an animated task of four circles, falling down and flipping back after one another. The participant had to press the appropriate button for each circle exactly when the circle hit the lowest point. If the participant did not press the right button in time, the circle turned red. In the subsequent actual task, the participant had to master the task with changing precision demands (error tolerance for timing imprecision of button press was varied), disturbances (circles did not fall in a particular order but randomly) and switches of the control device polarity (e.g. outer left circle was not represented anymore by outer left button, but by outer right button).

Experiment 4 - Detection of deception

Fifteen healthy volunteers (6 male, average age 26 SD 4.7) participated in a thief role-play and were subsequently interrogated using a video questioning and visual depiction of objects setup within the scanner (EPI TR=1.5 sec, 3x3x3.5 mm voxels, gap=1 mm, 21 transversal slices, TE 30ms, descending acquisition, 90 ° flip angle). Participants responded to the questions by the video interrogator by pressing a button for yes or no and by doing so, heard their own prerecorded voice over MR safe headphones, giving the answer. Participants tried to conceal their involvement in the deed by giving untruthful answers with respect to recognizing presented objects from the thief-role play room (Concealed Information Test).

Experiment 5-7 - Motor imagination, observation and execution

17 healthy participants (10 male, average age 23.47 SD 2.72) participated in three fMRI experiments (EPI TR=2 sec, 3x3x3.5 mm voxels, gap=1 mm, 32 transversal slices, TE 30ms, descending acquisition, 90 ° flip angle). Each participant performed a motor imagery, observation and execution experiment in the fMRI. Each experiment - as reported earlier in (Halder et al., 2011) - was repeated once, resulting in a total of six measurements (two of each task) per participant. One of the experiments consisted of seven blocks of 30 seconds in which participants were required to perform motor tasks such as execution of left hand, right hand or foot (preferred side) movements according to arrows displayed on the screen pointing to the left, right or down. Since each experiment was repeated there were in total 14 blocks per motor task. Each motor task block was followed by a 30 s resting period. In the observation condition, participants were instructed to attend to videos of ten seconds length. Videos showed either left or right hand squeezing of a ball, or feet moving their toes (recorded from a first person's perspective). The participants were instructed to mentally imitate the observed movement from a first person's perspective as opposed to a distanced, evaluative observation of the displayed movement from a third person perspective (Zentgraf et al., 2005). Finally, in the imagery condition, participants were asked to imagine movement according to certain displayed cues. The participants were specifically instructed to use kinesthetic and not visual movement imagery (Neuper and Scherer, 2005). The feeling one has when moving feet in sand was provided as an example of kinesthetic imagery to all participants. It was emphasized that the focus of the imagery should be kinesthetic sensation. The length of trial and pause were the same as during movement execution.

Experiment 8 - Resting state

Twenty-five subjects participated in a resting state (eyes closed) fMRI measurement (duration 10 min 20 s, 9 male, average age 41.3 SD 11,4, EPI TR=1.53 sec, 3x3x3 mm voxels, gap=1 mm, 25 transversal slices, TE 30ms, descending acquisition, 90 ° flip angle). Twelve of the participants were a subset of participants reported on in an earlier study (Keune et al., 2011) and had been diagnosed with repeated episodes of Major Depressive Disorder in the past but were in remission and symptom free at the time of measurement (as evaluated with ICD 10 Symptom Questionnaire which covers a time of up to two weeks before the time of measurement).

Data flow

fMRI data preprocessing

All fMRI image series were preprocessed session-wise using SPM8 (Wellcome Trust Centre for Neuroimaging, London). Functional images were realigned (4th degree B-Spline interpolation) to the mean image, slice timing corrected to the middle slice, normalized (4th degree B-Spline interpolation) into 3x3x3 mm MNI-space and smoothed using an 8-mm Full Width Half Maximum kernel.

Group ICA details

Each of the 8 experiment datasets (a total of 90 subjects distributed over five single-session and three two-session experiments resulting in a total of 175 sessions) was analyzed with one Group ICA (Correa et al., 2007) separately for each experiment using the 1.3d version of the GIFT-ICA toolbox (Calhoun, 2004). The optimal number of ICs was calculated for each Group ICA using the ICASSO (Himberg and Hyvarinen, 2003) approach (run 20 times, with both 'randinit' and 'bootstrap'). Each ICA was run with the Infomax algorithm (Bell and Sejnowski, 1995), back-reconstruction was performed using the GICA3 implementation (Erhardt et al., 2010), data-preprocessing was done by removing the mean per time point, PCA options were standard (double precision, selective eigen solver, maximum number of reduction steps was two, batch estimation, Minimum Description Length estimation option mean, number of principle components to reduce each subject down to at reduction step one was 20, at two 16) and results were scaled to z-scores. All further analysis such as IC image analysis, feature computations and listing of results were realized on the lowest level of abstraction - namely the subject-session image-level instead of the group-experiment mean images-level. The ICASSO results were further used to select only highly stable components for further processing, so that the component list was filtered and components with an ICASSO component stability value (how stably a component is extracted repeatedly by the partially stochastic ICA process from the data) below 0.9 were removed (from 7705 initial components, 847 equalling 10.9 % of all resulting components were removed due to low stability). A total of 7705 initial components in the list equal an average of 44 detected ICs per session.

Binary-coding of IC images

IC images were binary-coded for the calculation of spatial features by thresholding the z-scored output images at a cutoff value of 1.75. Although IC images contain negative values as well,

indicating parts of the IC whose activity is generally anti-correlated with the ICs positive value marked regions, we only used the IC image voxels above our positive threshold in this approach to characterize the components spatial features. The rationale for this is, that although a component is logically made up of two anti-correlated parts both of which contribute to the raw BOLD signal, a functional network of neural origin is most clearly defined as a region that coherently activates and deactivates together as one network, rather than two regions or networks whose activity patterns are opposing.

Feature Computation

Spatial Features

The T1 images of all participants were processed using the SPM VBM5 software package (Ashburner and Friston, 2001; Mechelli et al., 2005) and the individual GM, white matter (WM) and CSF modulated and unmodulated segmentation outputs were estimated. We used the tissue probability maps provided within the SPM5 template set since the subjects were drawn from the appropriate population. We applied the thorough clean-up option of the VBM toolbox and made use of a medium Hidden Markov Random Field model for an optimal denoising of the T1 image. As the modulated outputs can be corrected for non-linear warping only and therefore make any further correction for different brain size redundant, we created a study specific template by averaging all modulated segmentation outputs into a GM, WM and CSF template, respectively. These templates were resliced into the appropriate voxel space of the IC output images and the portion of each components spatial extent that resided in GM, WM, CSF or outside of all these three (termed Out-of-Brain (OFB)) was calculated as a percentage output (Features 1-4). Furthermore, we calculated the total number of voxels belonging to an IC (Feature 5) as well as the spatial fractionality/smoothness of the component (Feature 6) by calculating the number of neighbouring IC voxels (using a 3D 26-neighbours model) over the amount of total IC voxels (components scattered widely over the brain would get a lower value than e.g. components compromised of a single adjacent voxel mass). Each binary-coded component's percentage overlap with regions of the AAL atlas (Tzourio-Mazoyer et al., 2002) was calculated (with a separate calculation of overlap with a DBM regions mask) and saved for the first 90 cerebral regions of the atlas (see Attachment A).

Noise Features

We extracted and averaged the raw BOLD values from the preprocessed fMRI images of each session from the voxels within the CSF-template mask (see spatial features), an accordingly resliced ventricle mask (all ventricles, template from the WFU PickAtlas (Maldjian and Laurienti, 2003), dilated by 1 voxel) and the total volume (all voxels per image). The component timecourses were then correlated with the respective noise timecourses (p=0.05) and the correlation values were squared (Features 7-9). The six movement regressors (three translational, three rotational) derived for each session from the realignment-preprocessing step in SPM8 were used as predictors in a multiple regression to predict each component's timecourse. For components corresponding to head movements the multiple regression is significant and results in a high R^2 (Feature 10).

Spectral Features

The Power Spectral Density (PSD) plot for each component per session was calculated using a discrete Fast Fourier Transform, with the normalized and detrended component timecourse as input. The resulting PSD plot was characterized with respect to kurtosis, skewness and peak. As the lowest sampling frequency in the dataset was 0.5 Hz (TR=2 seconds) only information for the frequencies up to 0.25 Hz was utilized (Features 11-13). In analogy to the frequency bin power feature calculation function within GIFT (Spectral Group compare), we further calculated the power in the frequency bins 0-0.04, 0.04-0.08, 0.08-0.12, 0.12-0.16, 0.16-0.2, 0.2-0.24 Hz with a dynamic adaptation of bin width depending on session-specific frequency resolution/sampling rate (Features 14-19).

Interactivity features

Brain networks are known to interact with one another and such interactivity patterns can contain significant information on the underlying neural processes (Demirci et al., 2009). We calculated the Granger Causality interactions (time-domain) for all components of a session using their normalized and detrended back-reconstructed component timecourses as input for a multivariate Granger Causality implementation (Seth, 2005, 2010). In order to account for the variable TRs, the optimal model order was calculated using the Aikake Information Criterion (order range: 2-3) and time-delayed component interactivity was assessed using a Bonferroni-corrected p-value threshold of 0.05. The resulting component interactivity graphs were transformed into Granger Causal outflow, inflow, total flow, weighted outflow and weighted inflow metrics for each component per

session (Features 20-24). Furthermore, we calculated the interactions in the frequency-domain, based on Partial Directed Coherence (PDC) (Schelter et al., 2006) - employing the FDMa toolbox by the Freiburg Center for Data Analysis and Modeling, Albert-Ludwigs-Universität Freiburg - using the same component timecourses for all frequencies from 0.1 Hz to 0.24 Hz (in steps of 0.02 Hz) under consideration of the variable sampling frequencies (TR) and with a fixed model order of 4 (due to the relatively short total timecourse length). The resulting frequency resolved component interactivity graphs were transformed into PDC interactions to and from a given component per session (Features 25-39). Please see Table 1 for a list of all features.

Table 1 – Feature list

Feature	Number
Spatial Features	
Percent of IC in Gray Matter Mask	1
Percent of IC in White Matter Mask	2
Percent of IC in CSF Mask	3
Percent of IC out of Brain	4
Total number of IC voxels	5
IC spatial fractionality	6
Noise Features	
Correlation with CSF template voxels raw BOLD	7
Correlation with ventricle template voxels raw BOLD	8
Correlation with all voxels raw BOLD	9
R^2 with movement regressors	10
Spectral Features	
PSD kurtosis	11
PSD skewness	12
PSD peak	13
0-0.04 Hz Frequency Bin	14
0.04-0.08 Hz Frequency Bin	15
0.08-0.12 Hz Frequency Bin	16
0.12-0.16 Hz Frequency Bin	17
0.16-0.2 Hz Frequency Bin	18
0.2-0.24 Hz Frequency Bin	19
Interactivity Features	
Granger Causality outflow	20
Granger Causality inflow	21
Granger Causality total flow	22
Granger Causality weighted outflow	23
Granger Causality weighted inflow	24
PDC inflows and outflows between 0.1-0.24 Hz	25-39

Self-Organizing Feature Maps

SOFMs (Kohonen, 1990) are a type of unsupervised machine learning algorithms that belong to the artificial neural networks methods. The key advantage of SOFMs is their ability to represent high-dimensional spaces in a low-dimensional map of artificial neurons. For this purpose, the data points are presented to the input layer of the network and the weight vectors - connecting the input layer to the layer of artificial neurons (Kohonen-layer / competitive layer) - are compared to the input. The weights of the winning neuron (the one with the strongest correspondence with the input, termed the best matching unit) and its neighbors are then adjusted to match the input. This process is repeated a high number of times and with cyclically inputing the original data points until the final configuration (the iteratively derived topology) of the artificial neurons best matches the original inputs inherent structure. Since the topology of the map results from the weight vector of each artificial neuron, the final topology is a simplified representation of all the data points from the input space. In that sense, SOFM can as well be regarded as a data compression technique.

We used a hexagonal local topology of the artificial neurons and a rectangular grid as map, with a linear initialization of the neuron weight vectors and an automatic setting for the number of artificial neurons based on the data.

Clusot

Clusot is a MATLAB-toolbox for the automated detection of clusters in SOFM-maps that has been developed at the Wilhelm-Schickard-Institute for Informatics at the University of Tübingen. The Clusot algorithm (ver1.1) calculates the Clusot surface from the final trained SOFM-map based on splines (for the calculation of the standard deviation of the modified gaussian function on a 2-dimensional topology) and by using the Euclidian distance of the codebook vectors and the frequency of artificial neurons in the SOFM (defined as the hit number of a neuron divided by the number of input patterns). The algorithm automatically detects the clusters - local maxima in the surface - within that map. This principle is based on the idea that clusters of artificial neurons in the final SOFM correspond to clusters of data points in the original input/feature space. The number of detected clusters can be influenced by setting the theta-value for the recursive flooding after calculation of the Clusot surface (Brugger et al., 2008), the higher the theta-value the more clusters are detected. Recursive flooding operates by "flooding" the Clusot surface landscape with an imaginary waterline, by detecting cluster separations (e.g. when the valley between two

neighbouring peaks is submerged, the two peaks of earlier one cluster become two separate clusters) and by subsequently re-flooding only that specific area of the Clusot landscape again in order to reach an optimal clustering result (e.g. on one of the peaks there might be another valley with two smaller peaks, this way all three peaks become cluster centroids). The combination of SOFM and Clusot (with high theta-values and long-training length) for the detection of clusters in high-dimensional data is especially suited for our data-driven approach as the real number of clusters is a-priori unknown. An example of this approach would be organizing all ICs based on their spatial features' fingerprint. For this, the six features are normalized, and the data points (each representing a single IC from one subject and one session) in six dimensional feature space are used as input for an SOFM. The resulting SOFM map is clustered using Clusot and the clusters can be interpreted as the classes of spatial configuration an IC can possibly belong to (e.g. most of the IC in GM and unfractionated vs. most of the IC in CSF and highly fractionated).

Denoising

The result of defining the feature values for each IC is a list of all components from all experiments and their respective features (a 6858 ICs x 39 features matrix). This list can be converted into a 39-dimensional feature space where each point corresponds to one IC and be organized and clustered using a combination of SOFM and Clusot. This way the comprehensive information can be converted into a preliminary taxonomy of component types. Yet not each feature might be differentiating in a meaningful manner or be of equal importance. As all features are treated equally by the algorithms such an approach might not lead to an interpretable and meaningful classification of component types (e.g. is it more relevant that components are close which are similar in GM portion or similar in Granger Causality interactivity features). Therefore, a stepwise strategy was applied. The components were first organized and clustered using an SOFM-Clusot approach singularly based on their spatial features (GM, WM, CSF, out of brain, component size, component spatial fractionality). Subsequently, all clusters for which the centroid had a GM/WM, GM/CSF or GM/OFB ratio below one were classified as noise and removed. Secondly, noise features were used for organization of the data and clustering, and a small number of components from outlier noise feature value clusters were eliminated. Please see Figure 1 for an overview of the dataflow.

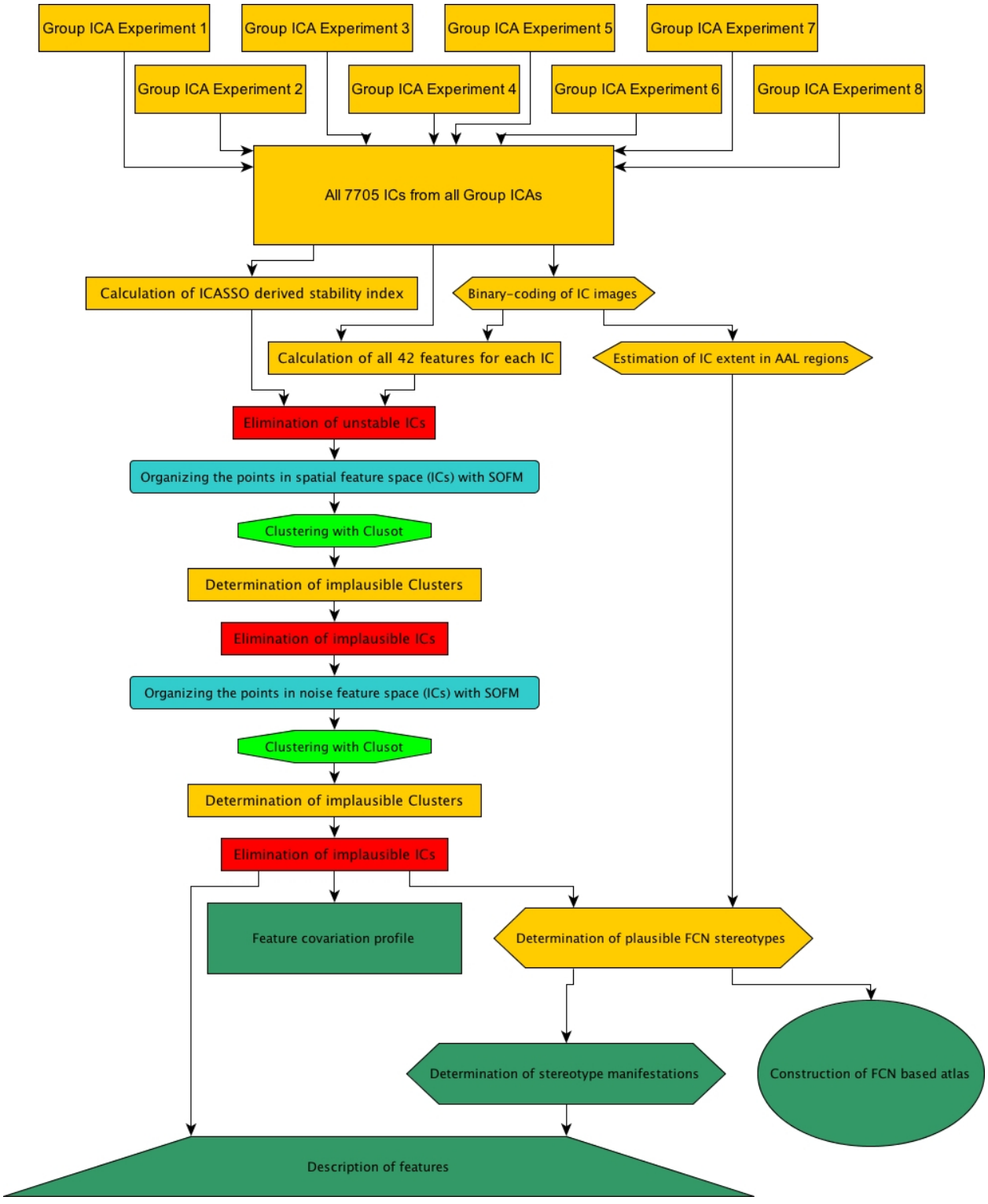

Figure 1 – **Dataflow.** After experiment-level Group ICA, component were eliminated that were not termed stable after an ICASSO step, subsequently ICs were organized based on their spatial features, clustered and implausible ICs were eliminated; the remaining ICs were organized based on their noise features and clustered, implausible ICs were eliminated. The remaining FCNs of supposedly neural origin were used for the calculation of the feature covariation profile, the determination of FCN stereotypes, the construction of an FCN based atlas as illustrated in Figure **??** and the overall description of typical networks.

Step One: Spatial Features

The 6858 components that were termed stable (ICASSO stability estimate above 0.9), were organized based on the spatial features GM, WM, CSF and OFB portion, total size counted in number of voxels and spatial fractionality index. The values for each of these six feature dimensions were normalized to zero mean and unit variance across the entire dataset. The points in the six-dimensional feature space (stable components) were then organized using the SOFM implementation and subsequent clustering was performed with the Clusot software, resulting in a total of 18 clusters from which 6 clusters showed feature characteristics that indicated a non-neural origin or an unclear estimation (for one cluster the average GM/WM ratio was below one, for three clusters the respective GM/CSF ratio was below one, for two the GM/OFB ratio was below one). Three of these clusters ranged among the top third of clusters with highest spatial fractionality and small component voxel mass. A total of 938 components from these six clusters were rejected.

Step Two: Noise Features

The remaining 5920 components that were stable, mostly unfractionated and located mainly in GM were organized based on the noise features squared correlation of component timecourse with total CSF, ventricles and entire volume-average and the R^2 value of the multiple regression of the movement regressors as predictors of the component time course. As these four features all ranged between zero and one, no further normalization was applied. The points in the four-dimensional feature space were then organized using the SOFM implementation and subsequent clustering was performed with the Clusot software (theta value for clustering 0.8), resulting in a total of 13 clusters from which 2 clusters showed feature characteristics that indicated a non-neural origin. One cluster showed the maximum average movement related R^2 value of all clusters (0.89), while another cluster showed the maxima average values for all three other noise features in one single cluster. An additional analysis using spectral features that were not used for the SOFM organization of the data revealed that the average kurtosis of the power spectrum density plot for components in this cluster was maximally leptokurtic (average kurtosis in the other 12 clusters was 63, SD=27, kurtosis for this cluster was 333), indicating that components in this cluster distinctly capture pulsation related noise in a rather narrow frequency range. A total of 108 components from these two noise clusters were disposed, resulting in the final component list of 5812 components that are stable, located in GM and show no predominant noise features.

Feature Covariation Pattern

The final component set can be used to correlate all available features with one another in order to infer on latent coherencies beyond the observable features. Due to the high number of correlations, only correlations with an absolute magnitude above 0.4 that passed a False Discovery Rate threshold correction ($p<0.05$) are reported in the online Supplementary Material. Please see the results section Selected Correlations from the Feature Covariation Pattern for more details.

Detection of distinct networks

There are multiple ways to organize the remaining ICs into clusters that are formed on the basis of spatial similarity of these components (e.g. all networks that contain the left Precuneus as one node could become one cluster). The goal of organizing the networks of neural origin into groups is to generate a fully data-driven and bottom-up derived typology of networks. With such a typology, we are capable of sorting any IC image into its network family (Figure 3) or to identify deformed networks in patient populations. Furthermore, the inherent structure of this typology can serve us with indicators on how FCNs form, since although theoretically there can be as many distinct FCNs as there are possible voxel-pair combinations in the brain we only observe an astronomically small fraction of all theoretically possible FCNs (assuming approx. 60.000 GM voxels the possibilities are practically infinite).

An analogy to illustrate this principle would be the periodic table - although we could know how many atom types or elements (distinct brain regions) there are, only by observing the types of molecules (FCNs) they form and by counting which elements tend to form which particular types of molecules (large or small, complex or simple etc.) could we finally be able to characterize the elements in terms of atomicity and preferred partners.

After evaluation of multiple approaches, we decided to organize the networks based on the number of network-voxels per AAL region. The initial binary-coded images were recoded as a 90 scalar-value vector by counting the network-voxels within each of the 90 cerebral regions of the AAL atlas. Each such coded vector was normalized to zero mean and unit variance to eliminate differences due to total component size as well as AAL region size and used as a 5812 observations x 90 features input to an SOFM. The circle of SOFM organization and clustering was repeated with the largest cluster as input into the next step (theta=0.9), until the largest output cluster had only less than 300 members (13 cycles). The results indicate that with this approach multiple outlier clusters

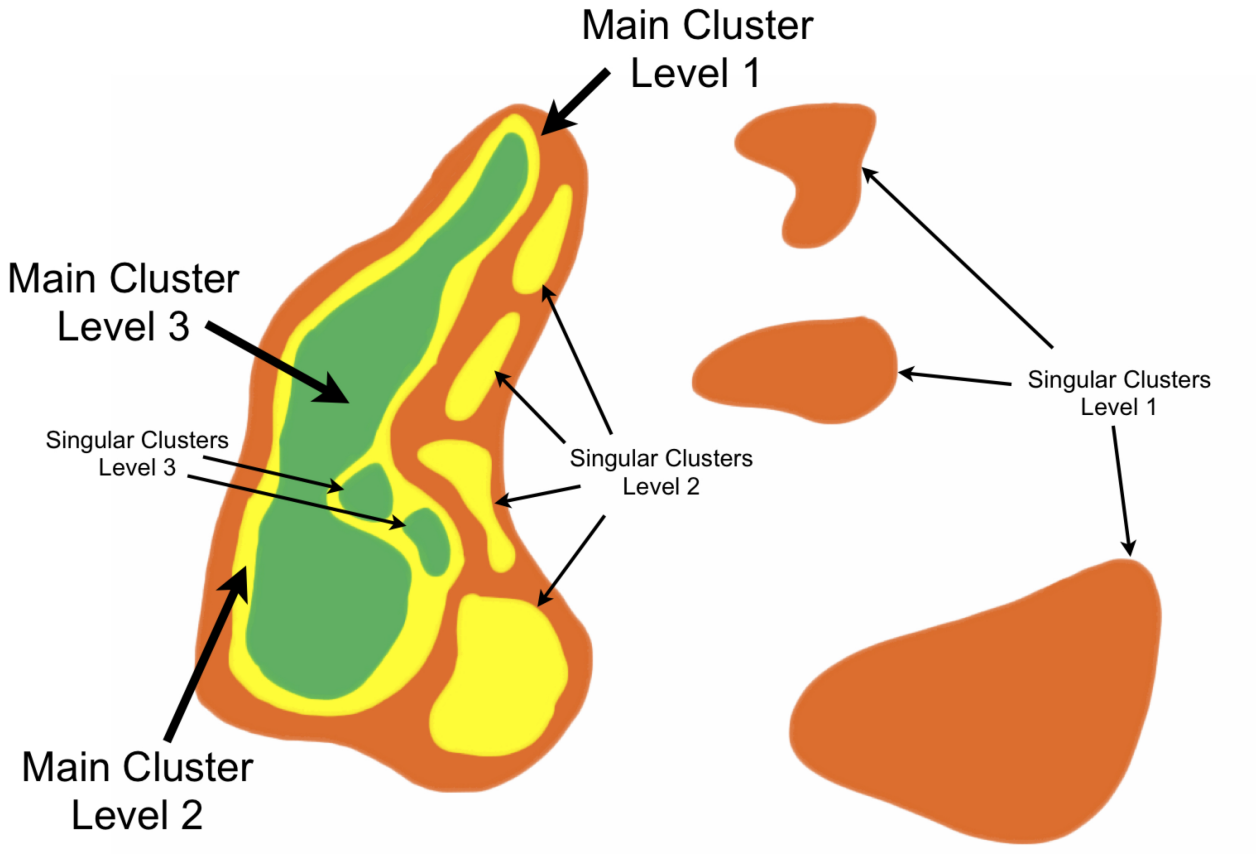

Figure 2 – Illustration of iterative clustering for a two-dimensional feature space. At each level the largest main cluster is subpartitioned again.

and one large cluster is found for each SOFM/clustering cycle. When taking the largest cluster again as input into the next cycle essentially this larger family/cluster of networks is subdivided based on finer differences into the constituting sub-classes (see Figure 2). For further information on alternate approaches please see Attachment A.

Results

The network stereotypes

With our approach for the detection of distinct networks, we identified a total of 172 network stereotypes (clusters resulting from the repeated cycle of SOFM organization and clustering). These 172 network stereotypes correspond to the cluster centroids of clusters in a 90 dimensional feature space where each data point is coding one IC for the relative IC spatial extent in AAL atlas space (which brain regions are in the network). The 172 network stereotypes, samples of

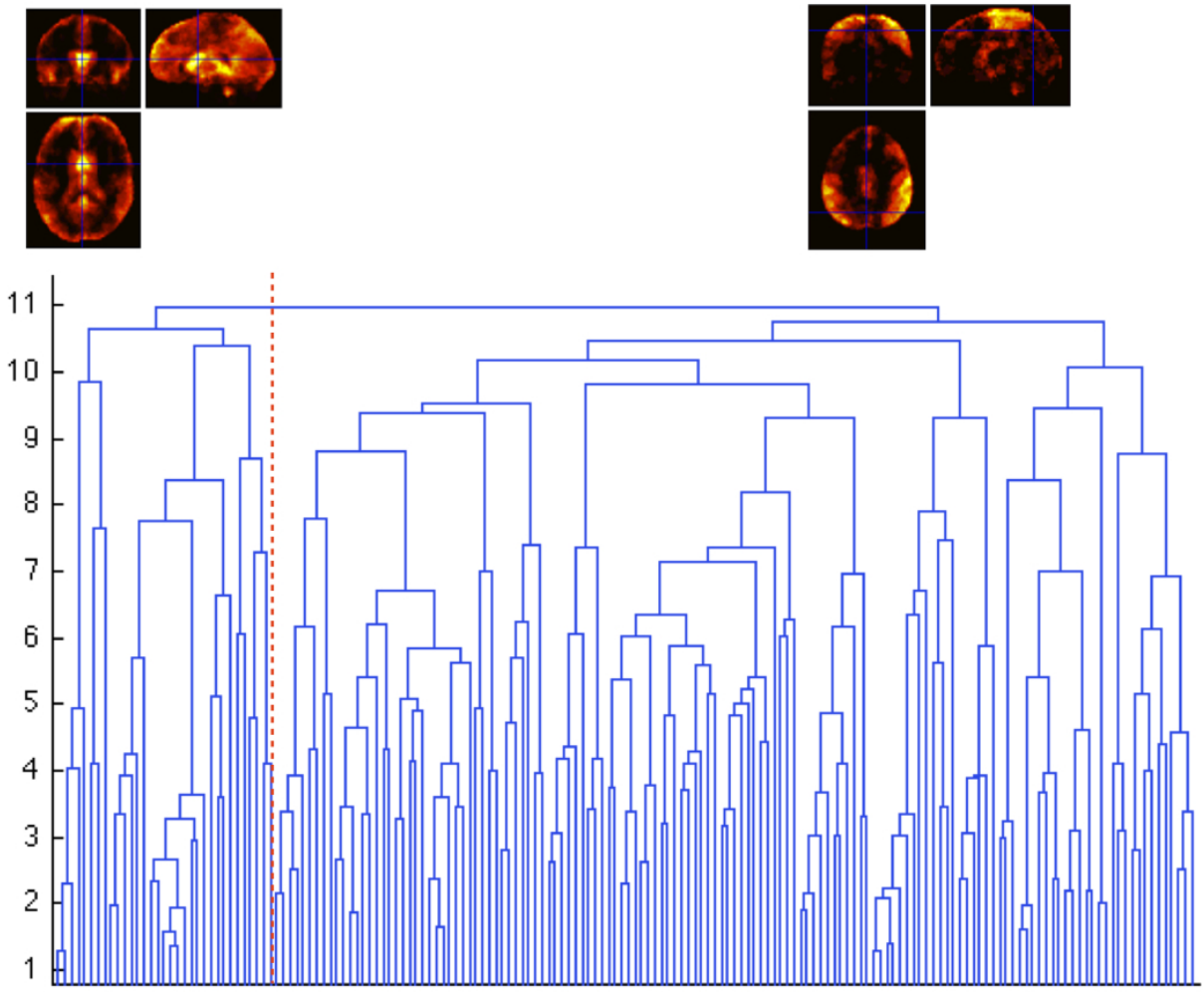

Figure 3 – Dendrogram of cluster centroids and overall network stereotype similarity. Two large groups of networks containing mainly subcortical-cortical FCNs and cortico-cortical FCNs can be subpartitioned into their subgroups based on the spatial similarity of the networks. As visible in the larger right group a significantly wider range of cortico-cortical networks is detected in the present sample.

each stereotype and member regions are available in the online Supplementary Material. The number of manifestations of each stereotypical network in the data is listed in Attachment Table 1 and Figure 3 displays the similarity structure of the network stereotypes and the network families they belong to. The full dataset is available in the online Supplementary Material, including a binary-coded sample image (in 3x3x3 mm MNI space) for fast matching.

Logically, a dendrogram based on the Euclidian length of each network stereotypes spatial extent in AAL atlas space strongly reflects the iterative SOFM-organization and Clusot-clustering cycles and depends on the level of complexity one wishes to display. The two main clusters

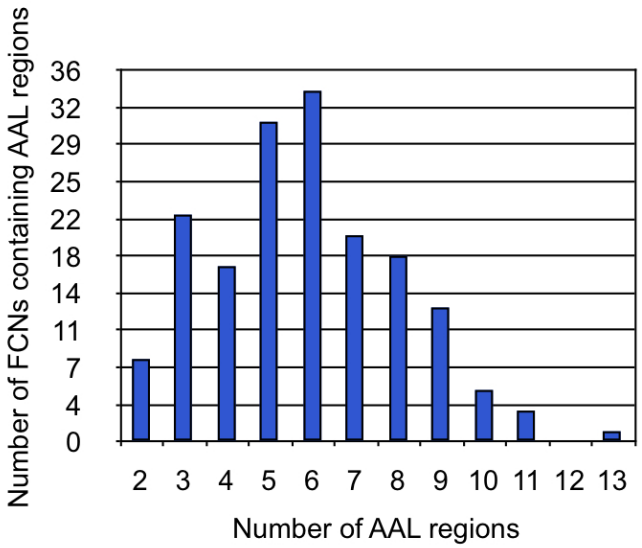

Figure 4 – Number of AAL brain regions per stereotypical FCN on x-axis, number of FCNs consisting of that number of regions on y-axis. 34 of the 172 stereotypical FCNs consist of 6 AAL brain regions (19.77 %).

of stereotypical networks (with 33 vs 139 members) correspond to subcortico-cortical FCNs with frontal and posterior midline parts vs. mainly cortico-cortical FCNs with posterior cortical regions. The further one moves down the dendrogram (reducing the level of abstraction and averaging) the more these main clusters split into the sub-clusters (e.g. FCNs corresponding to a bilateral auditory processing network decompose into a left and right network) until finally on the lowest level of abstraction they correspond to each of the 172 network stereotypes.

The 172 network stereotypes can be further characterized with respect to the number of AAL brain regions each FCN contains. Towards this end, we thresholded the 90 value vector of within AAL region voxels (no cerebellar regions) for each of the 172 stereotype FCNs and display the results (threshold was +1 SD) (see Figure 4). Such a categorization is strongly dependent on the applied threshold (when a region is counted as belonging to the network), therefore we supply the raw data in the Supplementary Material if the reader wants to apply a different thresholding (an overview of the average number of within-network regions over thresholds is supplied in Figure 5).

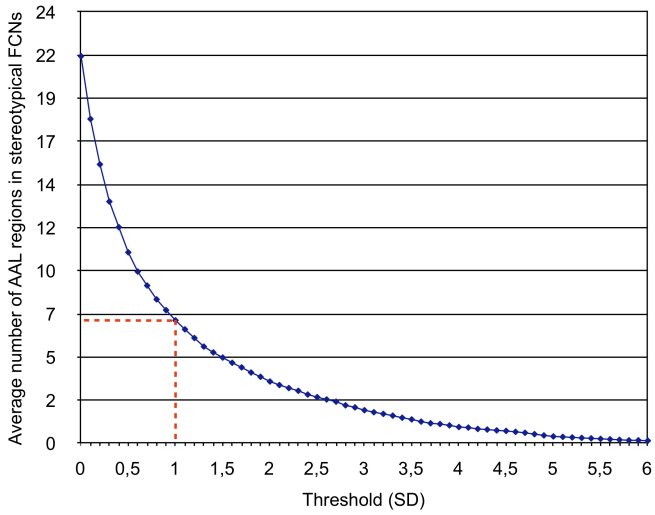

Figure 5 – Average number of cerebral AAL brain regions (y-axis) within all 172 stereotypical brain networks as a function of applied threshold (x-axis, in SD). When thresholding the unit variance zero mean normalized 90 value vector of FCN-voxels per cerebral AAL region at 1 (SD) the FCNs contain on average 7 cerebral AAL brain regions.

Top scorers in network membership

When summing up the 172 cluster means (each mean is a 90 value vector describing how strongly a cerebral region belongs to a network) to derive the regions of highest importance our results show, that the left and right Precuneus, the left and right Middle Frontal Gyrus, the left and right Superior Frontal Gyrus, the left Superior Frontal Medial Gyrus, the right Lingual Gyrus, the left Middle Occipital Gyrus and the right Middle Temporal Gyrus are the top scoring regions of the brain which could be considered as functional connectivity hubs (see Figure 6). Each of these regions is part of at least 18 % of all stereotypical networks. The Precuneus is part of approximately every third stereotypical network.

Regions of the Default Brain Mode network are significantly more often the members of FCNs than non-DBM regions (two-sample t-test, p=0.0343), further subcortical regions show a non-significant tendency to be less often members of functional networks than cortical regions (two-sample t-test, p=0.0672). When testing for differences regarding network membership of right (non-dominant) vs. left (dominant) hemisphere cortical regions, there is no significant difference (two-sample t-test, p=0.6442).

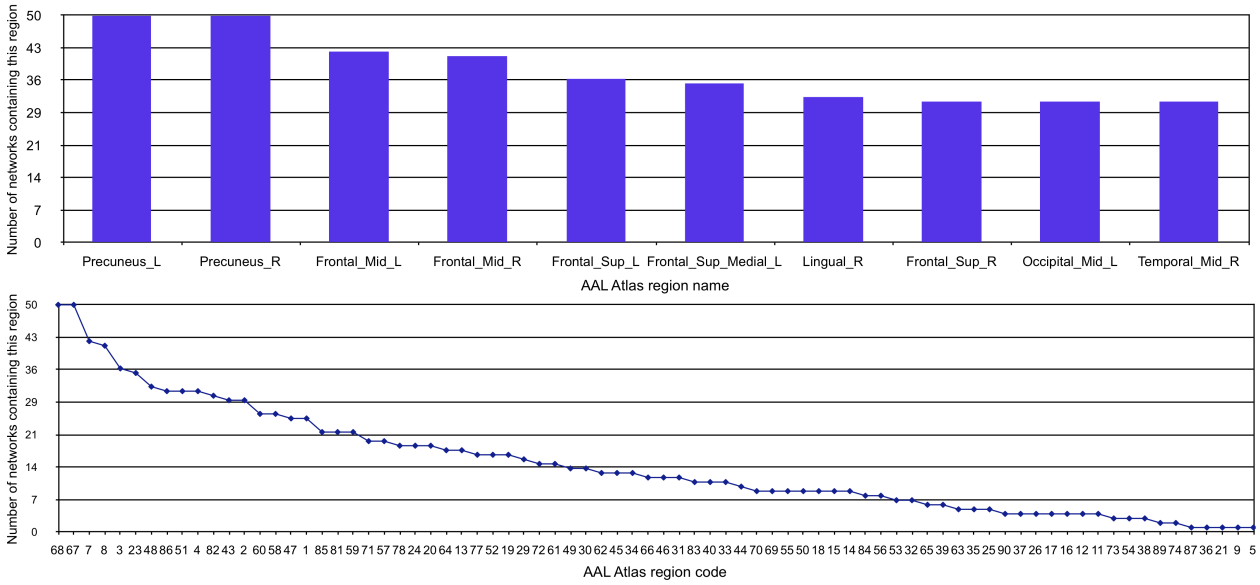

Figure 6 – **Regions which are members of most stereotypical networks** Upper row: the top ten regions are shown (y-axis is the number of stereotypical networks these regions are a member of, the top ten represent the ten far left regions of the lower row figure); Lower row: all regions of the AAL atlas with identical y-axis as upper row, but with AAL region code number on x-axis.

Structure/Function relationships

Region size and network membership

The size of an AAL region in terms of contained GM voxels (the average GM mass within that AAL region) and its score in terms of network membership are correlated on a r=0.8304 ($p<0.0001$) level, indicating that mere region size might influence strongly in how many distinct FCNs a region can participate or is counted into.

Within-network anatomical connectivity

Utilizing anatomical connectivity data from an earlier study (Várkuti et al., 2011), we thresholded the edge probabilities (derived using probabilistic tractography reconstruction of white matter tracts) in the anatomical connectivity adjacency matrix of each of the 23 subjects from (Várkuti et al., 2011) at a cortico-cortical sparsity of 14 % and averaged the adjacency matrices into an overall average group anatomical connectome (Sporns et al., 2005; Hagmann et al., 2007; Iturria-Medina et al., 2008; Gong et al., 2009; Bullmore and Sporns, 2009a). For methodical details on the Diffusion Tensor Imaging (DTI) measurements and the reconstruction of the indivdual anatomical connectomes please see (Várkuti et al., 2011) and (Kreher et al., 2008). This structural connectome contains the inter-individually most common and most probable inter-regional (nodes are AAL

regions) white matter connections (edges). In order to test the level of direct (path length = 1) within-network anatomical connectivity of the derived FCNs, all 172 network stereotypes were tested to quantify the level of accordance of anatomical and functional connectivity within FCNs. 100 % within-network direct anatomical connectivity is given, if all of the edges to connect all network members with each other with a path length of one are found, e.g. 4 members/nodes need a total of 6 edges to be fully connected as displayed in the illustration in Figure 7, if those 6 are found for that constellation of 4 nodes that results in a full within-network connectivity.

Approximately 42 % of network stereotypes show 100 % within-network direct anatomical connectivity, with a total of 73.26 % showing a within-network direct anatomical connectivity above 75 %. Furthermore, the ratio of within-network direct anatomical connectivity divided by out-of-network direct anatomical connectivity (quantifying the direct connectivity for each set of all out-of-network members equalling the inverse of each network membership binary coding) is greater than 1 for 94.77 % of network stereotypes.

We provided an alternate method of calculation based on randomly constructed FCNs instead of out-of-network connectivity in the Supplementary Material (Attachment B), the results are comparable.

Interestingly, the correlation between the number of manifestations of a stereotypical FCN and the within-FCN anatomical connectivity is close to significance (p=0.0595) but is very low in magnitude (r=0.1440). This indicates that strong correspondence of anatomical and functional connectivity of a FCN does not necessarily mean that it is more often observed, although it has to be noted that the five most frequently observed FCNs all show a within-FCN anatomical connectivity of above 80 % (see Figure 8).

Perfusion, gray matter volume and connectivity

As demonstrated in (Várkuti et al., 2011), an elevated level of covariation between relative perfusion and graph metrics of anatomical connectivity (while controlling for GM volume) can be found particularly for regions of the DBM network. In light of the present findings, it is possible that membership in distinct functional networks and anatomical connectivity/perfusion covariation are linked. We tested this hypothesis by calculating a correlation for graph theoretical, GM and perfusion metrics with the number of networks a region is a member of, for each region of the AAL atlas (for details on perfusion and graph information please see (Várkuti et al., 2011)).

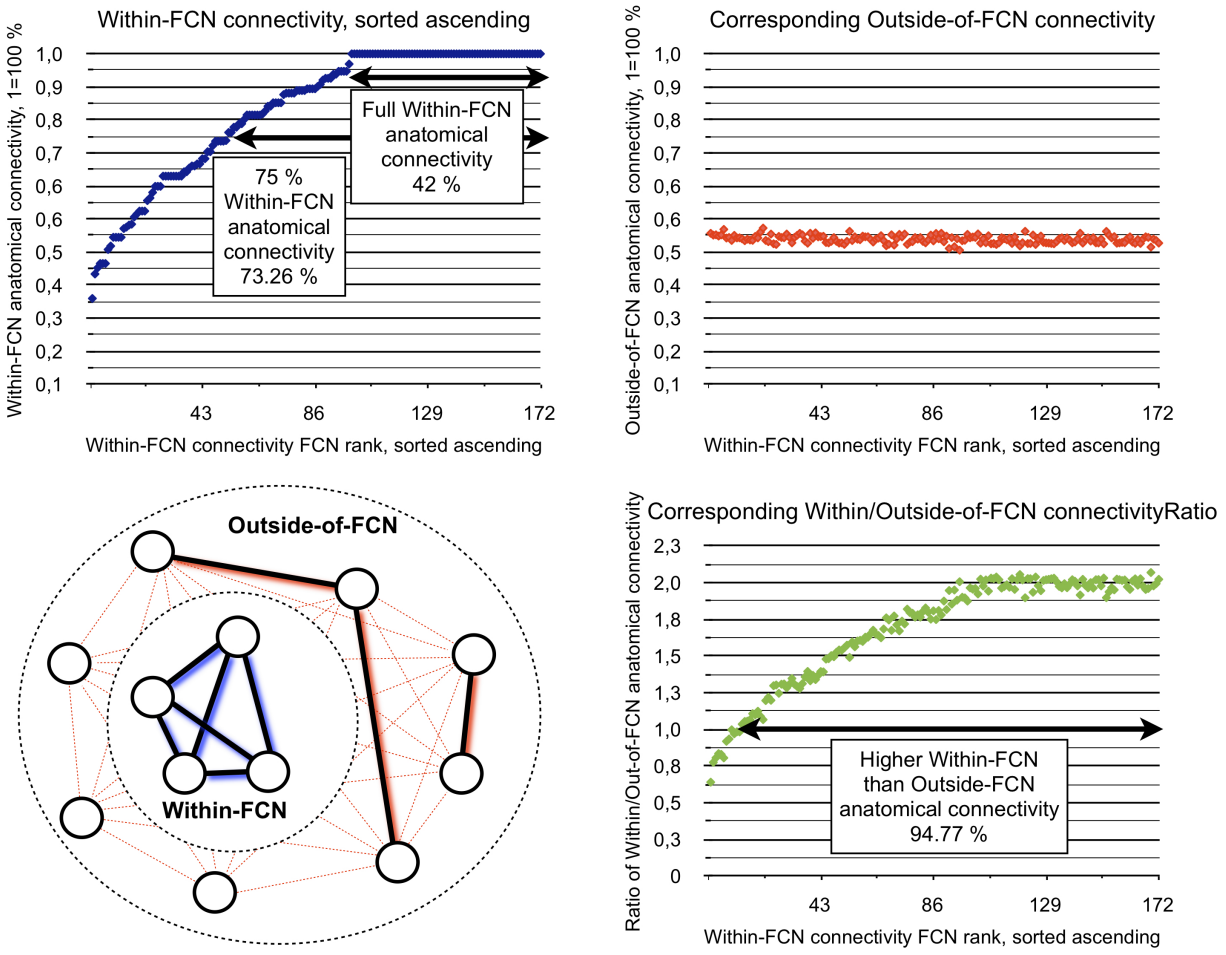

Figure 7 – **Results of Within-FCN anatomical connectivity (top right, blue, y-axis 1=100 %, x-axis FCN rank, sorted ascending), Outside-FCN anatomical connectivity (top left, red) and Ratio (lower right, green).** Within-FCN anatomical connectivity represents the percentage of functional connections (blue shadowing) for which a corresponding direct (path length = 1) anatomical connection (black edge) is identified in the group connectome. Outside-of-FCN is calculated for all non-FCN members, individually for each new FCN (see illustration lower left). Here 8 regions are not member of the 4-node-FCN, while the FCN is fully connected (100 % = 6 of 6 possible edges) the non-FCN regions are only connected at a level of 10.71 % = 3 of 28 edges).

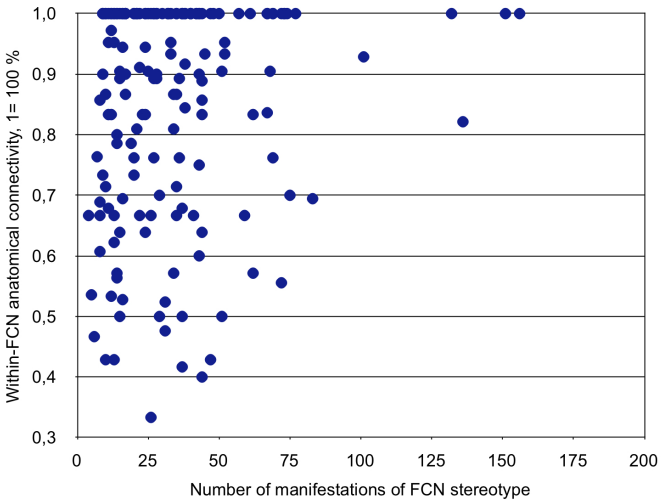

Figure 8 – The relationship of within-FCN anatomical connectivity (y-axis, 1=100 %) and number of manifestations of a FCN stereotype in the present dataset. Note that the five most frequently observed FCNs all show a within-FCN anatomical connectivity of above 80 %.

With this data, the number of network memberships for each region can be predicted (using multiple linear regression) with an R^2 of 0.78 (0.45 without the predictor GM volume). Relative perfusion, vulnerability and normalized degree are positively correlated (r=0.4365 for relative perfusion, r=0.2110 for vulnerability and r=0.3739 for normalized degree), and clustering coefficient and local efficiency are negatively correlated with the number of network memberships for each region (r=-0.4346 for the clustering coefficient and r=-0.3910 for local efficiency, all $p<0.001$ but the vulnerability covariation which is p=0.0459).

Selected Correlations from the Feature Covariation Pattern

We analyzed the list of IC fingerprinting features for covariation patterns. Strongest correlations included a negative correlation of spatial GM and CSF portion (r=-0.69). The GM portion is negatively correlated with WM, OFB and CSF portion, but most markedly with the latter. As these regions are the main sources of signal in the fluid-weighted sequences this is a plausible finding, indicating that the main portion of an IC is located either in the CSF or GM portion of the brain.

Furthermore, total component size in number of voxels is correlated at 0.3 with the GM portion (anti-correlated with WM and CSF portion) indicating that components of non-neural origin are smaller. Spatial fractionality is negatively correlated with the CSF portion (r=-0.48) indicating that CSF components rather occur in the form of an adjacent voxel mass, while it is positively

correlated with the OFB portion, indicating that OFB types of noise are rather scattered over the image.

A negative correlation of spatial WM portion and OFB regions (r=-0.40), a positive correlation of PSD kurtosis and skewness (r=0.95), a series of high correlations that show positive covariation of Partially Directed Coherence features across several frequency bins (r between 0.94 and 0.93) and high correlations of noise features with one another and with spectral features (r>0.82) are observed. The squared correlation of component timecourse with total CSF, ventricles and entire volume-average are all highly intercorrelated indicating one underlying main factor for all three noise features.

PSD kurtosis and skewness are correlated at r=0.95, indicating that the more leptokurtic the spectral profile of a component is, the more the peak is located in the lower frequency range. Given the insufficient frequency resolution of fMRI for frequencies above 0.25 Hz, this is a plausible finding. Furthermore, both are correlated with the R^2 of the head movement regressors (based on the realignment preprocessing step), which is plausible as this regression method best captures slow head movements. Component size (number of network-voxels) is anti-correlated around r=-0.3 with PSD skewness and kurtosis, indicating that larger components have rather platykurtic and higher peaking PSD profiles.

Discussion

Noise and networks of interest

The data-driven dissociation of networks of neural origin and networks not of interest allowed for the preclusion of significant portion of ICs from further processing steps. Although such exclusion of ICs based on IC-fingerprinting was mostly successful in our case, the approach can be refined with respect to the included features and the exclusion criteria. For such a system to be applied more broadly (e.g. in the automated denoising of images) the minimization of false-positive detections of confound ICs has to be of highest relevance, in order to avoid any elimination of valuable information. While, for our purposes, the ICs originating from scanner or physiological noise could mostly be excluded, the differentiation between FCNs of neural origin and FCNs detected due to homology can only be accomplished by the systematic experimental manipulation of network parts. FCNs of neural origin within which information is communicated,

will be disrupted or altered as a whole by the experimental suppression or activation of one isolated network node, while other FCNs detected due to homology should not be significantly affected by the manipulation of one single part.

Feature Covariation Patterns

The observed covariation patterns of features describe mostly intuitive general relationships between IC properties that can aid our understanding on the properties and sources of the fMRI signal (e.g GM or CSF). An enlargement of the available data would increase the number of ICs in specific subgroups and clusters which result from the SOFM and Clusot cycle, so that Feature Covariation Patterns could be calculated for each specific subgroup/family of ICs. Most likely such calculations would result in deviating covariation patterns (e.g. between spectral and noise features) for example of ICs originating from various types of physiological noise. The exact amount of useful information for FCN characterization that can be mined from Feature Covariation Patterns remains to be assessed in future work.

Detectability of networks

Our finding that regional GM volume is a strong predictor of network membership for a brain region could be interpreted in various ways. First of all, it could indicate that GM mass is largest in multimodal association areas of the brain that engage in a multitude of neurocomputational tasks. Secondly, it could indicate that our current fMRI measurement scheme (approx. 3x3x3 mm voxels and supra-second TRs) is most sensitive to the detection of macroscopic FCNs that emerge slowly (on broad timescales), with a large spatial extent and mainly in regions of the brain with relatively similar hemodynamic response functions. This could as well explain why there is a tendency for subcortical regions to less frequently be members of observed networks.
It is therefore not unlikely that there remains an entire universe of fast emerging and decomposing FCNs that contain only a small set of voxels which are presently invisible to us with fMRI. Faster, multiplexed EPIs (Feinberg et al., 2010) provide subsecond temporal resolution with whole brain coverage and high spatial resolution that may help unravel subcortical and rapidly transitioning FCNs. The systematic detection and recording of FCNs using electrophysiological methods and their projection onto the cortical surface could be used to significantly itemize the present taxonomy and answer a series of central questions. It can be hypothesized that there is a systematic relation between FCNs derived with electrophysiological methods and FCNs measured with hemo-

dynamics based methods. The relationship of brain activity captured by the hemodynamics of networks must restrict the state space within which electrophysiologically measured states can occur. If so, there should only be a limited number of electrophysiologically detectable networks while a FCN is considered coherently active in terms of hemodynamics, as the neural processes leaving their traces on these two timescales would have to be coupled and restricting each other in some systematic way - an issue presently mainly addressed by joint/parallel ICA approaches (Brown et al., 2010; Mantini et al., 2010; Lei et al., 2010; Edwards et al., 2011; Bullmore and Sporns, 2009b). Furthermore, there is growing evidence that properties of all of these networks (structural and functional) are tightly linked, irrespective of the applied measurement modalities (Teipel et al., 2009; Whitford et al., 2010; Valdés-Hernández et al., 2010).

Network Stereotypes and diagnostics

The list of 172 network stereotypes and their feature properties and similarity corresponds to the intended taxonomy (please see Figure 9 for exemplary stereotypes). These 172 networks correspond to the canonical brain networks observed in our data and can theoretically be used for diagnostic purposes. Evidently one does not need to test a person with tasks for all of the 172 networks but can as well test for a smaller number of main networks, by for example activating the FCNs that correspond to the most basic networks (are higher up in the network family tree, Figure 3).

It has to be noted that this detection of distinct networks is occurring on the atlas-level of abstraction, where each functional network is regarded as an entity which is dispersed over a limited set of regions. For a deeper analysis distinct networks could as well be identified directly on the level of voxelwise binary-coded IC images, but this would result in a much higher number of original functional networks, as already components that only differ in one single voxel (or any arbitrary number) might have to be regarded as two distinct networks. Furthermore, the use of this approach on the voxel-level would result in approx. 60.000-dimensional data (as many dimensions as non-empty voxels) which is computationally unfeasible.

This taxonomy can be validated in future studies by a multitude of methods, such as regenerating it with the same method from new datasets, analyzing the split-half reliability, actively impairing or facilitating the formation of certain network types by means of brain stimulation (e.g. TMS, tDCS) or by observing pathological populations. A clear prediction of this taxonomy is that

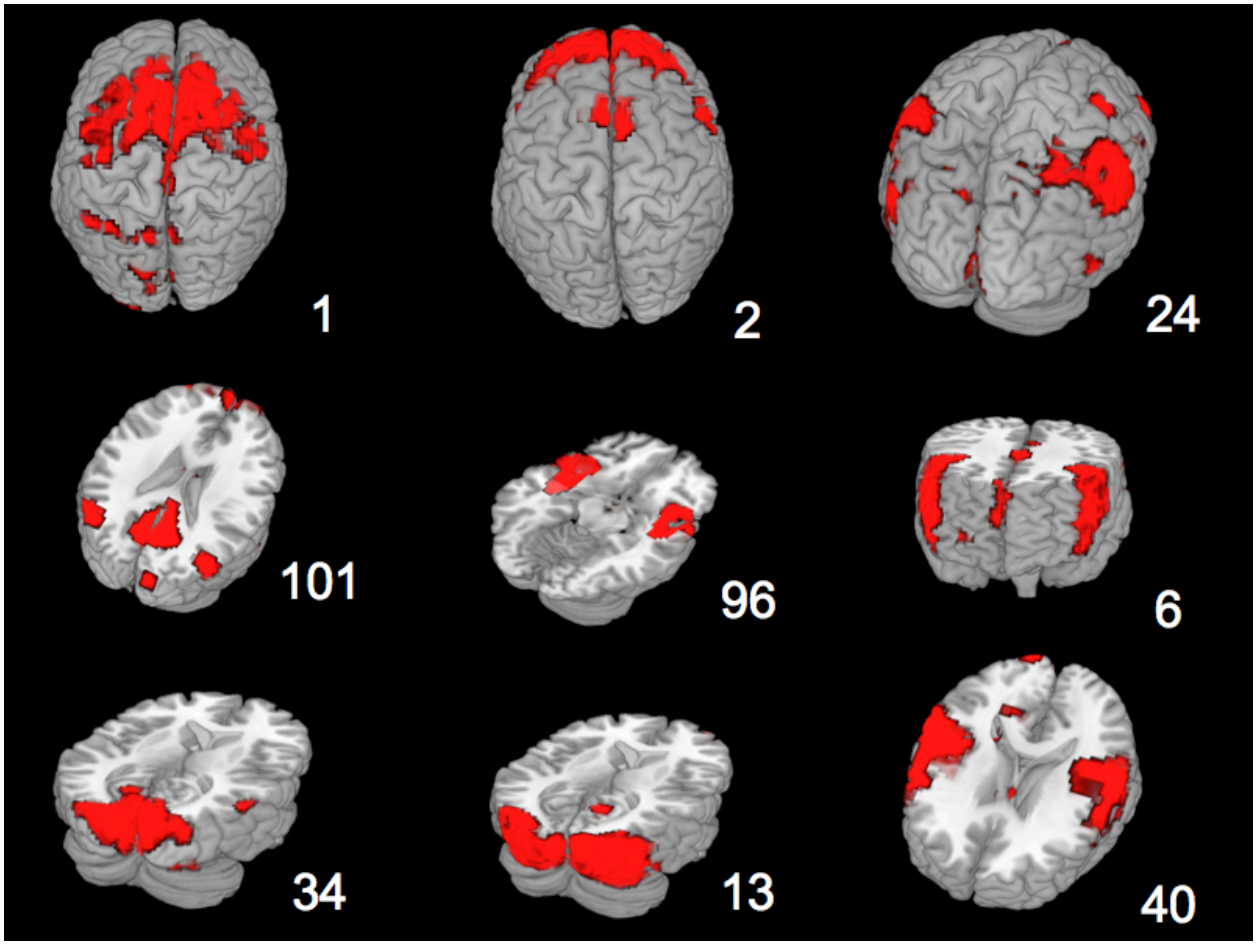

Figure 9 – Nine sample stereotype FCNs from the set of 172 overlayed onto a standard single brain using MicroGL. FCNs 1 and 2 correspond to various parts of the frontal cortex, FCN 24 comprises parts of the inferior Parietal and Supramarginal Gyri, FCN 101 shows a strong overlap with Default Brain Mode Regions, FCN 96 is a bilateral Insula network, FCN 6 contains lateral parts of the inferior Frontal Cortex such as pars opercularis and pars triangularis as well as an Anterior Gyrus Cinguli portion, FCN 34 contains primary and FCN 13 contains secondary visual areas, and FCN 40 corresponds to a bilateral auditory cortex network.

patients with mostly intact anatomy but functional impairments should first loose the ability to establish some of the network stereotypes on the lowest level of abstraction (the level of the 172 stereotypes, e.g. loss of a specific frontal executive network) while patients with more progressed or more severe diseases should be unable to generate the FCNs of an entire subgroup (e.g. disability to form any network with frontal involvement) until in most severe cases observable function should break down at the most global level (e.g. disability to generate subcortical-cortical or cortico-cortical FCNs). Thus, this taxonomy and methodology opens a new diagnostic potential for the classification of brain damage severity and functional abnormality. An example of such a diagnostic kit would be a diagnosis based on the elicited activity of 15 canonical FCNs, each belonging to one of the main network families (e.g. around level 9 in Figure 3). Abnormal properties of one network or the inability to establish any of the main networks could be associated with certain types of pathology. The combination of multiple such task-free (e.g. DTI analysis of the individual anatomical connectome or resting state functional measurements) and task-based methods with sophisticated data analysis approaches seems to hold great potential for the development of new diagnostic tools and is currently a strongly studied subject (Greicius et al., 2004; Lawrie et al., 2008; Stam et al., 2009; Whitfield-Gabrieli et al., 2009; Rubinov et al., 2009; Seeley et al., 2009; Dosenbach et al., 2010; Van Dijk et al., 2010; Wu et al., 2011; Bullmore and Sporns, 2009b).

The fact that the DBM regions are significantly more often members of FCNs than non-DBM regions suggests the possible interpretation of resting-state elevated DBM activity as a form of idling state, from which the DBM regions break away into task-dependent associations with other FCNs. If this hypothesis is true, disruption of normal DBM functional connectivity should impair the subsequent formation of certain FCNs. The documented uncoupling effects of anesthetics on DBM activity and the decrease of adaptive behavior with increasing anesthesia depth could be a first indicator. Nevertheless, if the presented taxonomy and the idling hypothesis are correct at least 54 stereotypical networks that do not contain DBM members should be less affected by experimental DBM activity manipulations. This hypothesis remains to be tested in future work.

The role of regional properties in the formation of Functional Connectivity Networks

Our results clearly underline that the observed stereotypical FCNs tend to form along direct anatomical connections. Nevertheless, the existence of a multitude of FCNs that form between regions that are not directly connected by macroscopic WM bundles can not be excluded based

on these findings. The present data only indicates, that networks which form for longer (supra-second) durations and between brain areas with a high GM mass generally rely on direct WM connections.

The documented covariations of perfusion, GM volume and graph theoretical indices of anatomical connectivity with the number of networks a region of the brain is observed to be a member of, can be interpreted either causally or as an isolated statistical coherence. Regions of the brain with high resting state perfusion, strong anatomical interconnectedness and high relevance (but not necessarily high damage resilience in terms of lesions to the anatomical connectome) apparently form networks more often. By the same token hypoperfusion, cortical atrophy and disconnection (e.g. in aging) might contribute in a major way to the decline of the brains ability to establish large-scale FCNs in an adaptive manner. If this assumption is correct, a series of hypotheses can be derived from this: Natural or experimental manipulation of anatomical connectivity, GM volume and relative perfusion should influence the ability of a brain region to engage in FCNs. While this has been clear to the scientific and clinical community on a qualitative basis, the data from our present study allow the creation of quantitative models and the formation of predictions on the basis of our multiple regression results. The successful prediction of the number of network memberships of a region from data on the regional properties of that region represents the quantitative formulation of an implicated balance in such structure/function relationships.

The top scoring regions in network membership mostly correspond to regions of the association cortex, many of them along the midline of the cerebrum and known anatomical connectivity hubs (Gong et al., 2009). These findings strengthen the concept of a strong association of regional properties and functional roles (association cortex, primary- or secondary motor/sensory cortex) of brain regions.

Further links between anatomical connectivity and the regional properties of brain regions have recently been documented by other groups (Chen et al., 2008; Cohen et al., 2008; Honey et al., 2009; van den Heuvel et al., 2009), such as for example the successful association of the covariation profiles of local cortical thickness with the underlying anatomical connectivity between brain regions (Gong et al., 2011). On a longitudinal level, engaging in a high number of FCNs might influence the properties of a brain region either on the phylogenetic level in terms of an evolutionary push to increase resting state perfusion, GM volume, cortical thickness and anatomical connectivity or on a rather ontogenetic level in terms of an association of functional and anatomical properties of a brain region in terms of co-maturation. Whether changes in the activity profile (participation

in FCNs) precedes a shift of regional properties during development or vice versa remains to be tested in future work, possibly by manipulating either the formation of regional properties by influencing local axon guidance and perfusion or by altering the functional connectivity profile of a region.

Impact and implications

We've demonstrated a data-driven system for the denoising of fMRI time series and for the sorting and analysis of Group ICA derived ICs. The derived cluster boundaries for the denoising steps can (after a cross-validation, that was not the scope of the present study) be directly utilized for noise vs. non-noise classification of ICs derived from newly measured data. Furthermore, we provide a rich description of multiple thousand ICs using a multitude of state of the art features and describe covariation patterns such as the covariation of Granger Causality features and spectral properties. While this dataset can be mined by the scientific community with alternate methods, we provide a taxonomy and list of stereotypical/canonical brain networks that remains to be refined by the integration of larger data bodies and to be validated experimentally by observing functional connectivity in patient populations. Data from new ICA analyses can be directly annotated with the information provided in our data set, including the display of parent-child relationships (e.g. the observed network of fronto-parietal regions belongs to the network family of networks forming along the cerebral midline). Furthermore, in Attachment C we provide a new functional parcellation scheme for the individual (or group) inspired by the concept of a chronoarchitectural analysis of brain activity (Bartels and Zeki, 2005) that is based on the idea, that the smallest macroscopic functional unit of the brain is the one that might participate in a multitude of networks but always does this as a whole.

The functional hubs of the brain are those regions with largest GM mass, relative perfusion and anatomical connectivity and evidently these regions form a multitude of different networks but with a clear tendency to follow direct and therefore short anatomical connections (path length = 1). In that sense, not only are the anatomical connectome and the functional connectome strongly overlapping, but are regional GM mass and resting state perfusion as well part of an equation that describes the healthy brain in terms of the harmonic interplay of its functional and structural parts.

Based on this finding, the decay of anatomical connectivity in aging and in certain disorders can clearly be related to systematic alterations in functional connectivity by using one comprehensive

model that encompasses all relevant parts. A major challenge of our future work will be the exploration of the question, whether these group level results derived from large data bodies can be reliably translated onto the single subject/case level for diagnostic use.

As illustrated in Figure 5, the detected networks take on specific formations in terms of the number of regions that participate. It is possible that these numbers represent the limits of network formation and maintenance in the healthy brain and that specifically these numbers might change due to certain forms of disease, so that the maximum number of nodes in the functional networks of such patients might decrease along with the brain's ability to maintain complex interactions.

Methodical limitations

We want to point out that it is possible that some regions of the brain do not show sufficient BOLD activity or do not show such a hemodynamic response sufficiently in sync with other regions, for them to appear as part of a network in fMRI studies. Due to the large and heterogenic data sample this is unlikely, but possible. Although the brain is extensively studied in the MR-scanner with a variety of stimuli and tasks, it is evident that certain types of networks and activations that the healthy brain is capable of producing will probably never be recorded in the artificial setting of the scanner environment. This environment restricts subjects in a way that makes real natural vision, movement through a scenery or e.g. complex prolonged social interactions very difficult. Therefore, the development of more accurate stimulation schemes and less restrictive scanner environments might lead to the discovery of yet undocumented functional networks in the future - as already addressed in (Bartels and Zeki, 2004). Furthermore, our results are based on one spatial parcellation scheme for the sorting of FCNs into clusters and the identification of stereotypical networks, namely the AAL atlas. It is possible that the use of different atlases might alter the results (Wang et al., 2009), but we do not expect any dramatic alteration as the AAL atlas offers a parcellation of both cortical and subcortical regions into a high number of functionally sound and well established brain areas.

Conclusions

This approach is merely a first step to form a taxonomy of FCNs on a purely data-driven basis that has been realized at one single center. Being scalable, the method can be transposed into cloud computing or other solutions for the high-throughput analysis of publicly shared functional data. Future experiments on the active manipulation of network formation, regional brain properties

and local activity suppression remain to be conducted and integrated in order to test the validity of the raised hypotheses on network formation.

Acknowledgements

This paper reflects the authors' views only and funding agencies are not liable for any use that may be made of the information contained herein. The funders had no role in study design, data collection and analysis, decision to publish, or preparation of the manuscript. This work was partially supported by the Deutsche Forschungsgemeinschaft (DFG), the 7th Framework Programme (FP7) of the European Commission and the Werner Reichardt Centre for Integrative Neuroscience (CIN) at the University Tübingen, Germany. The authors would like to thank Markus Schürholz, Björn Schiffler, Jana Kneslova and Jessica Rajandran for their contributions.

References

References

Achard, S., Salvador, R., Whitcher, B., Suckling, J., and Bullmore, E. (2006). A resilient, low-frequency, small-world human brain functional network with highly connected association cortical hubs. *The Journal of neuroscience : the official journal of the Society for Neuroscience*, 26(1):63–72.

Ashburner, J. and Friston, K. J. (2001). Why voxel-based morphometry should be used. *Neuroimage*, 14(6):1238–1243.

Baker, S., Rogers, R., and Owen, A. (1996). Neural systems engaged by planning: a PET study of the Tower of London task. *Neuropsychologia*.

Bartels, A. and Zeki, S. (2004). Functional brain mapping during free viewing of natural scenes. *Human brain mapping*, 21(2):75–85.

Bartels, A. and Zeki, S. (2005). The chronoarchitecture of the cerebral cortex. *Philosophical transactions of the Royal Society of London. Series B, Biological sciences*, 360(1456):733–50.

Bassett, D. S., Meyer-Lindenberg, A., Achard, S., Duke, T., and Bullmore, E. (2006). Adaptive

reconfiguration of fractal small-world human brain functional networks. *Proceedings of the National Academy of Sciences of the United States of America*, 103(51):19518–23.

Beckmann, C. F., DeLuca, M., Devlin, J. T., and Smith, S. M. (2005). Investigations into resting-state connectivity using independent component analysis. *Philosophical transactions of the Royal Society of London. Series B, Biological sciences*, 360(1457):1001–13.

Bell, A. J. and Sejnowski, T. J. (1995). An Information-Maximization Approach to Blind Separation and Blind Deconvolution. *Neural Computation*, 7(6):1129–1159.

Bogdan, M. and Rosenstiel, W. (1999). Application of Artificial Neural Networks for Different Engineering Problems. *Esprit*, pages 277–294.

Bogdan, M., Rosenstiel, W., Pavelka, J., Tel, G., and Bartošek, M. (1999). *SOFSEM'99: Theory and Practice of Informatics*, volume 1725 of *Lecture Notes in Computer Science*. Springer Berlin Heidelberg, Berlin, Heidelberg.

Brown, K. S., Ortigue, S., Grafton, S. T., and Carlson, J. M. (2010). Improving human brain mapping via joint inversion of brain electrodynamics and the BOLD signal. *NeuroImage*, 49(3):2401–15.

Brugger, D., Bogdan, M., and Rosenstiel, W. (2008). Automatic cluster detection in Kohonen's SOM. *IEEE transactions on neural networks / a publication of the IEEE Neural Networks Council*, 19(3):442–59.

Bullmore, E. and Sporns, O. (2009a). Complex brain networks: graph theoretical analysis of structural and functional systems. *Nature reviews. Neuroscience*, 10(3):186–98.

Bullmore, E. and Sporns, O. (2009b). Complex brain networks: graph theoretical analysis of structural and functional systems. *Nat Rev Neurosci*.

Calhoun, V. (2004). Group ICA of fMRI toolbox (GIFT). *Online at http://icatb. sourceforge. net*.

Chen, Z. J., He, Y., Rosa-Neto, P., Germann, J., and Evans, A. C. (2008). Revealing modular architecture of human brain structural networks by using cortical thickness from {MRI}. *Cerebral cortex*, 18(10):2374.

Cohen, A. L., Fair, D. a., Dosenbach, N. U. F., Miezin, F. M., Dierker, D., Van Essen, D. C., Schlaggar, B. L., and Petersen, S. E. (2008). Defining functional areas in individual human brains using resting functional connectivity MRI. *NeuroImage*, 41(1):45–57.

Correa, N., Adali, T., and Calhoun, V. D. (2007). Performance of blind source separation algorithms for fMRI analysis using a group ICA method. *Magnetic resonance imaging*, 25(5):684–94.

Demirci, O., Stevens, M. C., Andreasen, N. C., Michael, A., Liu, J., White, T., Pearlson, G. D., Clark, V. P., and Calhoun, V. D. (2009). Investigation of relationships between fMRI brain networks in the spectral domain using ICA and Granger causality reveals distinct differences between schizophrenia patients and healthy controls. *NeuroImage*, 46(2):419–31.

Dodel, S., Golestani, N., Pallier, C., Elkouby, V., Le Bihan, D., and Poline, J.-B. (2005). Condition-dependent functional connectivity: syntax networks in bilinguals. *Philosophical transactions of the Royal Society of London. Series B, Biological sciences*, 360(1457):921–35.

Dosenbach, N., Nardos, B., and Cohen, A. (2010). Prediction of individual brain maturity using fMRI. *Science*.

Dosenbach, N. U. F., Fair, D. a., Miezin, F. M., Cohen, A. L., Wenger, K. K., Dosenbach, R. a. T., Fox, M. D., Snyder, A. Z., Vincent, J. L., Raichle, M. E., Schlaggar, B. L., and Petersen, S. E. (2007). Distinct brain networks for adaptive and stable task control in humans. *Proceedings of the National Academy of Sciences of the United States of America*, 104(26):11073–8.

Edwards, B. G., Calhoun, V. D., and Kiehl, K. A. (2011). Joint ICA of ERP and fMRI during Error-Monitoring. *NeuroImage*.

Erhardt, E. B., Rachakonda, S., Bedrick, E. J., Allen, E. A., Adali, T., and Calhoun, V. D. (2010). Comparison of multi-subject ICA methods for analysis of fMRI data. *Human brain mapping*.

Fair, D. A., Cohen, A. L., Dosenbach, N. U. F., Church, J. A., Miezin, F. M., Barch, D. M., Raichle, M. E., Petersen, S. E., and Schlaggar, B. L. (2008). The maturing architecture of the brain's default network. *Proceedings of the National Academy of Sciences*, 105(10):4028.

Feinberg, D., Moeller, S., and Smith, S. (2010). Multiplexed Echo Planar Imaging for Sub-Second Whole Brain FMRI and Fast Diffusion Imaging. *PloS one*.

Gong, G., He, Y., Chen, Z. J., and Evans, A. C. (2011). Convergence and Divergence of Thickness Correlations with Diffusion Connections across the Human Cerebral Cortex. *NeuroImage*.

Gong, G., He, Y., Concha, L., Lebel, C., Gross, D. W., Evans, A. C., and Beaulieu, C. (2009). Mapping anatomical connectivity patterns of human cerebral cortex using in vivo diffusion tensor imaging tractography. *Cerebral Cortex*, 19(3):524.

Greicius, M. D., Srivastava, G., Reiss, A. L., and Menon, V. (2004). Default-mode network activity distinguishes Alzheimer's disease from healthy aging: evidence from functional MRI. *Proceedings of the National Academy of Sciences of the United States of America*, 101(13):4637–42.

Hagmann, P., Kurant, M., Gigandet, X., Thiran, P., Wedeen, V. J., Meuli, R., and Thiran, J.-P. (2007). Mapping human whole-brain structural networks with diffusion MRI. *PloS one*, 2(7):e597.

Halder, S., Agorastos, D., Veit, R., Hammer, E. M., Lee, S., Varkuti, B., Bogdan, M., Rosenstiel, W., Birbaumer, N., and Kübler, a. (2011). Neural mechanisms of brain-computer interface control. *NeuroImage*.

Himberg, J. and Hyvarinen, A. (2003). Icasso: software for investigating the reliability of ICA estimates by clustering and visualization. In *2003 IEEE XIII Workshop on Neural Networks for Signal Processing (IEEE Cat. No.03TH8718)*, pages 259–268. IEEE.

Honey, C. J., Sporns, O., Cammoun, L., Gigandet, X., Thiran, J. P., Meuli, R., and Hagmann, P. (2009). Predicting human resting-state functional connectivity from structural connectivity. *Proceedings of the National Academy of Sciences*, 106(6):2035.

Horwitz, B. (2003). The elusive concept of brain connectivity. *NeuroImage*, 19(2):466–470.

Iturria-Medina, Y., Sotero, R. C., Canales-Rodríguez, E. J., Alemán-Gómez, Y., and Melie-García, L. (2008). Studying the human brain anatomical network via diffusion-weighted MRI and Graph Theory. *NeuroImage*, 40(3):1064–76.

Keune, P. M., Bostanov, V., Hautzinger, M., and Kotchoubey, B. (2011). Mindfulness-based cognitive therapy (MBCT), cognitive style, and the temporal dynamics of frontal EEG alpha asymmetry in recurrently depressed patients. *Biological psychology*.

Kohonen, T. (1990). The self-organizing map. *Proceedings of the IEEE*.

Kreher, B. W., Schnell, S., Mader, I., Il'yasov, K. a., Hennig, J., Kiselev, V. G., and Saur, D. (2008). Connecting and merging fibres: pathway extraction by combining probability maps. *NeuroImage*, 43(1):81–9.

Lawrie, S. M., McIntosh, A. M., Hall, J., Owens, D. G. C., and Johnstone, E. C. (2008). Brain structure and function changes during the development of schizophrenia: the evidence from studies of subjects at increased genetic risk. *Schizophrenia bulletin*, 34(2):330–40.

Lei, X., Qiu, C., Xu, P., and Yao, D. (2010). A parallel framework for simultaneous EEG/fMRI analysis: methodology and simulation. *NeuroImage*, 52(3):1123–34.

Logothetis, N. K. (2008). What we can do and what we cannot do with fMRI. *Nature*, 453(7197):869–78.

Maldjian, J. and Laurienti, P. (2003). An automated method for neuroanatomic and cytoarchitectonic atlas-based interrogation of fMRI data sets. *Neuroimage*.

Mantini, D., Marzetti, L., Corbetta, M., Romani, G. L., and Del Gratta, C. (2010). Multimodal integration of fMRI and EEG data for high spatial and temporal resolution analysis of brain networks. *Brain topography*, 23(2):150–8.

McKeown, M. (2003). Independent component analysis of functional MRI: what is signal and what is noise? *Current Opinion in Neurobiology*, 13(5):620–629.

McKeown, M. J., Makeig, S., Brown, G. G., Jung, T. P., Kindermann, S. S., Bell, a. J., and Sejnowski, T. J. (1998). Analysis of fMRI data by blind separation into independent spatial components. *Human brain mapping*, 6(3):160–88.

Mechelli, A., Price, C. J., Friston, K. J., and Ashburner, J. (2005). Voxel-based morphometry of the human brain: methods and applications. *Current Medical Imaging Reviews*, 1(2):105–113.

Neuper, C. and Scherer, R. (2005). Imagery of motor actions: differential effects of kinesthetic and visual-motor mode of imagery in single-trial EEG. *Cognitive Brain Research*.

Perlbarg, V., Bellec, P., Anton, J.-L., Pélégrini-Issac, M., Doyon, J., and Benali, H. (2007). CORSICA: correction of structured noise in fMRI by automatic identification of ICA components. *Magnetic resonance imaging*, 25(1):35–46.

Raichle, M. E., MacLeod, A. M., Snyder, A. Z., Powers, W. J., Gusnard, D. A., and Shulman, G. L. (2001). A default mode of brain function. *Proceedings of the National Academy of Sciences of the United States of America*, 98(2):676.

Rubinov, M., Knock, S. a., Stam, C. J., Micheloyannis, S., Harris, A. W. F., Williams, L. M., and Breakspear, M. (2009). Small-world properties of nonlinear brain activity in schizophrenia. *Human brain mapping*, 30(2):403–16.

Schelter, B., Winterhalder, M., Eichler, M., Peifer, M., Hellwig, B., Guschlbauer, B., Lücking, C. H., Dahlhaus, R., and Timmer, J. (2006). Testing for directed influences among neural signals using partial directed coherence. *Journal of neuroscience methods*, 152(1-2):210–9.

Seeley, W. W., Crawford, R. K., Zhou, J., Miller, B. L., and Greicius, M. D. (2009). Neurodegenerative diseases target large-scale human brain networks. *Neuron*, 62(1):42–52.

Seeley, W. W., Menon, V., Schatzberg, A. F., Keller, J., Glover, G. H., Kenna, H., Reiss, A. L., and Greicius, M. D. (2007). Dissociable intrinsic connectivity networks for salience processing and executive control. *The Journal of neuroscience : the official journal of the Society for Neuroscience*, 27(9):2349–56.

Seth, A. (2010). A MATLAB toolbox for Granger causal connectivity analysis. *Journal of neuroscience methods*.

Seth, A. K. (2005). Causal connectivity of evolved neural networks during behavior. *Network: Computation in Neural Systems*, 16(1):35–54.

Smolders, A., De Martino, F., Staeren, N., Scheunders, P., Sijbers, J., Goebel, R., and Formisano, E. (2007). Dissecting cognitive stages with time-resolved fMRI data: a comparison of fuzzy clustering and independent component analysis. *Magnetic resonance imaging*, 25(6):860–8.

Sporns, O., Chialvo, D. R., Kaiser, M., and Hilgetag, C. C. (2004). Organization, development and function of complex brain networks. *Trends in cognitive sciences*, 8(9):418–25.

Sporns, O., Tononi, G., and Kötter, R. (2005). The human connectome: A structural description of the human brain. *PLoS computational biology*, 1(4):e42.

Sridharan, D., Levitin, D. J., and Menon, V. (2008). A critical role for the right fronto-insular cortex in switching between central-executive and default-mode networks. *Proceedings of the National Academy of Sciences of the United States of America*, 105(34):12569–74.

Stam, C. J., de Haan, W., Daffertshofer, a., Jones, B. F., Manshanden, I., van Cappellen van Walsum, a. M., Montez, T., Verbunt, J. P. a., de Munck, J. C., van Dijk, B. W., Berendse, H. W., and Scheltens, P. (2009). Graph theoretical analysis of magnetoencephalographic functional connectivity in Alzheimer's disease. *Brain : a journal of neurology*, 132(Pt 1):213–24.

Sui, J., Adali, T., Pearlson, G. D., and Calhoun, V. D. (2009). An ICA-based method for the identification of optimal FMRI features and components using combined group-discriminative techniques. *NeuroImage*, 46(1):73–86.

Teipel, S. J., Pogarell, O., Meindl, T., Dietrich, O., Sydykova, D., Hunklinger, U., Georgii, B., Mulert, C., Reiser, M. F., Möller, H.-J., and Hampel, H. (2009). Regional networks underlying interhemispheric connectivity: an EEG and DTI study in healthy ageing and amnestic mild cognitive impairment. *Hum Brain Mapp*, 30(7):2098–2119.

Tzourio-Mazoyer, N., Landeau, B., Papathanassiou, D., Crivello, F., Etard, O., Delcroix, N., Mazoyer, B., and Joliot, M. (2002). Automated anatomical labeling of activations in {SPM} using a macroscopic anatomical parcellation of the {MNI} {MRI} single-subject brain. *Neuroimage*, 15(1):273–289.

Valdés-Hernández, P. a., Ojeda-González, A., Martínez-Montes, E., Lage-Castellanos, A., Virués-Alba, T., Valdés-Urrutia, L., and Valdes-Sosa, P. a. (2010). White matter architecture rather than cortical surface area correlates with the EEG alpha rhythm. *NeuroImage*, 49(3):2328–39.

van den Heuvel, M. P., Mandl, R. C. W., Kahn, R. S., and Hulshoff Pol, H. E. (2009). Functionally linked resting-state networks reflect the underlying structural connectivity architecture of the human brain. *Human brain mapping*, 30(10):3127–41.

Van Dijk, K. R. a., Hedden, T., Venkataraman, A., Evans, K. C., Lazar, S. W., and Buckner, R. L. (2010). Intrinsic functional connectivity as a tool for human connectomics: theory, properties, and optimization. *Journal of neurophysiology*, 103(1):297–321.

Várkuti, B., Cavusoglu, M., Kullik, A., Schiffler, B., Veit, R., Yilmaz, O., Rosenstiel, W., Braun, C., Uludag, K., Birbaumer, N., and Sitaram, R. (2011). Quantifying the link between anatomical connectivity, gray matter volume and regional cerebral blood flow: an integrative MRI study. *PloS one*, 6(4):e14801.

Wang, J., Wang, L., Zang, Y., Yang, H., Tang, H., Gong, Q., Chen, Z., Zhu, C., and He, Y. (2009). Parcellation-dependent small-world brain functional networks: a resting-state fMRI study. *Human brain mapping*, 30(5):1511–23.

Whitfield-Gabrieli, S., Thermenos, H. W., Milanovic, S., Tsuang, M. T., Faraone, S. V., McCarley, R. W., Shenton, M. E., Green, A. I., Nieto-Castanon, A., LaViolette, P., Wojcik, J., Gabrieli, J.

D. E., and Seidman, L. J. (2009). Hyperactivity and hyperconnectivity of the default network in schizophrenia and in first-degree relatives of persons with schizophrenia. *Proceedings of the National Academy of Sciences of the United States of America*, 106(4):1279–84.

Whitford, T. J., Kubicki, M., Ghorashi, S., Schneiderman, J. S., Hawley, K. J., McCarley, R. W., Shenton, M. E., and Spencer, K. M. (2010). Predicting inter-hemispheric transfer time from the diffusion properties of the corpus callosum in healthy individuals and schizophrenia patients: A combined ERP and DTI study. *NeuroImage*, 54(3):2318–2329.

Wu, X., Li, R., Fleisher, A. S., Reiman, E. M., Guan, X., Zhang, Y., Chen, K., and Yao, L. (2011). Altered default mode network connectivity in alzheimer's disease-A resting functional MRI and bayesian network study. *Human brain mapping*, 00(November 2009).

Zentgraf, K., Stark, R., and Reiser, M. (2005). Differential activation of pre-SMA and SMA proper during action observation: Effects of instructions. *Neuroimage*.

Attachments

Attachment A: Percentage-threshold method

Duplicate networks were removed from the final set of components by first binarizing the component-onto-AAL percentage vectors with a percentage threshold and second marking and eliminating all duplicates. A percentage threshold of e.g. 5 percent binary-codes this vector in a way, that only regions of the AAL atlas that contain more than 5 percent of the components spatial extent will be set to one. The higher the threshold is, the less regions are added to the network and accordingly the total number of regions that are never part of a single- or multi-region component grows.

In order to account for that fact, we performed a sweep over plausible thresholds (starting with 4.9 percent, the threshold were no region is never considered part of a network) and selected a threshold from the plateau most likely representing the captured network dynamics most accurately.

The optimal percentage threshold can be derived from an analysis of the binary-coded component images. When thresholding all Independent Component (IC) images using a cluster-extent threshold, every image contains at least one cluster if the cluster-threshold has a size of 225 voxels (equalling 2,025 cm^3). Fifty percent of the components from the final list are single-cluster components, 28.39 % are two-cluster components, 14.38 % three-, 5.49 % four- and 1.45 % five-cluster components. Six-, seven- and eight-cluster components can be found as well but make for only less than 1 % of all components. Such clusters of adjacent voxels can lie within one single AAL region or on the boundary of two or multiple such regions. The optimal percentage threshold (5.14 %) is identified by performing a sweep over thresholds and correlating the number of found AAL regions in the network with the number of distinct clusters above 225 voxels in the image. The percentage threshold that maximizes this correlation best captures each networks extension in AAL atlas space.

An alternative method would be to use the number of manifestations, as it is highly unlikely that a distinct functional network can be found more than 175 times in a dataset composed of 175 sessions (that would mean instances of it are found several times within one session). Formally this is possible as spatially similar networks can be found with variable spectral properties. We calculated the mean variability of the spectral properties among the manifestations of one distinct functional network for each percentage threshold (so for each level of distinction). While for higher percentages the variability is rising as more and more fundamentally different networks are considered as one since they overlap

in one region of the AAL atlas, for a threshold of 13.96 % both the variability of spectral properties is minimal and the maximum number of manifestations for one network is 180 (around the number of sessions). Unfortunately if this threshold is selected - as it offers optimal differentiation of networks into spatially distinct classes which have homogenous spectral properties and a reasonable maximum number of manifestations - 2621 ICs (45 %) are not considered at all, as no region contains the chosen threshold percentage of the component.

It is most likely that more advanced denoising methods would improve the situation as less components would make it into the final list, which have no relevant spatial extent in AAL space. However, with the current approach we use the 5.14 % threshold, as with this threshold almost all components are considered. The fact, that the presently applied spatial ICA is not intended to provide optimal spectral and temporal differentiation of components further speaks for the first approach. Future sequences with higher temporal resolution might increase the information available in the time domain and improve the situation through better spectral characterization of components.

When counting the number of AAL regions which are part of one functional network, these numbers are close to normally distributed for low thresholds. Functional networks are mostly comprised of 4-6 AAL regions for a percentage threshold of 4.9-5.9 % (please see detection of distinct networks). Increasing the threshold leads to a lower number of mean AAL regions per network.

Furthermore, the percentage distribution of components over the AAL regions shows an exponential decay form, most components are located mainly within a few AAL regions, while almost all components have smaller portions in a wide range of regions (whether this is due to misestimations of the spatial extent of the component or natural can't be resolved presently).

Histograms depicting the number of instances each distinct functional network can be found in the data (how many manifestations of this network type are in the data), show an exponential decay form, irrespective of percentage threshold. This indicates that while many different networks can be found a limited number of times, only a few networks can be found in almost all datasets - logically these networks are composed of the most often found network members (e.g. Precuneus). We selected a percentage threshold of 5.14 %. With this method a total of 3874 distinct networks are found, with manifestation numbers ranging between 1 and 500 (network found multiple times within one session) and an average of 147 (SD: 91).

The eight top scoring regions in this exponentialy distributed ranking of network membership are the left

Precuneus (member of 19.41 % of all networks), the left Middle Frontal Gyrus (member of 18.02 % of all networks), the right Precuneus (member of 17.53 % of all networks), the right Lingual Gyrus (17.53 %), the left Middle Occipital Gyrus (16.96 %), the right Middle Frontal Gyrus (16.11 %), the left Frontal Superior Medial Gyrus (15.44 %), right Temporal Middle Gyrus (13.89 %) and left Lingual Gyrus (13.01 %).

The number of networks each region is a member of significantly differs for the Default Brain Mode (DBM) (Average:341) versus non-DBM (Average:215) regions (two-sample ttest, $p<0.0375$).

To assure that our results are not merely an artefact due to the percentage-threshold method we organized the data after counting the number of voxels within each AAL region for each IC (after removing irrelevant clusters in the images with less than 10 voxels). The resulting 5812 ICs x 90 cerebral AAL regions list was normalized row-by-row to zero mean and unit variance, organized using the Self-Organizing Feature Maps (SOFM) and clustered with Clusot (theta=0.9).

Finally, in favor of a much simpler interpretation we decided to report our results on the basis of component voxel-counts in AAL regions, as with this method network parts are immediately labeled on the basis of the most significant neuroanatomical landmarks.

Attachment B: Within-FCN anatomical connectivity

Instead of basing the calculation of out-of-network connectivity on the direct connectivity of all network nodes outside the Functional Connectivity Network (FCN) in question we constructed for each of the 172 stereotypical networks 172 clones, which consisted of an equal number of randomly picked network nodes (excluding those nodes which where in the FCN under consideration). After calculating the percentage of direct anatomical connections in analogy to the approach illustrated in the section Within-network anatomical connectivity and calculated the average direct anatomical connectivity percentage (100 % means all possible direct edges with a path length = 1 are present in the anatomical connectome) across the 172 clones per FCN. The results are displayed in Figure 1 and are comparable to the initial results.

Attachment C: Functional connectivity atlas

The binary-coded component images of the final set (stable, spatially plausible and denoised) can be used for the formation of a data-driven bottom-up atlas of Functional Units. Such connectivity based methods for the parcellation of the cerebrum have already been applied earlier using functional Magnetic

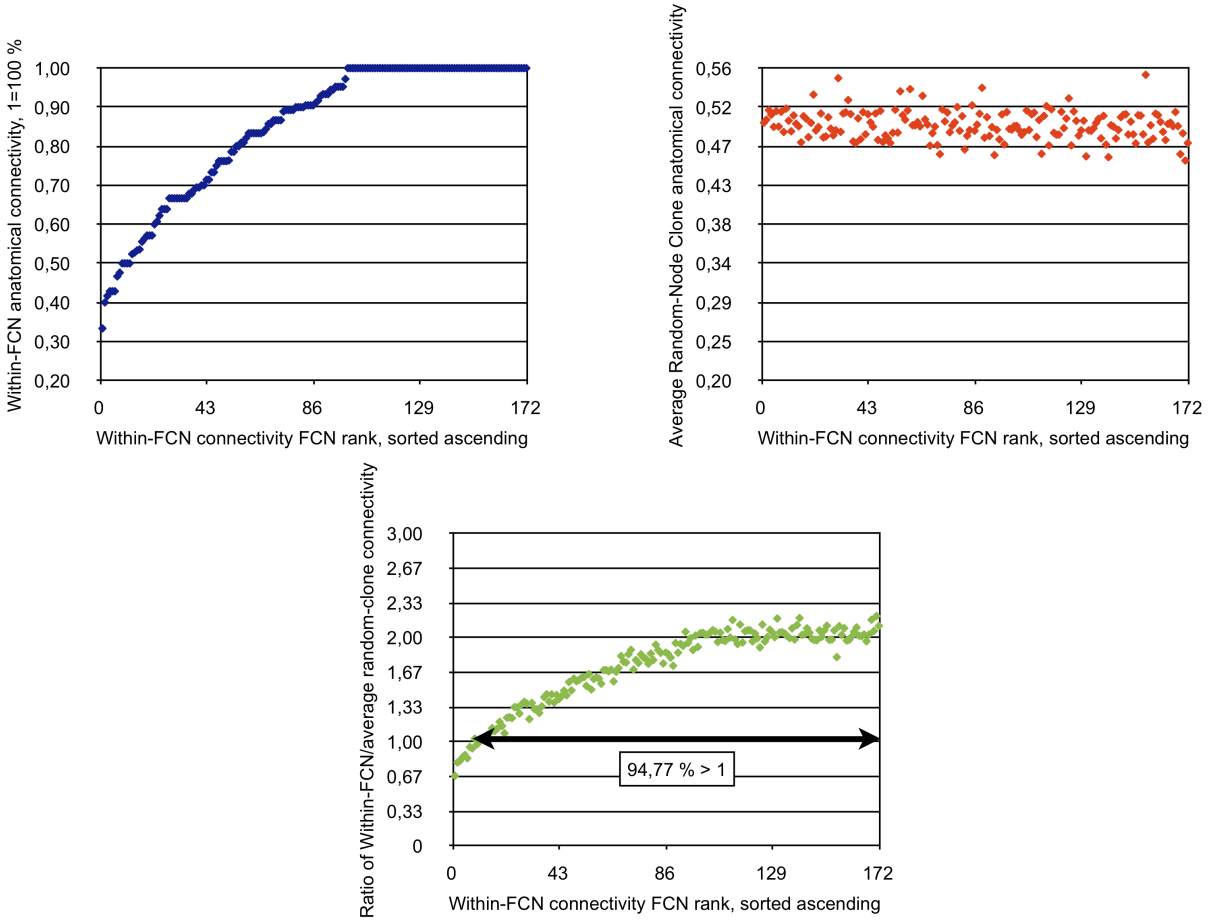

Figure 1. Results of Within-FCN anatomical connectivity. Top right, blue, y-axis 1=100 %, x-axis FCN rank, sorted ascending), corresponding average Outside-FCN anatomical connectivity of 172 corresponding clones with equal number of nodes (top right, red) and Ratio (middle right, green).

Resonance Imaging (fMRI) (Bartels and Zeki, 2005) or structural connectivity data (Perrin et al., 2008). Although a region of the brain might engage with a series of partner regions in multiple distinct functional networks, the adjacent group of voxels that always does this as a whole is logically the smallest functional building block. By adding up the binary-coded component images of the cluster centroids equalling the stereotype versions of all distinct functional networks (please see the detection of distinct networks section for details) the overlapping of networks automatically parcellates the brain into its natural subunits (see Figure 2). Only the stereotypes (cluster centroids) are added up in here in order to avoid that one network that can be found very often in the data is overly represented. This was achieved by parsing all IC images for the one with the maximum correlation with each cluster centroid (network stereotype) and thereby retrieving a set of 172 images that optimally represent the cluster centroids. In order to avoid strong fractioning of this atlas, with each addition-operation voxels belonging to a functional subunit with less than 6 voxels in total (and clusters of such subunits with less than 6 voxels) were removed from the atlas.

The final image containing all functional subunits derived from the 172 network stereotypes set contains more than 276 such subunits parcellating the brain into small macroscopic units (Figure 3). Sizes of Functional Units ranged from 15 to 1503 voxels (in a space defined by 53x63x46 voxels, 3x3x3 mm voxel size) and showed a markedly non-linear growth in the distribution of unit sizes (see Figure 4).

Naturally testing for the location of Functional Units reflects the general results for network membership of AAL regions. Although cortical regions still contain more Functional Units than subcortical regions (two-sample t-test, p=0.0068, Average Functional Units within subcortical regions: 9, Average Functional Units within cortical regions: 18.2821), Default-Brain Mode regions did not contain significantly more Functional Units than cortical non-DBM regions (two-sample t-test, p=0.4635, Average Functional Units within DBM regions: 19.6667, Average Functional Units within other cortical regions: 17.5143).

With respect to the distribution of Functional Units across the two hemispheres, strikingly on a purely numerical basis a higher number of Functional Units with exclusively left-dominant hemispheric localization can be observed, possibly indicating a relationship between the number of Functional Units and the

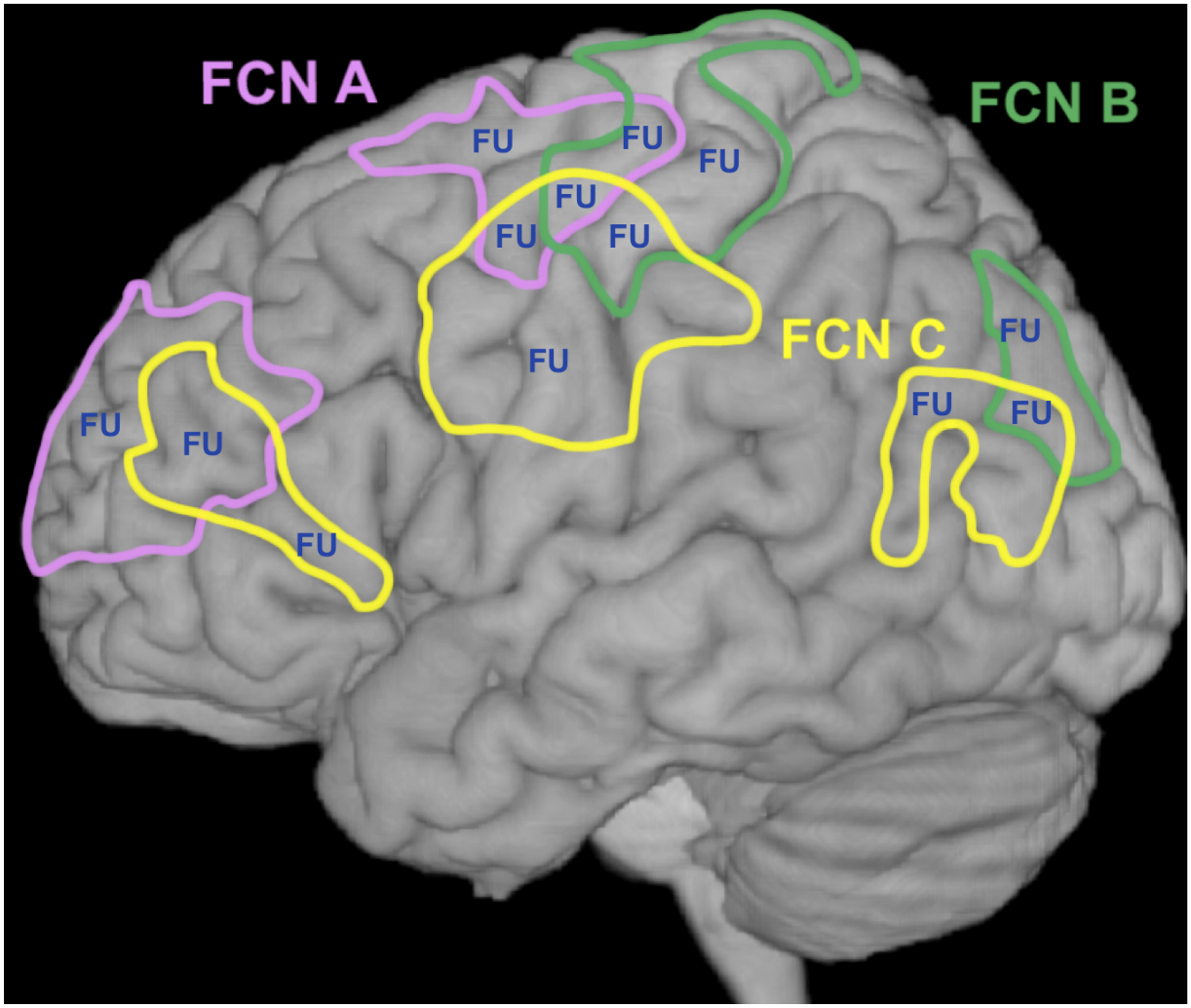

Figure 2. General principle. Functional Units (FU) are defined by spatial overlapping of FCNs, in this case 13 distinct FUs can be identified by analyzing the overlap of three FCNs (A,B and C)

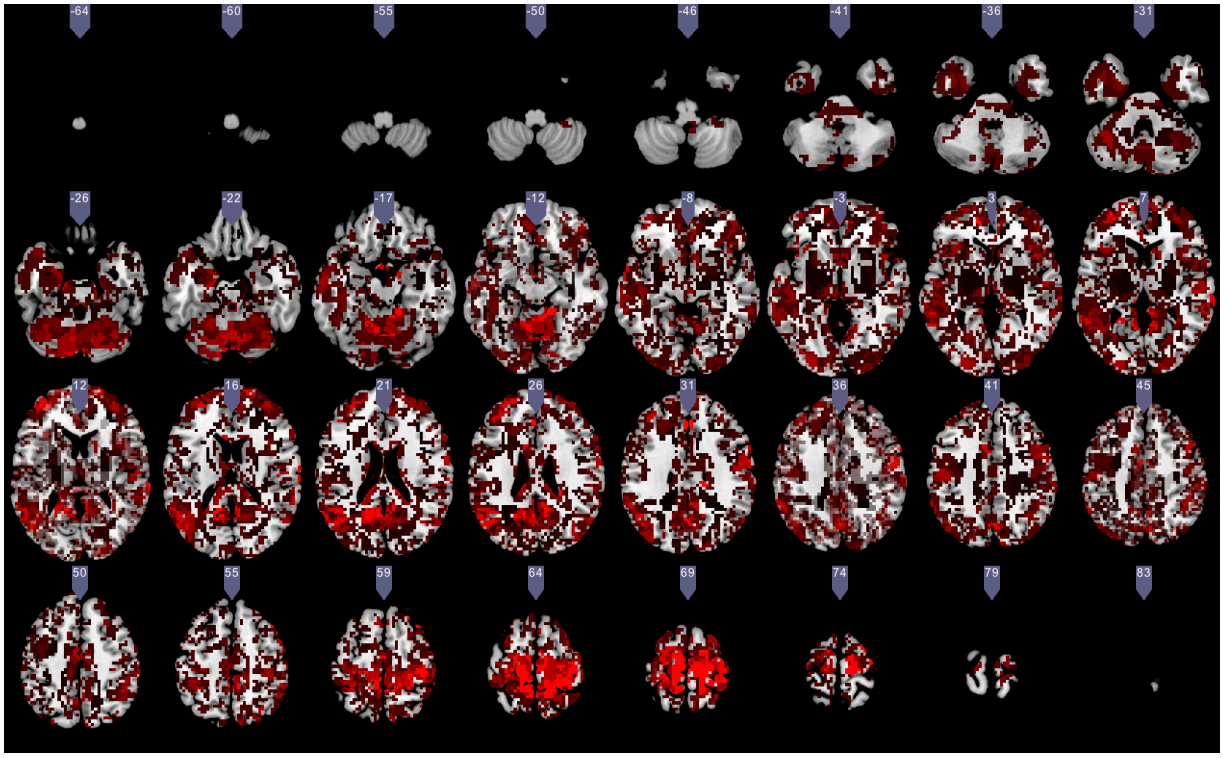

Figure 3. Exemplary atlas of Functional Units. Functional Units are based on the combination of 172 steoreotypical FCNs are represented by various shades of red overlayed onto a standard single subject brain using MicroGL, no interpolation is applied. Although the color spectrum resolution is not sufficient to display all subunits, the complex parcellation pattern in mainly GM is visible. As the FoV coverage of our experiments concentrated on the cerebrum no reliable parcellation of cerebellar areas could be obtained.

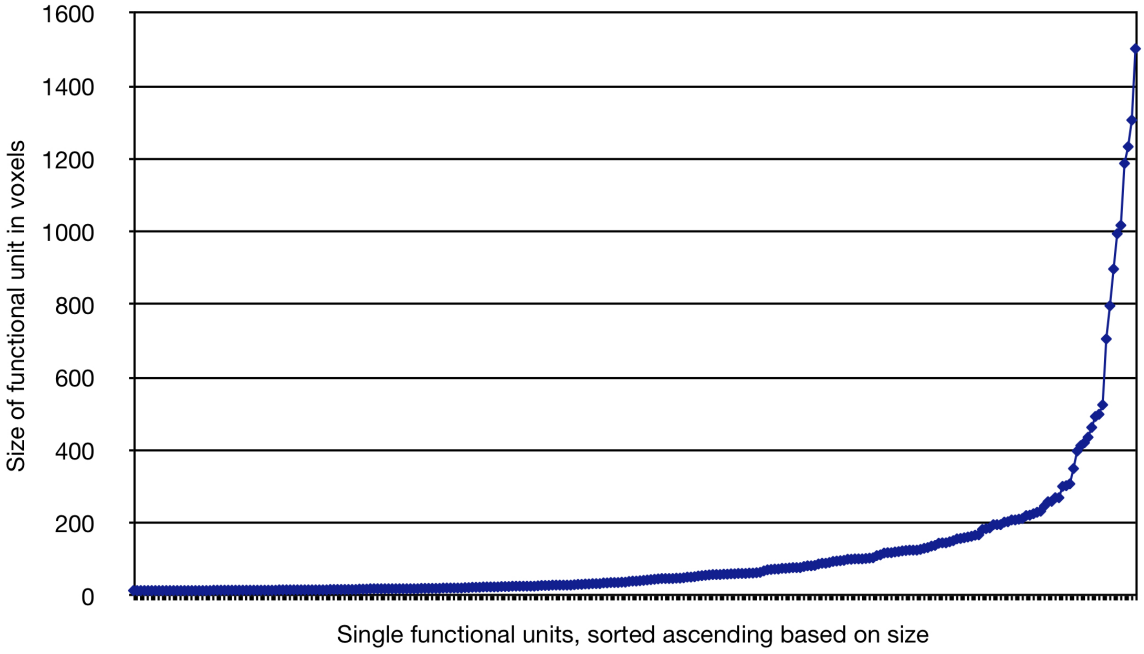

Figure 4. Size of each single Functional Unit in voxels, sorted ascending. Functional Units show a non-linear growth in size with a long-tail of small Functional Units consisting only of a few voxels and a few large Functional Units consisting of a large voxel mass.

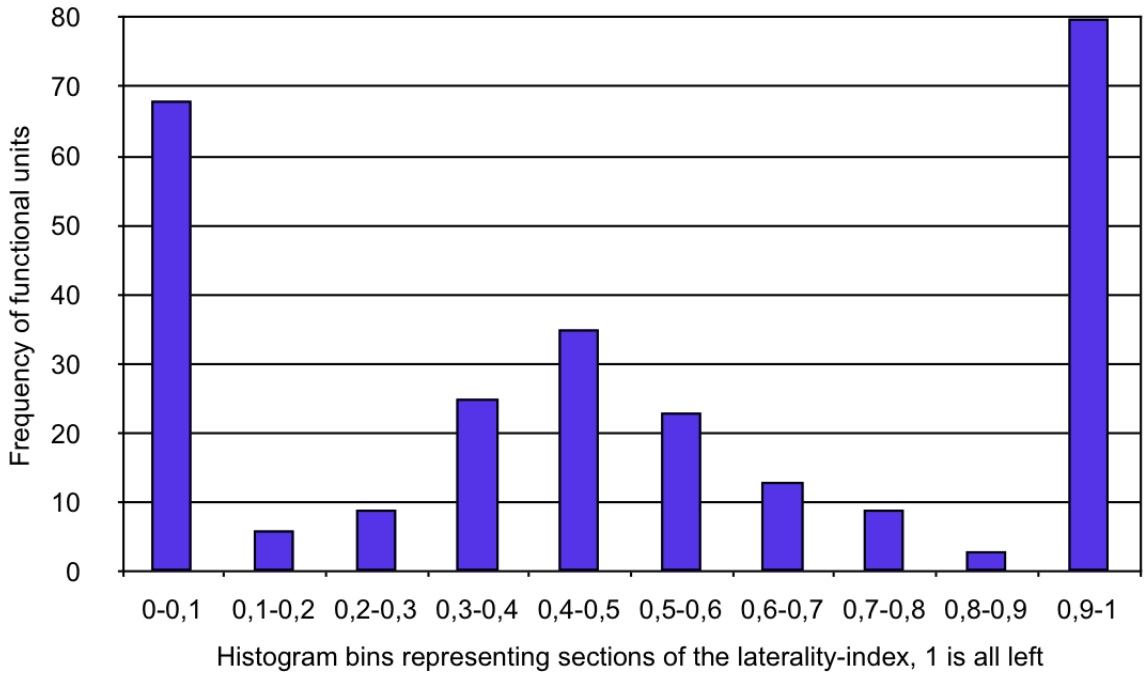

Figure 5. Histogram of the distribution of Functional Units across the two hemispheres. Y-axis is total count in bin, x-axis is left/right ratio. 0 indicates that all countable parts of a Functional Unit (the parts of it that lap into an AAL region) are located within the right hemisphere, 0.5 indicates that 50 % are located in the left and in the right hemisphere and 1 indicates that 100 % of the Functional Unit is located in the left hemisphere. A tendency towards midline and exclusively unilateral Functional Units can be observed with a stronger pronunciation of Functional Units in the left hemisphere.

dominant hemisphere (see Figure 5).

The atlas image with labelled subunits can be derived as online Supplementary Material. It will be the focus of future work, to unify structural and functional connectivity based parcellations of the cerebrum and to test the validity of this approach for the individual single subject level. This method can - in principle - be applied to a single subject brain as well (and far more accurately) in order to derive a functional parcellation of the individual brain - given that a sufficient number of distinct functional networks could be mapped for that individual and that the identified networks are meaningful networks of neural origin.

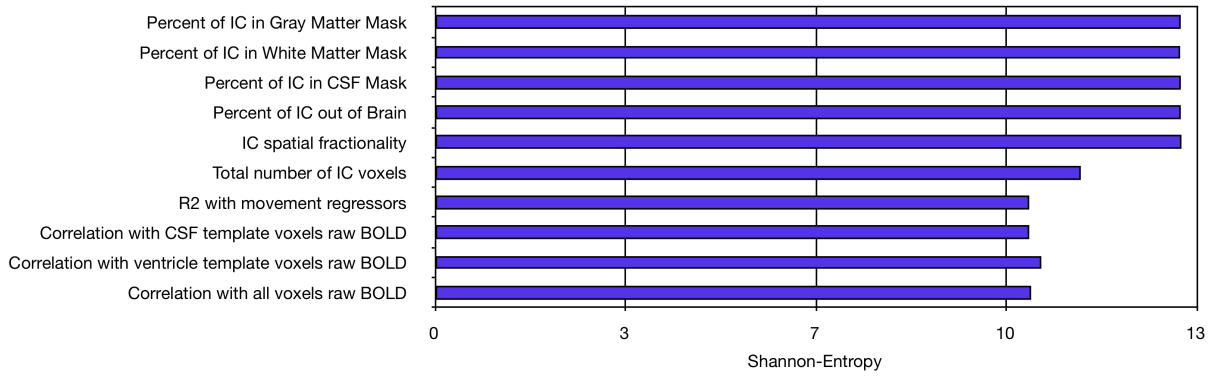

Figure 6. Shannon-Entropy of features used for denoising. The first 6 features that were used for the denoising step one, where spatial features were utilized for the sorting of ICs have a similar entropy level, while the features utilized for the second step of the denoising approach share another, slightly lower, Shannon-Entropy level.

Attachment D: Shannon-Entropy of IC fingerprint features

We estimated the Shannon-Entropy of each IC fingerprinting feature (features are described in Table 1) to assess each features information content. For this purpose we used a publicly available MATLAB implementation of Shannon-Entropy (David Fass, 2. November 2006, retrieved from MATLAB Central) and calculated the entropy value for each feature, based on the set of yet unfiltered 6858 stable components.

The rationale for this was that we wanted to estimate how similar in information content single features are which we wanted to use together in consecutive steps of our denoising approach. The results are displayed in Figure 6 and strengthen our rationale to utilize a stepwise approach for organizing the feature data with features on one comparable level of information content at a time.

Supplementary References

References

Bartels A, Zeki S. 2005. The chronoarchitecture of the cerebral cortex. Philosophical transactions of the Royal Society of London Series B, Biological sciences. 360:733–50.

Perrin M, Cointepas Y, Cachia A, Poupon C, Thirion B, Rivière D, Cathier P, El Kouby V, Constantinesco A, Le Bihan D, Mangin JF. 2008. Connectivity-Based Parcellation of the Cortical Mantle Using q-Ball Diffusion Imaging. International Journal of Biomedical Imaging. 2008:1–19.

Attachment Table 1

Included are all 172 network stereotypes with the AAL regions they contain and the number of manifestations (column Found), reflecting how often each of these networks is found in the data. The data is sorted according to the number of manifestations, so that the most prominent networks are on top.

														Found
Calcarine_L	Calcarine_R	Cuneus_L	Cuneus_R	Lingual_L	Lingual_R									156
Precuneus_L	Precuneus_R													151
Calcarine_L	Lingual_L	Lingual_R	Fusiform_L	Fusiform_R	Precuneus_L	Precuneus_R	Temporal_Inf_R							136
Frontal_Sup_L	Frontal_Sup_R	Frontal_Mid_L	Frontal_Mid_R	Supp_Motor_Area_L	Supp_Motor_Area_R	Frontal_Sup_Medial_L	Frontal_Sup_Medial_R							132
Calcarine_L	Calcarine_R	Lingual_L	Lingual_R	Occipital_Mid_L	Occipital_Mid_R	Occipital_Inf_L	Occipital_Inf_R							101
Precentral_L	Precentral_R	Frontal_Mid_L	Frontal_Mid_R	Frontal_Inf_Oper_L	Frontal_Inf_Oper_R	Frontal_Inf_Tri_L	Frontal_Inf_Tri_R	Frontal_Sup_Medial_L						83
Frontal_Sup_L	Frontal_Sup_Medial_L	Frontal_Sup_Medial_R	Frontal_Mid_Orb_L	Frontal_Mid_Orb_R	Cingulum_Ant_L	Cingulum_Ant_R								77
Rolandic_Oper_R	Temporal_Sup_L	Temporal_Sup_R	Temporal_Mid_L	Temporal_Mid_R										75
Cuneus_L	Cuneus_R	Occipital_Sup_L	Occipital_Sup_R	Occipital_Mid_L	Occipital_Mid_R	Precuneus_L	Precuneus_R							74
Frontal_Sup_L	Frontal_Sup_R	Frontal_Mid_L	Frontal_Mid_R	Frontal_Inf_Tri_L	Frontal_Inf_Tri_R									73
Calcarine_L	Calcarine_R	Cuneus_L	Cuneus_R	Lingual_L	Lingual_R	Occipital_Sup_L	Occipital_Sup_R	Occipital_Mid_L						73
Calcarine_L	Cuneus_L	Cuneus_R	Occipital_Sup_L	Occipital_Sup_R	Precuneus_L	Precuneus_R								72
Frontal_Sup_L	Frontal_Sup_R	Frontal_Mid_L	Frontal_Mid_R	Frontal_Sup_Medial_L	Frontal_Sup_Medial_R	Occipital_Mid_L	Occipital_Mid_R	Temporal_Mid_R						72
Precentral_R	Supp_Motor_Area_R	Postcentral_L	Postcentral_R	Parietal_Sup_L	Parietal_Sup_R	Precuneus_L	Precuneus_R	Paracentral_Lobule_L	Paracentral_Lobule_R					69
Hippocampus_L	Hippocampus_R	ParaHippocampal_L	ParaHippocampal_R	Lingual_L	Lingual_R	Temporal_Sup_L								69

														Found
Precentral_R	Supp_Motor_Area_R	Postcentral_L	Postcentral_R	Parietal_Sup_L	Parietal_Sup_R	Precuneus_L	Precuneus_R	Paracentral_Lobule_L	Paracentral_Lobule_R					69
Calcarine_L	Lingual_L	Lingual_R	Precuneus_L	Precuneus_R	Thalamus_L	Thalamus_R								68
Precentral_L	Postcentral_L	Parietal_Sup_L	Parietal_Inf_L											67
Occipital_Sup_L	Occipital_Sup_R	Occipital_Mid_L	Occipital_Mid_R	Occipital_Inf_L	Occipital_Inf_R	Fusiform_L	Fusiform_R	Parietal_Sup_L	Parietal_Sup_R	Temporal_Inf_R				67
Frontal_Sup_L	Frontal_Sup_R	Frontal_Mid_L	Frontal_Mid_R	Frontal_Sup_Medial_L	Frontal_Sup_Medial_R	Cingulum_Ant_L	Cingulum_Mid_L	Cingulum_Mid_R						67
Precentral_R	Rolandic_Oper_R	Postcentral_L	Postcentral_R											62
Rolandic_Oper_L	Rolandic_Oper_R	Insula_R	Postcentral_L	Postcentral_R	SupraMarginal_R	Temporal_Sup_L	Temporal_Sup_R							62
Cingulum_Mid_L	Cingulum_Mid_R	Precuneus_L	Precuneus_R											61
Frontal_Mid_L	Frontal_Sup_Medial_L	Frontal_Sup_Medial_R	Cingulum_Ant_L	Cingulum_Ant_R	Temporal_Sup_R									59
Parietal_Sup_L	Parietal_Sup_R	Precuneus_L	Precuneus_R											57
Precentral_L	Frontal_Sup_L	Frontal_Sup_R	Frontal_Mid_L	Frontal_Mid_R	Supp_Motor_Area_L	Supp_Motor_Area_R								52
Precentral_R	Frontal_Mid_R	Frontal_Inf_Oper_R	Frontal_Inf_Tri_R	Postcentral_R	Temporal_Sup_R									52
Precentral_L	Frontal_Mid_L	Frontal_Inf_Oper_L	Frontal_Inf_Tri_L	Occipital_Mid_L	Postcentral_L	Parietal_Inf_L								51
Rolandic_Oper_L	Rolandic_Oper_R	Insula_R	Temporal_Sup_L	Temporal_Sup_R										51
Precentral_R	Frontal_Sup_R	Frontal_Mid_R	Postcentral_R	Parietal_Sup_R	Parietal_Inf_R	SupraMarginal_R								50

														Found
Calcarine_L	Cuneus_L	Cuneus_R	Occipital_Sup_L	Occipital_Sup_R	Precuneus_L	Precuneus_R								48
Frontal_Sup_L	Frontal_Sup_R	Frontal_Mid_L	Frontal_Mid_R	Frontal_Sup_Medial_L	Frontal_Sup_Medial_R									47
Frontal_Inf_Orb_L	Insula_L	Insula_R	Temporal_Sup_L	Temporal_Sup_R	Temporal_Pole_Sup_L	Temporal_Pole_Sup_R								47
Angular_R	Precuneus_L	Precuneus_R	Temporal_Sup_R	Temporal_Mid_L	Temporal_Mid_R									45
Precentral_R	Postcentral_L	Postcentral_R	SupraMarginal_R											44
Frontal_Sup_L	Frontal_Sup_Medial_L	Frontal_Sup_Medial_R	Calcarine_L	Occipital_Mid_L	Angular_R	Precuneus_L	Precuneus_R	Temporal_Mid_R						44
Parietal_Inf_L	Parietal_Inf_R	SupraMarginal_L	SupraMarginal_R	Temporal_Sup_L										44
Cingulum_Ant_L	Hippocampus_L	Lingual_L	Lingual_R	Precuneus_L	Precuneus_R	Thalamus_L	Thalamus_R							44
Precentral_R	Frontal_Sup_R	Frontal_Mid_R	Frontal_Inf_Oper_R	Frontal_Inf_Tri_R	Frontal_Sup_Medial_R	Parietal_Sup_R	Parietal_Inf_R	Angular_R	Temporal_Mid_R					44
Caudate_L	Caudate_R	Thalamus_L	Thalamus_R											44
Parietal_Sup_L	Parietal_Sup_R	Precuneus_L	Precuneus_R											43
Precentral_L	Precentral_R	Frontal_Sup_L	Frontal_Sup_R	Supp_Motor_Area_L	Supp_Motor_Area_R									43
Precentral_R	Frontal_Sup_L	Frontal_Sup_R	Frontal_Mid_L	Frontal_Mid_R										43
Frontal_Sup_L	Frontal_Mid_L	Frontal_Sup_Medial_L	Occipital_Mid_L	Parietal_Inf_L	Parietal_Inf_R	Angular_L	Angular_R	Precuneus_L	Temporal_Mid_L					43

														Found
Rolandic_Oper_R	Supp_Motor_Area_L	Supp_Motor_Area_R	Insula_L	Insula_R	Cingulum_Mid_L	Cingulum_Mid_R	SupraMarginal_L	SupraMarginal_R						43
Cingulum_Post_L	Calcarine_L	Cuneus_L	Cuneus_R	Precuneus_L	Precuneus_R									42
Cingulum_Mid_R	Cuneus_L	Cuneus_R	Precuneus_L	Precuneus_R										42
Lingual_L	Lingual_R	Fusiform_R												41
Precentral_L	Frontal_Sup_L	Frontal_Mid_L	Postcentral_L	Parietal_Sup_L	Parietal_Inf_L									40
Parietal_Sup_L	Parietal_Sup_R	Precuneus_L	Precuneus_R											40
Calcarine_L	Calcarine_R	Lingual_L	Lingual_R	Precuneus_L	Precuneus_R									40
Frontal_Sup_L	Frontal_Sup_R	Frontal_Mid_L	Frontal_Mid_R	Frontal_Inf_Tri_L										40
Caudate_L	Caudate_R	Thalamus_L	Thalamus_R											38
Precentral_L	Precentral_R	Frontal_Sup_L	Frontal_Sup_R	Frontal_Mid_L	Frontal_Mid_R	Supp_Motor_Area_L	Supp_Motor_Area_R	Frontal_Sup_Medial_L						38
Frontal_Sup_Medial_L	Caudate_L	Caudate_R	Thalamus_L	Thalamus_R										38
Frontal_Mid_R	Occipital_Mid_R	Postcentral_R	Parietal_Sup_R	Parietal_Inf_L	Parietal_Inf_R	SupraMarginal_R	Angular_R	Precuneus_R	Temporal_Mid_R					38
Hippocampus_L	Hippocampus_R	ParaHippocampal_L	ParaHippocampal_R	Lingual_L	Lingual_R	Fusiform_L	Fusiform_R							37
Frontal_Inf_Orb_L	Olfactory_L	Frontal_Mid_Orb_L	Frontal_Mid_Orb_R	Cingulum_Ant_L	Cingulum_Ant_R	Caudate_L								37
Frontal_Inf_Orb_L	Frontal_Inf_Orb_R	Insula_L	Insula_R	Temporal_Sup_L	Temporal_Sup_R	Temporal_Pole_Sup_L	Temporal_Pole_Sup_R	Temporal_Mid_R						37

														Found
Frontal_Sup_L	Frontal_Sup_R	Frontal_Mid_L	Frontal_Mid_R	Frontal_Sup_Medial_L	Frontal_Sup_Medial_R									37
Precentral_L	Supp_Motor_Area_L	Supp_Motor_Area_R	Frontal_Sup_Medial_L	Cingulum_Mid_L	Cingulum_Mid_R									37
Insula_L	Insula_R	Temporal_Sup_L	Temporal_Sup_R											37
Frontal_Sup_L	Supp_Motor_Area_R	Frontal_Sup_Medial_L	Lingual_R	Precuneus_L	Precuneus_R	Temporal_Sup_R								36
Frontal_Sup_Medial_L	Cingulum_Post_L	Calcarine_L	Calcarine_R	Cuneus_L	Occipital_Mid_L	Precuneus_L	Precuneus_R							36
Occipital_Sup_L	Occipital_Sup_R	Occipital_Mid_L	Occipital_Mid_R	Parietal_Sup_L	Parietal_Sup_R	Temporal_Mid_R								35
Precentral_R	Supp_Motor_Area_R	Postcentral_R	Parietal_Sup_R	Parietal_Inf_R										35
Frontal_Sup_L	Frontal_Sup_R	Frontal_Mid_L	Frontal_Mid_R	Frontal_Inf_Tri_L										35
Frontal_Inf_Oper_L	Frontal_Inf_Tri_L	Frontal_Inf_Orb_L	Insula_L	Temporal_Sup_L	Temporal_Mid_L									35
Temporal_Sup_R	Temporal_Mid_L	Temporal_Mid_R												35
Frontal_Sup_R	Frontal_Mid_R	Parietal_Inf_R	SupraMarginal_R	Angular_L	Angular_R	Temporal_Mid_R								35
Precentral_R	Postcentral_R	Parietal_Sup_L	Parietal_Sup_R	Parietal_Inf_L	Parietal_Inf_R	SupraMarginal_R								34
Frontal_Inf_Orb_R	Calcarine_L	Lingual_R	Fusiform_L	Fusiform_R	Temporal_Mid_R	Temporal_Inf_R								34
Insula_L	Caudate_L	Caudate_R	Thalamus_L	Thalamus_R	Temporal_Sup_L									34
Insula_L	Caudate_R	Putamen_L	Putamen_R	Thalamus_L	Thalamus_R									33

														Found
Insula_L	Caudate_L	Caudate_R	Putamen_L	Putamen_R	Thalamus_L	Thalamus_R								33
Caudate_L	Caudate_R	Putamen_L												33
Frontal_Sup_L	Frontal_Mid_L	Parietal_Sup_L	Parietal_Inf_L	Angular_L	Precuneus_L									32
Cuneus_R	Parietal_Sup_L	Parietal_Sup_R	Precuneus_L	Precuneus_R										32
Precentral_R	Supp_Motor_Area_L	Supp_Motor_Area_R	Postcentral_L	Postcentral_R	Parietal_Sup_R	Precuneus_L	Precuneus_R	Paracentral_Lobule_L	Paracentral_Lobule_R					32
Insula_L	Insula_R	ParaHippocampal_R	Temporal_Sup_L	Temporal_Sup_R	Temporal_Pole_Sup_L	Temporal_Pole_Sup_R								31
Insula_L	Insula_R	Lingual_R	Temporal_Sup_L	Temporal_Sup_R	Temporal_Pole_Sup_L	Temporal_Mid_L								31
Calcarine_L	Calcarine_R	Lingual_L	Lingual_R	Occipital_Sup_L	Occipital_Mid_L	Occipital_Inf_L								30
Calcarine_L	Lingual_L	Lingual_R	Fusiform_L	Fusiform_R										29
ParaHippocampal_R	Lingual_L	Lingual_R	Caudate_L	Thalamus_R										29
Cingulum_Mid_L	Cingulum_Mid_R	Precuneus_L	Precuneus_R											28
Precentral_L	Precentral_R	Postcentral_L	Postcentral_R	Parietal_Inf_L										28
Calcarine_L	Calcarine_R	Cuneus_R	Occipital_Sup_L	Occipital_Sup_R	Occipital_Mid_L	Occipital_Mid_R								28
Frontal_Sup_R	Frontal_Mid_R	Occipital_Mid_R	Parietal_Sup_R	Parietal_Inf_R	Angular_R	Precuneus_R	Temporal_Mid_R							28
Caudate_L	Caudate_R	Thalamus_L	Thalamus_R											27

														Found
Frontal_Mid_L	Frontal_Inf_Oper_L	Frontal_Inf_Tri_L	Frontal_Inf_Orb_L	Supp_Motor_Area_L	Frontal_Sup_Medial_L	Insula_L	Temporal_Mid_L							27
Frontal_Sup_L	Frontal_Mid_L	Calcarine_L	Precuneus_L	Precuneus_R	Temporal_Sup_L	Temporal_Sup_R								27
Caudate_L	Caudate_R	Thalamus_L	Thalamus_R											27
ParaHippocampal_L	ParaHippocampal_R	Temporal_Pole_Sup_L	Temporal_Pole_Sup_R											26
Precentral_L	Precentral_R	Supp_Motor_Area_L	Supp_Motor_Area_R	Postcentral_L	Postcentral_R	Parietal_Sup_L	Parietal_Sup_R	Precuneus_L	Precuneus_R	Paracentral_Lobule_L	Paracentral_Lobule_R			26
Rolandic_Oper_L	Rolandic_Oper_R	Insula_L	Insula_R	Cingulum_Mid_L	Cingulum_Mid_R	SupraMarginal_R	Temporal_Sup_L	Temporal_Sup_R						26
Frontal_Inf_Orb_L	Frontal_Mid_Orb_L	Frontal_Mid_Orb_R	Cingulum_Ant_L	Cingulum_Ant_R	Caudate_L									25
SupraMarginal_R	Angular_R	Precuneus_L	Precuneus_R	Temporal_Sup_R	Temporal_Mid_L	Temporal_Mid_R								25
Cuneus_L	Cuneus_R	Occipital_Sup_L	Occipital_Sup_R	Occipital_Mid_L	Occipital_Mid_R									24
Frontal_Sup_L	Frontal_Sup_R	Frontal_Mid_L	Frontal_Mid_R	Frontal_Sup_Medial_L	Frontal_Sup_Medial_R									24
Hippocampus_L	Hippocampus_R	ParaHippocampal_R	Lingual_L	Lingual_R	Fusiform_R	Precuneus_R	Thalamus_L	Thalamus_R						24
Frontal_Sup_R	Frontal_Mid_L	Frontal_Mid_R	Calcarine_L	Occipital_Mid_L	Occipital_Mid_R	Precuneus_L	Precuneus_R	Temporal_Mid_R						24
Caudate_L	Caudate_R	Thalamus_L	Thalamus_R											24
Cingulum_Post_L	Cingulum_Post_R	Calcarine_L	Lingual_L	Lingual_R	Precuneus_L	Precuneus_R	Thalamus_L	Thalamus_R						24
Occipital_Mid_L	Temporal_Sup_L	Temporal_Mid_L	Temporal_Mid_R											23

														Found
Frontal_Sup_L	Frontal_Sup_R	Frontal_Mid_L	Frontal_Mid_R											22
Temporal_Sup_R	Temporal_Mid_L	Temporal_Mid_R												22
Calcarine_L	Calcarine_R	Lingual_L	Lingual_R	Occipital_Sup_L	Occipital_Mid_L	Occipital_Mid_R	Occipital_Inf_L	Occipital_Inf_R	Temporal_Mid_R					22
Occipital_Sup_L	Occipital_Mid_L	Parietal_Sup_L	Parietal_Inf_L	Angular_L	Precuneus_L									21
Frontal_Sup_L	Frontal_Sup_R	Frontal_Mid_L	Frontal_Mid_R	Supp_Motor_Area_L	Supp_Motor_Area_R	Frontal_Sup_Medial_L	Frontal_Sup_Medial_R							21
Precentral_L	Frontal_Mid_L	Frontal_Inf_Tri_L	Occipital_Mid_L	Parietal_Sup_L	Parietal_Inf_L	Precuneus_L								21
Frontal_Sup_L	Frontal_Sup_R	Frontal_Mid_L	Frontal_Mid_R	Frontal_Sup_Medial_L	Frontal_Sup_Medial_R	Cingulum_Ant_L								21
Parietal_Sup_L	Parietal_Sup_R	Precuneus_L	Precuneus_R											20
Frontal_Sup_L	Frontal_Sup_R	Frontal_Mid_L	Frontal_Mid_R	Frontal_Mid_Orb_L	Frontal_Inf_Tri_L									20
Frontal_Mid_L	Calcarine_L	Cuneus_L	Occipital_Sup_L	Occipital_Mid_L	Occipital_Mid_R	Parietal_Inf_L	SupraMarginal_R	Precuneus_L	Precuneus_R					20
Frontal_Mid_L	Occipital_Sup_L	Occipital_Mid_L	Occipital_Mid_R	Precuneus_L	Precuneus_R	Temporal_Mid_R								20
Precentral_R	Supp_Motor_Area_L	Supp_Motor_Area_R	Cingulum_Mid_L	Cingulum_Mid_R	SupraMarginal_R	Temporal_Sup_L	Temporal_Sup_R							19
Precuneus_L	Precuneus_R	Temporal_Sup_R	Temporal_Mid_L	Temporal_Mid_R										17
Frontal_Sup_L	Frontal_Sup_Orb_L	Frontal_Mid_L	Frontal_Sup_Medial_L	Frontal_Sup_Medial_R	Frontal_Mid_Orb_L	Frontal_Mid_Orb_R	Cingulum_Ant_L							17
Frontal_Sup_L	Frontal_Mid_L	Frontal_Mid_R	Frontal_Inf_Tri_L	Frontal_Sup_Medial_L	Precuneus_L									17

														Found
Precentral_L	Precentral_R	Postcentral_L	Postcentral_R	Parietal_Sup_L	Parietal_Sup_R	Precuneus_L	Precuneus_R	Paracentral_Lobule_L	Paracentral_Lobule_R					17
Precentral_R	Frontal_Sup_R	Frontal_Mid_R	Postcentral_R	Parietal_Sup_R	Parietal_Inf_R	SupraMarginal_R								17
Precentral_L	Precentral_R	Supp_Motor_Area_L	Supp_Motor_Area_R	Cingulum_Mid_L	Cingulum_Mid_R	Postcentral_L	Postcentral_R	Parietal_Sup_L	Parietal_Sup_R	Precuneus_L	Precuneus_R	Paracentral_Lobule_L	Paracentral_Lobule_R	17
Caudate_L	Caudate_R	Thalamus_L	Thalamus_R											16
Frontal_Sup_L	Frontal_Sup_R	Frontal_Mid_L	Frontal_Mid_R	Frontal_Sup_Medial_L	Frontal_Sup_Medial_R	Cingulum_Ant_L	Cingulum_Ant_R	Caudate_L	Caudate_R					16
Precentral_L	Frontal_Sup_L	Frontal_Sup_R	Frontal_Mid_L	Frontal_Mid_R	Supp_Motor_Area_L	Supp_Motor_Area_R	Frontal_Sup_Medial_L	Frontal_Sup_Medial_R						16
Precentral_L	Precentral_R	Frontal_Mid_R	Occipital_Mid_R	Postcentral_R	SupraMarginal_R	Temporal_Sup_R	Temporal_Mid_L	Temporal_Mid_R						16
Insula_L	Insula_R	ParaHippocampal_R	Lingual_L	Lingual_R	Thalamus_L	Thalamus_R	Temporal_Sup_L	Temporal_Pole_Sup_L						16
Frontal_Sup_R	Frontal_Mid_R	Occipital_Mid_R	Parietal_Sup_R	Parietal_Inf_R	Angular_R	Temporal_Mid_R								15
Postcentral_R	Parietal_Inf_L	Parietal_Inf_R	SupraMarginal_L	SupraMarginal_R										15
Occipital_Mid_L	SupraMarginal_R	Angular_R	Precuneus_L	Precuneus_R	Temporal_Sup_R	Temporal_Mid_L	Temporal_Mid_R							15
Frontal_Mid_R	Frontal_Inf_Tri_L	Frontal_Inf_Tri_R	Occipital_Mid_R	Postcentral_R	SupraMarginal_R	Temporal_Sup_R	Temporal_Mid_L	Temporal_Mid_R						15
Calcarine_L	Calcarine_R	Lingual_L	Lingual_R	Precuneus_L	Precuneus_R									15
Cingulum_Mid_R	Cingulum_Post_L	Cuneus_L	Cuneus_R	Precuneus_L	Precuneus_R									14
Precentral_L	Frontal_Mid_L	Frontal_Mid_R	Frontal_Inf_Tri_L	Frontal_Inf_Tri_R	Occipital_Mid_L	Postcentral_L	SupraMarginal_L	Temporal_Sup_R	Temporal_Mid_L	Temporal_Mid_R				14

														Found
Frontal_Sup_L	Frontal_Mid_L	Frontal_Mid_R	Frontal_Inf_Tri_L	Rolandic_Oper_L	Rolandic_Oper_R	Frontal_Sup_Medial_L	Insula_R	Cingulum_Ant_L	Caudate_L	Caudate_R				14
Occipital_Mid_L	SupraMarginal_L	Angular_L	Temporal_Sup_L	Temporal_Mid_L	Temporal_Mid_R									14
Frontal_Inf_Orb_L	Occipital_Mid_L	Occipital_Inf_L	Fusiform_L	Temporal_Sup_L	Temporal_Pole_Sup_L	Temporal_Mid_L	Temporal_Inf_L							14
Frontal_Sup_L	Frontal_Sup_R	Frontal_Sup_Medial_L	Frontal_Sup_Medial_R	Frontal_Mid_Orb_L	Cingulum_Ant_L	Cingulum_Ant_R								14
ParaHippocampal_L	ParaHippocampal_R	Fusiform_L	Temporal_Pole_Sup_L	Temporal_Pole_Sup_R	Temporal_Mid_L	Temporal_Pole_Mid_L	Temporal_Inf_L							14
Precentral_L	Precentral_R	Supp_Motor_Area_L	Supp_Motor_Area_R	Postcentral_L	Postcentral_R	Parietal_Sup_L	Parietal_Sup_R	Precuneus_L	Precuneus_R	Paracentral_Lobule_L	Paracentral_Lobule_R			13
Frontal_Sup_Medial_L	Cingulum_Ant_L	Cingulum_Ant_R	Cingulum_Mid_L	Cingulum_Mid_R	Cingulum_Post_L									13
Insula_L	ParaHippocampal_L	ParaHippocampal_R	Lingual_L	Lingual_R	Caudate_L	Temporal_Pole_Sup_L	Temporal_Pole_Sup_R							13
Precentral_L	Precentral_R	Postcentral_L	Postcentral_R	Parietal_Sup_L	Parietal_Sup_R	Parietal_Inf_L								13
Frontal_Mid_R	Frontal_Inf_Tri_L	Frontal_Inf_Tri_R	Frontal_Inf_Orb_R	Rolandic_Oper_R	Insula_R	Occipital_Mid_L	Temporal_Sup_R	Temporal_Pole_Sup_R	Temporal_Mid_R					13
ParaHippocampal_R	Lingual_L	Lingual_R	Fusiform_R											13
Precuneus_R	Temporal_Sup_R	Temporal_Mid_L	Temporal_Mid_R											12
Frontal_Sup_L	Frontal_Sup_R	Frontal_Mid_L	Frontal_Mid_R	Frontal_Inf_Oper_R	Frontal_Inf_Tri_L	Frontal_Inf_Tri_R	Frontal_Sup_Medial_L	Frontal_Sup_Medial_R						12

														Found
Occipital_Mid_L	Occipital_Inf_L	Temporal_Mid_L												12
Occipital_Mid_L	Angular_L	Temporal_Mid_L												12
Lingual_L	Lingual_R	Fusiform_L	Caudate_L	Thalamus_L	Thalamus_R									12
Calcarine_L	Calcarine_R	Cuneus_R	Lingual_L	Lingual_R	Occipital_Sup_L	Occipital_Sup_R	Occipital_Mid_L	Occipital_Mid_R	Occipital_Inf_L					11
Precentral_L	Frontal_Mid_L	Frontal_Mid_R	Supp_Motor_Area_L	Frontal_Sup_Medial_L	Cingulum_Mid_L	Cingulum_Mid_R								11
Frontal_Sup_L	Frontal_Sup_R	Frontal_Mid_L	Frontal_Mid_R	Frontal_Inf_Tri_L	Frontal_Sup_Medial_L	Frontal_Sup_Medial_R	Caudate_L	Temporal_Sup_R						11
Frontal_Sup_Medial_L	Frontal_Sup_Medial_R	Calcarine_L	Lingual_R	Occipital_Mid_L	Precuneus_L	Precuneus_R	Temporal_Mid_R							11
Precentral_L	Precentral_R	Rolandic_Oper_R	Postcentral_L	Postcentral_R	SupraMarginal_R	Temporal_Sup_R								10
Calcarine_L	Cuneus_L	Occipital_Mid_L	Precuneus_L	Precuneus_R										10
Calcarine_L	Cuneus_L	Lingual_L	Lingual_R	Precuneus_L	Precuneus_R									10
Frontal_Sup_R	Frontal_Mid_L	Frontal_Mid_R	Frontal_Inf_Tri_L	Frontal_Inf_Tri_R	Frontal_Inf_Orb_R									10
Frontal_Inf_Orb_L	ParaHippocampal_L	ParaHippocampal_R	Lingual_L	Lingual_R	Fusiform_L	Temporal_Pole_Sup_L								10
Precentral_L	Precentral_R	Postcentral_L	Postcentral_R	Parietal_Inf_L										9
Precentral_L	Precentral_R	Supp_Motor_Area_R	Postcentral_L	Postcentral_R	Parietal_Sup_L	Parietal_Sup_R	Precuneus_L	Precuneus_R	Paracentral_Lobule_L	Paracentral_Lobule_R				9
Frontal_Sup_L	Frontal_Mid_L	Frontal_Mid_R	Frontal_Sup_Medial_L											9

														Found
Calcarine_L	Lingual_R	Caudate_L	Caudate_R	Thalamus_L	Thalamus_R									9
Precentral_L	Precentral_R	Supp_Motor_Area_L	Supp_Motor_Area_R	Postcentral_L	Postcentral_R	Parietal_Sup_L	Parietal_Sup_R	Precuneus_L	Precuneus_R	Paracentral_Lobule_L	Paracentral_Lobule_R			9
Occipital_Mid_L	Temporal_Mid_L	Temporal_Mid_R												8
Frontal_Sup_Medial_L	Cingulum_Mid_L	Cingulum_Mid_R	Calcarine_L	Lingual_R	Precuneus_L	Precuneus_R								8
Frontal_Sup_Medial_L	Insula_L	Insula_R	Calcarine_L	Lingual_L	Lingual_R	Precuneus_R	Thalamus_R	Temporal_Sup_L	Temporal_Sup_R					8
Precentral_R	Frontal_Sup_L	Frontal_Sup_Medial_L	Lingual_R	Angular_R	Caudate_L	Caudate_R	Temporal_Sup_L							8
Precentral_L	Precentral_R	Frontal_Sup_L	Frontal_Sup_R	Frontal_Mid_L	Frontal_Mid_R	Postcentral_R	Parietal_Sup_R	Parietal_Inf_R	Angular_R	Precuneus_L				7
Insula_L	Insula_R	Temporal_Sup_L	Temporal_Sup_R	Temporal_Pole_Sup_L	Temporal_Pole_Sup_R									6
Frontal_Mid_L	Supp_Motor_Area_L	Frontal_Sup_Medial_L	Calcarine_L	Precuneus_R	Temporal_Sup_R	Temporal_Mid_R	Temporal_Inf_R							5
Precentral_L	Frontal_Sup_L	Frontal_Mid_L	Frontal_Mid_R	Frontal_Inf_Tri_L	Frontal_Inf_Orb_L	Temporal_Mid_R								4

7.3 Chapter 3 - Functional Connectivity Network alterations as an effect of stroke rehabilitation

Resting state functional connectivity changes predict movement recovery due to robot assisted BCI training in stroke patients

Author list and affiliations:

Bálint Várkuti[1,2,3]

Cuntai Guan[3]

Yaozhang Pan [3]

Kok Soon Phua [3]

Kai Keng Ang [3]

Christopher Wee Keong Kuah [4]

Karen Chua[4]

Beng Ti Ang[5]

Niels Birbaumer[1]

Sitaram Ranganathan[1,6]

1 Institute of Medical Psychology and Behavioral Neurobiology, University of Tübingen, Gartenstr. 29, 72074 Tübingen, Germany

2 Graduate Training Centre of Neuroscience, International Max Planck Research School, University of Tübingen, Österbergstr. 3, 72074 Tübingen, Germany

3 Institute for Infocomm Research, 1 Fusionopolis Way, #21-01 Connexis (South Tower), 138632 Singapore

4 Department of Rehabilitation Medicine, Tan Tock Seng Hospital, TTSH rehabilitation centre, 17 Ang Mo Kio Ave 9, 569766, Singapore.

5 National Neuroscience Institute, 11 Jalan Tan Tock Seng, 308433, Singapore

6 Sri Chitra Tirunal Institute of Medical Sciences and Technology, Thiruvananthapuram, 695 011, Kerala, India

Abstract

Background and Purpose—

We compared the effectiveness of standard robotic rehabilitation (MANUS) and a robotic rehabilitation paradigm involving Electroencephalography-based Brain Computer Interfaces and Motor Imagery (MI EEG-BCI) in a large population of stroke survivors. In order to assess changes in brain function due to the rehabilitation we conducted a resting state functional Magnetic Resonance Imaging (rs-fMRI) study with a subgroup of participants before and after the training.

Methods—

A total of 9 adults with upper extremity paresis were trained over a 4 week period with a MANUS (3) and a MI EEG-BCI (6) robotic rehabilitation paradigm. Pretraining and posttraining, rs-fMRI measurements and upper extremity assessments using Fugl-Meyer upper extremity Test (FM) were conducted for each participant. Functional connectivity networks of the motor system were identified using an Independent Component Analysis approach.

Results—

The individual gain in upper extremity function (FM) over a 12 week period could be predicted from pre-post functional connectivity changes (FCC). FCC of the Supplementary Motor Area, the contra- and ipsilesional Motor Cortex and parts of the Visuospatial System with regions in the Superior Medial Gyrus, Anterior Cingulate Cortex, Superior and Middle Temporal Gyrus, Inferior Parietal Lobe, Precuneus, Middle Orbital Gyrus and Cerebellum predicted individual upper extremity function improvement.

Conclusions—

Certain FCC predict the steepness of individual recovery in our sample. Following these lines, future training and rehabilitation methods might therefore focuss on inducing beneficial increases in functional connectivity such as those observed in this study through means of direct connectivity-neurofeedback. Exploratory treatment group comparison indicates that MI is a potential fascilitator of such beneficial neuroplasticity.

Key words:

rehabilitation, stroke, brain imaging, hemiparesis, neuroplasticity

1. Introduction

Stroke is known to be one of the leading causes of death and impairment in the industrialized world [1] – leaving not only the stroke survivors themselves severely affected, but impacting as well their families and work environment. [2-3]

Thus it is essential to identify the factors that contribute to optimal post-stroke motor recovery and to develop new methods that target beneficial effects on brain plasticity.

Electroencephalography-based Brain Computer Interfaces (EEG-BCIs) – particularly with paradigms including motor imagery (MI) - have recently been proposed as potentially successful therapeutic interventions.[4-5] Such approaches target the integrity and connectivity of the brain systems involved in the successfull execution of a movement that have been severed by the stroke.[6]

Instead of allowing the patient to use compensatory movement strategies to complete a given movement task, patients using EEG-BCIs volitionally generate patterns of brain activity that are detected by the BCI and translated into movement of the paretic limb by external effectors, thereby bridging the disconnection between intention to move and execution.

Hereby neural processes are stimulated that are intended to recombine the willfull intention of the patient to move a paretic limb and the perceived afferent sensory input. That sensory input is generated by a robot orthosis moving that limb. The reconnection of the severed parts of the motor system is to take place by learning processes induced by a combination of operant (the translation of the patients intention into a movement is a reward) and classical conditioning (the coincidence of volition and relevant afference). Thus the rationale behind such a BCI training is to restore neural cooperation within the motor system by means of conditioning the neuronal ensembles back into a functioning motor network and to generally stimulate adaptive processes.

In order to assure a close temporal association of the intention to move and the movement executed by a robot, EEG-BCI systems such as those utilized in this study adapt a two stage strategy.[7-8] In the first step the system is calibrated by asking the patient to imagine the movement and by saving the associated patterns of activation. In a second step – the actual

training – a patient imagines the movement of the paretic limb, the pattern of activation is recognized and the movement is instantly executed by the robot.

Although such systems are beginning to be used in clinical and research contexts, comprehensive evidence for their effectivity and a deeper understanding for their mechanisms of action remains low.

Using resting state functional Magnetic Resonance Imaging (rs-fMRI) we can identify connectivity traits of the individual brain, which are potentially related to neural cooperation at rest.[9] This is possible by analyzing the activity, spatial extent and integrity of common functional connectivity networks, such as the Default Brain Mode Network [10] or the sensorymotor network. Although there is still a lot of discussion about the nature of rs-fMRI functional connectivity, [11-13] in the light of recently published studies on the association of rs-networks with stages of brain maturation, [14] cognitive functioning [15] and dementia, [11] it promises to become a significant clinical diagnostic tool. Furthemrmore, it has been shown that major reorganizational processes occur in the brain during post-stroke motor recovery[16], which are reflected in rs-fMRI functional connectivity[17].

Following this notion, in the framework of a larger clinical study[7] investigating the effects of MI-BCI for upper limb robotic rehabilitation compared to standard robotic rehabilitation, two subgroups of participants (6:3) were measured before and after training with a MI-BCI and standard robotic rehabilitation respectively, using rs-fMRI.

By using Independent Component Analysis (ICA) for the rs-fMRI data analysis the common rs-networks could be identified in the data from both the before- and after-training scanning sessions of each participant. By substracting the functional connectivity (FC) maps, derived from the data collected before and after the training respectively, in a second step these individual FC changes (FCC) were used to predict motor recovery over and beyond the training period.

For the purpose of associating the FCC maps with the behavioral changes, we projected a slope through the data points of the measured functional motor outcome (Fugl-Meyer scores) and derived a gain steepness value for each participant, representing the magnitude of gain - irrespective of initial motor function level - over an identical timeperiod. Then finally we performed FCC map voxel-wise linear regression on the individual functional gain steepness values while incorporating a leave-one-out cross-validation, using the FCC maps of four motor system related FC networks. The results are discussed with respect to the potential

effect of MI-BCI motor rehabilitations and future approaches for FC enhancing real-time fMRI trainings.

2. Methods

2.1 Sample Group

Participants were included into the study if they met the following criteria: first ever ischaemic or haemorhagic stroke diagnosed by CT or MRI brain imaging within 6 hours of ictus who were more than 1 month post stroke onset, aged between 21 to 65 years, with a Fugly-Meyer Motor Assessment score of the affected upper limb from 0-45 at the Screening Evaluation. Abbreviated Mental Test score had to be >6/10, participants had to have the ability to maintain attention and sit supportedly for 1 hour continuously. In addition, resting brain states were detected during BCI screening using EEG based MI and successful subjects required at least 80% accuracy for participation.

Orthoslice views of each participants' T1 image (centered on the main lesion location, normalized and intensity corrected using the Voxel Based Morphometry 8 Toolbox) can be found in Supplementary Figure 1.

Exclusion criteria were severe aphasia, cognitive or behavioural impairment or uncontrolled psychiatric conditions like depression, medical instability including postural hypotension, unresolved sepsis, epilepsy, end stage renal failure and terminal illness, hemispatial neglect detected using the line bisection test or severe visual impairment despite visual orthotics, cranial defects or neurosurgical procedures. In addition, subjects were excluded if they had the following local arm factors such as upper limb spasticity with Modified Ashworth scale: >2 in any shoulder, elbow or wrist or finger region, shoulder pain with visual analogue scale >4/10, fixed joint contractures, impaired skin integrity or infections which could potentially be worsened by robotic shell or prolonged EEG cap usage.

From the initially scanned 11 participants (participant details are provided in Table 1) two had to be excluded due to failure to comply with the protocol (one participant was sleeping most of the time) and a significantly deviating lesion severity and location (massive cortical involvement), leaving 9 participants that were included in the analysis (3 in the MANUS group, 6 in the MI-BCI group). The study was approved by the local ethics committee. Stroke location in the sample encompassed mainly subcortical sites around the basal ganglia, with minimal thalamic involvement.

2.2 Training details for standard robotic rehabilitation (MANUS) and MI-BCI groups

Studies have shown that movement therapy delivered from robots can be effective for stroke rehabilitation.[18] Further, recent advances in machine learning and signal processing have enabled the use of EEG-based MI-BCI for neurorehabilitation. In this study, stroke patients were divided into two groups for different rehabilitation protocols. One group of patients carried out the clinically proven MANUS robotic rehabilitation.[19] Another group (MI-BCI group) of patients used a rehabilitation protocol exploiting synergy effects from the combination of an EEG-based MI-BCI with a MANUS robot.[7-8]

Stroke patients in the MANUS-only group used the MANUS robot for upper limb rehabilitation. During the training, the patient was required to move the impaired limb towards the goal displayed on the video screen in form of a video game, with their impaired limb being strapped to the robot end-effector.[19]

If a member of the MANUS group could not perform the motor task according to the recommended MANUS protocol due to weakness in their stroke-affected limb, the robot assisted to move the member's limb after a pre-defined period of 2 seconds after the onset of the visual cue. If a member could perform the motor task, the robot did not assist the training movements for the member of the MANUS group.[20] Patients in the MANUS-only group were not instructed to imagine movements.

In the MI-BCI group, the MANUS robot was coupled with an EEG-based MI-BCI. Here the training contained two phases: a calibration phase and a rehabilitation phase, as illustrated in Fig. 1.

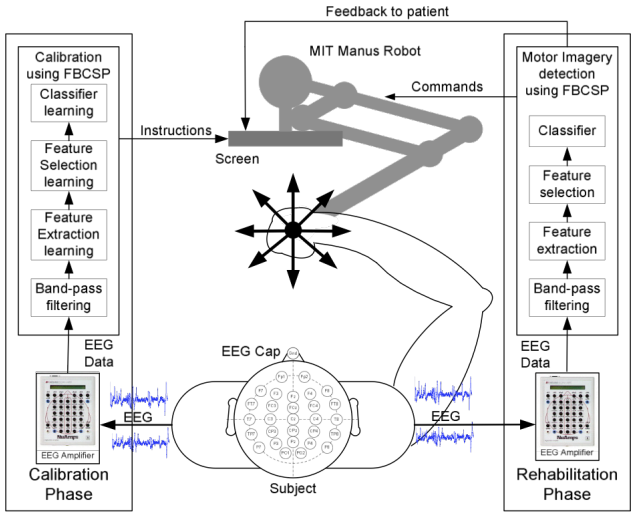

Fig. 1. Architecture of Motor Imagery-based Brain-Computer Interface (MI-BCI) for upper limb robotic rehabilitation

In the calibration phase, the patient's impaired upper limb is strapped to the MANUS robot, with a visual cue appearing on the screen and instructing the patient to perform MI or to rest. During the calibration, 160 trials (each trial lasted approximately 12 seconds) of EEG-data are collected from a total of 4 sessions, that comprised 80 MI trials of the stroke-affected upper limb and 80 rest condition trials, respectively. The EEG data were collected using a 27 channel Nuamps acquisition system (http://www.neuroscan.com), sampled at 250 Hz. The data collected in the calibration phase were subsequently used for constructing a subject-specific MI detection model by employing the Filter Bank Common Spatial Pattern (FBCSP) algorithm.[21] In the actual rehabilitation phase, the patient performed MI for 4 seconds after the onset of the visual cue. If MI was detected, a movement feedback was provided by the MANUS robot in moving the stroke-affected limb towards the goal displayed on the screen. A setup of the MI-BCI with the robotic feedback neurorehabilitation is shown in Fig. 2.

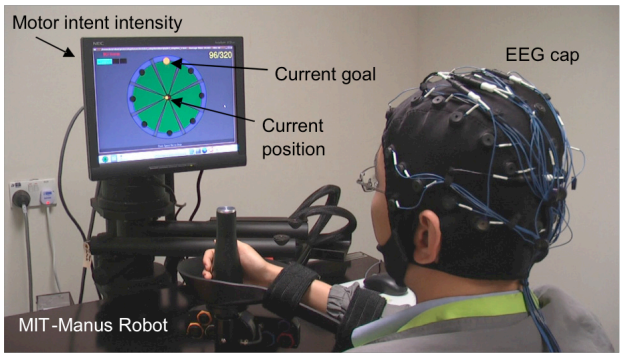

Fig. 2 The setup of the proposed Motor Imagery-based Brain-Computer Interface (MI-BCI) robotic rehabilitation in a local hospital.

All patients (both MANUS-only group and MI-BCI group) completed 12 rehabilitation sessions in approximately one month. In the MANUS group patients performed 960 fixed movements of the impaired limb, while the number of movements were variable in the MI-BCI group, due to the different protocol used. The main difference between the MANUS robotic rehabilitation protocol and the MI-BCI based robotic rehabilitation was that the former initiated robot-assisted movement if no movement was detected after a pre-defined period of 2 seconds, whereas the latter only initiated robot-assisted movement if actual voluntary motor intent was detected.

2.3 Rs-fMRI data acquisition

Rs-fMRI data of each participant was collected 6.33 (average) ± 6.98 (standard deviation) days before start of training (pre-timepoint, TP1) and 12.33 ± 6.10 days after stop of training (post-timepoint, TP2). For each measurement participants were instructed to remain

relaxed and awake with their eyes closed and not to engage in any specific activity. Each rs-fMRI session consisted of a 10 min block (400 volumes, 28 slices, 3x3x4 mm voxels, 0.4 mm slice gap, TR=1.5 secs, TE=30 ms, interleaved-ascending acquisition) and was performed in the same Siemens Magnetom Trio Tim syngo MR B15 scanner.

2.4 Calculation of functional motor gain from behavioral data

Fugl-Meyer (FM) scores were recorded for each participant at 0, 2, 4 and 12 weeks after beginning of training by a trained occupational therapist. By fitting a slope to the FM data of each participant an indicator of individual gain steepness was derived, by using the incline of each participants' functional outcome gain slope (see Figure 3). It is to note that by incorporating a 8 week post-training follow-up measurement (12 weeks after beginning), out-of-lab effects are part of the behavioral assessment thus reflecting the steepness of general recovery during and after treatment. The individual gain values were used as criteria in the subsequent regressions.

Patient - Internal Code	Oxford	Gender	Age	Side of Lesion	Stroke onset to therapy (months)	Screening to therapy (months)	FM Score at Screening Evaluation	Clinical Evaluation				Gain	Week 0 to Week 4 (in lab)	Week 4 to Week 12 (out-of-lab)
MANUS Group								Week 0 of Therapy	Week 2 of Therapy	Week 4 of Therapy	Week 12 of Therapy			
P1 - P015	BG	M	55	R	7,7	6,9	23	56	58	60	60	1,4	4,0	0,0
P2 - P033	BG	F	43	L	3,9	2,6	17	31	32	41	38	3,0	10,0	-3,0
P3 - P020	BG	M	54	R	8,8	8,1	4	54	55	59	59	1,9	5,0	0,0
Average			**50,67**		**6,80**	**5,87**	**14,67**	**47**	**48,33**	**53,33**	**52,33**	**2,1**	6,3	-1,0
MI-BCI Group			**6,66**		**6,50**	**5,52**	**9,71**	**13,9**	**14,2**	**10,7**	**12,4**	**0,82**		
P4 - P037	LENTIFORM NUCLEUS	M	33	L	3,2	1,3	4	24	24	23	27	0,8	-1,0	4,0
P5 - P010	MCA	M	23	R	18,6	7,9	39	47	47	54	53	2,5	7,0	-1,0
P6 - P012	BG	M	30	R	27,7	8,1	39	44	48	53	55	3,8	9,0	2,0
P7 - P029	CR	F	58	L	5,7	4,8	7	25	37	43	46	6,9	18,0	3,0
P8 - P034	MCA	M	40	R	4,4	2,3	9	19	16	19	23	1,5	0,0	4,0
P9 - P005	BG	M	57	R	35,1	10,2	28	24	26	31	24	0,5	7,0	-7,0
Average			**40,94**		**11,67**	**5,78**	**17,67**	**34,99**	**36,9**	**40,64**	**40,89**	**2,29**	5,6	0,2
SD			**14,50**		**13,51**	**3,54**	**16,28**	**11,84**	**13,08**	**15,08**	**14,97**	**2,40**		

Table 1, Participant data - including Oxford classification of stroke (BG=basal ganlia/thalamic, CR=Corona Radiata, MCA=Middle Cerebral Artey), Month is calculated as (Date1-Date2/30days). Time to therapy is the number of months that elapse between the stroke onset and week 0. Screening to therapy (month) is the number of months that elapse between the screening and week 0.

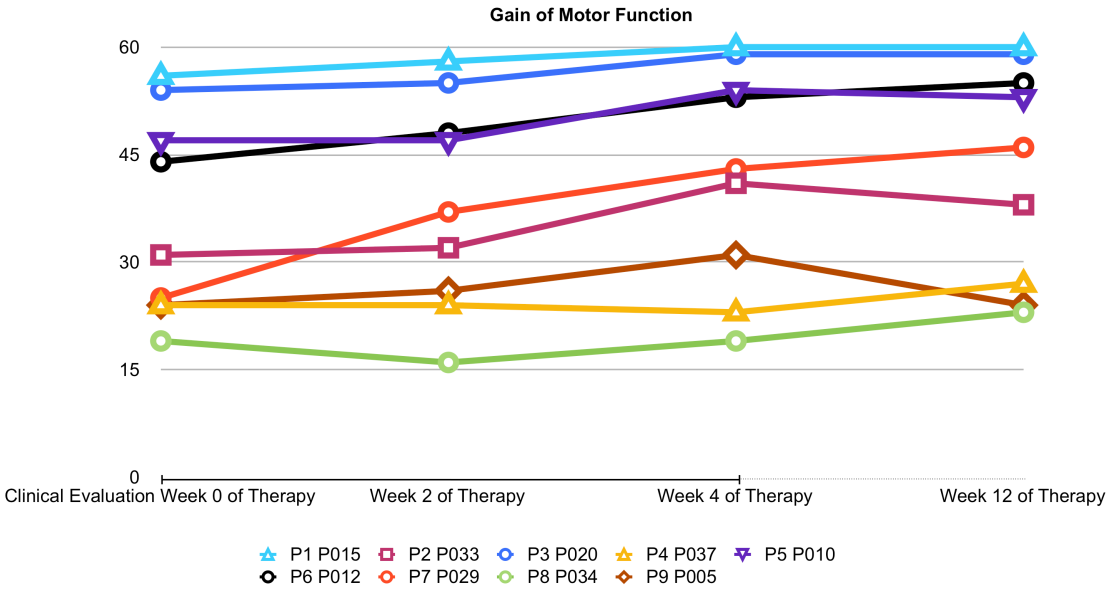

Figure 3, Gain of motor function in all participants over the four measurement timepoints and illustration of motor function gain calculation

2.5 Data preprocessing and ICA

Functional images were preprocessed (slice timing correction to middle slice, realignment with 4th degree B-spline interpolation, normalisation into Montral Neurological Institute space and smoothing at 8-mm FWHM) using SPM8 (Wellcome Trust Centre for Neuroimaging, London). For subjects with a deviating lesion location (three subjects had left hemispheric damage) all functional images were L/R flipped before the ICA step.

The rs-fMRI timeseries (9 subjects, 2 sessions per subject), recorded before the training (TP1), and the timeseries recorded after the training (TP2) were included into one Group ICA step using the 1.3d version of the MATLAB (The Mathworks, Natick, MA, USA) GIFT-ICA toolbox (main developer Calhoun & Adali, supported by NIH grant 1RO1EB000840, USA).[22]

The number of Independent Components (ICs) was calculated using the minimum description length criterion and was found to be 19. For estimation the ICASSO approach [23-24] was selected in order to ensure the validity and stability of the derived components (run 10 times, with both 'randinit' and 'bootstrap', component stability ranged above 0.9 for all used ICs). Each ICA was run with the Infomax algorithm, back-reconstruction was performed using the GICA3 implementation, data-preprocessing was done by removing the mean per time point, PCA options were standard (double precision, selective eigen solver, maximum number of reduction steps was two, batch estimation, minimum description length estimation

option mean, number of principle components to reduce each subject down to at reduction step one was 20, at two 16) and results were scaled to z-scores. After completion of the Group ICA calculation, the derived z-scored FC (IC) maps were used to form FC change (FCC) images by using the image-calc function of SPM8 and substracting for each subject and component the IC-images of TP1 from the IC-images of TP2. Thus positive values denoted increases of FC with the components functional centers (e.g. in Default Brain Mode ICs these are the Posterior Cingulate, medial Prefrontal Cortex etc.) in a given voxel, negative values a decrease respectively.

Depending on the IC and the center(s) of the component, these maps represent changes in FC from a region (the center of the component like e.g. SMA) or network (e.g. DMN) to any voxel in the brain. Although such maps might be highly similar to a correlation map acquired by correlating every voxel of the brain with a given seed region, IC maps show general covariation over the brain within a particular functional network. While an uncorrected seed-to-brain correlation map can contain statistical covariation that might partially be induced by signal covariations originating in non-neural phenomena (such as physiological noise), in theory such covariations (often spatially extending outside of gray matter tissue boundaries) would tendentially be grouped into separate ICs in an ICA analysis and not affect FC estimations. Changes in FC over time might reflect reorganizational processes, that have occured in between the measurements or minor fluctuations in measurement or estimation accuracy.

To guard against the latter possibility all FCC images were thresholded (FCC that did not exceed 0.5 in absolute value were set to zero) to assure that only substantial FCC beyond minor fluctuations was used. The resulting FCC images of these components were used as predictors in the subsequent regressions.

From the 19 identified components we selected four components that corresponded to FC networks of the motor system by comparing them with FC templates and inspecting them for spatial and spectral noise characteristica. The components centers were located in the contralesional Motor Cortex, ipsilesional Motor Cortex, Supplementary Motor Area (SMA) and visuospatial system (bilateral Parietal Cortex and Posterior Midline), respectively.

2.6 Linear Regression

In analogy to - but deviating from - the Multiple Regression approach as implemented in SPM8, we used an in-house Matlab script which substantiates linear regression with leave-one-out cross-validation.

In this approach the values of each observation (in our case each subjects FCC map) in each voxel are used to predict the corresponding criteria values. Prior to this step predictor and criteria values were z-scored for normalisation.

Predictor and criteria values were drawn from a training set corresponding to the entire set of observations minus one (N-1) which is withheld for subsequent testing. This is repeated N times, until each part of the set has served as a test set once, which substantiates a leave-one-out cross-validation.

For each cross-validation fold the squared error from predicting the criteria value using the predictor values of the withheld test set was recorded, giving N squared error values, from which the root mean squared error (RMSE) was calculated for each voxel. A voxel was considered as a significant predictor, thus indicating a plausible statistical link between the FCC in that voxel and the functional outcome gain, only if it fulfilled the following conservative criteria: (1) the RMSE was below one, so that the deviation of predicted value from real value was generally below one standard deviation, (2) the average of the linear regressions p-values was below 0.05, (3) the correlation of the predictor values (FCC) with the criteria values (FM gain) exceeds r=0.1, (4) the correlation of the predictor values (FCC) with the criteria values (FM gain) is significant (uncorrected) on a p=0.005 level and (5) the voxel is part of a cluster that passes an SPM-style cluster extent threshold (cubic) of 6 adjacent voxels. These criteria assure that only voxels which are statistcally significant predictors across all cross-validation folds (2) and with good prediction quality (1, 3 & 4) are considered further, which are located within clusters, where the probability of such a false-positive cluster of voxels where the FCC correlates with the criterion due to purely random variations in FCC equals $1{,}5625 * 10^{-14}$. It is to note that a cluster extent threshold of 6 is significantly above the empirically calculated extent thresholds provided by conventional SPM8 Multiple Regressions with identical significance thresholds for each components FCC maps (ipsilesional Motor Cortex component - expected voxels per cluster = 1,863, contralesional Motor Cortex component - expected voxels per cluster = 2,077, visuospatial component - expected voxels per cluster = 1,833, SMA component - expected voxels per cluster = 2,019).

This approach and these conservative thresholding criteria were chosen in order to compensate for the limited number of participants and to avoid obtaining results from overfitting, which might have occured for example if we would have used a whole-brain stepwise regression instead of a voxel-wise regression approach.

The procedure was repeated three times, first using all nine participants, second using only participants of the BCI group and third using only participants of the MANUS group.

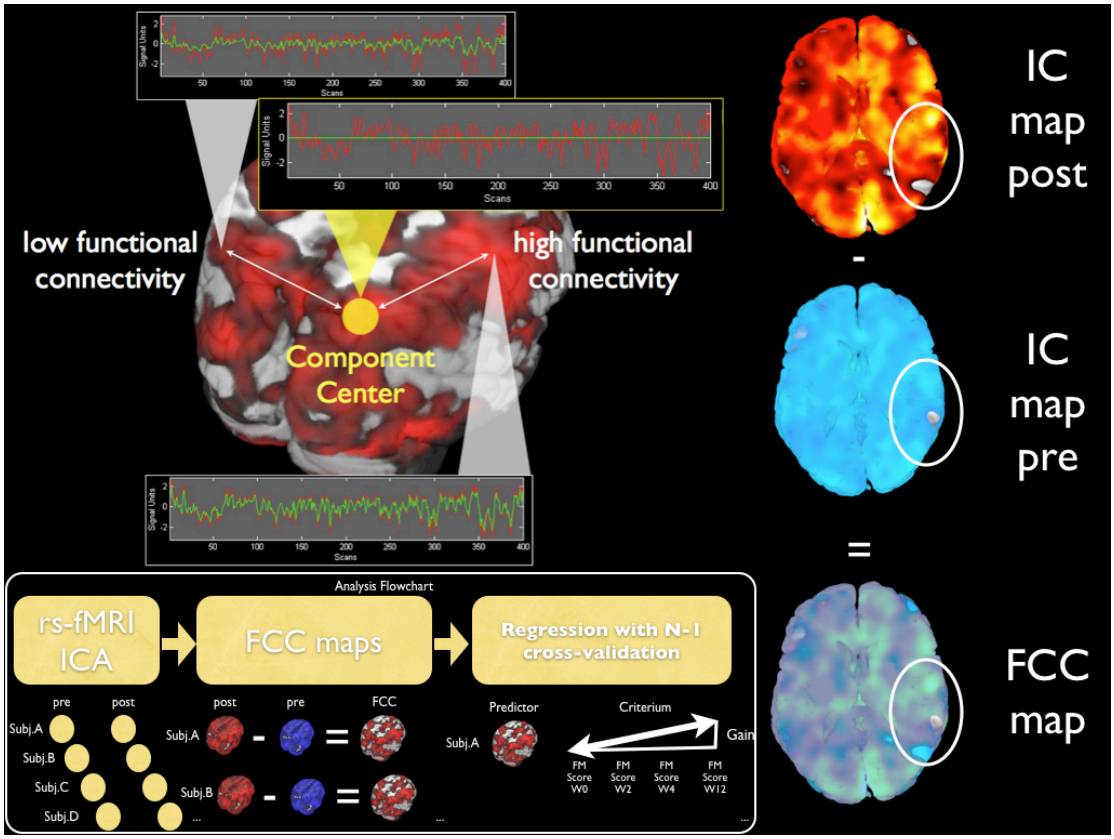

Figure 4, Method illustration, Generation of FC Change (FCC) maps from substraction of two IC maps, each representing magnitude of FC to a Component Center by image intensity

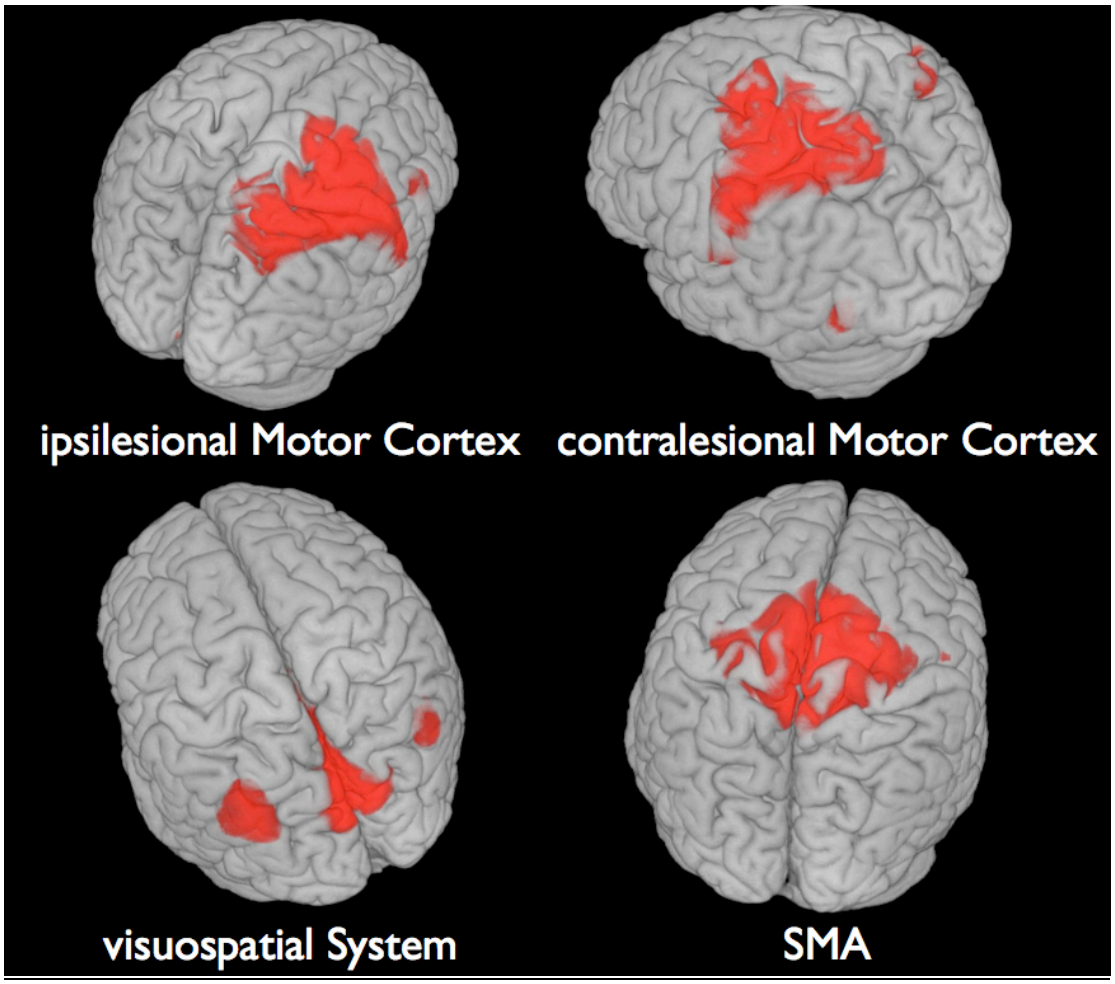

Figure 5, Four main components of the motor systems, as derived with ICA, red coloring indicates the IC centers

3. Results

3.1 ICA

Supporting earlier rs-fMRI findings [25] the classical sensorimotor component, comprising the bilateral motor cortices and an SMA part [26], could not be found in our stroke sample. The disconnection of the functional network into three distinct parts, but with bilaterally distinct intrahemispheric FC between primary somatosensory and Motor Cortex, is supported by the present findings using data-driven methods (ICA). The visuospatial system seems to be fully intact, as it would be expected in a healthy sample. A comparison of before training and after training component images reveals FCC in both directions (FC increases and FC decreases) in all components.

3.2 Motor gain prediction

The linear regression procedure and described thresholding produced no significant voxels for each group separately. When using both groups to associate voxel-wise FCC across all participants, significant voxels could be identified.

FCC of the ipsilesional Inferior Parietal Lobe (IPL, 12 voxels, FCC/motor-gain corr. r=0.87, RMSE 0.65) and contralesional Anterior Cingulate Cortex (ACC, 7 voxels, FCC motor gain corr. 0.88, RMSE 0.64) with the SMA were significant predictors of rehabilitation gain, as well as FCC of ipsilesional Middle Temporal Gyrus (MTG, 8 voxels, FCC motor gain corr. 0.89, RMSE 0.6), the ipsilesional Superior Medial Gyrus (SMG, 28 voxels, FCC motor gain corr. 0.88, RMSE 0.65) with the Visuospatial system, and FCC of ipsilesional Precuneus (17 voxels, FCC/motor-gain corr. r=0.87, RMSE 0.64), contralesional Precuneus (11 voxels, FCC/motor-gain corr. r=0.87, RMSE 0.63), contralesional Middle Orbital Gyrus (MOG, 7 voxels, FCC motor gain corr. 0.88, RMSE 0.64), contralesional MTG (9 voxels, FCC motor gain corr. 0.86, RMSE 0.66), ipsilesional Cerebellum (6 voxels, FCC/motor-gain corr. r=0.9, RMSE 0.57) with the contralesional Motor Cortex and FCC of contralesional MTG (12 voxels, FCC/motor-gain corr. r=0.88, RMSE 0.66), contralesional Superior Temporal Gyurs (STG, 35 voxels, FCC motor gain corr. 0.9, RMSE 0.55), contralesional Cerebellum (6 voxels, FCC/motor-gain corr. r=0.9, RMSE 0.52) with the ipsilesional Motor Cortex.

The changes in FC at rest in these regions are all positively correlated with the funtional motor gain values. When reviewing the correlations of individual FCC values and the motor gain values, strikingly no negative correlations could be identified. This indicates that in the present sample FC decreases were not positively correlated with individual motor gain. Higher FC increases on the other hand predicted better motor recovery (higher gain).

All results are provided in greater detail in the Supplementary Material, including those FCC that did not pass the cluster-extent threshold criterion but were observed in earlier studies as well, such as the beneficial FCC between the Middle Frontal Gyrus and ipsilesional Motor Cortex[27].

3.3 Exploratory group comparison

When further examining the group specific differences in terms of FCC, some functional connections seem to differ between the groups in terms of average FCC. The within-treatment-group FCC averages are different beyond both standard deviations for three functional connections (see Supplementary Material): Firstly, the FCC between the

ipsilesional Precuneus and the contralesional Motor Cortex, secondly the FCC between the contralesional Cerebellum and the ipsilesional Motor Cortex and thirdly between the STG and the ipsilesional Motor Cortex. The FCC values are consistently higher (equaling a relative FC increase) for the MI-BCI treatment group.

When comparing the gain steepness values from subjects of both groups, the average gain steepness is numerically higher in the MI-BCI treatment group (M:2,29 vs. MANUS M:2,1) but is as well more variable (MI-BCI SD:2,4 vs. MANUS SD:0,82), indicating a beneficial effect of BCI training on brain plasticity [28].

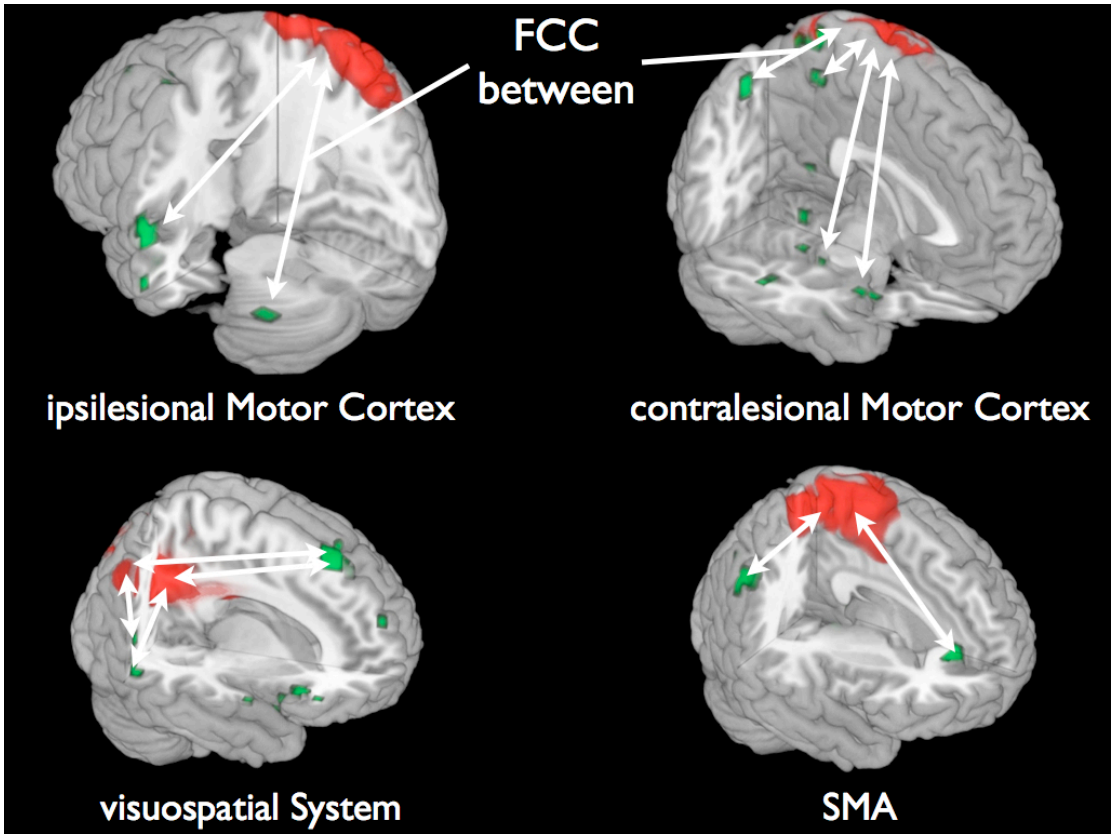

Figure 6, Functional connectivity (FC) between green and red changed (white arrows); FC Change (FCC) in green regions predict motor gain

4. Discussion

Over all subjects an increase of FC at rest, between the IPL and the SMA, as well as between the ACC and the SMA, was associated with better motor rehabilitation.

As reported earlier[29] the ACC can play a role in the attentional processes related to self-monitored movement predominantly in right hemispheric stroke – the IPL on the other hand, especially the posterior part, has been implicated [30,31] in the processes related to coding the intention to move and spatial processing in general. A strengthened association of these three

systems, namely the IPL, ACC and the SMA in a functional network could be beneficial for motor recovery, as it might constitute an adapted functional network for processing motor attention, cueing and movement initiation.

The visuospatial system has been associated with representing the world around us, as well as with processing visuo-spatial cues.[26] The FC increases with the ipsilesional MTG and Frontal Cortex (SMG), might indicate a strengthening of systems related to spatial awareness and spatial processing, which both have been associated with the Medial Gyrus and Temporal Lobe.[32] Especially the MTG has been associated with spatial mental imagery [33], which is a function that is targeted in the MI-BCI treatment.

The observed - supposedly beneficial - strengthening of functional connections between fronto-parietal regions which are known to play a key role in top-down processes and the visuospatial system and SMA, might be adaptations thate are counter-acting the deficits in the connectivity of these systems following stroke that have been described in resting-state studies earlier[34].

The functonal connectivity increases between the contralesional MTG, Precuneus, MOG and ipsilesional Cerebellum with the contralesional Motor Cortex, as well as the changes in FC between the contralesional MTG, STG, Cerebellum and the ipsilesional Motor Cortex, might reflect adaptive processes that occur during the reorganization of motor control and reflect increased recruitment of regions disconnected by the stroke[35] and have recently been described by other groups as well[36].

It has long been argued whether control from ipsilesional or contralesional Motor Cortex should be targeted as means of functional rehabilitation especially in subcortical stroke.[37-45] Our results indicate, that the process might be more complex than the idea of a mere role change for one single motor system and the silencing of another. It is possible that the contralesional Motor Cortex assumes only a temporary role in adaptive motor control, predominantly in the early stages of stroke recovery.[46]

We clearly recognize the limitations of our study, such as the limited group size and the short time between the two rs-fMRI sessions. It is possible that these results represent only a snapshot of the adaptive processes occuring in the recovering brain. Specifically in the light of recent findings on the link between perfusion, white matter connectivity[47] and FC future longitudinal studies need to evaluate the role of post-stroke changes in cerebral perfusion and tissue integrity in peri-lesional white matter bundles and gray matter structures[48] as potential mediators of FCC.

It might be an interesting experimental strategy, to form new trainings that target a strengthening of FC between the described regions, for example by means of real-time fMRI based neurofeedback training. In such a training the feedback could consist of not one single signal from one single region, merely giving the classical real time neurofeedback of activity, but rather consist directly of the correlation value itself, which could be derived from the voxel-to-voxel correlations calculated with a moving window and signals from multiple targeted sites (e.g. ACC and SMA). Such a neurofeedback could be used to directly train FC increases, rather than an activation of single sites.

4.1 Treatment group comparison

In an exploratory attempt we compared average FCC between the two treatment groups for all identified sites where the relation of FCC and motor recovery was significant.

Participants in the MI-BCI group showed stronger FC increases between the contralesional Cerebellum and the ipsilesional Motor Cortex, the contralesional STG and the ipsilesional Motor Cortex and the ipsilesional Precuneus and the contralesional Motor Cortex.

As these connections are known to be involved in MI performance, it might be hypothesized that the value of the MI-BCI treatment might not only be a numerically higher gain in upper limb motor function, but as well a strengthening of those functional networks which contribute to neural processing of MI. Good MI involving the paretic limb can not occur entirely outside of systems, that contain somatosensory and motoric memories of moving that limb, as it is unlikely that post-stroke MI involving the paretic limb is based on a re-creation of imagery, or any kind of mental content related to the limb, entirely from scratch. It is therefore not unlikely, that MI-BCI training strengthens the re-association of neural representations of the paretic limb and the experienced afference, and that this leads to better MI and better recovery.

5. Conclusions

Increases in rs-fMRI FC within parts of the motor system, and between motor regions and higher-order association cortices significantly predict better functional motor recovery. The increased FC at rest could be interpreted to reflect an after-effect of strenghtening neural connections within these networks. The fact that the extent of this FC increase is directly correlated with functional motor gain suggests a fascilatory effect of such connection strengthening on motor recovery, possibly implicating an increase in inter-regional

macroscopic neural cooperation as an explanation for this effect. Studies on larger populations and with sham-BCI-treament or control groups have to be conducted in order to clarify the stability of these results and to investigate the question, whether higher overall brain plasticity or only the strengthening of specific connections is beneficial for motor recovery.

Acknowledgments:

The authors thank the participants and the entire Singapore research team, recruiters, trainers, testers and nurses in the Tan Tock Seng Hospital rehabilitation center, as well as everybody involved in the data acquisition process. We would as well like to thank Prof. Chee for his help with the revision process and scanning.

Declaration of Conflicting Interests:

None.

Funding:

Author BV was partially funded by the European Union (HUMOUR 231724). We are thankful to the The Enterprise Challenge Grant, Singapore and Agency for Science, Technology and Research, Singapore for their funding support.

References:

1 McGinnis JM, Foege WH. Actual causes of death in the United States. Jama. 1993;270(18):2207.

2 Anderson CS, Linto J, Stewart-Wynne EG. A population-based assessment of the impact and burden of caregiving for long-term stroke survivors. Stroke. 1995;26(5):843.

3 Vestling M, Tufvesson B, Iwarsson S. Indicators for return to work after stroke and the importance of work for subjective well-being and life satisfaction. Journal of Rehabilitation Medicine. 2003;35(3):127–131.

4 Birbaumer N. Breaking the silence: brain–computer interfaces (BCI) for communication and motor control. Psychophysiology. 2006;43(6):517–532.

5 Buch E, Weber C, Cohen LG, et al. Think to move: a neuromagnetic brain-computer interface (BCI) system for chronic stroke. Stroke. 2008;39(3):910.

6 Grefkes C, Nowak DA, Eickhoff SB, et al. Cortical connectivity after subcortical stroke assessed with functional magnetic resonance imaging. Annals of neurology. 2008;63(2):236–246.

7 Ang KK, Guan C, Chua KSI et al. Clinical study of neurorehabilitation in stroke using eeg-based motor imagery brain-computer interface with robotic feedback. In: 32nd Annual International Conference of the IEEE Engineering in Medicine and Biology Society (EMBC), Buenos Aires, Argentina, 31 August - 4 September 2010.

8 Ang KK, Guan C, Chua SG, et al. A clinical study of motor imagery-based brain-computer interface for upper limb robotic rehabilitation. In: Engineering in Medicine and Biology Society, 2009. EMBC 2009. Annual International Conference of the IEEE.; 2009:5981–5984.

9 De Luca M, Beckmann CF, De Stefano N, Matthews PM, Smith SM. fMRI resting state networks define distinct modes of long-distance interactions in the human brain. Neuroimage. 2006;29(4):1359–1367.

10 Greicius MD, Srivastava G, Reiss AL, Menon V. Default-mode network activity distinguishes Alzheimer's disease from healthy aging: evidence from functional MRI. Proceedings of the National Academy of Sciences of the United States of America. 2004;101(13):4637.

11 Greicius MD, Krasnow B, Reiss AL, Menon V. Functional connectivity in the resting brain: a network analysis of the default mode hypothesis. Proceedings of the National Academy of Sciences of the United States of America. 2003;100(1):253.

12 Fransson P. Spontaneous low-frequency BOLD signal fluctuations: an fMRI investigation of the resting-state default mode of brain function hypothesis. Human brain mapping. 2005;26(1):15–29.

13 "Cordes D, Haughton VM, Arfanakis K, et al. Frequencies contributing to functional connectivity in the cerebral cortex in"" resting-state"" data. American Journal of Neuroradiology. 2001;22(7):1326. "

14 Dosenbach NU, Nardos B, Cohen AL, et al. Prediction of Individual Brain Maturity Using fMRI. Science. 2010;329(5997):1358.

15 Ystad M, Eichele T, Lundervold AJ, Lundervold A. Subcortical functional connectivity and verbal episodic memory in healthy elderly–A resting state fMRI study. NeuroImage. 2010;52(1):379–388.

16 Grefkes C, Fink GR. Reorganization of cerebral networks after stroke: new insights from neuroimaging with connectivity approaches. Brain : a journal of neurology. 2011;134(Pt 5):1264-76. Available at: http://www.pubmedcentral.nih.gov/articlerender.fcgi?artid=3097886&tool=pmcentrez&rendertype=abstract. Accessed August 6, 2011.

17 Westlake KP, Nagarajan SS. Functional connectivity in relation to motor performance and recovery after stroke. Frontiers in systems neuroscience. 2011;5(March):8. Available at: http://www.pubmedcentral.nih.gov/articlerender.fcgi?artid=3060711&tool=pmcentrez&rendertype=abstract. Accessed June 17, 2011.

18 Krebs HI, Hogan N. Therapeutic robotics: A technology push. Proceedings of the IEEE. 2006;94(9):1727–1738.

19 Krebs HI, Hogan N, Aisen ML, Volpe BT. Robot-aided neurorehabilitation. IEEE Transactions on Rehabilitation Engineering. 1998;6(1):75–87.

20 Krebs HI, Palazzolo JJ, Dipietro L, et al. Rehabilitation robotics: Performance-based progressive robot-assisted therapy. Autonomous Robots. 2003;15(1):7–20.

21 Ang KK, Chin ZY, Zhang H, Guan C. Filter bank common spatial pattern (FBCSP) in brain-computer interface. In: Neural Networks, 2008. IJCNN 2008.(IEEE World Congress on Computational Intelligence). IEEE International Joint Conference on.; 2008:2390–2397.

22 Calhoun VD, Liu J, AdalI T. A review of group ICA for fMRI data and ICA for joint inference of imaging, genetic, and ERP data. Neuroimage. 2009;45(1):S163–S172.

23 Himberg J, Hyvarinen A. Icasso: software for investigating the reliability of ICA estimates by clustering and visualization. In: Neural Networks for Signal Processing, 2003. NNSP'03. 2003 IEEE 13th Workshop on.; 2004:259–268.

24 Correa N, Adali T, Calhoun VD. Performance of blind source separation algorithms for fMRI analysis using a group ICA method. Magnetic resonance imaging. 2007;25(5):684–694.

25 van Meer M, van der Marel K, Wang K, et al. Recovery of sensorimotor function after experimental stroke correlates with restoration of resting-state interhemispheric functional connectivity. Journal of Neuroscience. 2010;30(11):3964.

26 Beckmann CF, DeLuca M, Devlin JT, Smith SM. Investigations into resting-state connectivity using independent component analysis. Philosophical Transactions of the Royal Society B: Biological Sciences. 2005;360(1457):1001.

27 Park C-hyun, Chang WH, Ohn SH, et al. Longitudinal changes of resting-state functional connectivity during motor recovery after stroke. Stroke; a journal of cerebral circulation. 2011;42(5):1357-62. Available at: http://www.ncbi.nlm.nih.gov/pubmed/21441147. Accessed June 19, 2011.

28 Caria A, Weber C, Brötz D, et al. Chronic stroke recovery after combined BCI training and physiotherapy: a case report. Psychophysiology. 2011;48(4):578-82. Available at: http://www.ncbi.nlm.nih.gov/pubmed/20718931. Accessed September 26, 2011.

29 Hanlon CA, Buffington AL, McKeown MJ. New brain networks are active after right MCA stroke when moving the ipsilesional arm. Neurology. 2005;64(1):114.

30 Ruiz S, Lee S, Schneider C, et al. Multivariate prediction of movement intention in the human fronto-parietal cortex. (submitted)

31 Desmurget M, Reilly KT, Richard N, et al. Movement intention after parietal cortex stimulation in humans. science. 2009;324(5928):811.

32 Karnath HO, Ferber S, Himmelbach M. Spatial awareness is a function of the temporal not the posterior parietal lobe. Nature. 2001;411(6840):950–953.

33 Mellet E, Tzourio N, Crivello F, et al. Functional anatomy of spatial mental imagery generated from verbal instructions. Journal of Neuroscience. 1996;16(20):6504.

34 Inman CS, James GA, Hamann S, et al. Altered resting-state effective connectivity of fronto-parietal motor control systems on the primary motor network following stroke. NeuroImage. 2011;59(1):227-237. Available at: http://www.ncbi.nlm.nih.gov/pubmed/21839174. Accessed September 23, 2011.

35 Bosnell R a, Kincses T, Stagg CJ, et al. Motor practice promotes increased activity in brain regions structurally disconnected after subcortical stroke. Neurorehabilitation

and neural repair. 2011;25(7):607-16. Available at: http://www.ncbi.nlm.nih.gov/pubmed/21646444. Accessed September 24, 2011.

36 Wang L, Yu C, Chen H, et al. Dynamic functional reorganization of the motor execution network after stroke. Brain : a journal of neurology. 2010;133(Pt 4):1224-38. Available at: http://www.ncbi.nlm.nih.gov/pubmed/20354002. Accessed July 18, 2011.

37 Calautti C, Baron JC. Functional neuroimaging studies of motor recovery after stroke in adults: a review. Stroke. 2003;34(6):1553.

38 Calautti C, Jones PS, Naccarato M, et al. The relationship between motor deficit and primary motor cortex hemispheric activation balance after stroke: longitudinal fMRI study. British Medical Journal. 2010.

39 Calautti C, Leroy F, Guincestre JY, Marié RM, Baron JC. Sequential activation brain mapping after subcortical stroke: changes in hemispheric balance and recovery. Neuroreport. 2001;12(18):3883.

40 Ward NS, Newton JM, Swayne OB, et al. Motor system activation after subcortical stroke depends on corticospinal system integrity. Brain. 2006;129(3):809.

41 Ward NS. Mechanisms underlying recovery of motor function after stroke. British Medical Journal. 2005;81(958):510.

42 Ward NS, Brown MM, Thompson AJ, Frackowiak RSJ. Neural correlates of motor recovery after stroke: a longitudinal fMRI study. Brain. 2003;126(11):2476.

43 Fridman EA, Hanakawa T, Chung M, et al. Reorganization of the human ipsilesional premotor cortex after stroke. Brain. 2004;127(4):747.

44 Tombari D, Loubinoux I, Pariente J, et al. A longitudinal fMRI study: in recovering and then in clinically stable sub-cortical stroke patients. Neuroimage. 2004;23(3):827–839.

45 Loubinoux I, Carel C, Pariente J, et al. Correlation between cerebral reorganization and motor recovery after subcortical infarcts. Neuroimage. 2003;20(4):2166–2180.

46 Rehme AK, Fink GR, von Cramon DY, Grefkes C. The Role of the Contralesional Motor Cortex for Motor Recovery in the Early Days after Stroke Assessed with Longitudinal fMRI. Cerebral Cortex. 2010.

47 Aslan S, Huang H, Uh J, et al. White matter cerebral blood flow is inversely correlated with structural and functional connectivity in the human brain. NeuroImage. 2011;56(3):1145-53. Available at:

http://www.pubmedcentral.nih.gov/articlerender.fcgi?artid=3085605&tool=pmcentrez&rendertype=abstract. Accessed August 17, 2011.

48 Várkuti B, Cavusoglu M, Kullik A, et al. Quantifying the link between anatomical connectivity, gray matter volume and regional cerebral blood flow: an integrative MRI study. Sporns O, ed. PloS one. 2011;6(4):e14801. Available at: http://dx.plos.org/10.1371/journal.pone.0014801. Accessed June 23, 2011.

Supplementary Table

Results of multiple regression analysis for all included components, green and orange colors mark particularly strong FCC differences between treatment groups

FCC to	from Region	No_of_voxels	Correlation with motor gain	RMSE	Average p-value	Average FCC MANUS	Average FCC BCI	SD FCC MANUS	SD FCC BCI	MNI coord
ipsilesional Motor Cortex	Ipsil. Calcarine Gyrus	1	0,84	0,76	0,0172	-0,113	0,511	0,36	0,226	12 -55 10
ipsilesional Motor Cortex	Ipsil. Precuneus	2	0,9	0,72	0,0224	-0,134	0,518	0,350	0,221	12 -55 14
ipsilesional Motor Cortex	Contral. Cuneus	2	0,85	0,73	0,0131	-0,150	0,471	0,359	0,31	-6 -76 26
ipsilesional Motor Cortex	Contral. Precuneus	3	0,88	0,66	0,0171	-0,14	0,464	0,348	0,306	-12 -49 18
ipsilesional Motor Cortex	Contral. Superior Parietal Lobule	1	0,85	0,7	0,0103	-0,14	0,464	0,349	0,304	-18 -64 46
ipsilesional Motor Cortex	Contral. Lingual Gyrus	1	0,85	0,7	0,0075	-0,149	0,459	0,352	0,320	-24 -61 -6
ipsilesional Motor Cortex	Contral. Middle Frontal Gyrus	1	0,85	0,75	0,0125	-0,145	0,480	0,349	0,275	-30 26 54
ipsilesional Motor Cortex	Contral. Inferior Parietal Lobule	1	0,85	0,73	0,0131	-0,145	0,47	0,349	0,295	-33 -74 42
ipsilesional Motor Cortex	Contral. Precentral Gyrus	1	0,91	0,59	0,0017	-0,134	0,471	0,35	0,29	-33 2 62
ipsilesional Motor Cortex	Contral. Cerebellum	6	0,90	0,53	0,0121	-0,105	0,577	0,357	0,242	-39 -55 -26
ipsilesional Motor Cortex	Contral. Fusiform Gyrus	2	0,86	0,70	0,0182	-0,122	0,581	0,350	0,249	-39 -58 -22
ipsilesional Motor Cortex	Contral. Middle Temporal Gyrus	12	0,9	0,67	0,0078	-0,085	0,377	0,373	0,316	-60 -7 -22
ipsilesional Motor Cortex	Contral. Superior Temporal Gyrus	35	0,90	0,55	0,0121	-0,133	0,507	0,354	0,229	-63 -10 6
ipsilesional Motor Cortex	Contral. SupraMarginal Gyrus	2	0,87	0,70	0,011	-0,105	0,522	0,364	0,215	-60 -28 22
ipsilesional Motor Cortex	Contral. Heschls Gyrus	1	0,89	0,6	0,0186	-0,091	0,524	0,385	0,215	-60 -10 10
ipsilesional Motor Cortex	OP 4	1	0,84	0,77	0,0261	-0,086	0,522	0,396	0,215	-63 -10 10
contralesional Motor Cortex	Ipsil. Middle Temporal Gyrus	2	0,89	0,6	0,0096	-0,135	0,499	0,356	0,2	60 -28 -14
contralesional Motor Cortex	Ipsil. Fusiform Gyrus	2	0,90	0,5	0,0125	-0,151	0,496	0,360	0,258	48 -31 -18
contralesional Motor Cortex	Ipsil. Superior Temporal Gyrus	1	0,85	0,72	0,0069	-0,138	0,511	0,351	0,223	45 -1 -14
contralesional Motor Cortex	Ipsil. Putamen	2	0,86	0,71	0,0067	-0,129	0,503	0,350	0,235	36 -13 -6
contralesional Motor Cortex	Ipsil. Amygdala	1	0,86	0,70	0,0098	-0,131	0,50	0,350	0,236	27 5 -18
contralesional Motor Cortex	Ipsil. Olfactory cortex	2	0,92	0,6	0,0019	-0,141	0,509	0,4	0,225	27 11 -18
contralesional Motor Cortex	Ipsil. Insula Lobe	1	0,84	0,78	0,0125	-0,133	0,511	0,349	0,223	27 14 -18
contralesional Motor Cortex	Ipsil. Cerebellum	6	0,90	0,58	0,0134	-0,087	0,499	0,404	0,239	15 -40 -14
contralesional Motor Cortex	Ipsil. Precuneus	17	0,88	0,65	0,0137	-0,176	0,492	0,37	0,283	12 -70 46
contralesional Motor Cortex	Ipsil. Superior Parietal Lobule	2	0,86	0,70	0,0211	-0,172	0,496	0,370	0,284	15 -67 50
contralesional Motor Cortex	Cerebellar Vermis	1	0,85	0,76	0,0150	-0,160	0,488	0,378	0,285	3 -46 -10
contralesional Motor Cortex	Contral. Cerebellum	1	0,87	0,67	0,022	-0,175	0,47	0,370	0,323	-3 -52 -14
contralesional Motor Cortex	Contral. Precuneus	11	0,88	0,63	0,0191	-0,19	0,357	0,416	0,331	-6 -58 66
contralesional Motor Cortex	Contral. Middle Cingulate Cortex	1	0,88	0,70	0,0074	-0,169	0,350	0,413	0,340	-3 -43 54
contralesional Motor Cortex	Contral. Calcarine Gyrus	1	0,91	0,53	0,0080	-0,182	0,362	0,412	0,328	-6 -52 6
contralesional Motor Cortex	Contral. Insula Lobe	4	0,87	0,70	0,0255	-0,216	0,36	0,432	0,328	-30 26 -6
contralesional Motor Cortex	Contral. Postcentral Gyrus	4	0,88	0,68	0,0048	-0,12	0,381	0,427	0,321	-42 -28 54
contralesional Motor Cortex	Contral. Middle Orbital Gyrus	7	0,89	0,65	0,0078	-0,161	0,414	0,411	0,30	-42 50 -6
contralesional Motor Cortex	Contral. Inferior Frontal Gyrus (p. Orbitalis)	4	0,89	0,64	0,005	-0,229	0,341	0,480	0,392	-45 29 -10
contralesional Motor Cortex	Contral. Inferior Frontal Gyrus (p. Opercularis)	1	0,88	0,66	0,0058	-0,220	0,354	0,481	0,379	-45 8 6
contralesional Motor Cortex	Contral. Middle Temporal Gyrus	9	0,87	0,67	0,0190	-0,133	0,492	0,390	0,454	-63 -43 -10
Visuospatial System	Ipsil. Temporal Pole	2	0,87	0,68	0,0062	-0,105	0,519	0,387	0,399	27 8 -22
Visuospatial System	Ipsil. Middle Temporal Gyrus	8	0,87	0,69	0,0071	-0,205	0,344	0,386	0,393	48 -55 14
Visuospatial System	Ipsil. Inferior Frontal Gyrus (p. Triangularis)	3	0,85	0,77	0,0119	-0,195	0,337	0,389	0,404	48 38 -2
Visuospatial System	Ipsil. Insula Lobe	5	0,87	0,69	0,0100	-0,150	0,352	0,388	0,389	42 17 -10
Visuospatial System	Ipsil. Inferior Frontal Gyrus (p. Orbitalis)	1	0,86	0,73	0,0138	-0,159	0,341	0,388	0,40	42 29 -2
Visuospatial System	Ipsil. Amygdala	2	0,86	0,76	0,006	-0,150	0,340	0,388	0,398	27 5 -18
Visuospatial System	Ipsil. Olfactory cortex	2	0,85	0,77	0,0158	-0,138	0,337	0,395	0,403	24 8 -14
Visuospatial System	Ipsil. Superior Orbital Gyrus	3	0,87	0,7	0,0180	-0,157	0,337	0,388	0,404	21 20 -14
Visuospatial System	Ipsil. Superior Medial Gyrus	28	0,89	0,62	0,0085	0,084	0,314	0,225	0,231	12 35 62
Visuospatial System	Contral. Superior Medial Gyrus	3	0,86	0,73	0,0117	0,107	0,314	0,220	0,251	0 32 58
Visuospatial System	Contral. Middle Frontal Gyrus	4	0,88	0,65	0,0158	0,076	0,244	0,236	0,32	-42 20 50
Visuospatial System	Contral. Middle Temporal Gyrus	4	0,88	0,64	0,0172	0,09	0,302	0,222	0,242	-60 -46 2
SMA	Ipsil. Inferior Parietal Lobule	12	0,87	0,69	0,0087	-0,180	0,265	0,513	0,302	51 -52 50
SMA	Ipsil. Postcentral Gyrus	1	0,84	0,80	0,0327	-0,156	0,282	0,481	0,271	45 -34 58
SMA	Ipsil. Angular Gyrus	1	0,85	0,73	0,0218	-0,167	0,279	0,491	0,274	39 -64 50
SMA	Cerebellar Vermis	1	0,86	0,70	0,0181	-0,147	0,284	0,479	0,270	3 -61 -38
SMA	Contral. Anterior Cingulate Cortex	7	0,90	0,65	0,0044	-0,033	0,181	0,391	0,404	-3 35 6
SMA	Contral. Cerebellum	3	0,86	0,71	0,0230	-0,008	0,249	0,378	0,363	-9 -34 -10
SMA	Contral. Thalamus	2	0,9	0,71	0,0138	0,001	0,262	0,380	0,365	-18 -19 10
SMA	Contral. Fusiform Gyrus	5	0,85	0,71	0,0248	0,003	0,290	0,365	0,317	-21 -46 -14
SMA	Contral. Hippocampus	4	0,86	0,70	0,0274	0,003	0,291	0,371	0,312	-21 -40 2
SMA	Contral. Superior Frontal Gyrus	1	0,88	0,64	0,0126	-0,008	0,278	0,368	0,308	-21 41 34
SMA	Contral. Precuneus	1	0,85	0,75	0,0236	0,007	0,297	0,374	0,32	-24 -52 10
SMA	Contral. Inferior Temporal Gyrus	3	0,87	0,71	0,0066	-0,018	0,250	0,377	0,322	-48 -25 -18
SMA	Contral. Middle Temporal Gyrus	1	0,8	0,73	0,0101	-0,039	0,24	0,380	0,340	-45 -25 -18

7.4 Chapter 4 - On the relationship of Brain-Computer Interface aptitude and Anatomical Connectivity

SMR EEG-BCI aptitude in healthy subjects varies with the integrity of Corpus Callosum white matter

Author list and affiliation:

Bálint Várkuti[1]

Sebastian Halder[1,2]

Martin Bogdan[2,3]

Andrea Kübler[4]

Wolfgang Rosenstiel[2]

Ranganatha Sitaram[1]

Niels Birbaumer[1,5]

1 Institute of Medical Psychology and Behavioral Neurobiology, University of Tübingen, Tübingen, Baden-Württemberg, Germany

2 Wilhelm-Schickard Institute for Computer Science, University of Tübingen, Tübingen, Baden-Württemberg, Germany

3 Computer Engineering, University of Leipzig, Johannisgasse 26, 04103 Leipzig, Germany

4 Department of Psychology I, University of Würzburg, Marcusstr. 9-11, 97070 Würzburg, Germany

5 Ospedale San Camillo, Istituto di Ricovero e Cura a Carattere Scientifico, Laboratorio di Neuroscience comportamentale, Venezia, Italy

Abstract

Healthy subjects differ in terms of their ability to control EEG based BCIs, but the reasons for this remain unclear. Deviating from the classical perspective of analyzing psychological intermediary variables we investigated whether the structural trait of inter-hemispheric white matter integrity differs between subjects that can be classified as low and high aptitude users. For this purpose 17 healthy subjects participated in a Diffusion Tensor Imaging measurement as well as in a SMR EEG-BCI session. We extracted the individual Corpus Callosum (CC) Fractional Anisotropy (FA) values from each subject and compared them across the two user groups. The difference is significant (two-sample t-test, p=0.0187) and the values differ in the expected direction (CC mean FA low aptitude users 0.53 vs. high aptitude users 0.58). We conclude that individual inter-hemispheric connectivity traits might influence our ability to optimally master SMR EEG-BCI control.

1 Introduction

The use of some EEG based BCIs depends critically on an individuals ability to voluntarily alter the own brain activity in a directed manner and with relatively precise timing. Psychological variables such as attention, training and the right mental strategy or technique, equipment related variables such as sufficient Signal-to-Noise-Ratio (SNR) during the EEG recording and adequate processing as well as functional variables such as individual neural plasticity and normality of the EEG features (spectral properties, modulability of BCI-critical features) are relevant to successful BCI control.

The link between the individual anatomy and these features becomes most apparent in patients with severe lesions (e.g. due to stroke) or neurodegenerative disease, who show altered EEG features, reduced neural plasticity, locally altered SNR and altered neuropsychological properties, all of which are strongly influencing their EEG-BCI capability. But how does this relate to the considerable variability in the BCI aptitude of healthy users with normal brain anatomy ?

Recent studies Valdés-Hernández et al. (2010a) have indicated a critical role of central white matter for the spectral properties of an individuals EEG, underlining the significance of certain fiber bundles for appropriate inter-regional conduction velocity in intra-cerebral neural signaling. The relative equivalency of this conduction velocity across individuals is critical in assuring that cognitive processes are running on comparable timescales. But there is as well considerable variability in

the integrity of fiber bundles between subjects. While the fiber bundles in the healthy brain form always some standard connections (the connectome core so to speak), there are connections that vary and which are an individual trademark of our brain - just like a fingerprint. While most of these connections are intra-hemispheric and located within diverse association fiber bundles (e.g. Superior Longitudinal Fascicle, Capsula Externa) that spread over each hemispheres cerebral white matter, roughly more than one third of all macroscopic inter-regional anatomical connections in the brain are inter-hemispheric and traverse through a few localized commissural structures such as the Corpus Callosum, which could be termed the bottlenecks of inter-hemispheric connectivity. SMR modulation through means of motor imagery is known to be a complex task, involving multiple cortical and subcortical structures and the timely integration of their respective neural computations into a coherent and continuous mental construct accessible to consciousness and voluntary control. The overall integration and the time-critical signaling processes within this bi-hemispheric task-dependent neural network must therefore strongly rely on commissural connections.

We tested the hypothesis that the structural substrate of inter-hemispheric anatomical connectivity has an influence on individual BCI aptitude, by splitting a group of SMR EEG-BCI users into a high and a low aptitude group and comparing the structural properties of their main commissural connection (namely the Fractional Anisotropy of the Corpus Callosum).

2 Methods

2.1 Participants

Twenty healthy participants (seven female and 13 male, mean age 24.5 years SD 3.7, range 19-36) took part in the study which was approved by the Internal Review Board of the Medical Faculty, University of Tu?bingen. All participants had no prior experience with SMR BCIs , had no history of neurological diseases and were German native speakers. The data from three subjects had to be excluded due to image and scanner artifacts. A detailed overview of EEG BCI performance, performed imagery tasks and demographic data of all participants can be found in Halder et al. (2011).

2.2 EEG-BCI setup and definition of low and high aptitude users

The EEG recording was performed using four 32 channel Brainamp DC amplifiers manufactured by Brainproducts, Munich, Germany. A 128 channel cap manufactured by Easy Cap, Munich, Germany was used. Of these 119 were used for EEG recording and positioned according to the extended 10-20 system Sharbrough et al. (1991), referenced to the nasion and grounded to an electrode between Fz and Fpz. The EEG was recorded at 1000 Hz, band-pass filtered between 0.05 Hz to 200 Hz and notch filtered at 50 Hz. Electromyogram (EMG) artifacts were monitored with bipolar electrodes on both forearms and the participants preferred leg. Electrooculogram (EOG) artifacts were recorded with electrodes placed above and below the right eye for vertical EOG (superior and inferior orbital fossa), and for horizontal EOG with electrodes placed at the outer canthi of the eyes. This data was used to exclude artifact contaminated trials. Each of the participants performed a single EEG BCI session. This included measurements in which the participant had to perform motor execution, observation and imagery. Three imagery measurements which totaled 75 trials of three classes (left hand, right hand, foot) were used to calibrate the feedback parameters. The calibration trials had a duration of 8 seconds, in 4 of which the participant performed the task. After calibration three feedback measurements were performed in which the participant had to use the two classes which showed the highest discriminability in the calibration data to control a cursor Blankertz et al. (2010b). Feedback trials had a length of 9 seconds, 4 of which were feedback. The additional second is used to indicate which class is to be performed in the current trial. In total 300 feedback trials were performed (150 per class). The accuracy of the participants achieved in these 300 trials was used to categorize them into high and low aptitude SMR BCI users by a median split.

2.3 MRI recording

The MRI measurements were performed in a Siemens Magneton Trio Tim 3T whole body scanner using a standard 12 channel head coil. Each subject participated in a DTI measurement (1.8 x 1.8 x 6.5 mm voxels, 5 mm gap, TR=3 sec, TE=93 ms, FoV=1150*1150, Flip Angle=90?, 20 transversal slices, 128x128 voxels per slice, 20 diffusion directions, b-value=1000 s/mm2) with the field of view (FoV) comprising the full cerebrum.

Subject	Gender	Age	Aptitude group	CC mean FA
1	M	23	high	0.6071
2	F	22	high	0.5815
3	M	22	low	0.5450
4	F	23	low	0.5183
5	F	22	low	0.6241
6	M	23	high	0.5567
7	F	30	high	0.5476
8	F	25	low	0.5379
9	F	26	low	0.5168
10	M	25	low	0.5458
11	M	22	low	0.4735
12	F	20	low	0.5557
13	M	22	high	0.5926
14	M	28	low	0.5250
15	M	23	high	0.5970
16	M	24	high	0.6321
17	M	19	high	0.5698

Table 1 – Sample characteristics

2.4 Analysis of DTI data

First the Fractional Anisotropy (FA) image from the DTI data was calculated for each individual participant. The voxel-wise Fractional Anisotropy values indicate the orientedness of the diffusion tensor - the more ellipsoid shaped a tensor is the more the surrounding tissue is restricting isotropic diffusion (which would produce a spheric diffusion tensor as it can be found e.g. in the ventricular cerebro-spinal fluid). High fiber density, large fiber diameter, high myelination, large directional similarity of fibers in the voxel and high structural integrity give higher FA values in white matter. White matter has usually FA values between 0.2/0.3 and 1. After calculation of the FA-image the normalization parameters to Montreal Neurological Institute (MNI) standard space (using the SPM8 EPI template) were estimated for the FA-image aligned B0-image of the DTI sequence using statistical parametric mapping (SPM) Version 8. The normalization parameters were then inverted to warp the standard label image of the ICBM-DTI-81 Atlas into each participants original DTI space, avoiding any interpolation of the original FA values. For region 4 of the ICBM-DTI-81 Atlas (Body of Corpus Callosum) the median and mean of FA values for all voxels with an FA value above 0.25 was extracted and saved in the participant/CC FA value table.

3 Results

CC mean FA does not significantly differ for Gender (p=0.64) nor does it correlate with Age (r=-0.24, p=0.35) but significantly differs between high and low aptitude users (two-sample t-test, p=0.0187). The result remains significant if CC median FA is used instead of mean FA (p=0.0136). High aptitude users have a higher CC mean FA value (0.58 vs 0.53), indicating higher fiber density, larger fiber diameter, higher myelination, stronger directional similarity of fibers or overall higher structural integrity (or a combination of all) for their CC region.

4 Discussion

A covariation of structural brain traits with BCI aptitude can be interpreted in various ways. Structural trait differences between high and low aptitude users could indicate the existence of a latent variable, that influences both BCI aptitude as well as the structural integrity of the CC. This variable could be a psychological or neurobiological trait that we have not yet been able to measure. On the other hand CC structural integrity could directly influence the EEG BCI use on the physical level of signal generation through restricting timely inter-hemispheric signaling and integration, as well as on the plasticity level as it could influence the timing of Hebb'ian learning and conditioning processes and impair or enhance general learning or learning speed. The higher structural integrity of the CC could further indicate a higher number of inter-hemispheric anatomical connections in the high aptitude group that might correspond to superior inter-hemispheric communication and integration. If any of these interpretations is true, one would expect further behavioral or psychological correlates of this altered connectivity pattern or connection quality.

5 Conclusion

Our study forms a starting point for the exploration of the influence of structural brain traits on BCI aptitude in general. While our first finding might indicate an influence of commissural connectivity on one's ability to use a SMR EEG BCI, further data is necessary to evaluate the overall impact of variations in inter-hemispheric connectivity on learning processes. We plan to extend our approach to incorporate further measures of individual structural brain traits into a more comprehensive model and to explore the role of inter-hemispheric connectivity in EEG BCI

use.

References

Allison, B. Z., McFarland, D. J., Schalk, G., Zheng, S. D., Jackson, M. M., and Wolpaw, J. R. (2008). Towards an independent brain-computer interface using steady state visual evoked potentials. *Clin Neurophysiol*, 119(2):399–408.

Ashburner, J. and Friston, K. J. (2005). Unified segmentation. *NeuroImage*, 26(3):839–51.

Berger, H. (1929). Über das elektrenkephalogramm des menschen. *Arch Psychiatr Nervenkr*, pages 527–570.

Birbaumer, N., Elbert, T., Canavan, A. G., and Rockstroh, B. (1990). Slow potentials of the cerebral cortex and behavior. *Physiol Rev*, 70(1):1–41.

Birbaumer, N., Ghanayim, N., Hinterberger, T., Iversen, I., Kotchoubey, B., Kübler, A., Perelmouter, J., Taub, E., and Flor, H. (1999). A spelling device for the paralysed. *Nature*, 398(6725):297–298.

Birbaumer, N., Murguialday, A. R., and Cohen, L. (2008). Brain-computer interface in paralysis. *Curr Opin Neurol*, 21(6):634–638.

Blankertz, B., Lemm, S., Treder, M., Haufe, S., and Müller, K.-R. (2010a). Single-trial analysis and classification of ERP components - A tutorial. *Neuroimage*.

Blankertz, B., Losch, F., Krauledat, M., Dornhege, G., Curio, G., and Müller, K.-R. (2008). The Berlin Brain–Computer Interface: accurate performance from first-session in {BCI}-na{ï}ve subjects. *IEEE Trans Biomed Eng*, 55(10):2452–2462.

Blankertz, B., Sannelli, C., \textbfHalder, S., Hammer, E. M., Kübler, A., Müller, K.-R., Curio, G., and Dickhaus, T. (2010b). Neurophysiological predictor of {SMR}-based {BCI} performance. *Neuroimage*, 51(4):1303–1309.

Farwell, L. A. and Donchin, E. (1988). Talking off the top of your head: toward a mental prosthesis utilizing even-related brain potentials. *Electroencephalogr Clin Neurophysiol*, 70:510–523.

Filippini, N., Douaud, G., Mackay, C. E., Knight, S., Talbot, K., and Turner, M. R. (2010). Corpus callosum involvement is a consistent feature of amyotrophic lateral sclerosis. *Neurology*, 75(18):1645–52.

Grosse-Wentrup, M., Schölkopf, B., and Hill, J. (2010). Causal influence of gamma oscillations on the sensorimotor rhythm. *Neuroimage*.

Guger, C., Daban, S., Sellers, E., Holzner, C., Krausz, G., Carabalona, R., Gramatica, F., and Edlinger, G. (2009). How many people are able to control a P300-based brain-computer interface (BCI)? *Neurosci Lett*, 462(1):94–98.

Halder, S., Agorastos, D., Veit, R., Hammer, E. M., Lee, S., Varkuti, B., Bogdan, M., Rosenstiel, W., Birbaumer, N., and Kübler, A. (2011). Neural mechanisms of brain-computer interface control. *Neuroimage*.

Hammer, E. M., \textbfHalder, S., Blankertz, B., Sannelli, C., Dickhaus, T., Kleih, S., Müller, K.-R., and Kübler, A. (subm). Psychological predictors of {SMR-BCI} performance. *Biol Psychol*.

Hari, R. and Salmelin, R. (1997). Human cortical oscillations: a neuromagnetic view through the skull. *Trends Neurosci*, 20(1):44–49.

Hochberg, L. R., Serruya, M. D., Friehs, G. M., Mukand, J. A., Saleh, M., Caplan, A. H., Branner, A., Chen, D., Penn, R. D., and Donoghue, J. P. (2006). Neuronal ensemble control of prosthetic devices by a human with tetraplegia. *Nature*, 442(7099):164–171.

Kübler, A. and Neumann, N. (2005). Brain-computer interfaces–the key for the conscious brain locked into a paralyzed body. *Prog Brain Res*, 150:513–525.

Kübler, A., Neumann, N., Kaiser, J., Kotchoubey, B., Hinterberger, T., and Birbaumer, N. P. (2001). Brain-computer communication: self-regulation of slow cortical potentials for verbal communication. *Arch Phys Med Rehabil*, 82(11):1533–1539.

Kübler, A., Neumann, N., Wilhelm, B., Hinterberger, T., and Birbaumer, N. (2004). Brain-computer predictability of brain-computer communication. *Journal of Psychophysiology*, 18(2-3):121–129.

Kübler, A., Nijboer, F., Mellinger, J., Vaughan, T. M., Pawelzik, H., Schalk, G., McFarland, D. J., Birbaumer, N., and Wolpaw, J. R. (2005). Patients with {ALS} can use sensorimotor rhythms to operate a brain-computer interface. *Neurology*, 64(10):1775–1777.

Kuhlman, W. N. (1978). Functional topography of the human {Mu} rhythm. *Electroencephalogr Clin Neurophysiol*, 44(1):83–93.

Mellinger, J., Schalk, G., Braun, C., Preissl, H., Rosenstiel, W., Birbaumer, N., and Kübler, A. (2007). An {MEG}-based brain-computer interface ({BCI}). *Neuroimage*, 36(3):581–593.

Middendorf, M., McMillan, G., Calhoun, G., and Jones, K. S. (2000). Brain-computer interfaces based on the steady-state visual-evoked response. *IEEE Trans Rehabil Eng*, 8(2):211–214.

Monti, M. M., Vanhaudenhuyse, A., Coleman, M. R., Boly, M., Pickard, J. D., Tshibanda, L., Owen, A. M., and Laureys, S. (2010). Willful modulation of brain activity in disorders of consciousness. *N Engl J Med*, 362(7):579–589.

Neuper, C., Müller, G. R., Kübler, A., Birbaumer, N., and Pfurtscheller, G. (2003). Clinical application of an {EEG}-based brain-computer interface: a case study in a patient with severe motor impairment. *Clin Neurophysiol*, 114(3):399–409.

Neuper, C., Scherer, R., Wriessnegger, S., and Pfurtscheller, G. (2009). Motor imagery and action observation: modulation of sensorimotor brain rhythms during mental control of a brain-computer interface. *Clin Neurophysiol*, 120(2):239–247.

Nijboer, F., Furdea, A., Gunst, I., Mellinger, J., McFarland, D. J., Birbaumer, N., and Kübler, A. (2008a). An auditory brain-computer interface ({BCI}). *J Neurosci Methods*, 167(1):43–50.

Nijboer, F., Sellers, E. W., Mellinger, J., Jordan, M. A., Matuz, T., Furdea, A., \textbfHalder, S., Mochty, U., Krusienski, D. J., Vaughan, T. M., Wolpaw, J. R., Birbaumer, N., and Kübler, A. (2008b). A {P300}-based brain-computer interface for people with amyotrophic lateral sclerosis. *Clin Neurophysiol*, 119(8):1909–1916.

Pfurtscheller, G. (1981). Central beta rhythm during sensorimotor activities in man. *Electroencephalogr Clin Neurophysiol*, 51(3):253–264.

Pfurtscheller, G., Allison, B. Z., Brunner, C., Bauernfeind, G., Solis-Escalante, T., Scherer, R., Zander, T. O., Mueller-Putz, G., Neuper, C., and Birbaumer, N. (2010). The hybrid BCI. *Front Neurosci*, 4:30.

Pfurtscheller, G. and da Silva, F. H. (1999). Event-related {EEG}/{MEG} synchronization and desynchronization: basic principles. *Clin Neurophysiol*, 110(11):1842–1857.

Pfurtscheller, G., Neuper, C., Andrew, C., and Edlinger, G. (1997). Foot and hand area mu rhythms. *Int J Psychophysiol*, 26(1-3):121–135.

Pistohl, T., Ball, T., Schulze-Bonhage, A., Aertsen, A., and Mehring, C. (2008). Prediction of arm movement trajectories from {ECoG}-recordings in humans. *J Neurosci Methods*, 167(1):105–114.

Polich, J. (2007). Updating {P300}: an integrative theory of {P3a} and {P3b}. *Clin Neurophysiol*, 118(10):2128–2148.

Raven, J., Raven, J. C., and Court, J. H. (2003). *Manual for {Raven}'s Progressive Matrices and Vocabulary Scales. {S}ection {I}: General overview.* Harcourt Assessment.

Regan, D. (1977). Steady-state evoked potentials. *J Opt Soc Am*, 67(11):1475–1489.

Sato, K., Aoki, S., Iwata, N. K., Masutani, Y., Watadani, T., Nakata, Y., Yoshida, M., Terao, Y., Abe, O., Ohtomo, K., and Tsuji, S. (2010). Diffusion tensor tract-specific analysis of the uncinate fasciculus in patients with amyotrophic lateral sclerosis. *Neuroradiology*, 52(8):729–33.

Schäfer, J. and Strimmer, K. (2005). A shrinkage approach to large-scale covariance matrix estimation and implications for functional genomics. *Stat Appl Genet Mol Biol*, 4:Article32.

Scholz, J., Klein, M. C., Behrens, T. E. J., and Johansen-Berg, H. (2009). Training induces changes in white-matter architecture. *Nature neuroscience*, 12(11):1370–1.

Senda, J., Kato, S., Kaga, T., Ito, M., Atsuta, N., Nakamura, T., Watanabe, H., Tanaka, F., Naganawa, S., and Sobue, G. (2011). Progressive and widespread brain damage in ALS: MRI voxel-based morphometry and diffusion tensor imaging study. *Amyotrophic lateral sclerosis : official publication of the World Federation of Neurology Research Group on Motor Neuron Diseases*, 12(1):59–69.

Sharbrough, F. W., Chatrian, G.-E., Lesser, R. P., Lüders, H., Nuwer, M., and Picton, T. W. (1991). American Electroencephalographic Society guidelines for standard electrode position nomenclature. *J Clin Neurophysiol*, 8(2):200–202.

Silvoni, S., Volpato, C., Cavinato, M., Marchetti, M., Priftis, K., Merico, A., Tonin, P., Koutsikos, K., Beverina, F., and Piccione, F. (2009). P300-Based Brain-Computer Interface Communication: Evaluation and Follow-up in Amyotrophic Lateral Sclerosis. *Front Neurosci*, 3:60.

Sitaram, R., Caria, A., Veit, R., Gaber, T., Rota, G., Kübler, A., and Birbaumer, N. (2007). {FMRI} brain-computer interface: a tool for neuroscientific research and treatment. *Comput Intell Neurosci*, page 25487.

Sorger, B., Dahmen, B., Reithler, J., Gosseries, O., Maudoux, A., Laureys, S., and Goebel, R. (2009). Another kind of 'BOLD Response': answering multiple-choice questions via online decoded single-trial brain signals. *Prog Brain Res*, 177:275–292.

Takeuchi, H., Sekiguchi, A., Taki, Y., Yokoyama, S., Yomogida, Y., Komuro, N., Yamanouchi, T., Suzuki, S., and Kawashima, R. (2010). Training of working memory impacts structural connectivity. *The Journal of neuroscience : the official journal of the Society for Neuroscience*, 30(9):3297–303.

Tang, Y.-Y., Lu, Q., Geng, X., Stein, E. A., Yang, Y., and Posner, M. I. (2010). Short-term meditation induces white matter changes in the anterior cingulate. *Proceedings of the National Academy of Sciences of the United States of America*, 107(35):15649–15652.

Teipel, S. J., Pogarell, O., Meindl, T., Dietrich, O., Sydykova, D., Hunklinger, U., Georgii, B., Mulert, C., Reiser, M. F., Möller, H.-J., and Hampel, H. (2009a). Regional networks underlying interhemispheric connectivity: an EEG and DTI study in healthy ageing and amnestic mild cognitive impairment. *Hum Brain Mapp*, 30(7):2098–2119.

Teipel, S. J., Pogarell, O., Meindl, T., Dietrich, O., Sydykova, D., Hunklinger, U., Georgii, B., Mulert, C., Reiser, M. F., Möller, H.-J., and Hampel, H. (2009b). Regional networks underlying interhemispheric connectivity: an EEG and DTI study in healthy ageing and amnestic mild cognitive impairment. *Human brain mapping*, 30(7):2098–119.

Valdés-Hernández, P. A., Ojeda-González, A., Martínez-Montes, E., Lage-Castellanos, A., Virués-Alba, T., Valdés-Urrutia, L., and Valdes-Sosa, P. A. (2010a). White matter architecture rather than cortical surface area correlates with the EEG alpha rhythm. *Neuroimage*, 49(3):2328–2339.

Valdés-Hernández, P. a., Ojeda-González, A., Martínez-Montes, E., Lage-Castellanos, A., Virués-Alba, T., Valdés-Urrutia, L., and Valdes-Sosa, P. a. (2010b). White matter architecture rather than cortical surface area correlates with the EEG alpha rhythm. *NeuroImage*, 49(3):2328–39.

Whitford, T. J., Kubicki, M., Ghorashi, S., Schneiderman, J. S., Hawley, K. J., McCarley, R. W., Shenton, M. E., and Spencer, K. M. (2010). Predicting inter-hemispheric transfer time from the diffusion properties of the corpus callosum in healthy individuals and schizophrenia patients: A combined ERP and DTI study. *NeuroImage*, 54(3):2318–2329.

Woolley, S. C., Zhang, Y., Schuff, N., Weiner, M. W., and Katz, J. S. (2011). Neuroanatomical correlates of apathy in ALS using 4 Tesla diffusion tensor MRI. *Amyotrophic lateral sclerosis*

: official publication of the World Federation of Neurology Research Group on Motor Neuron Diseases, 12(1):52–8.

Wriessnegger, S. C., Kurzmann, J., and Neuper, C. (2008). Spatio-temporal differences in brain oxygenation between movement execution and imagery: a multichannel near-infrared spectroscopy study. *Int J Psychophysiol*, 67(1):54–63.